

*If you can imagine it you can create it.
If you can dream it, you can become it.*

William A. Ward

UNIVERSITY OF ALBERTA

**EFFECT OF ULTRASONIC WAVES ON IMMISCIBLE AND
MISCIBLE DISPLACEMENT IN POROUS MEDIA**

by

Tarek Hamida



A thesis submitted to the Faculty of Graduate Studies and Research
in partial fulfillment of the requirements for the degree of

Master of Science
in
Petroleum Engineering

Department of Civil and Environmental Engineering

Edmonton, Alberta
Fall 2006



Library and
Archives Canada

Bibliothèque et
Archives Canada

Published Heritage
Branch

Direction du
Patrimoine de l'édition

395 Wellington Street
Ottawa ON K1A 0N4
Canada

395, rue Wellington
Ottawa ON K1A 0N4
Canada

Your file *Votre référence*
ISBN: 978-0-494-22279-9
Our file *Notre référence*
ISBN: 978-0-494-22279-9

NOTICE:

The author has granted a non-exclusive license allowing Library and Archives Canada to reproduce, publish, archive, preserve, conserve, communicate to the public by telecommunication or on the Internet, loan, distribute and sell theses worldwide, for commercial or non-commercial purposes, in microform, paper, electronic and/or any other formats.

The author retains copyright ownership and moral rights in this thesis. Neither the thesis nor substantial extracts from it may be printed or otherwise reproduced without the author's permission.

AVIS:

L'auteur a accordé une licence non exclusive permettant à la Bibliothèque et Archives Canada de reproduire, publier, archiver, sauvegarder, conserver, transmettre au public par télécommunication ou par l'Internet, prêter, distribuer et vendre des thèses partout dans le monde, à des fins commerciales ou autres, sur support microforme, papier, électronique et/ou autres formats.

L'auteur conserve la propriété du droit d'auteur et des droits moraux qui protègent cette thèse. Ni la thèse ni des extraits substantiels de celle-ci ne doivent être imprimés ou autrement reproduits sans son autorisation.

In compliance with the Canadian Privacy Act some supporting forms may have been removed from this thesis.

Conformément à la loi canadienne sur la protection de la vie privée, quelques formulaires secondaires ont été enlevés de cette thèse.

While these forms may be included in the document page count, their removal does not represent any loss of content from the thesis.

Bien que ces formulaires aient inclus dans la pagination, il n'y aura aucun contenu manquant.


Canada

Abstract

In recent years, field tests and laboratory experiments have demonstrated that high intensity acoustic stimulation may enhance oil recovery. Not only is such technology economically feasible but it also serves as an environmentally friendly and economical alternative to currently accepted tertiary recovery techniques. Despite a vast body of empirical and theoretical support, this technology lacks sufficient understanding to make meaningful, consistent engineering predictions. Much of what we believe is happening within ultrasonically stimulated porous media is speculative and theoretical, and lacks fundamental experimental research.

This work aims at studying the influence of high-frequency ultrasonic radiation on the miscible and immiscible displacement of oil in capillary media. Three experimental strategies are presented. We first investigate the effect of ultrasound on flow through a capillary via the pendant drop method. Water was injected into a capillary submerged into various processed mineral oils and kerosene. The average drop rate per minute was measured at several ultrasonic intensities, and we determined that there exists a peak drop rate at a characteristic intensity which depends on oil viscosity and the interfacial tension between water and the oil. The second set of experiments comprises of Hele-Shaw type experiments designed to study instabilities at liquid-liquid interfaces when ultrasound is applied. Fractal analysis techniques were used to quantify the degree of fingering and branching, allowing a rough assessment of the degree of perturbation generated at the interface. Miscible Hele-Shaw experiments are also presented to illustrate the effect of viscous forces alone. We found that ultrasound acts to stabilize the interfacial front, and that such effect is most pronounced at low viscosity ratios. The third series of experiments focuses on the effect of ultrasound on spontaneous (capillary) imbibition of an aqueous phase into oil-saturated Berea sandstone and Indiana limestone plugs. Both counter-current and co-current geometries were tested.

Acknowledgements

First and foremost, I would like to express my deepest gratitude and debt to my loving parents, Mohamed and Maritta Hamida, whose continual guidance and support has gotten me this far. They have taught me the value of love, dedication and hard work by their own example. Without them I could not have finished this work!

My sincere thanks to my supervisor, Dr. Tayfun Babadagli, who has supported my vision to embark on studying a relatively unorthodox branch of petroleum engineering. His courage and support to try new things are very much appreciated.

I also wish to extend my warmest appreciation and thanks to my friend Sean Watt, who did not only make my experiments possible, but also supported and encouraged me at every step of my thesis, especially in times of great frustration. His extraordinary commitment to students and colleagues make him one of the finest men I have ever had the pleasure of working with!

Many thanks to Dr. Peter Toma for so many valuable discussions and good advice on how to improve my experiments, especially the pendant drop experiments. I also would like to thank Dr. Ergun Kuru for supplying me with the necessary lab space to conduct my Hele-Shaw experiments, and Dr. Ramon Bentsen for his invaluable guidance through the complicated kaleidoscope of viscous fingering. Additionally, I am grateful to Dr. Zhenghe Xu for reading my thesis and providing me with insightful suggestions. The cooperation and knowledge I received from all faculty members of our department is also wholly acknowledged. Special thanks go to Dr. Yucel Akkutlu with whom I shared many stimulating discussions. His attitude towards teaching, knowledge and research is exemplary, and an inspiration to me!

This work was partly funded by an NSERC Grant (No: G121210595). The funds for the equipment used in the experiments were obtained from the Canadian Foundation for Innovation (CFI) (Project # 7566) and the University of Alberta. I gratefully acknowledge these supports.

Last but not least, I am grateful to my sisters, Nadja and Leila, for always being there for me, and giving me company during many stressful days. I also want to extend my love and appreciation to my lovely girlfriend, Jinxiu Qi, for supporting me in every step of my research and being so incredibly patient and understanding.

Tarek Hamida
July 1st, 2006

*This thesis is dedicated with great love and appreciation
to my wonderful parents*

MOHAMED and MARITTA HAMIDA

Their love and support have made me who I am today.

And

*Jalila
Nadia
Leila
Samira*

and my lovely Jinny.

TABLE OF CONTENTS

1	INTRODUCTION	1
1.1	STATEMENT OF THE PROBLEM.....	4
1.2	LITERATURE REVIEW.....	6
1.2.1	ACOUSTICS IN POROUS MEDIA	6
1.2.2	ACOUSTIC STIMULATION	12
1.3	SUMMARY.....	24
2	PENDANT DROP EXPERIMENTS	29
2.1	INTRODUCTION.....	29
2.2	EXPERIMENTAL SETUP.....	31
2.3	FLUID PROPERTIES.....	32
2.4	EXPERIMENTAL PROCEDURE.....	32
2.5	RESULTS AND DISCUSSION.....	33
2.6	CONCLUSIONS.....	35
3	HELE-SHAW EXPERIMENTS	39
3.1	INTRODUCTION.....	39
3.2	FRACTAL ANALYSIS.....	43
3.3	EXPERIMENTAL SETUP.....	46
3.4	EXPERIMENTAL PROCEDURE.....	47
3.5	IMAGE PROCESSING.....	49
3.6	RESULTS AND DISCUSSION.....	50
3.6.1	IMMISCIBLE HELE-SHAW EXPERIMENTS	50
3.6.1.1	Constant rate: Water.....	50
3.6.1.2	Constant rate: 3% DOWFAX 2A1.....	52
3.6.1.3	Constant pressure: Water.....	55
3.6.1.4	Constant pressure: 3% DOWFAX 2A1.....	58
3.6.2	MISCIBLE HELE-SHAW EXPERIMENTS	59
3.6.2.1	Constant Pressure.....	59
3.6.2.2	Constant Rate.....	61
3.7	CONCLUSIONS.....	62
4	SPONTANEOUS (CAPILLARY) IMBIBITION	120
4.1	INTRODUCTION.....	120
4.2	EXPERIMENTAL SETUP.....	123
4.2.1	ROCK AND FLUID PROPERTIES	123
4.2.2	EXPERIMENTAL SETUP	125
4.2.3	PROCEDURE	127
4.3	RESULTS AND DISCUSSION.....	128
4.3.1	WATER INTO DRY CORE SAMPLES	129

4.3.1.1	Berea sandstone	129
4.3.1.2	Indiana limestone	129
4.3.1.3	Discussion	129
4.3.2	WATER AND BRINE INTO MINERAL OIL AND KEROSENE	131
4.3.2.1	Water.....	131
4.3.2.2	Brine.....	134
4.3.3	ANIONIC AND NONIONIC SURFACTANT SOLUTIONS	135
4.3.3.1	DOWFAX 3B0	135
4.3.3.2	DOWFAX 2A1	136
4.3.3.3	Tergitol 15-S-7.....	137
4.3.3.4	Discussion	138
4.3.4	SPONTANEOUS IMBIBITION OF XANTHAN GUM SOLUTION INTO BEREA SANDSTONE	140
4.3.5	HUSKY CRUDE OIL	141
4.4	CONCLUSIONS	142
REFERENCES		173
APPENDIX A: EQUIPMENT		193
APPENDIX B: PUBLICATIONS RESULTING FROM THIS WORK		195

LIST OF TABLES

TABLE 2-1: PROPERTIES OF THE FLUIDS USED IN PENDANT DROP EXPERIMENTS.	36
TABLE 3-1: FRACTAL DIMENSIONS FOR VARIOUS KNOWN ANALYTICAL FRACTALS. THE MINKOWSKI-BOULIGAND FRACTAL DIMENSION (ALSO KNOWN AS HAUSDORFF DIMENSION) WAS CALCULATED USING FRACLAC V.2 (KARPERIEN 2005). THE CONTENTS OF THIS TABLE ARE PLOTTED ON A CROSS-COMPARISON PLOT IN FIGURE 3-4.....	64
TABLE 4-1: FLUID PROPERTIES OF OLEIC AND AQUEOUS PHASES USED IN SPONTANEOUS IMBIBITION EXPERIMENTS. ALL VALUES WERE MEASURED AT STANDARD ATMOSPHERIC CONDITIONS. DOWFAX 2A1 = SODIUM DODECYL DIPHENYLOXIDE DISULFONATE. TERGITOL 15-S-7 = ALCOHOL ETHOXYLATE.	147
TABLE 4-2: INTERFACIAL TENSION DATA FOR ALL FLUID PAIRS USED IN THIS THESIS. ALL VALUES WERE MEASURED AT STANDARD ATMOSPHERIC CONDITIONS.	148
TABLE 4-3: PROPERTIES OF DOWFAX 2A1 AND DOWFAX 3B0 SURFACTANTS (EXTRACTED FORM A PAMPHLET BY DOW CHEMICAL COMPANY).....	149
TABLE 4-4: PROPERTIES OF TERGITOL 15-S-7 SURFACTANT (EXTRACTED FORM A PAMPHLET BY DOW CHEMICAL COMPANY).....	149

LIST OF FIGURES

FIGURE 1-1: A SUMMARY OF CURRENTLY ACCEPTED ENHANCED OIL RECOVERY METHODS. OUTLINED IN BLACK ARE THE VIBRO-MECHANICAL OPTIONS WITH WHICH THIS DISSERTATION IS PRIMARILY CONCERNED. (ADOPTED FROM FAROUQ ALI AND THOMAS (1996)).	27
FIGURE 1-2: THE COMPARATIVE LENGTH SCALES IN RELATION TO BIOT'S MODEL OF POROELASTICITY AND GRAIN SIZES IN MILLIMETERS: (A) ASTM SOIL CLASSIFICATION, (B) EFFECTIVE PORE SIZE, (C) APPROXIMATE PERMEABILITY, (D) FREQUENCY. THE SHADED AREA CORRESPONDS TO BIOT'S ALLOWABLE FREQUENCY RANGE (BASED ON SOME OF HIS ASSUMPTIONS).	27
FIGURE 1-3: THE COMPLEX INTERPLAY OF VARIOUS PHYSICAL MECHANISMS BELIEVED TO BE PRESENT WHEN ULTRASOUND IS APPLIED TO POROUS MEDIA. ANY SUPERPOSITION OF THESE MECHANISMS MAY RESULT IN EITHER A REDUCTION OR ENHANCEMENT OF FLOW IN POROUS MEDIA.	28
FIGURE 2-1: EXPERIMENTAL SETUP OF THE PENDANT DROP EXPERIMENTS.	37
FIGURE 2-2: WATER DROP COUNT PER MINUTE VERSUS ULTRASONIC TRANSDUCER EXCITATION AMPLITUDE FOR VARIOUS OIL TYPES.	37
FIGURE 2-3: SNAP SHOTS OF PENDANT DROPS JUST BEFORE DETACHMENT. A WIDE RANGE OF VISCOSITY AND INTERFACIAL TENSION WAS INVESTIGATED BY USING (A) LIGHT MINERAL OIL, (B) HEAVY MINERAL OIL, (C) KEROSENE, AND (D) HIGH VISCOSITY PROCESSED MINERAL OIL N350. NUMBERS AT THE TOP OF EACH IMAGE INDICATES THE ULTRASONIC SETTING [0 = NO ULTRASOUND; 5 = HIGH ULTRASOUND]. AFTER INSPECTING THE SHAPE OF THE DROPS VISUALLY, IT CAN BE READILY CONCLUDED THAT INTERFACIAL TENSION DOES NOT NOTICEABLY CHANGE WITH ULTRASONIC INTENSITY.	38
FIGURE 3-1: DLA PATTERNS GENERATED WITH DIFFERENT AGGREGATES SIZES. SHOWN HERE ARE THE DLA PATTERNS AFTER 16700, 33400 AND 50,000 AGGREGATES. THE PATTERNS WERE GENERATED WITH IMAGEJ'S DLA GENERATOR (COURTESY OF AUDREY KARPERIEN (2006)).	65
FIGURE 3-2: ONE DIMENSIONAL POLYADIC CANTOR SETS WITH A GENERATOR OF 4^k INTERVALS AND A REDUCTION FACTOR OF $1/7^k$. ALL SETS HAVE A FRACTAL DIMENSION IN THE LIMITING CASE IS $D_B = \text{LOG}(4)/\text{LOG}(7) = 0.7124$. THIS EXAMPLE ILLUSTRATES THE IMPORTANCE OF TEXTURE OR LACUNARITY IN FRACTAL ANALYSIS, AND SHOWS THAT THE FRACTAL DIMENSION IS ONLY ONE OF SEVERAL FRACTAL DESCRIPTORS.	66
FIGURE 3-3: VARIOUS ANALYTICAL FRACTALS AND THEIR HAUSDORFF DIMENSION USED TO VERIFY FRACTALAC (KARPERIEN 2005). THE RESULTS ARE SHOWN IN TABLE 3-1, AND CROSS-PLOTTED IN FIGURE 3-4. ALL FRACTALS WERE GENERATED WITH WOLFRAM'S MATHEMATICA 5.	67
FIGURE 3-4: CROSS-COMPARISON PLOT OF THE FRACTAL DIMENSIONS OBTAINED FROM FRACTALAC V.2 (KARPERIEN 2005) VERSUS THE ANALYTICAL FRACTAL DIMENSION. THE 45° LINE CORRESPONDS TO THE CASE WHERE THE COMPUTED	

FRactal dimension through box counting equals the analytically determined value. Dashed lines represent the percent deviation from equality.	68
FIGURE 3-5: (A) HELE-SHAW CELL. (B) EXPERIMENTAL SETUP.	69
FIGURE 3-6: WORK FLOW OF IMAGE PROCESSING OF ALL HELE-SHAW PATTERNS.	70
FIGURE 3-7: IMMISCIBLE HELE-SHAW PATTERNS FOR WATER INJECTED INTO HEAVY MINERAL OIL AT A CONSTANT RATE OF 0.3 CC/MIN. THE SCALE IS IN CENTIMETERS. THE CONTOURS REPRESENT THE LOCATION OF THE INTERFACE AT 10 SECOND INTERVALS. $\mu_o = 167.0 \pm 1.7$ CP; IFT = 51.0 ± 1.0 DYNES/CM.	71
FIGURE 3-8: IMMISCIBLE HELE-SHAW PATTERNS FOR WATER INJECTED INTO HEAVY MINERAL OIL AT A CONSTANT RATE OF 1.0 CC/MIN. THE SCALE IS IN CENTIMETERS. THE CONTOURS REPRESENT THE LOCATION OF THE INTERFACE AT 10 SECOND INTERVALS. $\mu_o = 167.0 \pm 1.7$ CP; IFT = 51.0 ± 1.0 DYNES/CM.	71
FIGURE 3-9: IMMISCIBLE HELE-SHAW PATTERNS FOR WATER INJECTED INTO HEAVY MINERAL OIL AT A CONSTANT RATE OF 1.5 CC/MIN. THE SCALE IS IN CENTIMETERS. THE CONTOURS REPRESENT THE LOCATION OF THE INTERFACE AT 10 SECOND INTERVALS. $\mu_o = 167.0 \pm 1.7$ CP; IFT = 51.0 ± 1.0 DYNES/CM.	72
FIGURE 3-10: IMMISCIBLE HELE-SHAW PATTERNS FOR WATER INJECTED INTO HEAVY MINERAL OIL AT A CONSTANT RATE OF 2.0 CC/MIN. THE SCALE IS IN CENTIMETERS. THE CONTOURS REPRESENT THE LOCATION OF THE INTERFACE AT 10 SECOND INTERVALS. $\mu_o = 167.0 \pm 1.7$ CP; IFT = 51.0 ± 1.0 DYNES/CM.	72
FIGURE 3-11: (A) FRACTAL PERIMETER AND (B) FRACTAL AREA AS A FUNCTION OF TIME FOR WATER INTO HEAVY MINERAL OIL (HMO) AT FOUR CONSTANT INJECTION RATES: 0.3, 1.0, 1.5, AND 2.0 CC/MIN. THE VISCOSITY AND INTERFACIAL TENSION OF LMO (WITH SURFACTANT) IS 167.0 ± 1.7 CP AND 51.0 ± 1.0 DYNES/CM, RESPECTIVELY. PATTERNS FOR 0.3, 1.0, 1.5, AND 2.0 CC/MIN ARE SHOWN IN FIGURE 3-7 TO FIGURE 3-10. SOLID POINTS REPRESENT THE CASE WITHOUT ULTRASOUND, AND EMPTY POINTS WITH 72W, 20 KHZ ULTRASOUND.	73
FIGURE 3-12: (A) FRACTAL DIMENSION AND (B) LACUNARITY AS A FUNCTION OF TIME FOR WATER INTO HEAVY MINERAL OIL (HMO) AT FOUR CONSTANT INJECTION RATES: 0.3, 1.0, 1.5, AND 2.0 CC/MIN. THE VISCOSITY AND INTERFACIAL TENSION OF HMO (WITH SURFACTANT) IS 167.0 ± 1.7 CP AND 51.0 ± 1.0 DYNES/CM, RESPECTIVELY. PATTERNS FOR 0.3, 1.0, 1.5, AND 2.0 CC/MIN ARE SHOWN IN FIGURE 3-7 TO FIGURE 3-10. SOLID POINTS REPRESENT THE CASE WITHOUT ULTRASOUND, AND EMPTY POINTS WITH 72W, 20 KHZ ULTRASOUND.	74
FIGURE 3-13: IMMISCIBLE HELE-SHAW PATTERNS FOR WATER INJECTED INTO LIGHT MINERAL OIL AT A CONSTANT RATE OF 0.3 CC/MIN. THE SCALE IS IN CENTIMETERS. THE CONTOURS REPRESENT THE LOCATION OF THE INTERFACE AT 10 SECOND INTERVALS. $\mu_o = 46.5 \pm 0.5$ CP; IFT = 61.8 ± 1.2 DYNES/CM.	75
FIGURE 3-14: IMMISCIBLE HELE-SHAW PATTERNS FOR WATER INJECTED INTO LIGHT MINERAL OIL AT A CONSTANT RATE OF 1.0 CC/MIN. THE SCALE IS IN	

CENTIMETERS. THE CONTOURS REPRESENT THE LOCATION OF THE INTERFACE AT 10 SECOND INTERVALS. $\mu_o = 46.5 \pm 0.5$ CP; IFT = 61.8 ± 1.2 DYNES/CM.	75
FIGURE 3-15: IMMISCIBLE HELE-SHAW PATTERNS FOR WATER INJECTED INTO LIGHT MINERAL OIL AT A CONSTANT RATE OF 1.5 CC/MIN. THE SCALE IS IN CENTIMETERS. THE CONTOURS REPRESENT THE LOCATION OF THE INTERFACE AT 10 SECOND INTERVALS. $\mu_o = 46.5 \pm 0.5$ CP; IFT = 61.8 ± 1.2 DYNES/CM.	76
FIGURE 3-16: IMMISCIBLE HELE-SHAW PATTERNS FOR WATER INJECTED INTO LIGHT MINERAL OIL AT A CONSTANT RATE OF 2.0 CC/MIN. THE SCALE IS IN CENTIMETERS. THE CONTOURS REPRESENT THE LOCATION OF THE INTERFACE AT 10 SECOND INTERVALS. $\mu_o = 46.5 \pm 0.5$ CP; IFT = 61.8 ± 1.2 DYNES/CM.	76
FIGURE 3-17: (A) FRACTAL PERIMETER AND (B) FRACTAL AREA AS A FUNCTION OF TIME FOR WATER INTO LIGHT MINERAL OIL (LMO) AT FOUR CONSTANT INJECTION RATES: 0.3, 1.0, 1.5, AND 2.0 CC/MIN. THE VISCOSITY AND INTERFACIAL TENSION OF LMO (WITH SURFACTANT) IS 46.5 ± 0.5 CP AND 61.8 ± 1.2 , RESPECTIVELY. PATTERNS FOR 0.3, 1.0, 1.5, AND 2.0 CC/MIN ARE SHOWN IN FIGURE 3-13 TO FIGURE 3-16. SOLID POINTS REPRESENT THE CASE WITHOUT ULTRASOUND, AND EMPTY POINTS WITH 72W, 20 KHZ ULTRASOUND.	77
FIGURE 3-18: (A) FRACTAL DIMENSION AND (B) LACUNARITY AS A FUNCTION OF TIME FOR WATER INTO LIGHT MINERAL OIL (LMO) AT FOUR CONSTANT INJECTION RATES: 0.3, 1.0, 1.5, AND 2.0 CC/MIN. THE VISCOSITY AND INTERFACIAL TENSION OF LMO (WITH SURFACTANT) IS 46.5 ± 0.5 CP AND 61.8 ± 1.2 , RESPECTIVELY. PATTERNS FOR 0.3, 1.0, 1.5, AND 2.0 CC/MIN ARE SHOWN IN FIGURE 3-13 TO FIGURE 3-16. SOLID POINTS REPRESENT THE CASE WITHOUT ULTRASOUND, AND EMPTY POINTS WITH 72W, 20 KHZ ULTRASOUND.	78
FIGURE 3-19: IMMISCIBLE HELE-SHAW PATTERNS FOR 3% DOWFAX 2A1 INJECTED INTO HEAVY MINERAL OIL AT A CONSTANT RATE OF 0.6 CC/MIN. THE SCALE IS IN CENTIMETERS. THE CONTOURS REPRESENT THE LOCATION OF THE INTERFACE AT 10 SECOND INTERVALS. $\mu_o = 167.0 \pm 1.7$ CP; IFT = 10.8 ± 0.2 DYNES/CM.	79
FIGURE 3-20: IMMISCIBLE HELE-SHAW PATTERNS FOR 3% DOWFAX 2A1 INJECTED INTO HEAVY MINERAL OIL AT A CONSTANT RATE OF 1.5 CC/MIN. THE SCALE IS IN CENTIMETERS. THE CONTOURS REPRESENT THE LOCATION OF THE INTERFACE AT 10 SECOND INTERVALS. $\mu_o = 167.0 \pm 1.7$ CP; IFT = 10.8 ± 0.2 DYNES/CM.	79
FIGURE 3-21: (A) FRACTAL PERIMETER AND (B) FRACTAL AREA AS A FUNCTION OF TIME FOR 3% DOWFAX 2A1 INTO HEAVY MINERAL OIL (HMO) AT TWO CONSTANT INJECTION RATES: 0.6 AND 1.5 CC/MIN. THE VISCOSITY AND INTERFACIAL TENSION OF HMO (WITH SURFACTANT) IS 167.0 ± 1.7 CP AND 10.8 ± 0.2 DYNES/CM, RESPECTIVELY. PATTERNS ARE SHOWN IN FIGURE 3-19 AND FIGURE 3-20.	80
FIGURE 3-22: (A) FRACTAL DIMENSION AND (B) FRACTAL LACUNARITY AS A FUNCTION OF TIME FOR 3% DOWFAX 2A1 INTO HEAVY MINERAL OIL (HMO) AT TWO CONSTANT INJECTION RATES: 0.6 AND 1.5 CC/MIN. THE VISCOSITY AND INTERFACIAL TENSION OF HMO (WITH SURFACTANT) IS 167.0 ± 1.7 CP AND $10.8 \pm$	

0.2 DYNES/CM, RESPECTIVELY. PATTERNS ARE SHOWN IN FIGURE 3-19 AND FIGURE 3-20.....	81
FIGURE 3-23: IMMISCIBLE HELE-SHAW PATTERNS FOR 3% DOWFAX 2A1 INJECTED INTO LIGHT MINERAL OIL AT A CONSTANT RATE OF 0.6 CC/MIN. THE SCALE IS IN CENTIMETERS. THE CONTOURS REPRESENT THE LOCATION OF THE INTERFACE AT 10 SECOND INTERVALS. $\mu_o = 46.5 \pm 0.5$ CP; IFT = 11.2 ± 0.2 DYNES/CM.....	82
FIGURE 3-24: IMMISCIBLE HELE-SHAW PATTERNS FOR 3% DOWFAX 2A1 INJECTED INTO LIGHT MINERAL OIL AT A CONSTANT RATE OF 1.5 CC/MIN. THE SCALE IS IN CENTIMETERS. THE CONTOURS REPRESENT THE LOCATION OF THE INTERFACE AT 10 SECOND INTERVALS. $\mu_o = 46.5 \pm 0.5$ CP; IFT = 11.2 ± 0.2 DYNES/CM.....	82
FIGURE 3-25: (A) FRACTAL PERIMETER AND (B) FRACTAL AREA AS A FUNCTION OF TIME FOR 3% DOWFAX 2A1 INTO LIGHT MINERAL OIL (LMO) AT TWO CONSTANT INJECTION RATES: 0.6 AND 1.5 CC/MIN. THE VISCOSITY AND INTERFACIAL TENSION OF LMO (WITH SURFACTANT) IS 46.5 ± 0.5 CP AND 11.2 ± 0.2 DYNES/CM, RESPECTIVELY. PATTERNS FOR 0.6 AND 1.5 CC/MIN ARE SHOWN IN FIGURE 3-23 AND FIGURE 3-24.....	83
FIGURE 3-26: (A) FRACTAL DIMENSION AND (B) FRACTAL LACUNARITY AS A FUNCTION OF TIME FOR 3% DOWFAX 2A1 INTO LIGHT MINERAL OIL (LMO) AT TWO CONSTANT INJECTION RATES: 0.6 AND 1.5 CC/MIN. THE VISCOSITY AND INTERFACIAL TENSION OF LMO (WITH SURFACTANT) IS 46.5 ± 0.5 CP AND 11.2 ± 0.2 DYNES/CM, RESPECTIVELY. PATTERNS FOR 0.6 AND 1.5 CC/MIN ARE SHOWN IN FIGURE 3-23 AND FIGURE 3-24.....	84
FIGURE 3-27: (A) FRACTAL DIMENSION VERSUS MODIFIED CAPILLARY NUMBER FOR LIGHT MINERAL OIL AND HEAVY MINERAL OIL AT DIFFERENT TIMES OF PATTERN FORMATION. (B) DIFFERENCE IN FRACTAL DIMENSION FOR LIGHT AND HEAVY MINERAL OIL VERSUS MODIFIED CAPILLARY NUMBER.....	85
FIGURE 3-28: (A) FRACTAL DIMENSION VERSUS MODIFIED REYNOLDS NUMBER FOR LIGHT MINERAL OIL AND HEAVY MINERAL OIL AT DIFFERENT TIMES OF PATTERN FORMATION. (B) DIFFERENCE IN FRACTAL DIMENSION FOR LIGHT AND HEAVY MINERAL OIL VERSUS MODIFIED REYNOLDS NUMBER.....	86
FIGURE 3-29: IMMISCIBLE HELE-SHAW PATTERNS FOR WATER INJECTED INTO HEAVY MINERAL OIL (HMO) AT A CONSTANT HEAD PRESSURE OF 0.455 PSI. THE VISCOSITY AND INTERFACIAL TENSION OF HMO IS 167.0 ± 1.7 CP AND 51.0 ± 1.0 DYNES/CM, RESPECTIVELY. THE SCALE IS IN CENTIMETERS. THE CONTOURS REPRESENT THE LOCATION OF THE INTERFACE AT 10 SECOND INTERVALS.....	87
FIGURE 3-30: (A) FRACTAL PERIMETER AND (B) FRACTAL AREA AS A FUNCTION OF TIME FOR WATER INTO HMO AT A CONSTANT INJECTION PRESSURE OF 0.455 PSI. THE VISCOSITY AND INTERFACIAL TENSION OF HMO IS 167.0 ± 1.7 CP AND 51.0 ± 1.0 DYNES/CM, RESPECTIVELY. PATTERNS ARE SHOWN IN FIGURE 3-29.....	88
FIGURE 3-31: (A) FRACTAL DIMENSION AND (B) LACUNARITY AS A FUNCTION OF TIME FOR WATER INTO HMO AT A CONSTANT INJECTION PRESSURE OF 0.455 PSI. THE VISCOSITY AND INTERFACIAL TENSION OF HMO IS 167.0 ± 1.7 CP AND 51.0 ± 1.0 DYNES/CM, RESPECTIVELY. PATTERNS ARE SHOWN IN FIGURE 3-29.....	89

FIGURE 3-32: IMMISCIBLE HELE-SHAW PATTERNS FOR WATER INJECTED INTO REFINED MINERAL OIL (S60) AT A CONSTANT HEAD PRESSURE OF 0.455 PSI. THE VISCOSITY AND INTERFACIAL TENSION OF S60 IS 141.4 ± 0.2 CP AND 22.6 ± 0.5 DYNES/CM, RESPECTIVELY. THE SCALE IS IN CENTIMETERS. THE CONTOURS REPRESENT THE LOCATION OF THE INTERFACE AT 10 SECOND INTERVALS.....90

FIGURE 3-33: (A) FRACTAL PERIMETER AND (B) FRACTAL AREA AS A FUNCTION OF TIME FOR WATER INTO S60 AT A CONSTANT INJECTION PRESSURE OF 0.455 PSI. THE VISCOSITY AND INTERFACIAL TENSION OF S60 IS 141.4 ± 0.2 CP AND 22.6 ± 0.5 DYNES/CM, RESPECTIVELY. PATTERNS ARE SHOWN IN FIGURE 3-32.....91

FIGURE 3-34: (A) FRACTAL DIMENSION AND (B) LACUNARITY AS A FUNCTION OF TIME FOR WATER INTO S60 AT A CONSTANT INJECTION PRESSURE OF 0.455 PSI. THE VISCOSITY AND INTERFACIAL TENSION OF S60 IS 141.4 ± 0.2 CP AND 22.6 ± 0.5 DYNES/CM, RESPECTIVELY. PATTERNS ARE SHOWN IN FIGURE 3-32.....92

FIGURE 3-35: IMMISCIBLE HELE-SHAW PATTERNS FOR WATER INJECTED INTO REFINED MINERAL OIL (S200) AT A CONSTANT HEAD PRESSURE OF 0.455 PSI. THE VISCOSITY AND INTERFACIAL TENSION OF S200 IS 577.9 ± 0.9 CP AND 30.7 ± 0.6 DYNES/CM, RESPECTIVELY. THE SCALE IS IN CENTIMETERS. THE CONTOURS REPRESENT THE LOCATION OF THE INTERFACE AT 10 SECOND INTERVALS.....93

FIGURE 3-36: (A) FRACTAL PERIMETER AND (B) FRACTAL AREA AS A FUNCTION OF TIME FOR WATER INTO S200 AT A CONSTANT INJECTION PRESSURE OF 0.455 PSI THE VISCOSITY AND INTERFACIAL TENSION OF S200 IS 577.9 ± 0.9 CP AND 30.7 ± 0.6 DYNES/CM, RESPECTIVELY. PATTERNS ARE SHOWN IN FIGURE 3-35.....94

FIGURE 3-37: (A) FRACTAL DIMENSION AND (B) LACUNARITY AS A FUNCTION OF TIME FOR WATER INTO S200 AT A CONSTANT INJECTION PRESSURE OF 0.455 PSI THE VISCOSITY AND INTERFACIAL TENSION OF S200 IS 577.9 ± 0.9 CP AND 30.7 ± 0.6 DYNES/CM, RESPECTIVELY. PATTERNS ARE SHOWN IN FIGURE 3-35.....95

FIGURE 3-38: IMMISCIBLE HELE-SHAW PATTERNS FOR WATER INJECTED INTO REFINED MINERAL OIL (N350) AT A CONSTANT HEAD PRESSURE OF 0.9947 PSI. THE VISCOSITY AND INTERFACIAL TENSION OF N350 IS 1112.0 ± 1.8 CP AND 35.3 ± 0.8 DYNES/CM, RESPECTIVELY. THE SCALE IS IN CENTIMETERS. THE CONTOURS REPRESENT THE LOCATION OF THE INTERFACE AT 10 SECOND INTERVALS.96

FIGURE 3-39: (A) FRACTAL PERIMETER AND (B) FRACTAL AREA AS A FUNCTION OF TIME FOR WATER INTO N350 AT A CONSTANT INJECTION PRESSURE OF 0.455 PSI THE VISCOSITY AND INTERFACIAL TENSION OF N350 IS 1112.0 ± 1.8 CP AND 35.3 ± 0.8 DYNES/CM, RESPECTIVELY. PATTERNS ARE SHOWN IN FIGURE 3-38.....97

FIGURE 3-40: (A) FRACTAL DIMENSION AND (B) LACUNARITY AS A FUNCTION OF TIME FOR WATER INTO N350 AT A CONSTANT INJECTION PRESSURE OF 0.455 PSI THE VISCOSITY AND INTERFACIAL TENSION OF N350 IS 1112.0 ± 1.8 CP AND 35.3 ± 0.8 DYNES/CM, RESPECTIVELY. PATTERNS ARE SHOWN IN FIGURE 3-38.....98

FIGURE 3-41: IMMISCIBLE HELE-SHAW PATTERNS FOR WATER INJECTED INTO SYNTHETIC MINERAL OIL (S600) AT A CONSTANT HEAD PRESSURE OF 0.455 PSI. THE VISCOSITY AND INTERFACIAL TENSION OF S600 IS 1973 ± 3.2 CP AND 38.7 ± 0.8 DYNES/CM, RESPECTIVELY. THE SCALE IS IN CENTIMETERS. THE CONTOURS REPRESENT THE LOCATION OF THE INTERFACE AT 10 SECOND INTERVALS.....99

FIGURE 3-42: (A) FRACTAL PERIMETER AND (B) FRACTAL AREA AS A FUNCTION OF TIME FOR WATER INTO S600 AT A CONSTANT INJECTION PRESSURE OF 0.455 PSI THE VISCOSITY AND INTERFACIAL TENSION OF S600 IS 1973±3.2 CP AND 38.7±0.8 DYNES/CM, RESPECTIVELY. PATTERNS ARE SHOWN IN FIGURE 3-41.....	100
FIGURE 3-43: (A) FRACTAL DIMENSION AND (B) LACUNARITY AS A FUNCTION OF TIME FOR WATER INTO S600 AT A CONSTANT INJECTION PRESSURE OF 0.455 PSI THE VISCOSITY AND INTERFACIAL TENSION OF S600 IS 1973±3.2 CP AND 38.7±0.8 DYNES/CM, RESPECTIVELY. PATTERNS ARE SHOWN IN FIGURE 3-41.....	101
FIGURE 3-44: IMMISCIBLE HELE-SHAW PATTERNS FOR WATER INJECTED INTO SYNTHETIC MINERAL OIL (S600) AT A CONSTANT HEAD PRESSURE OF 0.9947 PSI. THE VISCOSITY AND INTERFACIAL TENSION OF S600 IS 1973±3.2 CP AND 38.7±0.8 DYNES/CM, RESPECTIVELY. THE SCALE IS IN CENTIMETERS. THE CONTOURS REPRESENT THE LOCATION OF THE INTERFACE AT 10 SECOND INTERVALS.....	102
FIGURE 3-45: (A) FRACTAL PERIMETER AND (B) FRACTAL AREA AS A FUNCTION OF TIME FOR WATER INTO S600 AT A CONSTANT INJECTION PRESSURE OF 0.9947 PSI THE VISCOSITY AND INTERFACIAL TENSION OF S600 IS 1973 ± 3.2 CP AND 38.7 ± 0.8 DYNES/CM, RESPECTIVELY. PATTERNS ARE SHOWN IN FIGURE 3-44.....	103
FIGURE 3-46: (A) FRACTAL DIMENSION AND (B) LACUNARITY AS A FUNCTION OF TIME FOR WATER INTO S600 AT A CONSTANT INJECTION PRESSURE OF 0.9947 PSI THE VISCOSITY AND INTERFACIAL TENSION OF S600 IS 1973 ± 3.2 CP AND 38.7 ± 0.8 DYNES/CM, RESPECTIVELY. PATTERNS ARE SHOWN IN FIGURE 3-44.....	104
FIGURE 3-47: (A) STEADY STATE FRACTAL DIMENSION (FROM LOGARITHMIC FIT FITTED) VERSUS VISCOSITY RATIO FOR VARIOUS PROCESSED MINERAL OILS. (B) BAR CHART ILLUSTRATING THE RELATIVE CHANGE (ARROWS) OF FRACTAL DIMENSION FOR EACH PROCESSED OIL.....	105
FIGURE 3-48: IMMISCIBLE HELE-SHAW PATTERNS FOR 3% DOWFAX 2A1 INJECTED INTO HEAVY MINERAL OIL (HMO) AT A CONSTANT HEAD PRESSURE OF 0.1421 PSI. THE VISCOSITY AND INTERFACIAL TENSION OF HMO IS 167.0±1.7 CP AND 51.0±1.0 DYNES/CM, RESPECTIVELY. THE SCALE IS IN CENTIMETERS. THE CONTOURS REPRESENT THE LOCATION OF THE INTERFACE AT 10 SECOND INTERVALS.	106
FIGURE 3-49: IMMISCIBLE HELE-SHAW PATTERNS FOR 3% DOWFAX 2A1 INJECTED INTO HEAVY MINERAL OIL (HMO) AT A CONSTANT HEAD PRESSURE OF 0.2373 PSI. THE VISCOSITY AND INTERFACIAL TENSION OF HMO IS 167.0±1.7 CP AND 51.0±1.0 DYNES/CM, RESPECTIVELY. THE SCALE IS IN CENTIMETERS. THE CONTOURS REPRESENT THE LOCATION OF THE INTERFACE AT 10 SECOND INTERVALS.	107
FIGURE 3-50: IMMISCIBLE HELE-SHAW PATTERNS FOR 3% DOWFAX 2A1 INJECTED INTO HEAVY MINERAL OIL (HMO) AT A CONSTANT HEAD PRESSURE OF 0.357 PSI. THE VISCOSITY AND INTERFACIAL TENSION OF HMO IS 167.0±1.7 CP AND 51.0±1.0 DYNES/CM, RESPECTIVELY. THE SCALE IS IN CENTIMETERS. THE CONTOURS REPRESENT THE LOCATION OF THE INTERFACE AT 10 SECOND INTERVALS.....	108
FIGURE 3-51: (A) FRACTAL PERIMETER AND (B) FRACTAL AREA AS A FUNCTION OF TIME FOR 3% DOWFAX 2A1 INTO HEAVY MINERAL OIL (HMO) AT THREE CONSTANT INJECTION PRESSURES: 0.1421, 0.237 AND 0.357 PSI. THE VISCOSITY AND INTERFACIAL TENSION OF HMO (WITH SURFACTANT) IS 167.0 ± 1.7 CP AND	

10.8 ± 0.2 DYNES/CM, RESPECTIVELY. PATTERNS ARE SHOWN IN FIGURE 3-48 TO FIGURE 3-50.....	109
FIGURE 3-52: (A) FRACTAL DIMENSION AND (B) FRACTAL LACUNARITY AS A FUNCTION OF TIME FOR 3% DOWFAX 2A1 INTO HEAVY MINERAL OIL (HMO) AT TWO CONSTANT INJECTION PRESSURES: 0.1421 PSI AND 0.235 PSI. THE VISCOSITY AND INTERFACIAL TENSION OF HMO (WITH SURFACTANT) IS 167.0 ± 1.7 CP AND 10.8 ± 0.2 DYNES/CM, RESPECTIVELY. PATTERNS ARE SHOWN IN FIGURE 3-48 TO FIGURE 3-50.....	110
FIGURE 3-53: IMMISCIBLE HELE-SHAW PATTERNS FOR 3% DOWFAX 2A1 INJECTED INTO LIGHT MINERAL OIL (LMO) AT A CONSTANT HEAD PRESSURE OF 0.1421 PSI. THE VISCOSITY AND INTERFACIAL TENSION OF LMO IS 46.5±0.5 CP AND 61.8±1.2 DYNES/CM, RESPECTIVELY. THE SCALE IS IN CENTIMETERS. THE CONTOURS REPRESENT THE LOCATION OF THE INTERFACE AT 10 SECOND INTERVALS.....	111
FIGURE 3-54: IMMISCIBLE HELE-SHAW PATTERNS FOR 3% DOWFAX 2A1 INJECTED INTO LIGHT MINERAL OIL (LMO) AT A CONSTANT HEAD PRESSURE OF 0.235 PSI. THE VISCOSITY AND INTERFACIAL TENSION OF LMO IS 46.5±0.5 CP AND 61.8±1.2 DYNES/CM, RESPECTIVELY. THE SCALE IS IN CENTIMETERS. THE CONTOURS REPRESENT THE LOCATION OF THE INTERFACE AT 10 SECOND INTERVALS.....	112
FIGURE 3-55: (A) FRACTAL PERIMETER AND (B) FRACTAL AREA AS A FUNCTION OF TIME FOR 3% DOWFAX 2A1 INTO LIGHT MINERAL OIL (LMO) AT TWO CONSTANT INJECTION PRESSURES: 0.1421 PSI AND 0.235 PSI. THE VISCOSITY AND INTERFACIAL TENSION OF LMO (WITH SURFACTANT) IS 46.5 ± 0.5 CP AND 11.2 ± 1.2 DYNES/CM, RESPECTIVELY. PATTERNS ARE SHOWN IN FIGURE 3-53 AND FIGURE 3-54.....	113
FIGURE 3-56: (A) FRACTAL DIMENSION AND (B) FRACTAL LACUNARITY AS A FUNCTION OF TIME FOR 3% DOWFAX 2A1 INTO LIGHT MINERAL OIL (LMO) AT TWO CONSTANT INJECTION PRESSURES: 0.1421 PSI AND 0.235 PSI. THE VISCOSITY AND INTERFACIAL TENSION OF LMO IS 46.5 ± 0.5 CP AND 11.2 ± 0.2 DYNES/CM, RESPECTIVELY. PATTERNS ARE SHOWN IN FIGURE 3-53 AND FIGURE 3-54.	114
FIGURE 3-57: INJECTION PROFILES OF MISCIBLE HELE-SHAW EXPERIMENTS, IN WHICH KEROSENE IS INJECTED AT A CONSTANT HEAD OF 9.5 CM INTO (A) HEAVY MINERAL OIL ($\mu_{HMO}/\mu_k = 57.6$) AND (B) LIGHT MINERAL OIL ($\mu_{LMO}/\mu_k = 16.0$). TWO INTENSITIES OF ULTRASOUND (SETTING 2 = 72W, SETTING 5 = 168 W) WERE APPLIED TO THE CELLS. PATTERNS ARE COMPARED TO THE NO-ULTRASOUND CASE (NUS).....	115
FIGURE 3-58: INJECTION PROFILES OF MISCIBLE HELE-SHAW EXPERIMENTS, IN WHICH KEROSENE IS INJECTED AT A CONSTANT HEAD OF 20 CM INTO (A) HEAVY MINERAL OIL ($\mu_{HMO}/\mu_k = 57.6$) AND (B) LIGHT MINERAL OIL ($\mu_{LMO}/\mu_k = 16.0$). TWO INTENSITIES OF ULTRASOUND (SETTING 2 = 72W, SETTING 5 = 168 W) WERE APPLIED TO THE CELLS. PATTERNS ARE COMPARED TO THE NO-ULTRASOUND CASE (NUS).....	116
FIGURE 3-59: INJECTION PROFILES OF MISCIBLE HELE-SHAW EXPERIMENTS, IN WHICH HEPTANE IS INJECTED AT A CONSTANT HEAD OF 3 CM INTO LIGHT MINERAL OIL ($\mu_{LMO}/\mu_H = 110.7$). ULTRASOUND AT SETTING 2 (72W) WAS APPLIED TO THE CELLS. THE ULTRASONICALLY STIMULATED PATTERN IS COMPARED TO THE NO-ULTRASOUND CASE (NUS).	117

FIGURE 3-60: INJECTION PROFILES OF MISCIBLE HELE-SHAW EXPERIMENTS, IN WHICH HEPTANE IS INJECTED AT A CONSTANT HEAD OF 5 CM INTO (A) HEAVY MINERAL OIL ($\mu_{HMO}/\mu_H = 397.6$) AND (B) LIGHT MINERAL OIL ($\mu_{LMO}/\mu_H = 110.7$). TWO INTENSITIES OF ULTRASOUND (SETTING 2 = 72W, SETTING 5 = 168 W) WERE APPLIED TO THE CELLS. PATTERNS ARE COMPARED TO THE NO-ULTRASOUND CASE (NUS).....	117
FIGURE 3-61: INJECTION PROFILES OF MISCIBLE HELE-SHAW EXPERIMENTS, IN WHICH HEPTANE IS INJECTED AT A CONSTANT HEAD OF 9.5 CM INTO HEAVY MINERAL OIL ($\mu_{HMO}/\mu_H = 397.6$). TWO INTENSITIES OF ULTRASOUND (SETTING 2 = 72W, SETTING 5 = 168 W) WERE APPLIED TO THE CELLS. PATTERNS ARE COMPARED TO THE NO-ULTRASOUND CASE (NUS).....	118
FIGURE 3-62: SNAP-SHOTS OF FULLY DEVELOPED FRACTAL PATTERNS FOR VARIOUS INJECTED MISCIBLE FLUIDS: (A) KEROSENE INTO LIGHT MINERAL OIL AT A RATE OF 1 CC/MIN ($\mu_{LMO}/\mu_K = 16.0$), (B) KEROSENE INTO LIGHT MINERAL OIL AT A RATE OF 5 CC/MIN ($\mu_{LMO}/\mu_K = 16.0$), (C) N-PENTANE INTO MINERAL OIL AT 5CC/MIN ($\mu_{LMO}/\mu_P = 186$). ULTRASOUND AT SETTING 2 (72W) WAS APPLIED TO THE CELLS. PATTERNS ARE COMPARED TO THE NO-ULTRASOUND CASE (NUS).....	119
FIGURE 4-1: ILLUSTRATION OF SPONTANEOUS AND FORCED IMBIBITION AND DRAINAGE CAPILLARY PRESSURE CURVES. ADAPTED FROM MORROW AND MASON (2001).....	150
FIGURE 4-2: CROSS CORRELATION PLOT OF PORE VOLUMES MEASURED FROM OIL SATURATED CORES VS. PORE VOLUMES FROM WATER SATURATED CORES. THIS PLOT ILLUSTRATES THE SEVERITY OF CLAY CONTENT IN BEREA SANDSTONE.	150
FIGURE 4-3: ILLUSTRATION OF (A) CO-CURRENT AND (B) COUNTER-CURRENT FLUID INVASION INTO PORES BY SPONTANEOUS CAPILLARY IMBIBITION. IN (A), THE WETTING PHASE (BLUE) PENETRATES THE PORE FROM THE “ENTRANCE” THROAT VIA PORE ADSORPTION, AND PUSHES OIL (WHITE) INTO ADJACENT PORES. IN (B), THE WETTING PHASE ENTERS THE PORE BY WETTING THE PORE WALLS, WHILE THE OIL IS FLOWING IN THE OPPOSITE DIRECTION, MAINLY DUE TO HIGH CAPILLARY PRESSURE AT THE “EXIT” THROAT. [W = WETTING PHASE, NW = NON-WETTING PHASE.].....	151
FIGURE 4-4: DEFINITION OF BOUNDARY CONDITIONS FOR CORE SAMPLES USED IN THE WORKS OF MATTAX AND KYTE (1962), ZHANG <i>ET AL.</i> (1996), AND BABADAGLI <i>ET AL.</i> (2005). FIGURE ADAPTED FROM MORROW AND MASON (2001). ...	151
FIGURE 4-5: FLOW CHART ILLUSTRATING ALL SPONTANEOUS IMBIBITION EXPERIMENTS WITH DIFFERENT FLUID PAIRS, ROCK TYPES AND BOUNDARY CONDITIONS.	152
FIGURE 4-6: AQUEOUS SURFACE TENSION AND INTERFACIAL TENSION WITH LIGHT MINERAL OIL VS. CONCENTRATION FOR TERGITOL™ 15-S-7 SURFACTANT AT 25°C. (SURFACE TENSION VALUES ADOPTED FROM DOW CHEMICAL COMPANY BROCHURE).....	152
FIGURE 4-7: AQUEOUS SURFACE TENSION AND INTERFACIAL TENSION WITH LIGHT MINERAL OIL VS. CONCENTRATION FOR (A) DOWFAX™ 2A1 AND (B) DOWFAX™ 3B0 SURFACTANT AT 25°C. (SURFACE TENSION VALUES ADOPTED FROM DOW CHEMICAL COMPANY BROCHURE).	153

FIGURE 4-8: (A) SCHEMATIC OF THE EXPERIMENTAL SETUP OF IMBIBITION EXPERIMENTS, (B) THE GLASS IMBIBITION CELL USED TO COLLECT OIL AFFLUENT FROM A SATURATED CORE IMMERSSED IN AN AQUEOUS PHASE..... 154

FIGURE 4-9: CONVERSION CHART OF PEAK-TO-PEAK AMPLITUDE FOR A 3/4" HORN VERSUS SETTING NUMBER..... 155

FIGURE 4-10: TEMPERATURE CHANGE WITHIN THE ULTRASONIC BATH AT SETTING 2 (LO) AND 5 (HI). THESE SETTINGS CORRESPOND TO PEAK TO PEAK AMPLITUDES OF 0.012 MM AND 0.03 MM, RESPECTIVELY..... 155

FIGURE 4-11: EMULSIFICATION DURING SURFACTANT EXPERIMENTS. (A) 3% DOWFAX 2A1 WITH LIGHT MINERAL OIL, (B) 3% DOWFAX 2A1 WITH HUSKY CRUDE OIL. 155

FIGURE 4-12: SUMMARY OF FINAL RECOVERY WITH AND WITHOUT ULTRASOUND FOR ALL FLUID PAIRS. THE 45° LINE IN (B) REPRESENTS THE CASE WHEN THE RESPONSE EQUALS TO THAT OF THE CONTROL. DASHED LINES SIGNIFY THE PERCENT DEVIATION (%) FROM THE CONTROL CASE. RECOVERY BELOW ±5% DEVIATION FROM THE 45° LINE IS BELIEVED TO BE WITHIN THE UNCERTAINTY RANGE OF IMBIBITION EXPERIMENTS, AND THEREFORE ASSUMED TO BE UNAFFECTED BY ULTRASOUND. 156

FIGURE 4-13: AIR RECOVERY VS. IMBIBITION TIME OF WATER IMBIBING INTO DRY BEREA SANDSTONE. BLUE CURVES REPRESENT THE IMBIBITION PERFORMANCE UNDER ULTRASOUND WITH A HORN (20 KHZ, SETTING 5). RED CURVES REPRESENT THE CONTROL WITHOUT THE APPLICATION OF ULTRASOUND. BOTH CO-CURRENT AND COUNTER-CURRENT SCENARIOS ARE SHOWN. 157

FIGURE 4-14: AIR RECOVERY VS. IMBIBITION TIME OF WATER IMBIBING INTO DRY INDIANA LIMESTONE. BLUE AND GREEN CURVES REPRESENT THE IMBIBITION PERFORMANCE UNDER ULTRASOUND WITH A HORN (20 KHZ, SETTING 5) AND ULTRASONIC BATH (40 KHZ), RESPECTIVELY. RED CURVES REPRESENT THE CONTROL WITHOUT THE APPLICATION OF ULTRASOUND. BOTH CO-CURRENT AND COUNTER-CURRENT SCENARIOS ARE SHOWN..... 158

FIGURE 4-15: ILLUSTRATION OF THE FRONTAL PROPAGATION OF WATER IMBIBING INTO DRY, STRONGLY WATER-WET BEREA SANDSTONE IN THE ABSENCE OF A BOUNDARY. (BASED ON THE CT SCANNER RESULTS BY GARG, NIKRAVESH *ET AL.* (1996). THE DISPLACEMENT IS GOVERNED BY PARTIALLY COUNTER-CURRENT, CAPILLARY DOMINATED IMBIBITION WITH BUOYANT FORCES PRESENT. AIR PREFERENTIALLY IS MOVES UPWARDS..... 159

FIGURE 4-16: ILLUSTRATION OF THE FRONTAL PROPAGATION OF WATER IMBIBING INTO DRY, STRONGLY WATER-WET BEREA SANDSTONE WHEN ALL SIDES EXCEPT THE BOTTOM END ARE SEALED WITH EPOXY. (BASED ON THE CT SCANNER RESULTS BY GARG, NIKRAVESH *ET AL.* (1996). THE DISPLACEMENT IS ENTIRELY GOVERNED BY COUNTER-CURRENT, CAPILLARY DOMINATED IMBIBITION WITH AIR FLOWING OPPOSITE TO THE UPWARD BUOYANT FORCE..... 159

FIGURE 4-17: OIL RECOVERY VS. TIME DURING SPONTANEOUS IMBIBITION OF WATER INTO KEROSENE AND LIGHT MINERAL OIL SATURATED BEREA SANDSTONE AT TWO INTENSITIES OF ULTRASOUND FOR TWO BOUNDARY CONDITIONS: (A) ALL SIDES OPEN (UNCOATED), (B) BOTTOM END OPEN

(COATED). THE DASHED INTERVAL OUTLINES THE RECOVERY WHEN IMBIBITION CELLS ARE REVERSED..... 160

FIGURE 4-18: (A) OIL RECOVERY VS. TIME, AND (B) CROSS-COMPARISON PLOT, OF SPONTANEOUS IMBIBITION OF 15,000 PPM AND 150,000 PPM NaCl AQUEOUS SOLUTION INTO LIGHT MINERAL OIL SATURATED BEREa SANDSTONE (ALL SIDES OPEN) AT TWO INTENSITIES OF ULTRASOUND, AS COMPARED TO NO ULTRASOUND. RED CURVES CORRESPOND TO CONTROL CONDITIONS WITHOUT ULTRASOUND. THE 45° LINE IN (B) REPRESENTS THE CONDITION WHEN THE RESPONSE UNDER ULTRASOUND EQUALS THAT OF THE CONTROL. DASHED LINES SIGNIFY THE PERCENT (%) DEVIATION FROM THE CONTROL..... 161

FIGURE 4-19: (A) OIL RECOVERY VS. TIME AND (B) CROSS-COMPARISON PLOT, DURING SPONTANEOUS IMBIBITION UNDER ULTRASOUND OF 150,000 PPM NaCl BRINE SOLUTION INTO LIGHT MINERAL OIL SATURATED BEREa SANDSTONE (ALL SIDES OPEN) BEFORE AND AFTER AGING FOR ONE MONTH. THE 45° LINE IN (B) REPRESENTS THE CONDITION WHEN THE RESPONSE UNDER ULTRASOUND EQUALS THAT OF THE CONTROL. DASHED LINES SIGNIFY THE PERCENT (%) DEVIATION FROM THE CONTROL..... 162

FIGURE 4-20: OIL RECOVERY VS. TIME DURING SPONTANEOUS IMBIBITION OF (A) 1% ALKYLdIPHENYLOXIDE DISULFONIC ACID, AND (B) 5% ALKYLdIPHENYLOXIDE DISULFONIC ACID, INTO LIGHT MINERAL OIL SATURATED BEREa SANDSTONE (ALL SIDES OPEN) AT TWO INTENSITIES OF ULTRASOUND. RED CURVES ILLUSTRATE CONTROL CONDITIONS WITHOUT ULTRASOUND. 163

FIGURE 4-21: CROSS-COMPARISON PLOT OF OIL RECOVERY DURING SPONTANEOUS IMBIBITION OF 1% ALKYLdIPHENYLOXIDE DISULFONIC ACID, AND 5% ALKYLdIPHENYLOXIDE DISULFONIC ACID, INTO LIGHT MINERAL OIL SATURATED BEREa SANDSTONE (ALL SIDES OPEN) AT TWO INTENSITIES OF ULTRASOUND. THE 45° LINE REPRESENTS THE CONDITION WHEN THE RESPONSE UNDER ULTRASOUND EQUALS THAT OF THE CONTROL. DASHED LINES SIGNIFY THE PERCENT (%) DEVIATION FROM THE CONTROL..... 164

FIGURE 4-22: (A) OIL RECOVERY VS. TIME, AND (B) CROSS-COMPARISON PLOT, OF THE SPONTANEOUS IMBIBITION OF VARIOUS ALKYLdIPHENYLOXIDE DISULFONIC ACID SOLUTIONS INTO LIGHT MINERAL OIL SATURATED BEREa SANDSTONE (ALL SIDES OPEN) UNDER ULTRASOUND. FOR COMPARISON, WE ALSO ADDED THE IMBIBITION PERFORMANCE AFTER USING A 150,000 PPM BRINE SOLUTION AS AQUEOUS PHASE. THE 45° LINE IN (B) REPRESENTS THE CASE WHEN THE RESPONSE EQUALS TO THAT OF THE CONTROL. DASHED LINES SIGNIFY THE PERCENT DEVIATION (%) FROM THE CONTROL CASE..... 165

FIGURE 4-23: (A) OIL RECOVERY VS. TIME, AND (B) CROSS-COMPARISON PLOT, OF THE SPONTANEOUS IMBIBITION OF 5% ALKYLdIPHENYLOXIDE DISULFONIC ACID SOLUTIONS INTO KEROSENE SATURATED BEREa SANDSTONE (ALL SIDES OPEN) AT TWO INTENSITIES OF ULTRASOUND. THE 45° LINE IN (B) REPRESENTS THE CASE WHEN THE RESPONSE EQUALS TO THAT OF THE CONTROL. DASHED LINES SIGNIFY THE PERCENT DEVIATION (%) FROM THE CONTROL CASE..... 166

FIGURE 4-24: (A) OIL RECOVERY VS. TIME, AND (B) CROSS-COMPARISON PLOT, OF THE SPONTANEOUS IMBIBITION OF VARIOUS ALKYLdIPHENYLOXIDE DISULFONIC ACID SOLUTIONS INTO LIGHT MINERAL OIL SATURATED BEREa SANDSTONE (ALL SIDES OPEN) UNDER ULTRASOUND AFTER AGING SAMPLES FOR ONE MONTH. FOR COMPARISON, WE ALSO ADDED THE IMBIBITION PERFORMANCE OF 150,000 PPM BRINE SOLUTION AS AQUEOUS PHASE. THE 45°

LINE IN (B) REPRESENTS THE CASE WHEN THE RESPONSE EQUALS TO THAT OF THE CONTROL. DASHED LINES SIGNIFY THE PERCENT DEVIATION (%) FROM THE CONTROL CASE..... 167

FIGURE 4-25: (A) OIL RECOVERY VS. TIME, AND (B) CROSS-COMPARISON PLOT, OF THE SPONTANEOUS IMBIBITION OF VARIOUS ALCOHOL ETHOXYLATE SOLUTIONS INTO LIGHT MINERAL OIL SATURATED BERA SANDSTONE (ALL SIDES OPEN) UNDER ULTRASOUND (SETTING 5). THE 45° LINE IN (B) REPRESENTS THE CASE WHEN THE RESPONSE EQUALS TO THAT OF THE CONTROL. DASHED LINES SIGNIFY THE PERCENT DEVIATION (%) FROM THE CONTROL CASE..... 168

FIGURE 4-26: (A) OIL RECOVERY VS. TIME, AND (B) CROSS-COMPARISON PLOT, OF THE SPONTANEOUS IMBIBITION OF 1% ALCOHOL ETHOXYLATE SOLUTION INTO KEROSENE AND LIGHT MINERAL OIL SATURATED BERA SANDSTONE (ALL SIDES OPEN) UNDER ULTRASOUND (SETTING 5). THE 45° LINE IN (B) REPRESENTS THE CASE WHEN THE RESPONSE EQUALS TO THAT OF THE CONTROL. DASHED LINES SIGNIFY THE PERCENT DEVIATION (%) FROM THE CONTROL CASE..... 169

FIGURE 4-27: (A) OIL RECOVERY VS. TIME, AND (B) CROSS-COMPARISON PLOT, OF THE SPONTANEOUS IMBIBITION OF VARIOUS XANTHAN GUM SOLUTIONS INTO LIGHT MINERAL OIL SATURATED BERA SANDSTONE (ALL SIDES OPEN) UNDER ULTRASOUND (SETTING 2). FOR COMPARISON, WE ALSO ADDED THE IMBIBITION PERFORMANCE AFTER USING A 150,000 PPM BRINE SOLUTION AS AQUEOUS PHASE. THE 45° LINE IN (B) REPRESENTS THE CASE WHEN THE RESPONSE EQUALS TO THAT OF THE CONTROL. DASHED LINES SIGNIFY THE PERCENT DEVIATION (%) FROM THE CONTROL CASE. 170

FIGURE 4-28: CROSS-COMPARISON PLOT OF THE SPONTANEOUS IMBIBITION OF 0.03 WT% AND 0.09 WT% XANTHAN GUM SOLUTIONS INTO LIGHT MINERAL OIL SATURATED BERA SANDSTONE (ALL SIDES OPEN) UNDER TWO ULTRASONIC SETTINGS. THE 45° LINE REPRESENTS THE CASE WHEN THE RESPONSE EQUALS TO THAT OF THE CONTROL. DASHED LINES SIGNIFY THE PERCENT DEVIATION (%) FROM THE CONTROL CASE..... 171

FIGURE 4-29: CUMULATIVE WATER IMBIBED VERSUS ULTRASONIC INTENSITY FOR VARIOUS FLUID PAIRS..... 171

FIGURE 4-30: (A) OIL RECOVERY VS. TIME, AND (B) CROSS-COMPARISON PLOT, OF THE SPONTANEOUS IMBIBITION OF 150,000 PPM NA CL BRINE AND 3% ALYLDIPHENYLOXIDE DISULFONIC ACID SOLUTION INTO CRUDE OIL SATURATED BERA SANDSTONE (ALL SIDES OPEN) UNDER ULTRASOUND (SETTING 2). THE 45° LINE IN (B) REPRESENTS THE CASE WHEN THE RESPONSE EQUALS TO THAT OF THE CONTROL. DASHED LINES SIGNIFY THE PERCENT DEVIATION (%) FROM THE CONTROL CASE..... 172

1 Introduction

Developing new methods of oil extraction from reservoirs has become an increasingly important challenge in modern petroleum research. As more fields deplete, and less new fields are discovered, the petroleum industry must find new ways to extract the residual oils left behind in reservoirs after primary (natural drive) and secondary (waterflood) recovery. During primary recovery, the natural reservoir pressure, as well as gravity, pushes oil into the wellbore, yielding about 10% of the oil originally in place (OIIP). Once such pressure depletes, artificial lift methods are usually employed to pump the fluids to the surface. Secondary methods such as water-flooding and gas injection result in an additional 10 – 30% recovery.

During the past 40 years, a variety of enhanced oil recovery (EOR) methods have been developed to maximize the output of mature and mostly depleted reservoirs. These methods manipulate the capillary and viscous forces within the pores, thereby enhancing the displacement of hydrocarbons. Four major types of EOR operations are chemical flooding, miscible displacement, thermal recovery, and mechanical stimulation (**Figure 1-1**). The optimal application of each of these methods depends on reservoir temperature, pressure, depth, net pay, permeability, residual oil and water saturations, porosity and fluid properties. All of these techniques are costly, require extensive surface equipment, and severely impact the environment.

In this work, we explore the capillary physics of an unconventional EOR candidate: acoustic stimulation. Numerous field pilots and laboratory experiments have demonstrated that acoustic vibration may significantly enhance mobilization of carbohydrates in porous media. Such method may prove to be a viable alternative to

mainstream techniques because of its economical and ecological benefits, as well as its potential applications in cleaning wellbores, mobilizing fines and clays, breaking of asphaltenes, paraffin deposits and hydrates, and finally, in soil remediation.

One of the most significant advantages of elastic wave stimulation over conventional oil recovery mechanisms is the means of delivering the mobilizing energy in the reservoir. In conventional methods, the driving force is delivered via hydraulic forcing. Hydraulic methods suffer from bypassing effects, since fluids always chose the path of least resistance. Hence, many EOR methods fail in heterogeneous formations, leaving large oil pools un-swept. Acoustic energy propagates in all directions, and is unaffected by the pore network or permeability of the formation. Thus, it is possible to influence every point in the reservoir simultaneously, and obtain the maximum efficiency at all times (Beresnev *et al.* 2005).

Despite this apparent advantage, this method still suffers from a lack of understanding of the physical mechanisms by which elastic waves stimulate fluids within porous media. No reliable theoretical model exists to date, which can fully describe the phenomena and make reliable, accurate predictions. Consequently, it is not yet possible to optimize the process, assess limitations, and evaluate whether such technology is applicable for any particular field.

Another apparent limitation of acoustic stimulation is attenuation, especially at high frequencies (Dunn 1986). As with all waves, amplitude and wave speed attenuate and disperse in the presence of dampening fields. A saturated porous medium, being a complex, poroelastic system, exhibits highly nonlinear acoustic properties where acoustic pressure waves are scattered, dispersed and retarded. Ultrasonic waves may only

propagate a few feet into the formation, before they are entirely absorbed by the dampening forces of the solid and the fluid(s). For that reason, most research in recent years shifted towards low frequency stimulation such as seismic stimulation (Simonov, Oparin et al. 2000; Kostrov and Wooden 2005) and pressure pulsing technology (Dusseault et al. 2000; Spanos et al. 2003). Nevertheless, based on the analytical works of Dunin and Nikolaevskii (2005), and Nikolaevskii and Stepanova (2005) ultrasonic waves are generated as a consequence of low frequency oscillation in porous media. Moreover, high frequency waves have short wavelengths and significantly contribute to mechanical perturbation at the pore scale. High wavelength elastic vibration, on the other hand, only influences the bulk behavior of the porous solid. Consequently, although ultrasonic stimulation may be considered a “secondary” driving mechanism, it still has a subtle impact on the overall performance of field applications.

This chapter will provide a statement of the problem as well as the goals of this thesis. This is followed by a comprehensive literature review covering major developments in our understanding of elastic wave theory in porous media, as well as the governing mechanisms of acoustic stimulation. The interested reader is referred to the corresponding references for further detail. We conclude this chapter with a brief summary.

Chapter 2 will provide a discussion of the pendant drop experiments used to illustrate the effect of ultrasound on flow through a capillary. We start with a brief introduction on dripping dynamics, and the motivation of this study, and continue to describe the experimental apparatus and the fluid properties used. We then present and discuss the experimental results of four different oils covering a broad range of viscosity

ratios and interfacial tension. The chapter is closed with a few conclusions recommendations for further research.

Based on the results observed from Chapter 2, Chapter 3 focuses on the effect of ultrasound on liquid-liquid fronts within a glass Hele-Shaw cell. After a brief introduction into radial Hele-Shaw cells, we will discuss the experimental setup and procedure, and present some major results of immiscible and miscible experiments. After a thorough discussion, we conclude this chapter with a few remarks, and suggestions for further work.

In Chapter 4 provides the results of spontaneous (capillary) imbibition experiments. We first start with a brief introduction on the nature of spontaneous imbibition. This is followed by a brief description of the fluids used, and the relevant errors arising from the experimental setup. After describing the experimental procedure, we present and discuss the results of the experiments. Finally, we conclude with the major findings of this study, and give some suggestions for further research to better understand some of the phenomena observed.

1.1 Statement of the Problem

The potential of ultrasonic irradiation to enhance fluid percolation in porous media has been recognized for more than five decades, yet the physics of the acoustic interaction between fluid and rock is not yet well understood (Beresnev and Johnson 1994). Although numerous analytical and numerical models have been developed, the considerable lack of fundamental (simplified) experiments representing finite degrees of freedom still hampers the progress of improving our knowledge in this subject. Most

documented experiments in literature explore complex systems, such as waterfloods in porous media, where a superposition of mechanisms may yield inconclusive results. Various mechanisms have been proposed to explain the enhanced flow of oil through porous media in the presence of an acoustic field. These mechanisms are based on capillary and viscous forces, and depend on additional factors such as frequency, intensity, rock elasticity, fluid properties, porosity, cementation and clay content. Capillary related mechanisms are peristaltic transport due to mechanical deformation of the pore walls, reduction of capillary forces due to the destruction of surface films generated across pore boundaries, coalescence of oil drops due to Bjerknes forces, oscillation and excitation of capillary trapped oil drops, forces generated by cavitating bubbles, and sonocapillary effects. Gaining insight into the governing mechanism(s) is vital for optimizing any field application, and for assessing limitations and feasibility. Hence, it is essential to return to the basics, and perform standard experiments that allow for stringent control of experimental parameters. In this thesis, we designed three types of experiments which focus on several capillary phenomena.

Pendant drop experiments at standard conditions were run to evaluate both the interfacial tension, as well as the percolation rate of water into oil within a capillary when ultrasound is applied. This type of experiment yields valuable insight into the effect of ultrasound on Poiseuille's law, and may explain various observations made during spontaneous capillary imbibition experiments.

Hele-Shaw type experiments were used to study instabilities at the liquid-liquid interface of immiscible liquid films. The branching rate and finger width allows evaluation of the degree of perturbation induced when ultrasound is applied, and estimate

the alteration in capillary pressure. The presence of instabilities may explain phenomena such as surface film breaking, oscillation of droplets, and vibrating oil-water interfaces on pore throats.

Spontaneous (capillary) imbibition experiments were run to study the effect of ultrasound on wettability, interfacial tension, density, and viscosity during unforced fluid invasion into porous media. Such process is intrinsically gentle and fully (and/or gravity) controlled, eliminating the presence of viscous forces, which arise during fluid injection.

These types of experiments have not been performed previously under ultrasound, and it is hoped that the results presented herein provide useful insight to better understand the nature of ultrasonic stimulation, and whether such process is a viable alternative to currently accepted EOR methods.

1.2 Literature Review

1.2.1 Acoustics in Porous Media

The development of the theory of elastic wave propagation in fluid saturated porous media is important in fully appreciating the potential of ultrasonic stimulation as a viable enhanced oil recovery technique. Most of the literature relating to that topic was found in the areas of geophysics and petrophysics, and is predominantly applied to analyze sonic logs and seismic profiles. The groundwork for such theory was set in the seminal papers of Frenkel (1944) and Biot (1956a, 1956b) and Biot (1962) who developed a comprehensive analytical model to describe the propagation of stress waves in poroelastic solids containing a viscous, compressible fluid. He considered that the pore fluid may move relative the skeletal porous frame, and found that two compressional waves are admissible; namely the slow (P2-wave) and the fast wave (P1-wave). The slow wave

describes the case in which the fluid and the solid oscillate out of phase, while the fast wave forms when the fluid and solid are in phase. Attenuation occurs mainly with the slow wave due to the dissipative forces generated by the pore fluid viscosity. Such dissipation results in attenuation which depends on frequency, ω , and scales as ω^2 for low frequencies, and as $\omega^{1/2}$ for frequencies above a critical frequency, ω_{crit} . Additionally, such waves are dispersive, increasing as $\omega^{1/2}$ at high frequencies. Therefore, due to the quadratic increase in attenuation with frequency, the slow waves do not exist at low frequencies. At high frequency, tangential slip and inertial effects give rise to the slow wave. Additionally, Biot neglected the dissipation due to fluid-solid slip and grain boundary motion, which would introduce additional frictional forces. The range in which Biot's theory of poroelasticity is valid is illustrated in **Figure 1-2**.

Deresiewicz and Rice (1962), Deresiewicz and Levy (1967), and Deresiewicz (1974) applied Biot's theory to model wave scattering in fluid saturated porous media, and derived analytical expressions for the phase velocities, attenuation coefficients, angles of reflection and the amplitude ratios, and introduced first order corrections to the rock porosity and fluid viscosity at the limiting low and high frequency cases. Stoll and Bryan (1970) and Norris (1989) developed a mathematical model based on Biots theory, describing the propagation of low-amplitude waves in saturated sediments, and demonstrated that attenuation is controlled by the inelasticity of the skeleton (frictional dissipation at grain contacts) and by viscodynamic dissipation of the fluid. In later work, Stoll (2002) showed that for P-wave velocities between 125Hz to 50 kHz, significant velocity dispersion was observed during experiments in the Gulf of Mexico. Such

dispersion was attributed to viscous damping in the fluid as it percolates in the skeletal frame, an observation consistent with Biot's theory.

Bonnet (1987) reviewed various poroelastic problems and extensions of Biot's formulism, and provided a complete singular solution of a series of dynamic poroelasticity problems in analogy with thermoelasticity. The solution of displacements and pressure profiles for the harmonic excitation is given in the frequency domain. Zobnin, Kudryavtsev *et al.* (1988) explored the flow in inhomogeneous porous systems through the analysis of model periodic structures and obtained an integrodifferential, linearized equation that describes the motion of a viscous fluid in a periodically structured, rigid porous media. They presented solutions for the case of infinitely-long adjacent cylinders with constant cross-section where a compressible viscous fluid occupies the void space between them, and a system of orthogonal fluid-saturated rectilinear channels.

Feng and Johnson (1983a, 1983b) numerically predicted the presence of a new surface mode on a fluid/fluid interface with a saturated porous solid. Such pseudo-Stoneley wave was later experimentally measured by Nagy (1992).

Zimmermann and Stern (1994) presented several closed-form analytical solutions of Biot's equations, such as radiation from a harmonically driven plane wall, radiation from a pulsating sphere, and the interior eigenvalue problem for a sphere for rigid and traction-free surfaces. They also presented a series solution to describe the scattering of a planar compression wave as it impinges a spherical, poroelastic inhomogeneity with different elastic properties than the skeleton, and found that the solution is a superposition of fast and slow waves. Abousleiman *et al.* (1996) investigated the phenomena of

mechanical creep and deformation in rock formations, coupled with hydraulic effects of fluid flow. They used a modified linear poroviscoelastic model based on Biot's theory that incorporates viscoelastic effects through the principle of correspondence. They also solved two practical problems, a borehole and a cylinder for rocks with a wide range of permeability.

Tsiklauri (2002) modified Biot's model to include the effect of nonzero boundary slip velocity, and found that such modification yields better agreement with experimental data. It also predicts higher attenuation coefficients of both the rotational and dilatational waves in the intermediate frequency domain. Ravazzoli *et al.* (2003) estimated bulk volume compressibility, effective pressure, ultrasonic phase velocities and quality factors of real reservoir sandstone saturated with immiscible oils at various saturations and pressures, in order to correlate acoustic velocity to micro-structural properties and pressure conditions in the reservoir. Analyzing the influence of capillary pressure on the acoustic properties, they found that with the exception of the initial water case, where capillary pressure is highest, there was almost no difference in type I P- and S-wave velocities. Type II P-waves, however, showed significant differences. Quality factors, which represent the level of dispersion, seemed to be more sensitive to capillary pressure than phase velocities.

The above mentioned theoretical development of elastic wave propagation has been validated by a vast body of laboratory observation. We will only briefly mention the most significant works. Plona (1980) performed a series of laboratory pulse propagation experiments using water saturated sintered glass beads as porous structure. He unambiguously identified three modes of propagation as described by Biot: (i) a fast

compressional wave, (ii) a slow compressional wave, and (iii) a shear wave. Fast and slow compressional wave speeds were measured by Berryman (1981), who found good agreement with Biot's theory for a fully consolidated frame. Plona's work was later modified by Rasolofosaon (1988), who sealed off the end caps of saturated porous plates with a thin coating of paint in order to vary (reduce) the effective permeability. Rasolofosaon's experimental and synthetic signals showed good agreement with Biot's formalism.

Experiments by Johnson and Mccall (1994) showed a substantial non-linear elastic wave response in porous rock, as compared to homogeneous fluids and solids. Such non-linear response is attributed to structural discontinuities such as micro-cracks and grain boundaries, which may cause a local increase in density and modulus during compression, and a local decrease in density and modulus during rarefaction. Buckingham (1997), Buckingham (1999) and Buckingham (2005) extended Biot's theory for consolidated and unconsolidated porous material, by also considering stress relaxation associated with grain boundaries and micro-cracks. After developing two linear wave equations, and solving for expressions of wave speed and attenuation, he found that attenuation scales with the first power of frequency, while the wave speed exhibited a weakly logarithmic dispersion. This observation is consistent with previous observations in sandstone, limestone and some shales. Again, such dispersion and attenuation is believed to be a consequence of grain-boundary interactions, rather than bulk rock properties such as density or porosity.

Gurevich *et al.* (1999) performed a numerical simulation of the ultrasonic experiments of Plona (1980), Rasolofosaon (1988) and their own experiments, and found

good agreement with Biot's theory at ultrasonic frequencies. Winkler *et al.* (1989) performed laboratory experiments to assess theoretical models of borehole Stoneley wave propagation in permeable rock. Samples were saturated with synthetic silicone oils, and subjected to acoustic waves. They measured the velocity and attenuation over a frequency range of 10 kHz to 90 kHz for various viscosities in order to evaluate the low-frequency and high-frequency regions of Biot's theory. As expected, they found that velocity and attenuation are frequency dependent, especially in the case of low frequency, and that velocity decreases and attenuation increases with increasing fluid mobility. Nagy (1993) explored the propagation of slow compressional waves in air saturated permeable solids at a frequency range between 10 and 500 kHz and found good agreement with theoretical predictions for the lower frequencies. At high frequency, they found good agreement for phase velocities, but were not able to match the attenuation coefficient. As expected, the phase velocity asymptotically approaches the maximum value based on the tortuosity of the sample, while the attenuation becomes linearly proportional to frequency, instead of the expected square-root dependence. Nagy speculated that this discrepancy was due to the irregular pore geometry of his samples, which significantly reduced the dynamic permeability at high frequency. Ohkawa (2006) studied the absorption and scattering of high frequency sound in water saturated sands, claiming that scattering has a severe impact on attenuation, and challenging the notion that the frequency dependence of the attenuation coefficient is linear, rather than $\omega^{1/2}$.

Two frequency regimes are generally recognized when modeling fluid dynamics in pores under acoustic fields. At low frequency, the flow is dominated by viscous forces, whereas at high frequencies, the flow is dominated by inertial forces. From numerous

experimental and theoretical studies, it was found that all porous materials exhibit the same behavior in these two domains (Johnson *et al.* 1987; Charlaix *et al.* 1988; Sheng and Zhou 1988; Zhou and Sheng 1989; Chapman and Higdon 1992; Smeulders *et al.* 1992; Pride *et al.* 1993). As the frequency, ω , decreases to zero, the dynamic permeability $k(\omega)$ asymptotically approaches the steady state permeability of the rock. As the frequency increases to infinity, the real component of the dynamic permeability falls as $\omega^{-3/2}$, while the imaginary part falls as ω^{-1} . Both the JDK model (Johnson *et al.* 1987) and Biot (1956) underestimate the imaginary part of the dynamic permeability at low frequencies at high convergent or divergent flow conditions (maximum pore wall slope). Pride *et al.* (1993) showed that when the JDK model is modified to account for drag forces, a much better agreement with experiment could be found. Bernabe (1997) simulated the frequency dependence of dynamic permeability ω during the transition from macroscopic viscous flow at low frequency to inertial flow at high frequency, and observed that in networks with large pore volume, the fluid compressibility could affect the dynamic permeability dramatically.

1.2.2 Acoustic Stimulation

The interest in vibro-seismic stimulation dates back to the early 50's when increased oil recovery was observed as a consequence to cultural noise and earthquakes. Most of the observations, however, are of very little use to developing functional theoretical models, because of the complex nature of the phenomena involved. For example, the improvement of oil rate after an earthquake may not be due to elastic vibrations alone, but also due to fracturing and geomechanical effects such as subsidence

or compression. In most cases, the observations are inconsistent and contradictory, with explanations that are speculative and inconclusive. Beresnev and Johnson (1994) provided an excellent critical review of the major developments in acoustic stimulation in the USA and Russia. This section will summarize major experimental and theoretical contributions in this field, as well as the latest efforts in cracking the mystery.

The potential of ultrasound as a viable method to enhance oil recovery in mature fields was first experimentally investigated by Duhon (1964) and Duhon and Campbell (1965). They performed a series of brine flood experiments on an oil-saturated, epoxy-coated sandstone disk. After applying ultrasound at frequencies between 1 – 5.5 MHz, they observed that ultrasonic energy did have a considerable effect on displacement efficiency by creating a more uniform displacement front. Such enhancement was not noticeably dependent on initial oil saturation, and seemed to yield higher recovery with decreasing viscosity and frequency. They also noted a substantial drop in permeability ratio with ultrasonically stimulated waterfloods, implying a reduced mobility ratio and an enhancement in the sweep efficiency. Although the 1 MHz flood resulted in the highest ultimate recovery, Duhon argued that this may not necessarily imply the optimum operating condition; lower frequency stimulation may generate higher ultimate recovery. To explain the observed increase in recovery, and the reduction in mobility ratios, Duhon postulated that localized pressure surges during cavitation, as well as oscillating air bubbles, may force trapped oil into adjacent pores. Heating due to ultrasound was ruled out as they did not observe a considerable increase in effluent temperature during all experiments. It is not clear, however, whether the observed results were due to ultrasound, or due to alterations in wettability as consequence of using Diesel oil, or due

to the cleaning procedure of the Berea disc. Motivated by Duhon's observations, Ellis (1966) performed numerous waterflood experiments into linear Berea cores at a broad range of pressures below 1 MHz. For all pressure ranges investigated, he found that ultrasound recovered less oil than regular waterfloods. He attributed this surprising reduction to surface waves between grains, which may retard the liquid flow through pores. The discrepancy may have also been due to two major differences between Duhon's and Ellis' experimental setup: 1) Duhon's system was radial, while Ellis' system was linear, 2) Duhon applied the ultrasonic energy into both the fluid and the rock, while Ellis applied the ultrasound to the injection water only.

Chen (1969) and Fairbanks and Chen (1971) investigated the influence of ultrasonic energy (20 kHz and 10 W/cm^2) on the flow of water and oil through a stainless steel filter, through porous sandstone and through a capillary. He found that in the case of porous medium, ultrasound enhanced the percolation rate by a factor of three. Chen also showed that the observed increase is only partially due to ultrasonic heating. In a later study, Fairbanks (1976) presented three systems by which the introduction of ultrasound resulted in enhanced liquid flow through porous media. Such systems included (1) flow of crude oil through porous sandstone, (2) flow of oil filtrate through a porous stainless steel filter, and finally (3) flow of water from a filter to an evaporation surface during drying. In all three systems, ultrasonic stimulation increased the percolation rate of liquid in the porous material. Within Biot's frequency regime, the liquid flow changes from normal viscous flow to plug type flow, thereby reducing the friction factor within pore throats. They also showed that there exists an optimal intensity at which the liquid filtration rate is maximized. Percolation of oil in different porous rock types was also

investigated by Mikhailov *et al.* (1975), Neretin and Yudin (1981), and Dyblenko *et al.* (1989).

Cherskiy *et al.* (1977) applied ultrasound to core samples that were saturated with fresh water, and found that the permeability sharply increases almost immediately when a pulsed ultrasonic field (26.5 kHz) was applied. However, after shutting off the ultrasound, the permeability returned to its original value. When varying the intensity, Cherskiy found that the pulsed treatment improved the permeability up to 10-15 times as compared to continuous insonication. One possible explanation for the dramatic permeability increase is traveling waves along pore walls, which may cause fluid displacement similar to “peristaltic transport”. This mechanism was first proposed by Ganiev *et al.* (1989). They proposed that ultrasound deforms the wall of a pore, altering the radius of the pore. This vibration causes fluctuations in capillary pressure, as well as dilation of surface films. Unfortunately, they provide only a very succinct description of their model, and a few results. They were also not particular about the acoustic power required to cause such effect, and neglected to elaborate on the poroelastic properties of the porous medium. Their model was later simplified by Jaffrin *et al.* (1969), Shapiro *et al.* (1969), Yin and Fung (1969), Jaffrin and Shapiro (1971), Takabatake *et al.* (1988), Aarts and Ooms (1998), Aarts *et al.* (1999), who derived close-form analytical solutions to the problem. Tsiklauri and Beresnev (2001) and Tsiklauri (2002) included the influence of non-Newtonian flow behavior into the model to account for the behavior of oil and polymers. Aarts and Ooms (1998) showed that the method of peristaltic transport works only at ultrasonic frequencies, and that the intensity of the ultrasonic field must

exceed 10^4 W/cm². Therefore, due to the high attenuation of ultrasound, such effect is only significant near the well bore.

Gadiev (1977) introduced audible sound (40 Hz – 15 kHz) to oil saturated unconsolidated sand packs and observed considerable increase in oil production rate and cumulative oil production. Additionally, he observed that sound decreases the surface tension of transformer oils and the viscosity of polyacrylamid solutions. Considering the duration of excitation, these effects may have been due to a temperature increase in the fluids. He postulated that this effect was caused by a phenomenon called “sono-capillary effect”, by which the liquid level within a capillary is raised due to an additional pressure generated by compressional waves. In fact, at ultrasonic frequencies, cavitation may magnify this effect and cause a dramatic increase in the level of the meniscus within a narrow capillary. Such effect was extensively studied by numerous authors from Russia and Ukraine, most notably Prokhorenko *et al.* (1982), Rozin *et al.* (1984), Rozina and Rozin (1994), Rozin *et al.* (2001), Rozina (2002), and Dezhkunov and Leighton (2004). For an excellent coverage on cavitation and bubble dynamics under ultrasound, the interested reader is referred to Gaitan *et al.* (1992). Gadiev (1977) also noted in his paper that ultrasound can reduce the viscosity of high-polymeric liquids by up to 22%. In fact, prolonged exposure of polymer solutions to high-intensity ultrasound permanently reduces its viscosity. Gronroos *et al.* (2004) demonstrated that ultrasound preferentially degrades larger carboxymethylcellulose (CMC) molecules, and that there is an optimal concentration at which degradation is most effective. Once all the larger molecules are degraded, the process ceases and stabilizes. Similar observations were made with Xanthan gum (Kulicke *et al.* 1993).

Neretin and Yudin (1981) applied a continuous ultrasonic field to lose sand saturated with water or oil, and they observed that both recovery rate and final recovery were noticeably increased (65% to 85%).

Simkin and Surguchev (1991) and Simkin (1993) observed a gradual increase in oil droplet size when continuous ultrasound was applied. They credited this improvement to ultrasonically induced coalescence due to primary Bjerknes forces. Such coalescence may assist in accelerating gravity phase separation within porous media, and improve the relative permeability of oil. Bjerknes forces acting between particles can be attractive or repulsive depending on the droplet's location relative to the wave field (Bjerknes 1906; Blake 1949; Mettin *et al.* 1997). The magnitude of such force depends on the density of the continuous phase, and the radius of the droplet. Unfortunately, there are no micro-model experiments to date that visually demonstrate droplet coalescence in a porous medium due to Bjerknes forces. Simkin *et al.* (1991) demonstrated in a series of experiments that during elastic vibration, ultrasound is generated within oil-saturated core blocks, which accelerates the process of capillary imbibition. Unfortunately, this report is in Russian, and I was not able to fully evaluate the findings. The interested reader is directed to this work. Schoepel and Howard (1966) treated various samples of crude oil-water emulsions with ultrasound, and observed a considerable acceleration in coalescence.

Nikolaevskii (1989) and Nikolaevskii (1992) reviewed some possible physical processes of acoustic and seismic stimulation, and speculated that one possible mechanism is the so called vibrocreep effect. Such nonlinear effect associated with viscoelastic resonance restores the phase permeability of dispersed oil ganglia by either

coalescing or emulsifying the oil. At the same time, such elastic wave fields may considerably reduce capillary forces by vibrating, and consequently, breaking surface films adsorbed to pore walls. When taking colloidal rotation into account, they showed that it is possible to generate bimodal waves which manifest in secondary nonlinear ultrasonic vibrations. Such ultrasonic vibrations may mobilize oil droplets into adjacent pores, or may result in coalescence due to Bjerknes forces. Ultrasonic fields may also cause additional non-linear effects such as in-pore turbulence, acoustic streaming and cavitation. Such effects are however only consequential at very high intensities. Dunin and Nikolaevskii (2005) and Nikolaevskii and Stepanova (2005) proposed a theory on the generation of ultrasonic waves as consequence of nonlinear effects associated with seismic and low frequency acoustic action in fluid saturated porous media. They claim that the attenuation and dispersion of seismic waves in porous or fractured porous media introduces additional vibration modes at much higher frequency (dominant frequencies). The physical mechanisms responsible for such wave spectrum transformations are dry friction in contacts, instability of viscoelastic oscillations, seismic energy pumping into rotational modes, and resonance of gas bubbles and oil droplets. These mechanisms are believed to improve oil recovery. Abrashkin *et al.* (2005) derived a series of analytical equations describing the motion of a drop in an axially symmetric capillary with varying cross section in high frequency and low frequency acoustic fields, taking into account wettability and hysteresis. They assumed that at high frequency, viscous forces can be ignored, while at low frequency, viscosity becomes significant.

Nikolaevskiy *et al.* (1996) provided an interpretation of a vibro-seismic recovery process describing the wave requirements, wave generation and propagation in oil

saturated porous media. He found that one must determine a characteristic frequency depending on reservoir lithology, fluid saturation, and layer stratification. Such frequency could alter oil and water production characteristics and enhance oil production near the residual oil saturation, while increasing water production near immobile water saturation regions. Kuznetsov *et al.* (1998) studied the effect of vibro-energy on waterflood displacement rates and relative permeability ratios. They observed an increase in the oil/water relative permeability ratios when vibration is applied. In a subsequent study Kuznetsov *et al.* (2002), they reported significant incremental oil recovery from wells in Russia when they were stimulated by vibro-energy, and pointed out that decreased water cut was caused by the reduction of water/oil interfacial tension and increase in the relative permeability of the oil. They argued that in some cases, oscillating pressure fields induced by acoustic waves can result in reduction of local pressures below the bubble point, thereby liberating dissolved gas. In fact, even at reservoir pressures much above the bubble point, alternating pressure fields with a wavelength exceeding that of the oil droplets may mobilize the phases because of the density contrast (effective gas drive). This theory was extensively developed by Vakhitov and Simkin (1985) and Kuznetsov and Simkin (1990).

Graham (1997), Graham (1999), Graham and Higdon (2000a, 2000b) numerically studied the motion of fluid droplets in harmonically forced capillary tubes and constricted tubes subject to a mean pressure gradient. In the case of capillary tubes, they observed a significant enhancement in mobility for large droplets, i.e. droplet diameter exceeding the diameter of the capillary, especially when oscillatory forcing is strong, and the drop capillary number is low. Such enhancement is primarily associated with increased droplet

deformation, and is dependent on frequency, amplitude and type of waveform. For constricted tubes, Graham and Higdon (2000a) showed that oscillatory forcing effectively “unplugs” the tube by deforming the droplet. Therefore, acoustic stimulation enables oil droplets to overcome the critical threshold capillary pressure, and consequently initiates percolation. They also identified the minimum oscillatory forcing required to cause such mobilization. Later, Graham and Higdon (2002a, 2002b) considered the role of oscillatory forcing on flow through porous media. Graham and Higdon (2002a), considered the effects of non-zero inertial forces on steady flow, and developed a numerical model based on the steady-state Navier-Stokes equations. They used two geometries to simulate a porous structure: constricted channels and an array of cylindrical capillaries. In both cases, they observed strong nonlinear flow patterns, which may yield to enhanced mobilization under oscillatory forcing. They also observed in-pore turbulence. Graham and Higdon (2002b) extended their earlier model to include unsteady velocity fields. The effectiveness of the percolation rate is a strong function of dimensionless oscillation amplitude. One interesting observation was that oscillation may retard the phase mobility of the lower viscosity component, while keeping the high viscosity phase unaffected. Such process therefore enhances the permeability of higher viscosity phases, and may prove to be an effective “oscillatory filter” capable of separating two fluids with different viscosities.

Zaslavskii (2002) performed experiments to study the motion of small droplets in a capillary. They applied a static pressure on the droplet to control the level of the fluid within the capillary, and altered the frequency of vibration. They noticed a hysteretic dependence of surface tension forces on the velocity of the meniscus.

Tamura *et al.* (2005) showed in a series of intriguing experiments that liquids may adhere to flat ultrasonically driven surfaces. The shape of the droplet depends on the amplitude of vibration. After investigating the effects of intrinsic surface tension and intensity, they developed a simple model to predict drop shapes. The predicted drop dimensions matched closely with the experimental observations.

Li *et al.* (2005) studied the mobilization of oil ganglia in a 2D etched glass micro-model under low frequency vibrations. They observed an increase in the recovery of trichloroethylene (TCE) with higher acceleration amplitude and lower frequency. They attributed these findings to the fact that vibrations provide the necessary mechanical force to overcome capillary entrapment, thereby mobilizing oil drops within pores.

High power ultrasound may also be applied to reduce formation damage caused by fines and drilling mud solids, and help mobilize clays in rocks, thus increasing rock permeability and porosity (Venkitaraman *et al.* 1995; Roberts, Venkitaraman *et al.* 2000; Wong *et al.* 2003; Champion *et al.* 2004; Poesio and Ooms 2004; Poesio *et al.* 2004; Van der Bas *et al.* 2004; Wong *et al.* 2004). Venkitaraman *et al.* (1995) conducted a series of laboratory experiments to investigate the feasibility of using ultrasound to remove formation damage caused by water-based drilling mud and fines. They damaged Berea sandstone and limestone cores with drilling mud, and then treated it with ultrasonic radiation at various frequencies and intensities. After backflow, they found that permeability was greatly increased. Roberts *et al.* (2000) showed that ultrasonic energy can be effectively applied to reduce near-wellbore damage caused by organic deposits and polymers by suspending paraffin deposits and restoring the effective permeability of the rock. Wong *et al.* (2004) tested a prototype oval-mode downhole ultrasonic emitter,

and determined the required acoustic power to remove fines and particles plugging the near wellbore region. Poesio and Ooms (2004) and Poesio *et al.* (2004) developed an extensive theoretical model to predict removal of small particles and fines in porous media. Gollapudi *et al.* (1994) demonstrated that ultrasound may be successfully utilized to remove asphaltenes from wellbores. They applied a thin layer of asphaltene onto glass beakers, and insonicated them in aqueous or kerosene solutions for different time intervals and intensities. Subsequently, they applied the same ultrasound on asphaltene/sand mixtures while circulating in a flow cell, and observed that the maximum time required to clean the sand was two minutes. They recommend continuous pumping during insonication in order to avoid reprecipitation, and to disrupt maltenes. Shedid (2002) and Shedid (2004) looked into the influence of ultrasonic irradiation on U.A.E. crude oil viscosity and asphaltene deposition, and found that ultrasound breaks down asphaltene clusters, and enhances asphaltene solubility into crude oil after chemical treatment. He also proposed a correlation to predict the permeability recovery factor using sonication time and frequency. Paraffin deposits may also be effectively removed from pipes and wellbores (Horblit 1951; Dvali and Sumarokov 1968). Abad-Guerra (1976) studied the effect of ultrasonic energy on sandstone cores initially plugged by paraffins. He observed dramatic improvements in the permeability, which he attributed to ultrasonic cavitation and heating.

Additionally, researchers have toyed with the idea of utilizing ultrasound to improve the upgrading of heavy oil and tar sands in-situ or in pipes (Sadeghi *et al.* 1990; Sadeghi *et al.* 1992; Lin and Yen 1993; Sadeghi *et al.* 1994; Yen and Dunn 1999; Dunn and Yen 2001; Bjorndalen and Islam 2004).

Besides its promising role in the oil & gas industry, high power ultrasonics has also been applied by environmental engineers to accelerate remediation of nonaqueous-phase liquids (NAPL) from soils (Reddi *et al.* 1993; Reddi and Challa 1994; Iovenitti *et al.* 1996; Reddi and Wu 1996; Hilpert *et al.* 2000; Roberts *et al.* 2001; Iassonov and Beresnev 2003; Kim and Wang 2003; Vogler and Chrysikopoulos 2004). Ultrasonics is often used by the textile industry to enhance the mass transfer of dyes into porous fabric (Johnson and Mccall 1994; Yachmenev *et al.* 1998; Moholkar and Warmoeskerken 2004; Moholkar *et al.* 2004; Vouters *et al.* 2004) and in dry cleaning applications. The food industry has also successfully applied ultrasonic stimulation to extract oil from food products such as soy beans (Li and Horne 2004; Riera *et al.* 2004).

1.3 Summary

Applications of ultrasound range from enhanced oil recovery (EOR) to well stimulation, in-situ upgrading, wellbore cleaning, and soil remediation. Acoustic energy may be delivered into a reservoir via three methods:

- In-situ sonication
- Seismic methods
- Pressure Pulsing Technology

In the case of in-situ sonication, an acoustic emitter is lowered into the well bore, generating acoustic waves at a high intensity. The acoustic waves travel through the porous media, and excite the fluids mechanically. Seismic methods are applied via explosives, earthquakes, and surface vibrators, and are generally low frequency, high intensity methods of delivering compressional waves into reservoirs. Finally, pressure pulsing is a method, by which sharp pressure waves at a particular frequency depending on fluid and reservoir properties are hydraulically applied to the liquid in wells.

Despite numerous promising field trials, laboratory experiments, and patents, the exact mechanism behind ultrasonic stimulation is still poorly understood. Most of the findings have been speculative with limited experimental verification. The reason for this is two-fold. Firstly, the problem is very complex, involving a superposition of several competing mechanisms (**Figure 1-3**). Secondly, it is not certain how far an acoustic wave propagates into the reservoir, nor how such propagation occurs. Ultrasonic applications are limited to the near-wellbore area due to the high attenuation through the rock or fluids. When using Biot's theory, one expects that the attenuation length of ultrasound at 20 kHz ranges from 2 – 10 cm. As a consequence, most research in recent years has

shifted to low energy, low frequency waves that can propagate several kilometers into the reservoir. Nevertheless, because dispersion of low frequency waves within porous media forms high-frequency harmonics (ultrasonic noise), one would still expect ultrasonic waves to be present in the reservoir. Additionally, because of its very short wavelength, one would expect that ultrasound is more influential in the capillary dynamics within a pore than large wavelength alternatives.

Ultrasonic radiation introduces mechanical vibrations, which strongly influence interfacial forces by enhancing momentum and heat transfer across the phase interfaces. The following mechanisms are believed to be responsible for the observed improvement in percolation of oil within porous media:

- Increasing the relative permeability of the phases by promoting phase separation.
- Due to nonlinear acoustic effects such as in-pore turbulence, acoustic streaming, cavitation, and perturbation in local pressures, ultrasound reduces the adherence of wetting films onto the rock matrix. This effect is only relevant at high ultrasonic intensities.
- Reducing surface tension, density and viscosity as a consequence of heating by ultrasonic radiation. In the case of polymers, ultrasonic degradation may reduce the viscosity, as well.
- Altering of rheological properties of non-Newtonian fluids.
- Enhancing mobilization of oil blobs due to mechanical vibration of pore walls (peristaltic fluid transport), by which fluid is “squeezed” into adjacent pores
- Strengthening the adhesion of liquid films onto vibrating pore walls
- Micro-emulsification of oil in the presence of natural or introduced surfactants.

- Coalescence and dispersion of oil drops due to the Bjerknes forces.
- Increasing in rock permeability and porosity due to deformation of pores, and removal of fines, clays, paraffin wax and asphaltenes.
- Oscillation and excitation of capillary trapped oil drops due to pressure perturbations generated by cavitating bubbles and mechanical vibrations of rock and fluid

These mechanisms, which are principally governed by capillary and viscous forces (Bear 1988; Hilpert *et al.* 2000), depend on the frequency and intensity of the acoustic field, as well as on rock elasticity, fluid properties, porosity, cementation, and clay content. Frequency plays an important role in wave dispersion, attenuation and heat dissipation. At higher intensity, mechanical stresses, and therefore, temperature increase. As such, the destruction of deposits and films on pore walls, as well as the reduction of viscosity and interfacial tension, may only occur with high frequency/high intensity acoustic fields. Fluid properties, such as density, viscosity and surface tension directly affect the wave propagation, compressibility, and shear response. Porosity, cementation and clay content enhance the wave dispersion, and strongly attenuate Biot's slow wave.

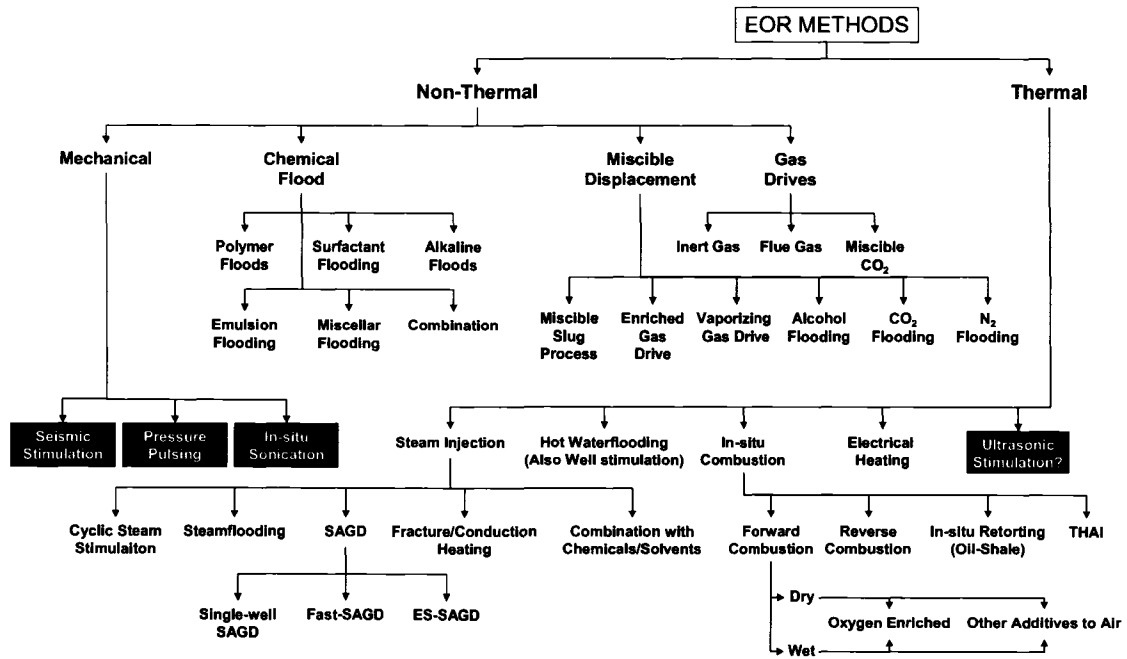


Figure 1-1: A summary of currently accepted Enhanced Oil Recovery methods. Outlined in black are the vibro-mechanical options with which this dissertation is primarily concerned. (Adopted from Farouq Ali and Thomas (1996)).

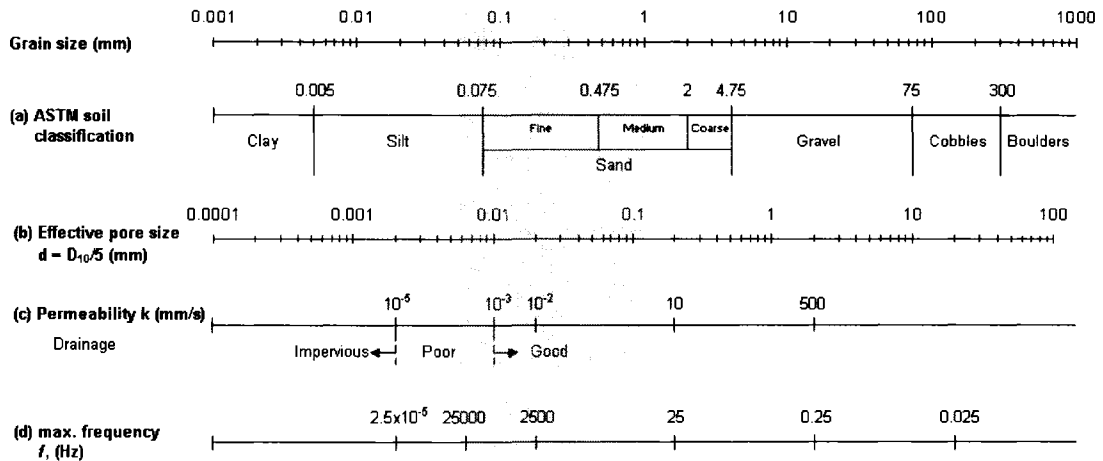


Figure 1-2: The comparative length scales in relation to Biot's model of poroelasticity and grain sizes in millimeters: (a) ASTM soil classification, (b) effective pore size, (c) approximate permeability, (d) frequency. The shaded area corresponds to Biot's allowable frequency range (based on some of his assumptions).

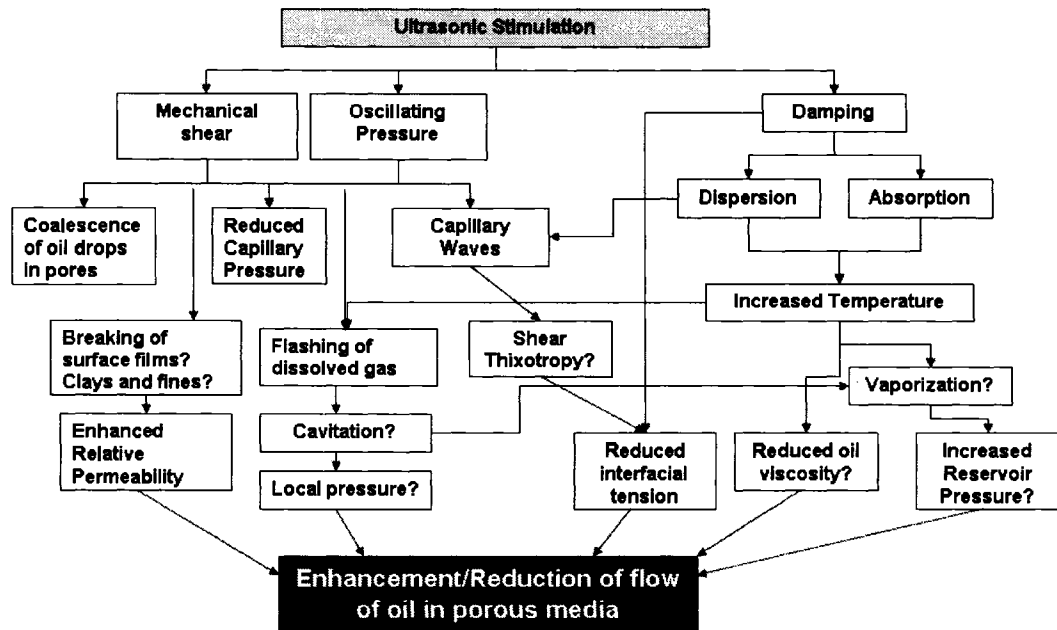


Figure 1-3: The complex interplay of various physical mechanisms believed to be present when ultrasound is applied to porous media. Any superposition of these mechanisms may result in either a reduction or enhancement of flow in porous media.

2 Pendant drop experiments

2.1 Introduction

Many researchers have investigated the rise of liquid level within a capillary tube subjected to an ultrasonic field (Prokhorenko *et al.* 1982; Rozin *et al.* 1984; Rozina and Rozin 1994; Rozin *et al.* 2001; Rozina 2002; Dezhkunov and Leighton 2004). Most of the investigations attribute this rise to ultrasonic cavitation at the tip of the capillary. A collapsing vapor bubble can exert thousands of pounds per inch of pressure locally, causing a temporary increase in phase pressure. Assuming that thousands of bubbles collapse within a minute, the cumulative pressure increase results in a rise in fluid level. It was also shown that the wettability of liquids on solid ultrasonically driven surfaces is enhanced (Tamura *et al.* 2005). Therefore, applying ultrasonic radiation onto a capillary may increase capillary forces, and increase wetting of the denser phase.

The drop formation at a capillary tip has been studied extensively by many authors in the past century. Two types of flow regimes have been identified to describe fluid ejection from a capillary. At high rates, drops exit the capillary in form of a jet (connected set of drops), while at low rates, distinct droplets form at the tip. An excellent experimental treatise on this topic may be found in the dissertation of Cramer (2004). Drop formation is usually divided into two stages: (a) early static growth at the capillary, and (b) necking/detaching. The first study on drop development into air was performed by Harkins and Brown (1919). Their work formed the basis for later developments to account for liquid-liquid systems (Hayworth and Treybal 1950; Null and Johnson 1958; Wilkinson 1972), and is used to determine interfacial tension (pendent drop method).

They developed a simple equation that relates the weight of a falling drop to fluid and drop properties based on a simple force balance:

$$m_d = \frac{2\mu r_c \sigma}{g} \cdot f\left(\frac{r_c}{V_d^{1/3}}\right) \quad 2-1$$

where r_c is the radius of the capillary, μ is the viscosity of the drop fluid, σ is the surface tension, g is a conversion factor, and V_d is the volume of the detached drop. Therefore, the size of a drop is inversely proportional to the cubic of interfacial tension, and viscosity. He also introduced a correction factor, f , to account for the deformation and ellipticity of the drop, as well as the lost fluid remaining at the tip of the capillary. Although very effective at predicting the shape of a droplet at static conditions, this approach did not provide sufficient insight into the dynamic process of dripping, which involves a time evolution of drop shape, velocity and pressure field within the drop, and the generation of a liquid thread connecting the drop to the capillary. Eggers and Dupont (1994) have simulated the one-dimensional problem using a finite difference method to solve the conservation of mass and axial momentum equations. In a later study, Zhang and Basaran (1995) performed a series of experiments to study the dynamics of liquid dripping into air. They showed that the viscosity of the disperse phase plays a key role in the stabilization of the droplet by dampening interfacial instabilities. A full transient solution to the two-dimensional mass-momentum equations was developed by Zhang (1999a; 1999b). He studied the drop profiles and rates based on various dimensionless parameters, such as Reynolds number and Capillary number, in an effort to quantify the dependence of drop formation on inertial, viscous, gravitational and surface tension forces.

Several investigations concentrated on the parameters governing the dripping rate of droplets from a capillary (e.g. Martien *et al.* 1985; Katsuyama and Nagata 1999; and Renna 2001). When a droplet breaks off the capillary tip, it leaves some liquid behind. This liquid oscillates, causing mechanical vibrations which induce the development of a new drop. The mechanical vibrations also effect the generation and dynamics of a new droplet. (Martien *et al.* 1985; Kiyono and Fuchikami 1999; Tufaile *et al.* 1999; Renna 2001). A detailed discussion of the flow dynamics of droplets from capillaries is beyond the scope of this thesis, and the interested reader is referred to the relevant references, as well as the excellent work by Cramer (2004).

Based on the dynamics of dripping, a series of pendant drop experiments were performed to explore the effect of ultrasound on drop-rate within narrow capillaries. As mentioned earlier, the drop rate is a strong function of both viscosity and interfacial tension. This section starts with a brief description of the experimental setup, as well as the fluid properties used in the subsequent experiments, and concludes with results and a discussion.

2.2 Experimental Setup

A Hastelloy C-276 0.1 mm capillary was used to inject water at a constant pressure into various oleic fluids. A tear drop shaped glass vessel was utilized to maintain a constant hydrostatic head pressure of 10 cm H₂O (0.1422 psi). A 3/4" ultrasonic horn was employed to deliver continuous ultrasound at a broad range of intensities at an angle of approximately 45°. The oleic phase was contained in a 2 mm thick glass cylinder (5 cm diameter) which was sealed with a rubber stopper at the bottom end. The glass container served to protect the capillary from the intense cavitation zone generated by the horn, and

ensured that the observed drop rate was entirely due to ultrasound alone. It also reduced the level of emulsification which may affect the rheology of the oleic phase. One inch of the capillary was immersed into the oleic phase. Images of the falling drops were recorded using a Canon Xi video camera, and digitized using Windows Moviemaker. The experimental setup is presented in **Figure 2-1**. Snap shots of the droplets just before detachment are shown in **Figure 2-3** for increasing ultrasonic intensities.

2.3 Fluid Properties

Three types of refined paraffin oil and kerosene were used in these experiments. The fluid properties are shown in **Table 2-1**. Fluids were chosen to cover a broad range of interfacial tension and viscosity. N350 (Canon Instruments calibration oil) is a high viscosity, low IFT oil. Light mineral oil and heavy mineral oil are low viscosity, high IFT oils. Kerosene has very low viscosity, and intermediate IFT to water. De-aerated water was used as the injected phase, primarily to prevent emulsification at higher intensities of ultrasound, as well as to increase the cavitation threshold due to the absence of dissolved air.

2.4 Experimental Procedure

After applying a constant fluid pressure of 10 cm H₂O onto the pipette, we allowed the flow rate through the capillary to stabilize to a constant rate. Ordinarily, a constant flow rate was achieved after 2 minutes of dripping. Once a constant flow rate was maintained, we initiated ultrasound at gradually increasing power settings. Experiments at a particular setting usually last more than 10 minutes to assure a consistent time averaged drop rate. In order to get an accurate drop count, we used a Canon Xi camera to record the process.

The analog film was then digitized, and drops were counted during the period of time. Drop rate per minute was estimated by dividing the number of drops over the time interval at which these drops were measured. For example, if we counted 43 drops in 10 minutes and 32 seconds, the resulting drop rate is 4.23 drops/minute. In order to avoid emulsification of the oil-water system, we carefully monitored the texture of the liquids and did not exceed the emulsification intensity.

2.5 Results and Discussion

Figure 2-2 shows the results of all experiments. The drop count increased up to a critical threshold after which it linearly decreased with increasing intensity. It is apparent that the dripping rate is dependent on both viscosity and interfacial tension between the oil and water. The peak drop rate tends to shift to higher intensities as viscosity is increased, and shifts to lower intensity settings with decreasing interfacial tension. Therefore, as the viscosity of the continuous phase increases, a higher intensity is required to maximize the water expulsion rate through the capillary. Lower intensities are necessary when interfacial tension is reduced. One of the reasons behind such observation is that in the presence of ultrasound, the event of neck-breaking between the capillary tip and the droplet is enhanced. Since the rate of droplet formation is directly related to neck breaking, which in turn is a function of the mechanical oscillations at the neck, it is expected that one observes a lower drop rate as intensity is increased. At low intensity, however, oscillations at the neck are reduced, resulting in a more steady state droplet formation. Due to viscous damping, the same effect occurs when the viscosity of the oil is increased. This causes droplets to form at a higher rate.

It has also been shown that fluids tend to adhere to ultrasonically driven surfaces (Tamura *et al.* 2005). Therefore, as one increases the intensity, vibration of the capillary due to the ambient acoustic field causes an increase in wetting of the water onto the capillary. Increased water wetting results in higher positive capillary pressure, thereby retarding the flow of water through the capillary. Apparently, this effect is magnified at high intensity. At low intensities, on the other hand, such process may be reversed. Water wetting is reduced, hence reducing the capillary pressure. As a consequence, more water is expelled from the capillary. One key feature, namely the peak water rate at a characteristic intensity value, indicates a switch in the physics of the process.

A less likely explanation, which should still be considered, is the formation of micro-bubbles within the capillary. Micro-bubbles may form during cavitation, and may stick to the inner wall of the capillary. This effect results in a lowered effective diameter of the capillary, resulting in a reduced flow rate of water. Nevertheless, the de-aeration of the water considerably reduced the probability of this to happen.

The hypothesis that interfacial tension between the water and the oil was altered under ultrasound is questionable after comparing the drop shape at different ultrasonic intensities. From **Figure 2-3**, it can be readily concluded that the drop shape did not noticeably vary with increasing intensity. Since the images taken are of limited resolution, it was not possible to estimate interfacial tension via the geometric method, since the error due to digital processing would have exceeded the variation.

The relevance of these findings may explain various observations made during the imbibition experiments. In essence, the capillary represents a pore throat. When applying ultrasound to porous media, a series of physical mechanisms, such as increased local

wettability and vibrations of ganglia at the pore throat, may induce a higher capillary snap-off threshold. This mechanism may considerably improve the percolation of oil ganglia into adjacent pores, and ultimately lead to higher recovery.

2.6 Conclusions

1. Ultra-sound affects the dripping rate of water through a capillary into various oleic phases.
2. The dripping rate reaches a maximum at a characteristic intensity, which depends on interfacial tension and oil viscosity. Increase in viscosity results in a shift of the peak to higher intensities. Reduction in interfacial tension causes a shift of the peak to lower intensities.
3. We speculated that ultrasound affects the breaking of droplets from the capillary tip, causing mechanical vibrations at the fluid which remains attached. These vibrations may slow down the development of consecutive drops. Another mechanism may be improved adherence of water films onto the inner wall of the capillary, thereby increasing the capillary pressure. Increase in capillary pressure reduces the ability of water to exit the capillary. At low intensities, this effect does not seem to be considerable.
4. The interference of trapped air bubbles within the capillary (generated during cavitation) is not believed to be the source of our observations.
5. Alteration of interfacial tension under ultrasound was not observed.
6. Further work is needed to analytically match the results, and estimate the contribution of mechanical vibrations on neck breaking. Perturbation theory on

Navier-Stokes equation may give valuable insights into the governing mechanism, and the relative impact of ultrasound.

Table 2-1: Properties of the fluids used in pendant drop experiments.

Fluid	Density⁽¹⁾ g/cc	Viscosity⁽²⁾ cp	Surface Tension⁽³⁾ dynes/cm	Interfacial Tension⁽³⁾ dynes/cm
Light Mineral Oil	0.8383 ± 0.0050	46.5 ± 0.5	9.9 ± 0.2	61.8 ± 1.2
Heavy Mineral Oil	0.8508 ± 0.0050	167.0 ± 1.7	46.2 ± 0.9	51.0 ± 1.0
Kerosene	0.768 ± 0.0050	2.9 ± 0.03	53.2 ± 1.1	40.7 ± 0.8
N350	0.8885 ± 0.0014	1112.0 ± 1.8	8.6 ± 0.2	35.3 ± 0.7

(1) Weight-Volume method using a 5cc syringe

(2) Rotational viscometer (Fann 35A) at 300 rpm; Viscosity values for S60, S200, N350 and S600 were obtained from Canon Instrumentation Company (A2LA Certificate #1262.01)

(3) Du Nouy type tensiometer (Fisher Scientific Tensiometer; Platinum-Iridium ring)

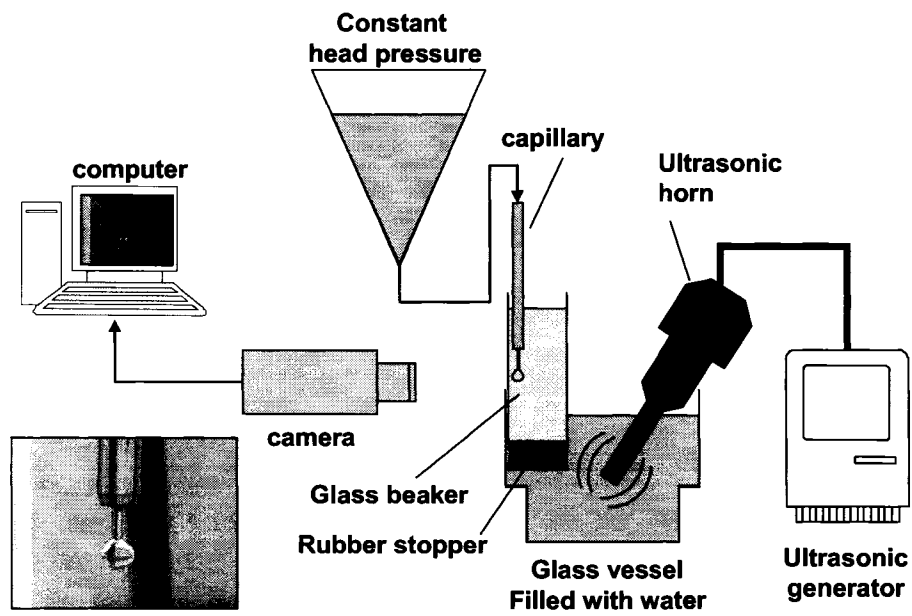


Figure 2-1: Experimental setup of the pendant drop experiments.

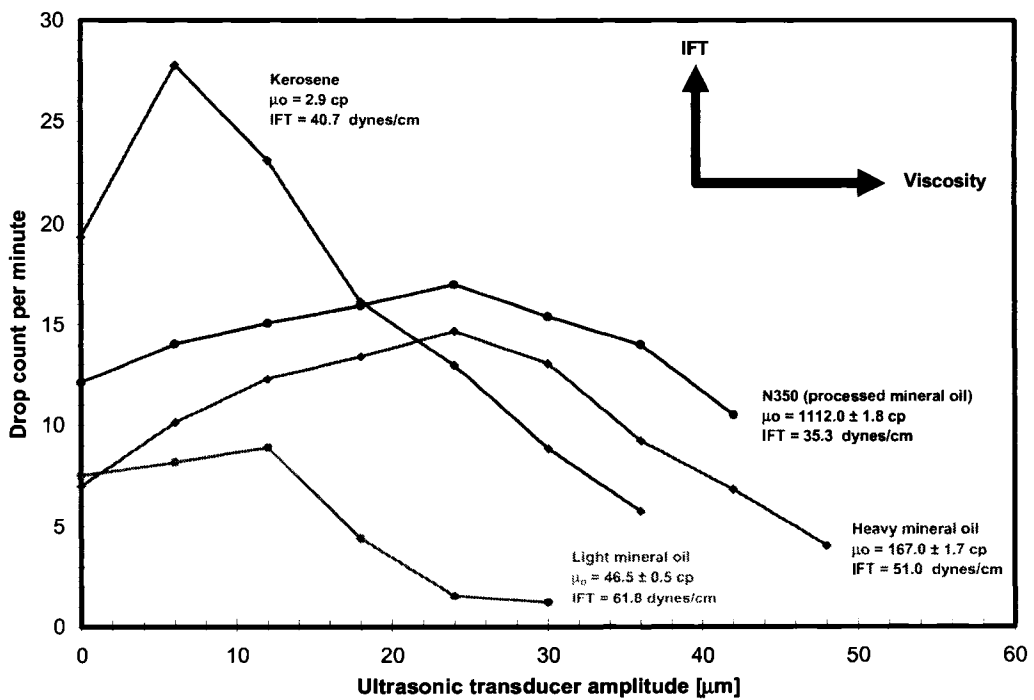


Figure 2-2: Water drop count per minute versus ultrasonic transducer excitation amplitude for various oil types.

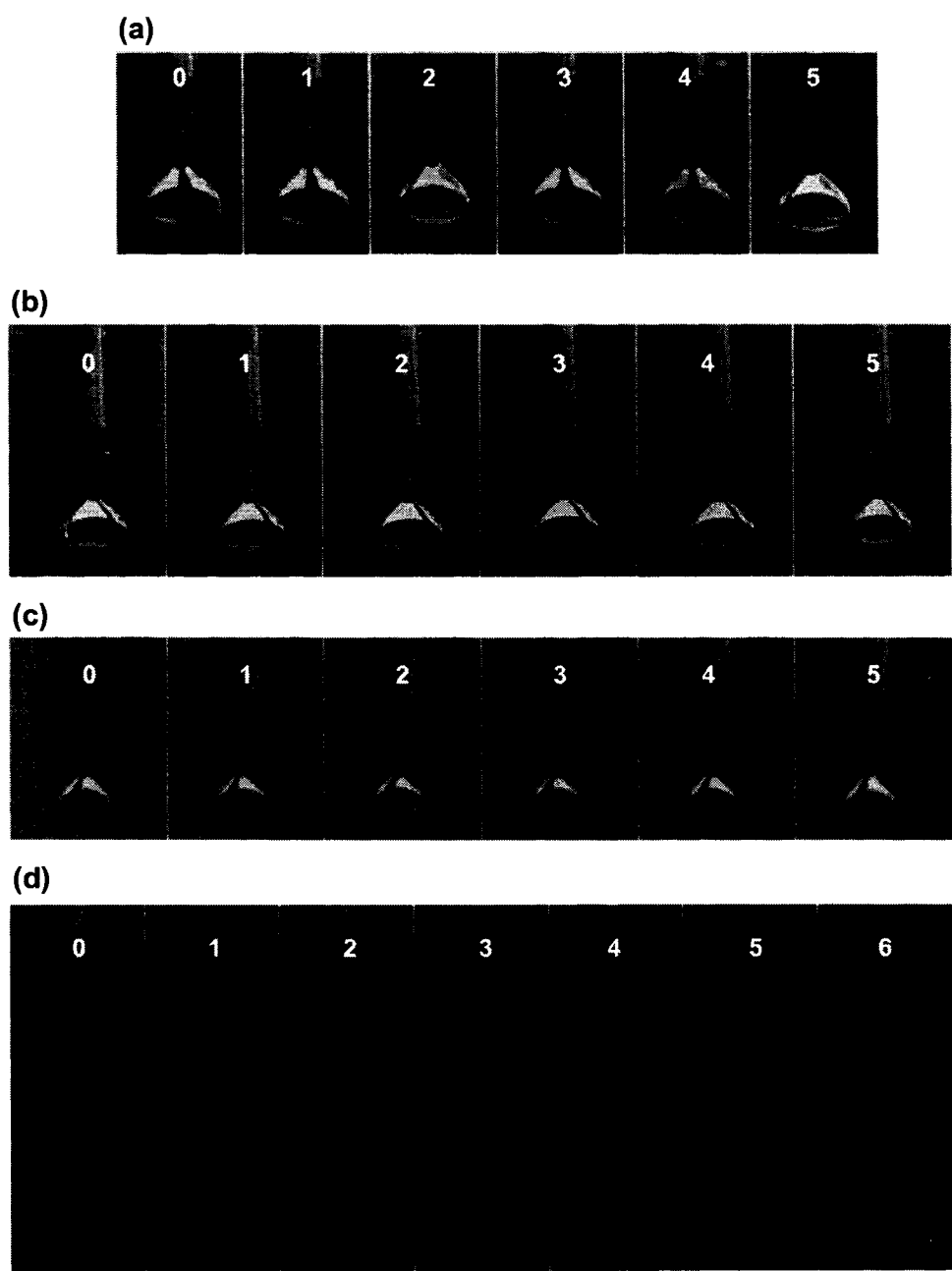


Figure 2-3: Snap shots of pendant drops just before detachment. A wide range of viscosity and interfacial tension was investigated by using (a) light mineral oil, (b) heavy mineral oil, (c) kerosene, and (d) high viscosity processed mineral oil N350. Numbers at the top of each image indicates the ultrasonic setting [0 = no ultrasound; 5 = high ultrasound]. After inspecting the shape of the drops visually, it can be readily concluded that interfacial tension does not noticeably change with ultrasonic intensity.

3 Hele-Shaw Experiments

3.1 Introduction

Based on the observations from the capillary imbibition experiments (Chapter 4), we decided to minimize the effects of the viscous or interfacial forces to identify other possible effects on the recovery alteration under ultrasonic energy. We achieved this through a series of immiscible and miscible viscous displacement experiments using a Hele-Shaw model.

When a viscous fluid is displaced by a less viscous fluid, one generally observes finger-like patterns known as “viscous fingers”. These structures, first studied by Saffman and Taylor (1958), are subject to much research, and are relevant to many applications, both fundamental and industrial, such as flow through porous media, combustion in two dimensions and electrochemical deposition. A Hele-Shaw cell is made up of two parallel plates separated by a thin spacer. The flow is governed by the Hele-Shaw equation for Newtonian fluid films:

$$\mathbf{u}_i = \frac{-b}{12\mu_i} \nabla P_i \quad (3.1)$$

where the subscript refers to the fluid phase, \mathbf{u}_i is the depth averaged velocity within the cell of thickness b , μ_i is the dynamic fluid viscosity and P_i is the fluid pressure. Note that this equation reduces to a Laplacian formulation in the case of incompressible fluids, i.e. when $\nabla \cdot \mathbf{u}_i = 0$. In the presence of an interface, as is the case with immiscible fluids, the pressure differential at the interface is related to the interfacial tension and the

curvature of the interface, i.e. from the Young-Laplace equation (e.g. Pellicer *et al.* 2000), we obtain

$$P_1 - P_2 = \sigma \left(\frac{1}{r_1} - \frac{2 \cos \theta}{b} \right) \quad (3.2)$$

where r_1 is the horizontal curvature of the interface, and σ is the interfacial tension between phase 1 and 2. The growing fingers continuously split into sub-branches due to the interfacial instability at the liquid-liquid interface, thereby generating a fractal structure whose smallest element is determined by a balance between viscous and interfacial forces. The morphology of viscous fingers has been studied extensively by Mclean and Saffman (1981), Park and Homsy (1985), and Maxworthy (1987), and can be described by the modified capillary number (Rauseo *et al.* 1987; Chen 1989)

$$Ca' = \frac{U\mu}{\sigma b^2} \quad (3.3)$$

where U is the volumetric velocity of the fluid at the interface, μ the dynamic viscosity of the displaced fluid, σ the interfacial tension, and b the spacing between the plates. In order to generate a complex fingering pattern, one must minimize the characteristic scale length λ_c (Chuoque *et al.* 1959; Plouraboue and Hinch 2002), defined as

$$\lambda_c = \pi b \sqrt{\frac{\sigma}{\mu U}} \quad (3.4)$$

This parameter, also called capillary length, represents the most unstable wavelength from linear instability analysis between two immiscible fluids with high viscosity ratio.

The capillary length is small when b and σ are small, and μ and U are large (e.g. Guan and Pitchumani (2003)). The different mechanisms of finger splitting, shielding and spreading are thoroughly discussed by Homsy (1987).

One striking feature of viscous finger growth within a planar geometry is the observation that the propagation of a Laplacian flow field has a close similarity to the growth of aggregates generated by Diffusion Limited Aggregation (DLA) (Witten and Sander 1981; Paterson 1984; Shraiman and Bensimon 1984). Whether there is a mathematical correspondence between these distinctively different processes is still heavily under debate.

Since most of the governing mechanisms behind ultrasonic stimulation are dominated by interfacial forces, it was hoped to gain valuable insights into interfacial behavior from Hele-Shaw experiments. In fact, Hele-Shaw experiments very accurately illustrate how perturbations influence the liquid-liquid interface, without the additional complexity arising from porous (channeled) structures, such as rocks. Since ultrasound introduces a perturbation in the form of pressure fluctuations, one would expect to observe a more complex pattern than with viscous fingering in the absence of ultrasound. This is partially due to the fact that ultrasound adds additional points of instability at the interface. However, the exact effect of ultrasound is unknown. We speculate that ultrasound increases finger splitting when the wavelength of the field equals that of the instability length λ_c . If the wavelength of the ultrasound is 90° out of phase with the instability length, however, ultrasonic waves may actually stabilize the interface, and reduce finger splitting. This hypothesis must yet be proven mathematically or empirically, however.

May it be as it is, if any changes in fractal morphology are observed within a Hele-Shaw cell, one can conclude that ultrasound introduces a perturbation onto the interface, which either enhances or reduces the complexity of the fingering pattern. High complexity implies more severe frontal instability, and is directly related to the effective capillary number of the system. This change in complexity may be quantified by use of fractal dimension. May and Maher (1989) measured the fractal dimension for a wide range of capillary numbers (N_{Ca}), and found that the fractal dimension took on the value of approximately 1.71 for N_{Ca} ' between a critical value and 35, and 1.79 at intermediate values, after which it plateaus at 1.79.

To gain more insight into the capillary interaction between oil and aqueous phase, we designed a series of immiscible Hele-Shaw experiments at constant pressure and injection rate. A similar approach as employed by Fernandez and Homsy (2003) was adopted in this study. They studied the change in fingering pattern in a Hele-Shaw cell during a chemical reaction, and used fractal methods, as well as dimensionless groups, to quantify changes in interfacial tension during the exothermal heating of the front. Additionally, we performed a series of miscible, high viscosity-ratio Hele-Shaw experiments, where interfacial phenomena are entirely absent and the process is entirely dominated by viscous forces, convective dispersion and molecular diffusion.

This chapter starts with a brief overview on fractal analysis, and the image processing conducted to facilitate accurate determination of fractal dimension and lacunarity. It is then followed by an overview of the experimental equipment and methodology. Next we present all major observations, and discuss their implications.

Finally we end the chapter with some conclusive statements, and a reflection of how to improve the experiments.

3.2 Fractal analysis

As demonstrated by Paterson (1984) and others, viscous fingers can be represented semi-quantitatively by fractal DLA patterns. DLA patterns are created via a seed particle at the origin of some constraint area. Consecutive particles are introduced from a large distance, and randomly walk across the constraint area. If they are within a certain radius from the seed, they are directed to the seed, and stick to it. This is repeated with a new particle. Such patterns are quantified by two distinctly independent parameters: aggregate size, and sticking radius. The aggregate size defines the fineness of the DLA pattern, while the sticking radius determines how compact a DLA pattern is. In this study, we used a custom program donated by Audriey Karperien (2006), which can be readily downloaded at the ImageJ plug-ins page: <http://rsb.info.nih.gov/ij> (Rasband (1997-2005)). **Figure 3-1** shows various DLA patterns for different aggregate sizes. One can observe that as the aggregate size increases, the pattern becomes coarser, wider, and more compact. Therefore, it is possible to correlate aggregate size to capillary number.

Given the nature of fractality of Hele-Shaw pattern development, one may also use the fractal dimension to characterize instabilities. Fractal dimension has been employed extensively to quantify the morphology of radial viscous fingering (Daccord and Nittmann 1986; May and Maher 1989; Praud and Swinney 2005), and is a useful tool to assess the degree of complexity. It defines the scaling rule which dictates the number and scale of new branches. The scaling rule of a fractal is modeled by a power-law transformation of scale, or mathematically, as

$$N(\varepsilon) = \varepsilon^{-D_B} \quad (3.5)$$

where N is the minimum number of open sets of diameter ε needed to cover the set (Mandelbrot 1983). The fractal dimension can be obtained by taking the logarithm of Equation 3.5, rearranging for D_B and taking the limit as ε goes to zero:

$$D_B = \lim_{\varepsilon \rightarrow 0} \frac{\log N(\varepsilon)}{\log \varepsilon} \quad (3.6)$$

One can attain D_B from box counting, by overlaying a binary image onto a grid (Liebovitch and Toth 1989). For consecutively decreasing grid size ε , we count the number of pixels that are contained within one grid box is $N(\varepsilon)$, and plot the resulting data on a log-log plot. The best fit to the straight line denotes the fractal dimension.

Besides fractal dimension, we also decided to employ an additional parameter, namely lacunarity to analyze the displacement patterns. Lacunarity assesses the degree of “gappiness” or “visual texture”, and represents the amount of heterogeneity or translational/rotational invariance of a binary image (Plotnick *et al.* 1996). This measure supplements fractal dimension by introducing a notion of “compactness”. A fractal may have the same fractal dimension, but may display an entirely different texture. **Figure 3-2** demonstrates three one-dimensional polyadic Cantor sets to illustrate lacunarity. Although all sets have the same fractal dimension of $D_B = \log(4)/\log(7) = 0.712$, they vary considerably in appearance. At low lacunarity, the fractal is homogeneous, and grows symmetrically and uniformly. As the lacunarity increases, one observes more void space. It is clear that fractal dimension alone is not sufficient as a descriptor of complex

patterns. The lacunarity, Λ_ε , is calculated as the variation in pixel density at different ε . First the number of pixels within each grid box of dimension ε is counted using a standard non-overlapping box count. For each ε , a coefficient of variance is computed from the standard deviation (s) and the mean (M) of number of pixels per box:

$$\Lambda_\varepsilon = \left(\frac{s}{M} \right)^2 \quad (3.7)$$

Thus, the lacunarity is related to the distribution of empty spaces (lacuna) of an image. If an empty region of an image with fractal geometry displays a high diversity of sizes, the lacunarity is usually high. On the other hand, if the fractal is invariant in empty spaces distribution, lacunarity is low (Plotnick *et al.* 1996).

The open source ImageJ plug-in [FracLac V.2.44](#) (Rasband 1997-2005; Karperien 2005) was used to compute both fractal dimension and the lacunarity of binary images. The source code is readily available online. To test the reliability of the program for 800x800 pixel images, we generated a series of analytical fractals using Wolfram Mathematica 5. The fractals (**Figure 3-3**) as well as their corresponding Hausdorff dimension and the box counting dimension obtained with FracLac is tabulated in **Table 3-1**. A cross-comparison plot of analytical fractal dimension versus box counting dimension (**Figure 3-4**) reveals that for most patterns a deviation of less than 3% is expected when using FracLac. Therefore, for a pattern with $D_B = 1.5$ we anticipate a nominal error of ± 0.045 . It was also shown by Karperien (2005) that FracLac performs especially well on contours and fractal outlines.

3.3 Experimental Setup

The experimental setup of all Hele-Shaw experiments is sketched in **Figure 3-5**. The Hele-Shaw cell consists of a pair of rectangular glass plates, 23 x 23 cm² wide and 1.0 cm thick, which are separated by eight borosilicate glass spacers approximately $b = 0.17$ mm in height, and 1.5 x 1.5 cm wide (Fischer Scientific microscope cover glasses). The glass spacers were glued onto the bottom plate with a 5-minute high-adhesion UV-resistant epoxy. To avoid any bending of the glass plates, four additional spacers were introduced on each side. The plates were held together tightly by two fastening clamps. The locations of the spacers are not believed to interfere greatly with the outflow of fluids from the cell, causing minimum disturbance of the pattern front. A white epoxy layer was painted on the bottom plate to provide a white screen, improving the image contrast and facilitating easier image processing. Illumination of the Hele-Shaw cell was accomplished using a standard fluorescent ultraviolet (UV-B) dark light. A syringe pump (Genie Pro) was used to inject the aqueous phase into a 1/8 in. injection port via a 1 m of chemically resistant vinyl tube. It can provide accurate flow rates between 0.001 cc/min and 10 cc/min. We used a tear drop vessel (same unit as used in Chapter 2) to maintain a constant hydrostatic pressure at a precision of around ± 0.005 psi. A digital 6.7 megapixels camera (Canon EOS Rebel) was installed 0.7 m above the cell, and set to continuously record the injection process at intervals of 10 seconds.

As an ultrasonic bath, we used a standard 4 gallon tank filled with water. An ultrasonic dual-horn was positioned 15 cm away from the plates in order to avoid undesired pressure fluctuations at the boundary due to the cavitation zone at the tip, and to minimize vibration of the plates. De-aerated water was used within the bath to

minimize the dispersion and absorption of ultrasonic energy due to cavitation, and to facilitate more effective propagation of the sound waves. The Hele-Shaw cell was immersed sufficiently deep into the bath to allow transfer of ultrasonic energy into the liquid. A leveling table was used to horizontally adjust the plates.

3.4 Experimental Procedure

The pair of glass plates was carefully cleaned with surfactant, and pressure dried with air and dry tissue paper. We then wiped the active sides with acetone and water to remove any surfactant on the plates. The plates were then pre-wetted with thin film of mineral oil (or processed oil). After a few minutes, the spacers were applied, and mineral oil was carefully poured evenly onto the plates. Once the mineral oil uniformly spread on the bottom plate, the top plate was slowly applied, and fastened. We also made sure to spread mineral oil along the edges to facilitate a smooth transition of the interface between the fluids within the Hele-Shaw cell and the ultrasonic bath. Great effort was taken to avoid any development of bubbles within the plates or the injection tubing. The saturated plates are then semi-immersed into the ultrasonic bath, and the low-viscosity phase was injected at a constant rate. In order to reduce the capillary transition between the plates and the bath, we maintained a thin 0.3 cm film (red in **Figure 3-5-a**) of oil above of the bath-water (blue in **Figure 3-5-a**). This film was in direct contact with the annulus between the two plates, and mitigated the sudden jump in capillary pressure due to the oil-water interface.

Water and 3% DOWFAX 2A1 (Alkyldiphenyloxide Disulfonic Acid: anionic surfactant) were used as the aqueous phase. Both solutions were dyed with water-soluble fluorescent tracer dye (Risk Factor IFWB-C0) that glows under UV darklight to ease

subsequent image analysis. DOWFAX 2A1 was used to reduce the interfacial tension, and thus allow for a broader range of capillary numbers. The reader is referred to **Table 4-1** and **Table 4-2** for a detailed description of the fluid properties. For miscible injection, we used three different oleic fluids with different miscibility characteristics to heavy mineral oil:

1. kerosene (non-volatile)
2. heptane (volatile)
3. pentane (volatile)

These fluids were dyed with an oil soluble fluorescent dye (Risk Factor DFSB-K43) to ease subsequent image analysis.

Every experiment consists of two runs; one with ultrasound and one without. Experiments were repeated at least three times to ensure repeatability. A successful run was evaluated according to the following criteria:

- (a) Consistency in fractal pattern
- (b) Repeatability
- (c) Radial symmetry

Due to the stochastic nature of the flow, it was not always possible to observe a perfectly radial propagation of the finger front. This was especially the case with surfactant, where frontal instabilities are pronounced. After each experiment, the resulting images were digitized, and converted into binary images (see Section 3.5). The fractal perimeter, area, fractal dimension and lacunarity were determined via fractal analysis software (ImageJ FracLac).

3.5 Image processing

In order to apply the box counting algorithm to determine the fractal properties, all images obtained from the Canon EOS Rebel camera had to be first digitized, and then converted into binary images. The original images were 1536 x 1024 pixels in dimension. After cropping, the average size of the patterns was reduced to 750 x 750 pixels. We used known fractals, such as the “Koch’s snowflake” and the “Box Fractal” to test FracLac’s accuracy due to image size. In all cases, the resulting computation yielded errors less than 3% from the exact fractal dimension of the sets. Binary image thresholding was achieved by first contrasting the image, and then converting to an 8-bit tiff-file. We then ran a series of background subtraction algorithms (1000 Pixel and 500 pixel rolling ball radius), as well as an intensity-threshold algorithm to convert all images into binary data. This was followed by a careful removal of any additional pixels due to noise, lighting or thresholding. It is vital for the calculation of fractal dimension and lacunarity that the image is absolutely clean and devoid of any pixels far from the pattern. The binary images were converted into contours, and added to generate contour composite plots. The work-flow is illustrated in **Figure 3-6**. In total, over 1582 images were converted and analyzed. Due to space constraints, we will only present contour composites in this dissertation.

3.6 Results and Discussion

3.6.1 Immiscible Hele-Shaw experiments

3.6.1.1 Constant rate: Water

Immiscible fingering patterns due to constant injection of water into heavy mineral oil are shown in **Figure 3-7** to **Figure 3-10**. All patterns have been scaled so that each tick mark represents 0.5 cm in real scale. Due to space constraints we will only present composite contour plots in this thesis. Each contour outlines the state of the liquid-liquid interface as it evolves through time at 10 second intervals. Two qualitative features may be extracted visually from contour composites: (a) the curvature of the interface, and (b) the direction of interface propagation. In some cases, the interface does not only propagate radially outward from the injection port, but also expands sideways. This type of flow is easily distinguished by darkening the outline around the viscous fingers.

Figure 3-7 shows the fractal pattern generated after injecting water into heavy mineral oil at a constant injection rate of $0.3 \text{ cm}^3/\text{min}$. The viscosity ratio of such system is 166.7 ± 1.7 and the interfacial tension is $51 \pm 1 \text{ dynes/cm}$. There is a clear difference between the patterns obtained without ultrasound, compared to the patterns after ultrasonic stimulation. When no ultrasound is applied, we observed the formation of 6 major branches with only small secondary branches. The curvature of the contours is relatively low, with tips gradually flattening as the pattern matures. Additionally, we noticed that there was a substantial thickening of the branches. On the other hand, the ultrasonically stimulated pattern displayed thinner primary fingers, and pronounced, longer secondary branches. The curvature of the interface was high at early times, and

also flattened as the pattern matured. Branch thickening was relatively low, and the fingers primarily advanced at the tips.

As we stepped up to consecutively higher injection rates, we observed a similar, but less severe response as observed at low rate. **Figure 3-8** displays the contour development after injecting water into heavy mineral oil at $1 \text{ cm}^3/\text{min}$. Again, the non-ultrasonic pattern was more compact, exhibiting more uniform branching. After applying ultrasound, however, we noted less compact branching with erratic secondary divisions. It is apparent that ultrasound acts to stabilize the front, resulting in long primary fingers and suppressed secondary fingering. This observation was also confirmed after injecting water into HMO at $1.5 \text{ cm}^3/\text{min}$ (**Figure 3-9**). After raising the injection rate to $2.0 \text{ cm}^3/\text{min}$ (**Figure 3-10**), the patterns exhibited similar branching behavior with secondary branching occurring at regular intervals.

Figure 3-11 presents the growth rate of the perimeter and area of such patterns versus time. These plots illustrate the consistent linear growth of the pattern, as well as the consistency and repeatability of our experiments, and serve to demonstrate the reliability of our image processing method. In all cases, ultrasound enhanced the length of the perimeter of the fractal pattern, but did not noticeably affect the area growth. A plot of fractal dimension versus time (**Figure 3-12-a**) clearly shows that ultrasound stabilizes the front, and that it reduces the level of instability at the interface. A higher fractal dimension implies that there are bigger secondary branches with a larger number of fine irregularities along the interface. Visually, this reflects as a reduction in branching, and more primary fingers. For injection rates below $1.5 \text{ cm}^3/\text{min}$, we observed that ultrasonic patterns are characterized with a considerably higher fractal dimension, and that the

difference of fractal dimensions between ultrasound and no ultrasound declines with increasing injection rate. Interestingly, at an injection rate of $2.0 \text{ cm}^3/\text{min}$, the fractal dimension due to ultrasound is less than that without. This can be attributed to the viscous forces dominated frontal propagation. Apparently the effect of ultrasound is insignificant.

Ultrasound did not seem to influence the texture of the patterns, as can be seen from the lacunarity plots shown in **Figure 3-12-b**. Interestingly, lacunarity decreases with increasing injection rate.

After reducing the oil viscosity by using lighter mineral oil, the pattern growth characteristics were exactly opposite to what was observed with heavy mineral oil. **Figure 3-13** shows the resulting patterns after injecting water into light mineral oil at $0.3 \text{ cm}^3/\text{min}$. Unlike with heavy mineral oil, ultrasonic stimulation resulted in patterns with thicker, more pronounced primary branches, and a significant reduction in secondary branching. No ultrasound exhibited thinner primary branches with more secondary branches. This is reflected in a reduction of perimeter length, an increase the area, and a significant drop in fractal dimension (**Figure 3-17** and **Figure 3-18**). The same reduction in fractal dimension was noticed at an injection rate of $1.0 \text{ cm}^3/\text{min}$. At higher rates ($1.5 \text{ cm}^3/\text{min}$ and $2.0 \text{ cm}^3/\text{min}$) the difference in fractal dimension between ultrasound and no ultrasound decreases considerably. Again, lacunarity showed now change with ultrasound.

3.6.1.2 Constant rate: 3% DOWFAX 2A1

From the above stated observations, we can conclude that the change in fractal dimension under ultrasound depends on capillary number. If the capillary number is low, fractal dimension is reduced under ultrasound. On the other hand, if capillary number is high, the

fractal dimension increases under ultrasonic vibrations. To test this conclusion, we decided to reduce the interfacial tension to increase the capillary number further. This was accomplished by adding 3 wt% of anionic surfactant (DOWFAX 2A1) to the water. The resulting interfacial tension between the surfactant solution and light mineral oil is 11.2 ± 0.2 dynes/cm, while for heavy mineral oil it is 10.8 ± 0.2 .

Figure 3-19 and **Figure 3-20** display the resulting fingering patterns after injecting 3% DOWFAX 2A1 solution into heavy mineral oil at 0.6 and 1.5 cm³/min. No discernable difference in fingering or tip curvature was observed. In fact, in both cases, the fractal perimeter, area growth and fractal dimension of the patterns were identical (**Figure 3-21** and **Figure 3-22**).

Reducing the viscosity of the oil by employing light mineral oil at an injection rate of 0.6 cm³/min (**Figure 3-23**) appreciably reduced the perimeter of the pattern while maintaining the same area (**Figure 3-25**). The fractal dimension under ultrasound decreased, as well (**Figure 3-26-a**). At higher injection rates, we observed similar perimeter and area growth. The fractal dimension was also unaffected at a higher rate of 1.5 cm³/min (higher capillary number). These results are consistent with observations made during constant water injection.

Based on these findings, we decided to extend our analysis by plotting fractal dimension versus the modified capillary number. The results for both light and heavy mineral oil are shown in **Figure 3-27**. This plot shows the relationship between fractal dimension after 10, 50, 100 and 200 seconds. The values of such fractal dimensions have been extrapolated from best fits using a logarithmic model. In fact, experimentally, all fractal dimension versus time curves fitted very well to a logarithmic function. As can be

seen from **Figure 3-27-a**, the fractal dimension continuously increases as the pattern evolves, and more branching occurs, until it stabilizes at a characteristic fractal dimension. For heavy mineral oil, the characteristic fractal dimension is approximately 1.55, while for mineral oil, it is 1.42. Although light mineral oil shows slightly lower fractal dimension at $N_{Ca}' = 400$, the curves are relatively well connected, and show an overall logarithmic trend. At low capillary numbers ($N_{Ca}' < 250$) we observed a steep decline of fractal dimension, ranging between 1.05 to 1.45. At higher capillary numbers ($N_{Ca}' > 300$), the fractal dimension stabilizes at a constant value that depends on the oleic phase viscosity. To illustrate the contribution due to ultrasound, we also plot the difference in fractal dimension obtained with and without ultrasound. The plot is shown in **Figure 3-27-b**. Note that for heavy mineral oil, ultrasound increases the fractal dimension at low capillary number (up to 7%), but declines at high capillary numbers (up to 3%). The opposite occurs with light mineral oil.

Plotting fractal dimension versus Reynolds number also proves to be a valuable tool to assess the effect of ultrasound onto the system. **Figure 3-28-a** shows the change in fractal dimension as a function of modified Reynolds number at various times during pattern growth. The solid symbols indicate the response without ultrasound, while the empty symbols represent the ultrasonically stimulated response (this is the general convention adopted herein). One key feature of these curves is that for both light and heavy mineral oil, fractal dimension increases with Reynolds number. Additionally, the rate of increase in fractal dimension is higher at low Reynolds numbers, especially in the case of heavy mineral oil. The relative performance of ultrasound as compared to no ultrasound is illustrated in **Figure 3-28-b**. From this graph, we can clearly see that heavy

mineral oil exhibits an entirely different response than light mineral oil. For heavy mineral oil, the difference in fractal dimension generally decreases with Reynolds number, and ultrasound increases the fractal dimension (up to 7%). For light mineral oil, the difference in fractal dimension decreases with increasing fractal dimension, but the fractal dimension is lowered under ultrasound. It can be concluded, therefore, that ultrasound acts to stabilize the front when oil viscosity is low, and perturbs the front when oil viscosity is high. The sharp contrast between the fluids indicates that both Capillary and Reynolds numbers are insufficient descriptors of the process, and that there is another property that differentiates the response of both oils. On such property may be the acoustic characteristics of the fluids, especially pertaining to their resonance behavior. As mentioned earlier, we believe that the relationship between ultrasonic wavelength and the instability length λ_c (Equation 3.4) are key to answering this question. When the wavelength of the ultrasound is in phase with λ_c , we expect a perturbation to grow. However, when the wavelength is out of phase with λ_c , we expect stabilization. This speculation must be confirmed by experiment, however, and would require equipment that can deliver multiple frequencies.

3.6.1.3 Constant pressure: Water

Up till now, we only discussed the effect of ultrasound at constant injection of water and surfactant. This scenario is intrinsically forced and dominated by viscous forces. It is therefore necessary to also perform a series of Hele-Shaw experiments at constant pressure injection. This process is more natural, and dictated by the system, i.e. injectivity depends on the mobility of the oil within the Hele-Shaw cell. Given the same injection

pressure, injectivity is lower for high viscosity oil than for low viscosity oil, and thus, one would expect that the pattern shows reduced branching.

In this section, we will present the results of a series of constant pressure Hele-Shaw experiments with water as the injection phase, and several processed mineral oils as the viscous phase. Five oils were selected to cover a broad range of viscosity values, and are state of the art calibration oils from Canon Instruments Company. These oils are designed to yield accurate, consistent viscosity readings, and are used to calibrate high precision viscometers. The physicochemical properties of all fluids are given in Table 4-1 and Table 4-2.

Figure 3-29 shows the resulting patterns after injecting water at a constant pressure of 0.455 psi in a Hele-Shaw cell saturated with heavy mineral oil ($\mu_o = 167.0 \pm 1.7$, IFT = 51.0 ± 1.0 dynes/cm). Two settings of ultrasound were applied to the system to explore the effect of intensity on the process. Although it is very difficult to discern any differences visually, **Figure 3-30** and **Figure 3-31** show that ultrasound increases the fractal perimeter, area, and fractal dimension of the pattern. A significant increase in lacunarity was observed at early times only.

Figure 3-32 provides contour composite plots after using S60 ($\mu_o = 141.4 \pm 0.2$, IFT = 22.6 ± 0.5 dynes/cm) as the viscous fluid. S60 has similar viscosity as heavy mineral oil, but half the interfacial tension. We noted that the reduction in interfacial tension (and therefore, Capillary number) did not considerably affect the fractal perimeter and area when ultrasound is introduced (**Figure 3-33**). The fractal dimension on the other hand increased dramatically at high ultrasonic intensity (**Figure 3-34**). Lacunarity did not change greatly during insonication.

Figure 3-35 shows the fractal patterns obtained when using S200 ($\mu_o = 577.9 \pm 0.9$, IFT = 30.7 ± 0.6 dynes/cm). The fractal perimeter and area decrease remarkably with intermediate intensity ultrasound, while it did not show much response at high intensity (**Figure 3-36**). This may not necessarily be due to ultrasound, but possibly an artifact of the box counting method. What we know for sure is that ultrasound reduces the perimeter and area in both cases. The fractal dimension and lacunarity did not witness a noteworthy change with ultrasound (**Figure 3-37**). As can be seen in **Figure 3-38**, **Figure 3-39**, and **Figure 3-40**, a similar response may be noted with N350 ($\mu_o = 1112.0 \pm 1.8$ cp, IFT = 35.3 ± 0.8 dynes/cm).

Finally, we investigated the effect of ultrasound on very high viscosity oil, S600 ($\mu_o = 1973 \pm 3.2$ cp, IFT = 38.7 ± 0.8 dynes/cm), and found that regardless of pressure, the fractal perimeter, area and fractal dimension did not react significantly to vibrations (see **Figure 3-41** to **Figure 3-46**).

Figure 3-47 summarizes the previous results by plotting the change in fractal dimension versus viscosity ratio at various stages of pattern development. The switch between heavy mineral oil HMO and S60 may be due to the reduction in interfacial tension. In all cases, fractal dimension decreases with increasing viscosity ratio, and increases with time. Additionally, the difference between the fractal dimension from ultrasonically stimulated patterns and those without ultrasound decreases with increasing viscosity ratio. Therefore, ultrasound only effectively perturbs the interface when the viscosity ratio between aqueous phase and the oil is low. **Figure 3-47-b** shows a histogram of steady state fractal dimension with increasing viscosity ratio. Each set of three bars indicates the fractal dimension at progressively smaller time steps: i.e. dark

blue indicates the fractal dimension at 200 seconds, while light blue at 50 seconds. Arrows illustrate the trend as the ultrasonic intensity is raised from 0 to 169 W. The slope of the arrows gradually decreases with increasing viscosity ratio, except for the last case, where we increased the injection pressure from 0.455 psi to 0.9947 psi.

3.6.1.4 Constant pressure: 3% DOWFAX 2A1

Because of the observed difference in fractal behavior between HMO and S60 at constant pressure, we decided to run a series of Hele-Shaw experiments at reduced interfacial tension by adding 3 wt% DOWFAX 2A1 to the water. **Figure 3-48** to **Figure 3-50** show the resulting fractal patterns after 3 wt% DOWFAX 2A1 solution is injected to displace heavy mineral oil at three injection pressures: 0.1421 psi, 0.2373 psi, and 0.357 psi. In all cases, both the fractal perimeter and the area did not change considerably with ultrasound (**Figure 3-51**). With the exception of the 0.2373 psi case, fractal dimension and lacunarity remained unaffected as well (**Figure 3-52**). Again, the high viscosity of the heavy mineral oil reduced the efficacy of ultrasound. Experiments with light mineral oil yielded more promising results. **Figure 3-53** and **Figure 3-54** show the injection profiles of 3 wt% DOWFAX 2A1 into light mineral oil at two injection pressures: 0.1421 and 0.235 psi, respectively. Although ultrasound did not affect the perimeter and area of the pattern obtained at 0.235 psi, we did notice a measurable response with 0.1421 psi (**Figure 3-55**). Such effect is clearly reflected in the profile of the fractal dimension (**Figure 3-56**). Increasing the intensity of ultrasound reduced the fractal dimension of the pattern dramatically. Lacunarity was unaffected.

3.6.2 Miscible Hele-Shaw experiments

3.6.2.1 Constant Pressure

To investigate the fingering behavior of miscible floods in Hele-Shaw cells under ultrasound, we injected kerosene (non-volatile) and heptane (volatile) at a constant pressure into light and heavy mineral oil. During a miscible flood, the interfacial tension is zero, and the process is entirely viscosity dominated. Therefore, these experiments provide valuable insight into viscous displacement processes while entirely eliminating complexities associated with the interfacial forces such as interfacial tension and wettability.

Figure 3-57 shows various injection profiles into Hele-Shaw cells, in which kerosene is injected into heavy and light mineral oil at a constant head of 9.5 cm. The viscosity ratio of kerosene to light and heavy mineral oil is 16 and 57.6, respectively. Patterns are shown for two intensities of ultrasound, and are labeled as 72 W (setting 2) and 168 W (setting 5). One can clearly see that in the absence of interfacial forces, the displacement front is perfectly circular. In the case when kerosene displaces heavy mineral oil (**Figure 3-57-a**), the ultrasound dramatically increased both the length of the fingers, as well as the spacing. Without ultrasound, the injection profile is compact, with a large circular mixing zone at the center. As the ultrasonic intensity is increased, the central mixing zone becomes gradually smaller, and the fingers become longer, and more branched. At high intensity, both primary and secondary branches are long, and the central mixing zone is relatively small. The mixing zone at the finger tips is not noticeably affected by ultrasound. The patterns observed with light mineral oil exhibited an entirely different behavior (**Figure 3-57-b**). Ultrasound reduced the number of

secondary branches at the tip, and yielded an extremely diffuse mixing zone at the center of the pattern, as well as at the primary fingers. The pattern at intermediate intensities showed short primary fingers, and thick secondary fingers which branch out radially. After raising the hydrostatic head to 20 cm, we did not notice a dramatic change in finger properties when kerosene is injected into heavy mineral oil, but observed a more subtle change in finger thickness with light mineral oil. It is apparent that ultrasound is more effective at low injection pressures, and low viscosity ratios. The diffusivity constants of both fluids may also play a key role in our observations. Unfortunately, we did not have the necessary equipment to measure the rate of diffusion of kerosene into light and heavy mineral oil.

Injecting heptane into light mineral oil resulted in an extraordinary change in branching behavior. **Figure 3-59** shows the injection profiles of heptane after injection into light mineral oil at a constant hydrostatic head of 3 cm. It can be seen that the primary branches visibly longer after ultrasound, and that the pattern is less compact than without ultrasound. The diffusive mixing zone, however, seems to be suppressed at the finger tips and at the center of the pattern. Raising the hydrostatic head to 5 cm resulted in similar behavior as observed with kerosene. For both light and heavy mineral oil (**Figure 3-60**), the length and width of the primary and secondary branches increased with higher intensity. We observed a substantial improvement in diffusivity at the mixing zone under ultrasound, especially the regions around the finger tips. A similar observation was also made when the hydrostatic head is raised to 9.5 cm (**Figure 3-61**).

3.6.2.2 Constant Rate

Kerosene was injected into light mineral oil to explore the pattern development of miscible, non-volatile fluids under forced injection. The displacement fronts at two constant injection rates; 1cc/min (**Figure 3-62-a**) and 5 cc/min (**Figure 3-62-b**) were investigated to see whether the rate influences the relative contribution of ultrasound onto the system. At low kerosene rates and no ultrasound, we observed a steady distribution of short, radially expanding branches and a very small mixing zone. On the other hand, an ultrasonically stimulated pattern showed long branches with a diffuse mixing zone. The pattern was less compact, and diffusive mixing was enhanced along the branches. At high kerosene rates, ultrasound did not increase the mixing zone at all, and was entirely dominated by dispersive viscous splitting.

Injection of pentane at 5cc/min illustrated that for volatile fluids, and a much higher viscosity ratio, ultrasound dramatically altered the branching morphology of the Hele-Shaw patterns. Not only were the fingers longer, they also displayed more secondary branches. Due to the high rate, however, it was not possible to discern whether ultrasound enhances the mixing zone for volatile liquids, or whether dispersive viscous forces were dominant. We suggest further research in this topic, since the results from such study may provide a valuable technique to enhance miscible floods and solvent based EOR processes.

3.7 Conclusions

1. A series of immiscible and miscible Hele-Shaw experiments were run to investigate the formation of ultrasonically induced instabilities at the liquid-liquid interface. Fractal analysis methods were employed, and proved to be helpful in assessing the contribution of ultrasonic stimulation.
2. Experiments were conducted to test a broad range of viscosity ratios and interfacial tension. High precision calibration oil was used to control the viscosity ratio. An anionic surfactant was employed to lower the interfacial tension between the injected fluid and the viscous fluid within the Hele-Shaw cell.
3. We found that in the case of constant rate water injection into heavy oil, the fractal dimension increased with ultrasound, but remained unchanged at high injection rates. The opposite was true for light mineral oil.
4. Reducing the interfacial tension of the water seemed to suppress the contribution of ultrasound with heavy mineral oil. On the other hand, light mineral oil responded to a reduction in interfacial tension in a similar manner as with high interfacial tension.
5. Plots of fractal dimension versus modified Capillary and Reynolds numbers lead to the conclusion that ultrasound only perturbs the interfaces of low viscosity oil, and that it is strongly dependent on interfacial tension. Ultrasound is ineffective at higher viscosities, as well as higher injection rates.
6. We then proceeded in studying the effect of ultrasound on constant pressure displacement. We found that for a broad range of viscosities, ultrasound increases the fractal dimension of the interface. As the viscosity is raised above 1000 cp,

however, no discernable change in fractal dimension was observed under ultrasound.

7. A plot of fractal dimension versus viscosity ratio showed that the fractal dimension of the pattern increases with time, and decreases with viscosity ratio. The difference between patterns with and without ultrasound is greater at low viscosity ratios, and converges at high viscosity ratios.
8. The rate of increase in fractal dimension as we raise the ultrasonic intensity decreases with increasing viscosity ratio, and increases with increasing pressure.
9. A reduction in interfacial tension did not affect the response of heavy oil to ultrasound. On the other hand, the fractal dimension under ultrasound decreased considerably with a reduction of interfacial tension when light mineral oil was used.
10. Miscible Hele-Shaw experiments with kerosene, heptane and pentane showed that ultrasound improves miscibility of solvents into mineral oil. This is especially true for low injection rates and low pressures, when diffusive mechanisms dominate. At higher injection rates and pressures, the process is dominated by dispersive viscous displacement, and the mixing zone is not noticeably altered with ultrasound.
11. Ultrasound may be a useful tool to enhance miscible floods and solvent based EOR techniques. More research is necessary in this topic.

Table 3-1: Fractal dimensions for various known analytical fractals. The Minkowski-Bouligand fractal dimension (also known as Hausdorff dimension) was calculated using FracLac V.2 (Karperien 2005). The contents of this table are plotted on a cross-comparison plot in Figure 3-4.

Fractal	D_B Analytical	D_B FracLac ⁽¹⁾
Koch Curve (snowflake, 960x960)	1.2618595	1.2684
Koch Curve (snowflake, 800x800)	1.2618595	1.2602
Koch Curve (1D, 600x176)	1.2618595	1.2767
Koch Antisnowflake 6 (692x800)	1.2618595	1.2634
KochSnowflake 6 (692x800)	1.2618595	1.2629
Koch Island (650x650)	1.5	1.4781
Koch Island segment (944x648)	1.5	1.4781
Horizontal Line (300x300)	1	1
Vertical Line (300x300)	1	1
Diagonal Line (300x300)	1	0.9946
Black box (300x300)	2	1.9247
White box, black border (300x300)	1	1.0164
Sierpinski Gasket (727x717)	1.5849625	1.5686
Sierpinski Gasket (1255x1086)	1.5849625	1.5868
Sierpinski Gasket Variation1 (1255x1086)	1.5849625	1.5436
Sierpinski Carpet (black)	1.8927893	1.8629
Sierpinski Carpet (white)	1.8927893	1.8635
Apollonian Gasket (large circle)	1.3058	1.3337
Apollonian Gasket (1 component)	1.3058	1.2989
DLA - Point Attractor	1.712	1.6672
DLA - Line Attractor	1.712	1.5924
Invasion percolation	1.83	1.7438
Brownian Motion	1.5	1.6011
Henon Map	1.26	1.2652
Box Fractal 3 (800x800)	1.4649735	1.4562
Box Fractal 4 (800x800)	1.4649735	1.4361
Box Fractal 5 (800x800)	1.4649735	1.427
Exterior Snowflake 3 (800x692)	1.2618595	1.2294
Flowsnake Fractal 4 (756x800)	1.1291501	1.1173

⁽¹⁾Minkowski-Bouligand dimension

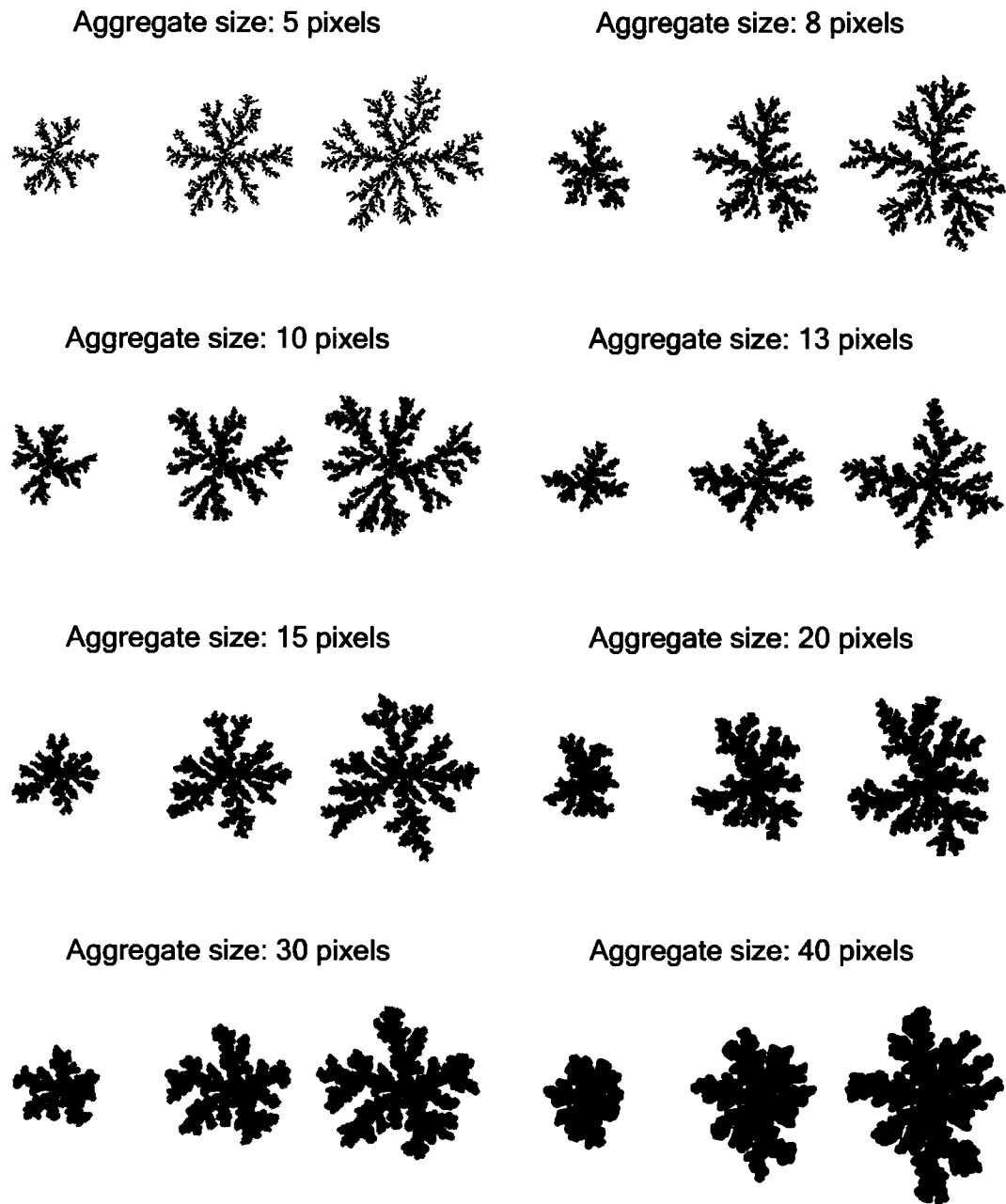


Figure 3-1: DLA patterns generated with different aggregates sizes. Shown here are the DLA patterns after 16700, 33400 and 50,000 aggregates. The patterns were generated with ImageJ's DLA Generator (courtesy of Audrey Karperien (2006)).

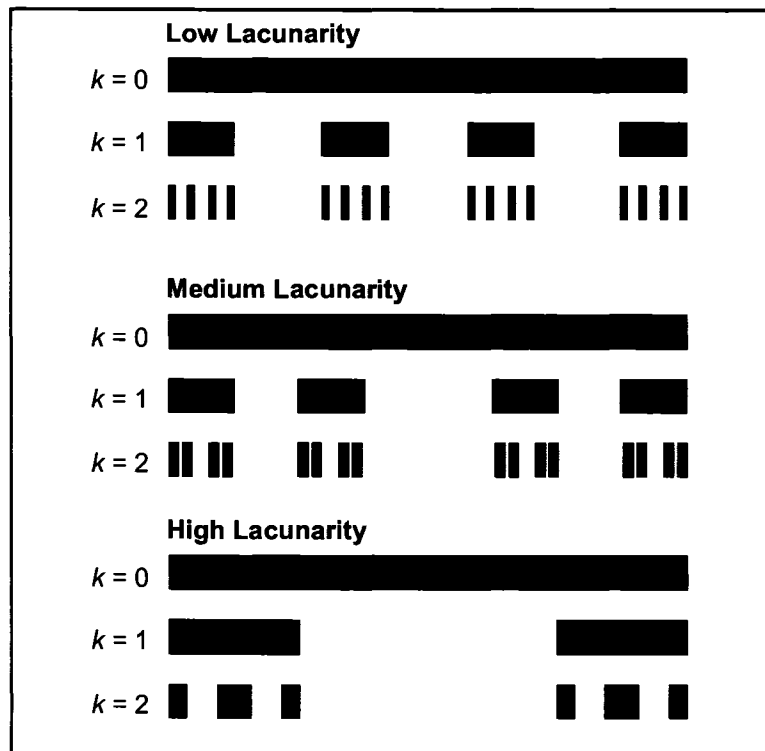
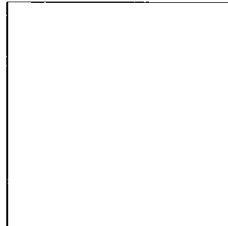


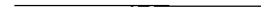
Figure 3-2: One dimensional polyadic Cantor sets with a generator of 4^k intervals and a reduction factor of $1/7^k$. All sets have a fractal dimension in the limiting case is $D_B = \log(4)/\log(7) = 0.7124$. This example illustrates the importance of texture or lacunarity in fractal analysis, and shows that the fractal dimension is only one of several fractal descriptors.



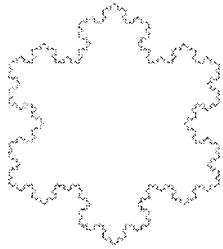
Filled square box
 $D_B = 2$



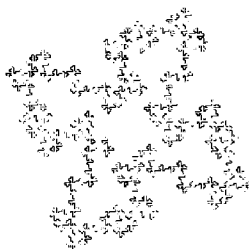
Outlined square box
 $D_B = 1$



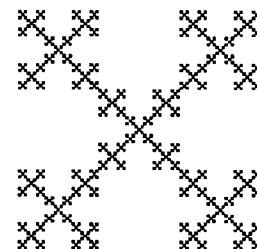
Horizontal line
 $D_B = 1$



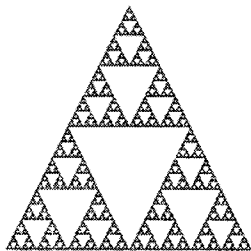
Koch Snowflake
 $D_B = 1.26186$



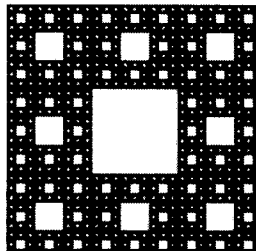
Koch Island
 $D_B = 1.5$



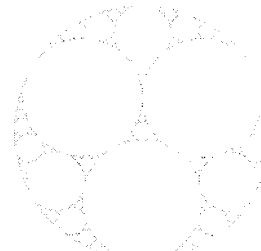
Box Fractal 5
 $D_B = 1.46497$



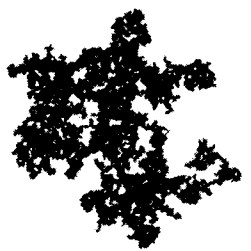
Sierpinski Gasket
 $D_B = 1.58496$



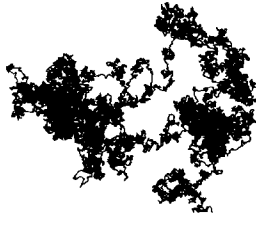
Sierpinski Carpet
 $D_B = 1.89279$



Apollonian Gasket
 $D_B = 1.3058$



Invasion Percolation
 $D_B = 1.83$



Brownian motion
 $D_B = 1.15$



Henon map
 $D_B = 1.26$

Figure 3-3: Various analytical fractals and their Hausdorff dimension used to verify FracLac (Karperien 2005). The results are shown in Table 3-1, and cross-plotted in Figure 3-4. All fractals were generated with Wolfram's Mathematica 5.

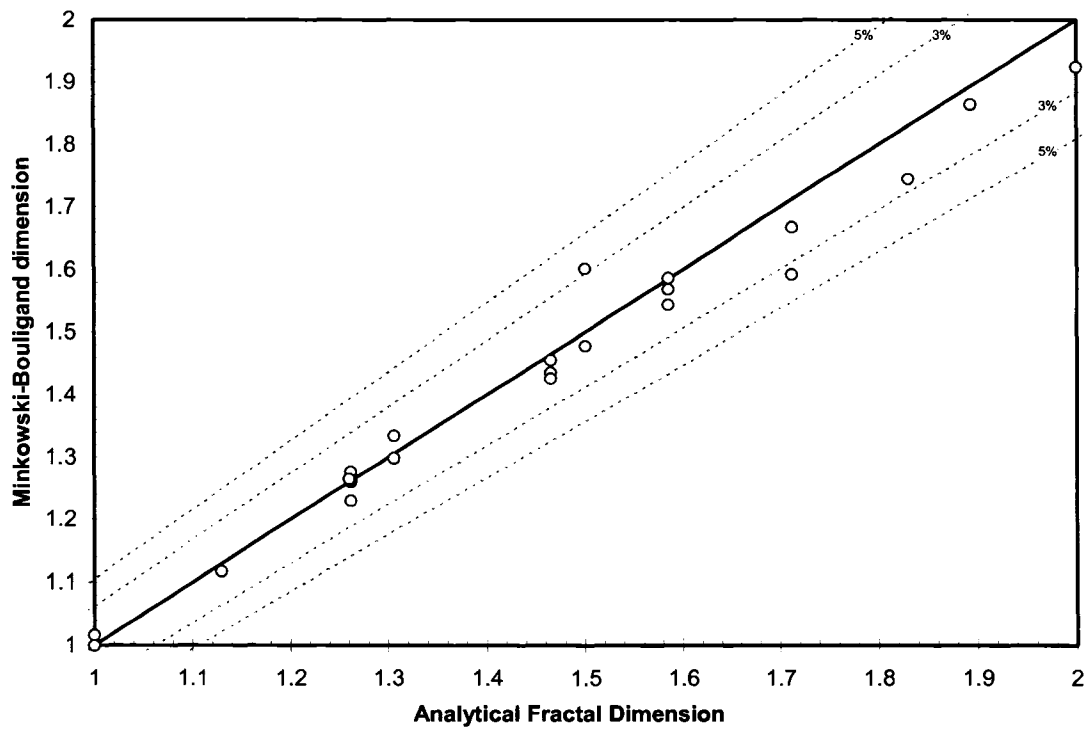


Figure 3-4: Cross-comparison plot of the fractal dimensions obtained from FracLac V.2 (Karperien 2005) versus the analytical fractal dimension. The 45° line corresponds to the case where the computed fractal dimension through box counting equals the analytically determined value. Dashed lines represent the percent deviation from equality.

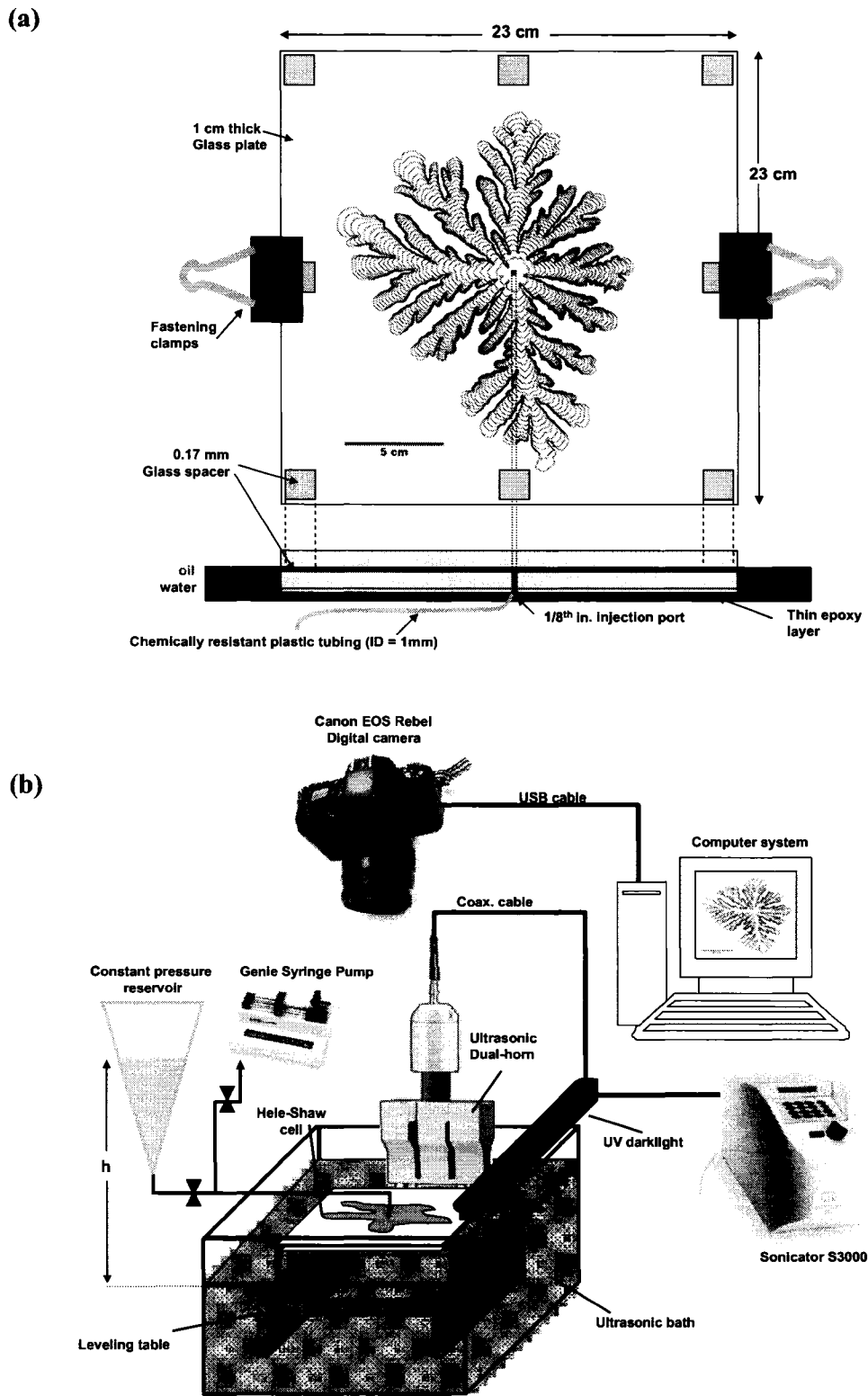
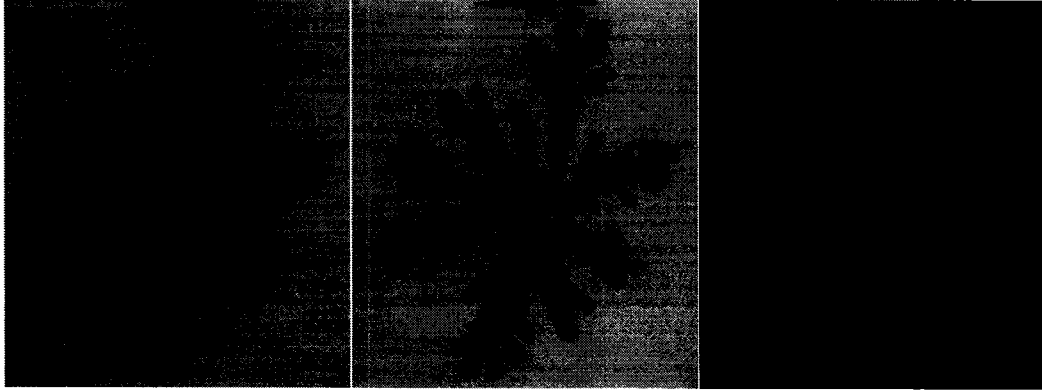
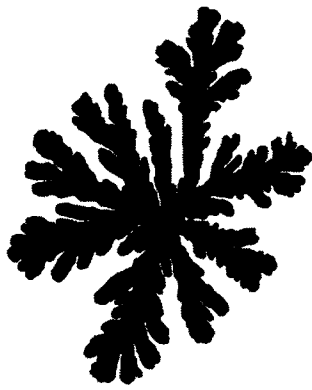


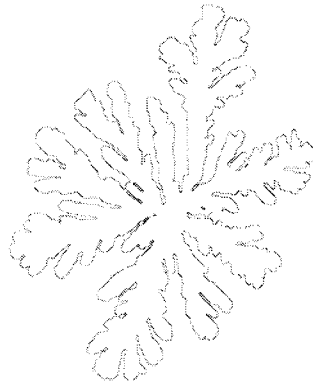
Figure 3-5: (a) Hele-Shaw cell. (b) Experimental setup.



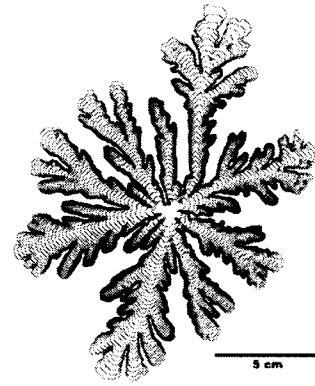
(1) Original cropped image (2) 8-bit converted image (3) Background subtraction



(4) Binary image thresholding



(5) Contouring



(6) Final composite image

Figure 3-6: Work flow of image processing of all Hele-Shaw patterns.

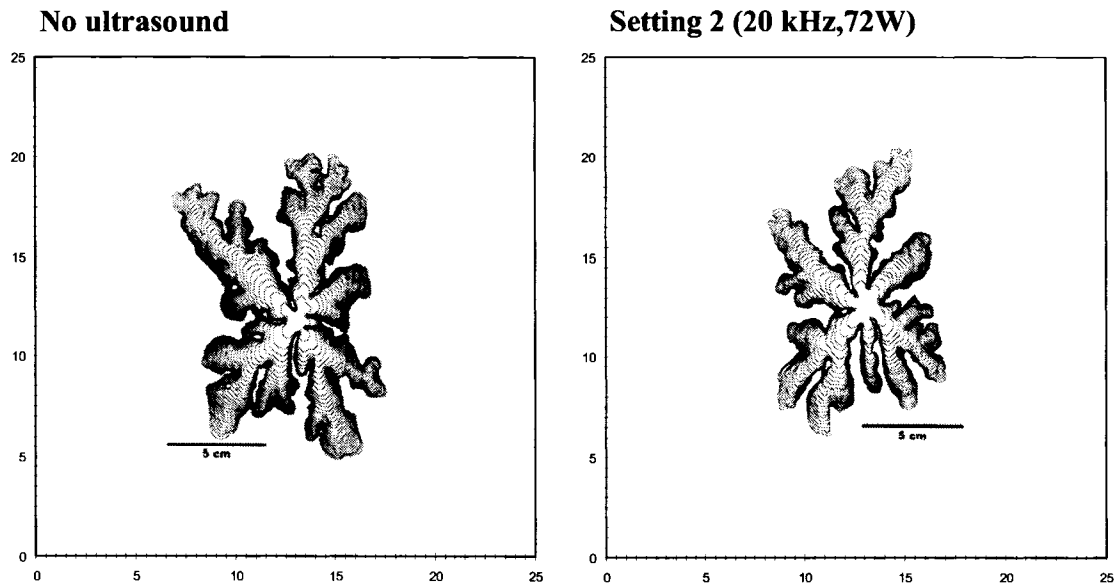


Figure 3-7: Immiscible Hele-Shaw patterns for water injected into heavy mineral oil at a constant rate of 0.3 cc/min. The scale is in centimeters. The contours represent the location of the interface at 10 second intervals. $\mu_o = 167.0 \pm 1.7$ cp; IFT = 51.0 ± 1.0 dynes/cm.

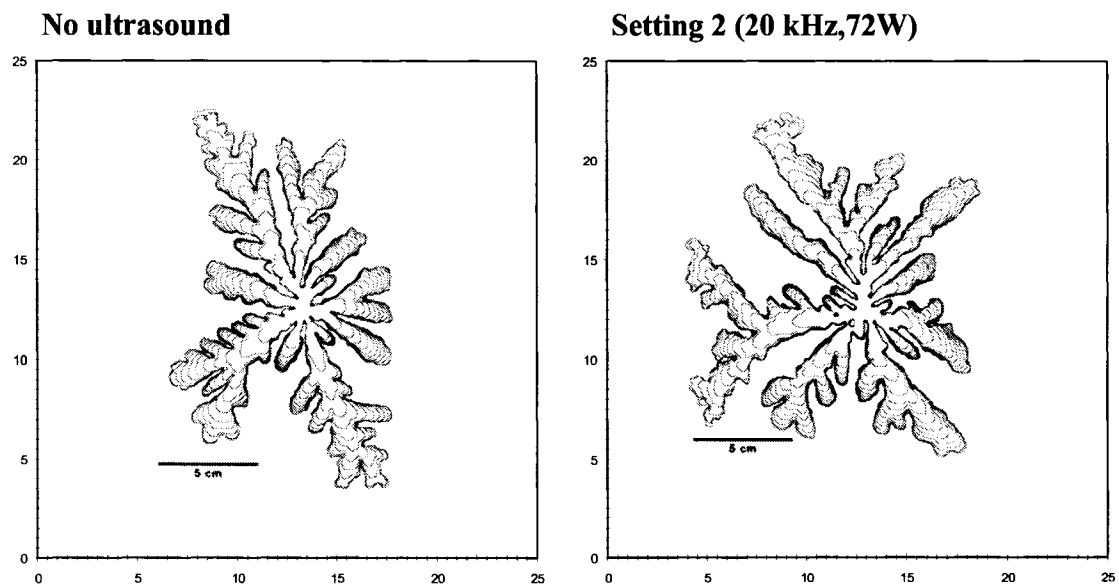


Figure 3-8: Immiscible Hele-Shaw patterns for water injected into heavy mineral oil at a constant rate of 1.0 cc/min. The scale is in centimeters. The contours represent the location of the interface at 10 second intervals. $\mu_o = 167.0 \pm 1.7$ cp; IFT = 51.0 ± 1.0 dynes/cm.

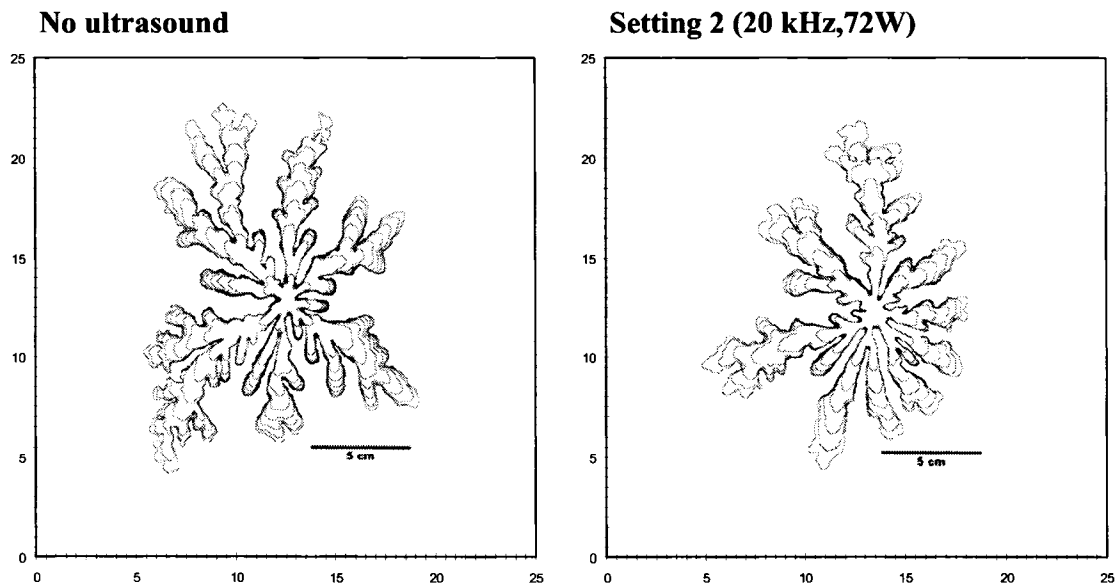


Figure 3-9: Immiscible Hele-Shaw patterns for water injected into heavy mineral oil at a constant rate of 1.5 cc/min. The scale is in centimeters. The contours represent the location of the interface at 10 second intervals. $\mu_o = 167.0 \pm 1.7$ cp; IFT = 51.0 ± 1.0 dynes/cm.

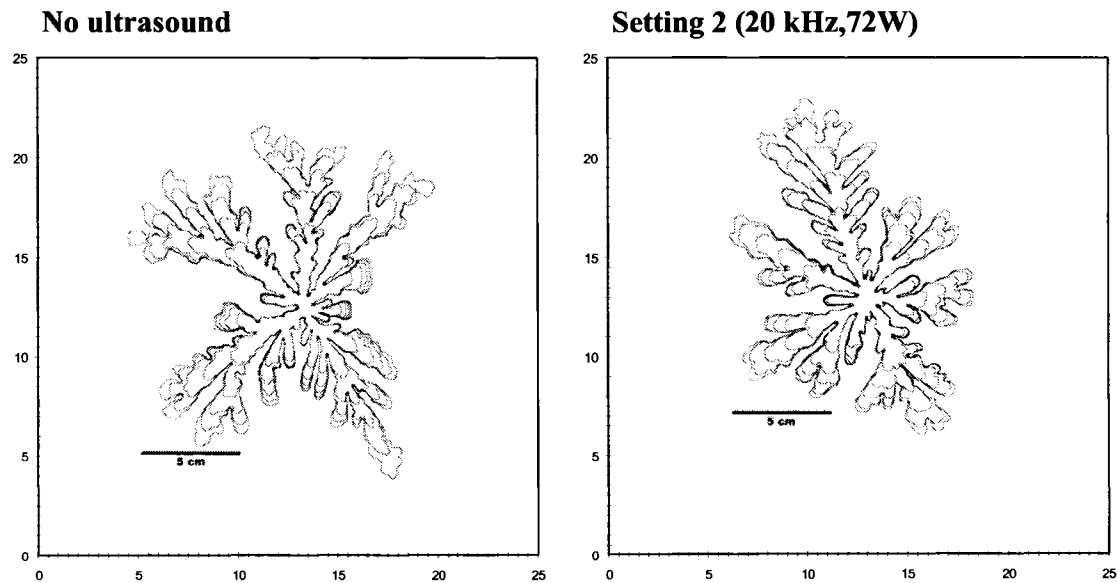


Figure 3-10: Immiscible Hele-Shaw patterns for water injected into heavy mineral oil at a constant rate of 2.0 cc/min. The scale is in centimeters. The contours represent the location of the interface at 10 second intervals. $\mu_o = 167.0 \pm 1.7$ cp; IFT = 51.0 ± 1.0 dynes/cm.

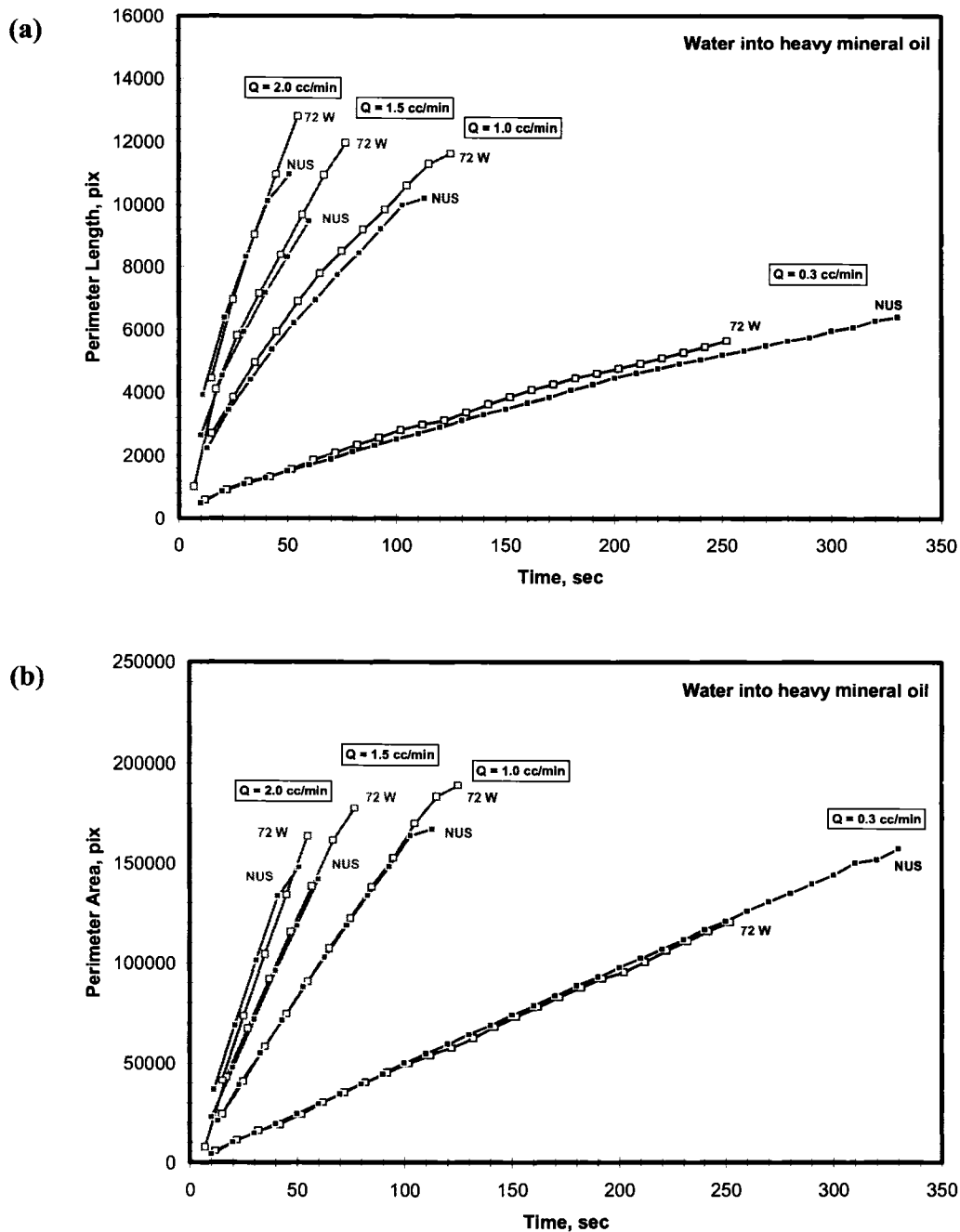


Figure 3-11: (a) Fractal perimeter and (b) fractal area as a function of time for water into heavy mineral oil (HMO) at four constant injection rates: 0.3, 1.0, 1.5, and 2.0 cc/min. The viscosity and interfacial tension of LMO (with surfactant) is 167.0 ± 1.7 cp and 51.0 ± 1.0 dynes/cm, respectively. Patterns for 0.3, 1.0, 1.5, and 2.0 cc/min are shown in Figure 3-7 to Figure 3-10. Solid points represent the case without ultrasound, and empty points with 72W, 20 kHz ultrasound.

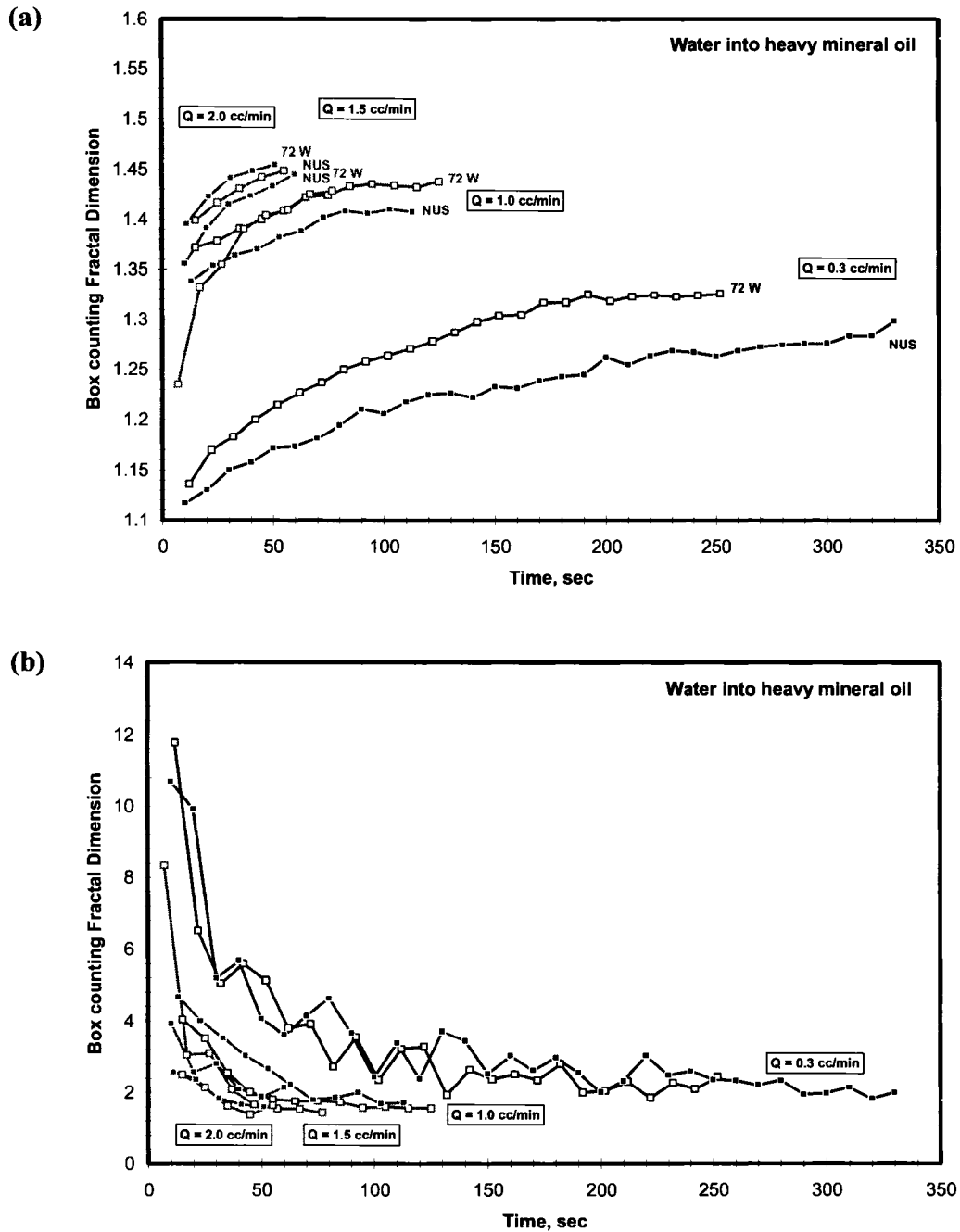


Figure 3-12: (a) Fractal dimension and (b) lacunarity as a function of time for water into heavy mineral oil (HMO) at four constant injection rates: 0.3, 1.0, 1.5, and 2.0 cc/min. The viscosity and interfacial tension of HMO (with surfactant) is 167.0 ± 1.7 cp and 51.0 ± 1.0 dynes/cm, respectively. Patterns for 0.3, 1.0, 1.5, and 2.0 cc/min are shown in Figure 3-7 to Figure 3-10. Solid points represent the case without ultrasound, and empty points with 72W, 20 kHz ultrasound.

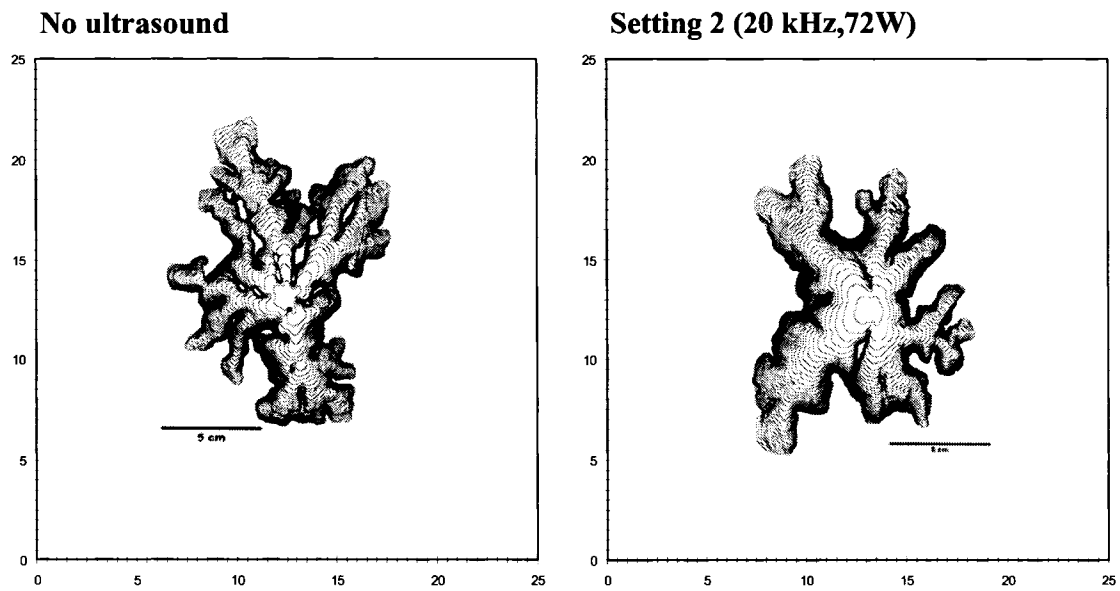


Figure 3-13: Immiscible Hele-Shaw patterns for water injected into light mineral oil at a constant rate of 0.3 cc/min. The scale is in centimeters. The contours represent the location of the interface at 10 second intervals. $\mu_o = 46.5 \pm 0.5$ cp; IFT = 61.8 ± 1.2 dynes/cm.

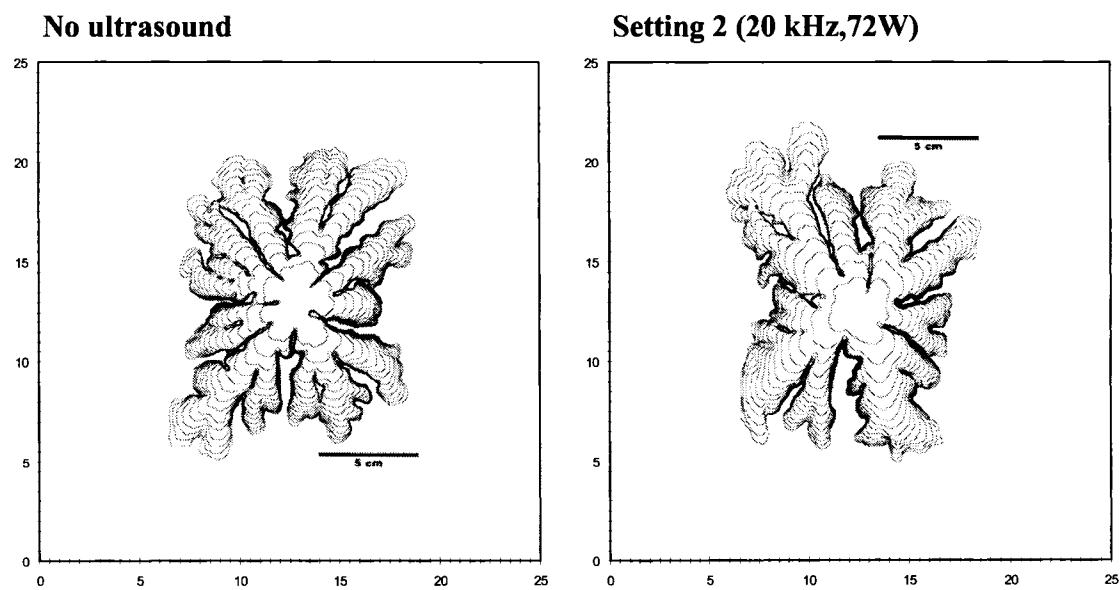


Figure 3-14: Immiscible Hele-Shaw patterns for water injected into light mineral oil at a constant rate of 1.0 cc/min. The scale is in centimeters. The contours represent the location of the interface at 10 second intervals. $\mu_o = 46.5 \pm 0.5$ cp; IFT = 61.8 ± 1.2 dynes/cm.

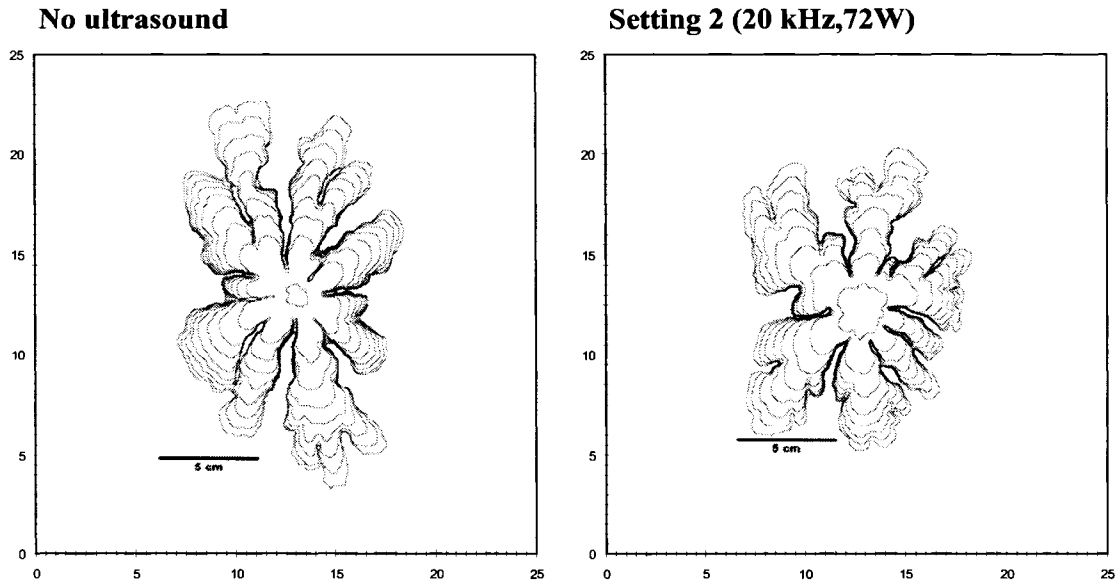


Figure 3-15: Immiscible Hele-Shaw patterns for water injected into light mineral oil at a constant rate of 1.5 cc/min. The scale is in centimeters. The contours represent the location of the interface at 10 second intervals. $\mu_o = 46.5 \pm 0.5$ cp; IFT = 61.8 ± 1.2 dynes/cm.

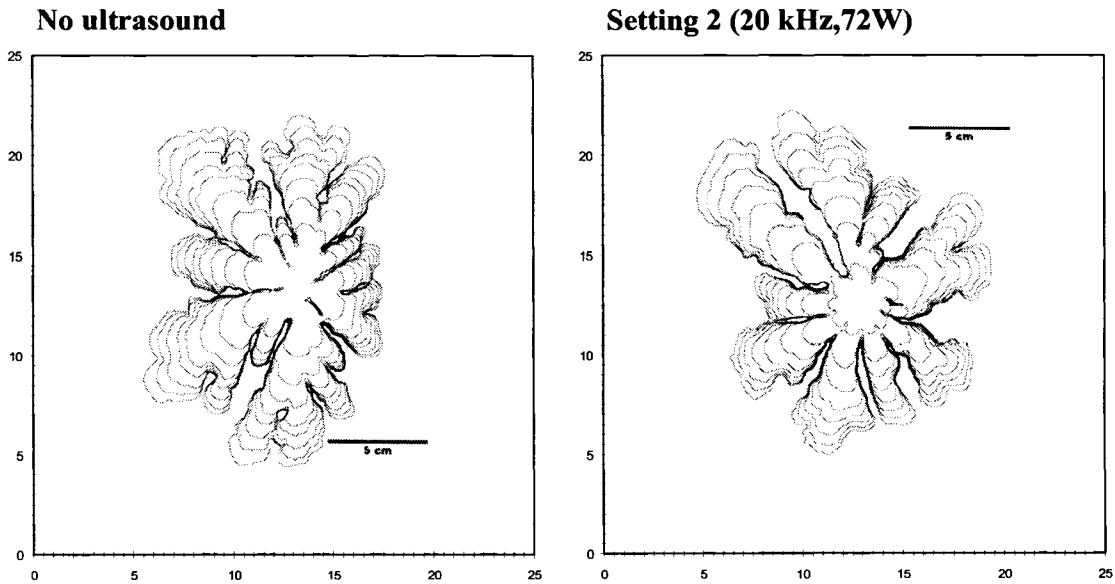


Figure 3-16: Immiscible Hele-Shaw patterns for water injected into light mineral oil at a constant rate of 2.0 cc/min. The scale is in centimeters. The contours represent the location of the interface at 10 second intervals. $\mu_o = 46.5 \pm 0.5$ cp; IFT = 61.8 ± 1.2 dynes/cm.

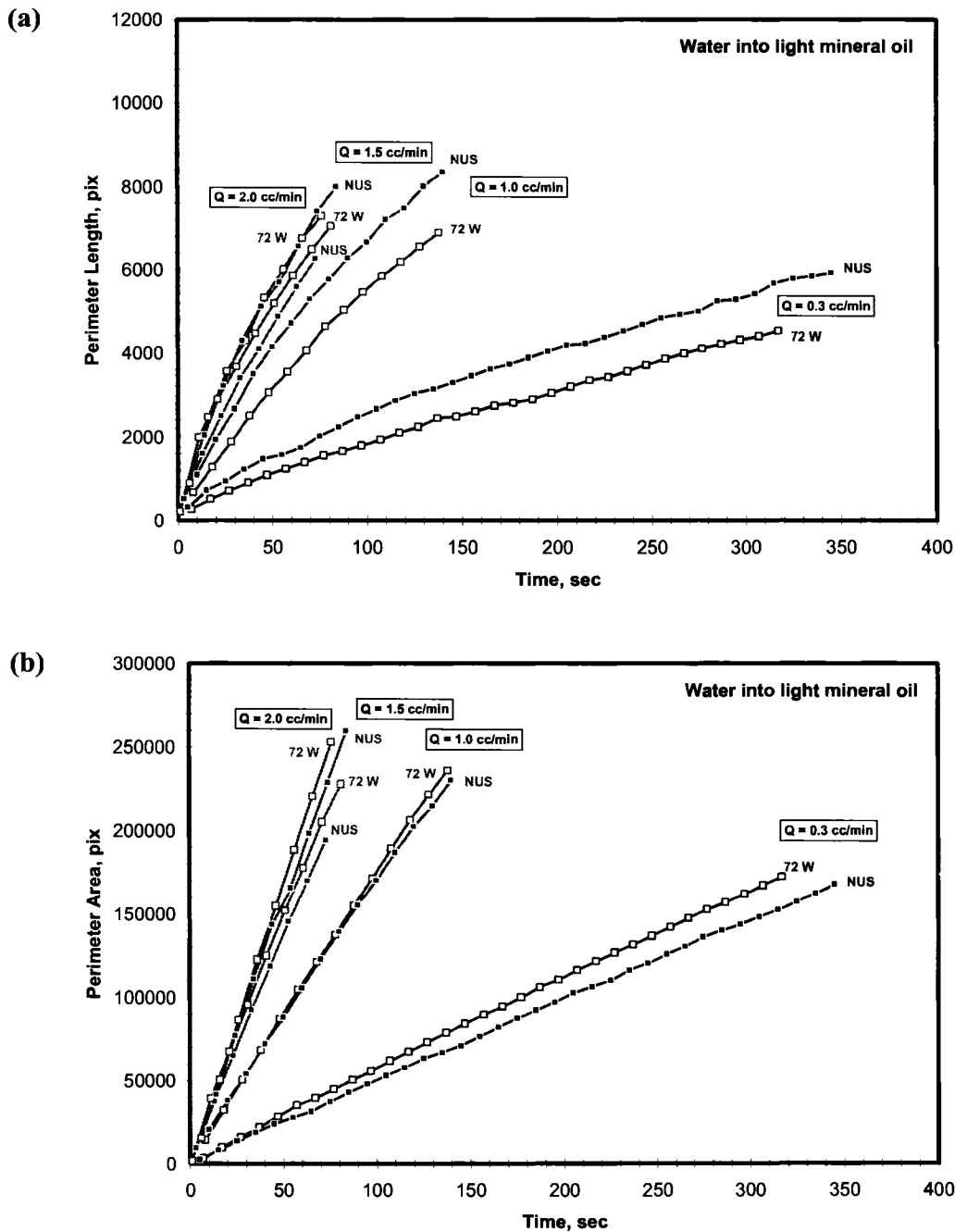


Figure 3-17: (a) Fractal perimeter and (b) fractal area as a function of time for water into light mineral oil (LMO) at four constant injection rates: 0.3, 1.0, 1.5, and 2.0 cc/min. The viscosity and interfacial tension of LMO (with surfactant) is 46.5 ± 0.5 cp and 61.8 ± 1.2 , respectively. Patterns for 0.3, 1.0, 1.5, and 2.0 cc/min are shown in Figure 3-13 to Figure 3-16. Solid points represent the case without ultrasound, and empty points with 72W, 20 kHz ultrasound.

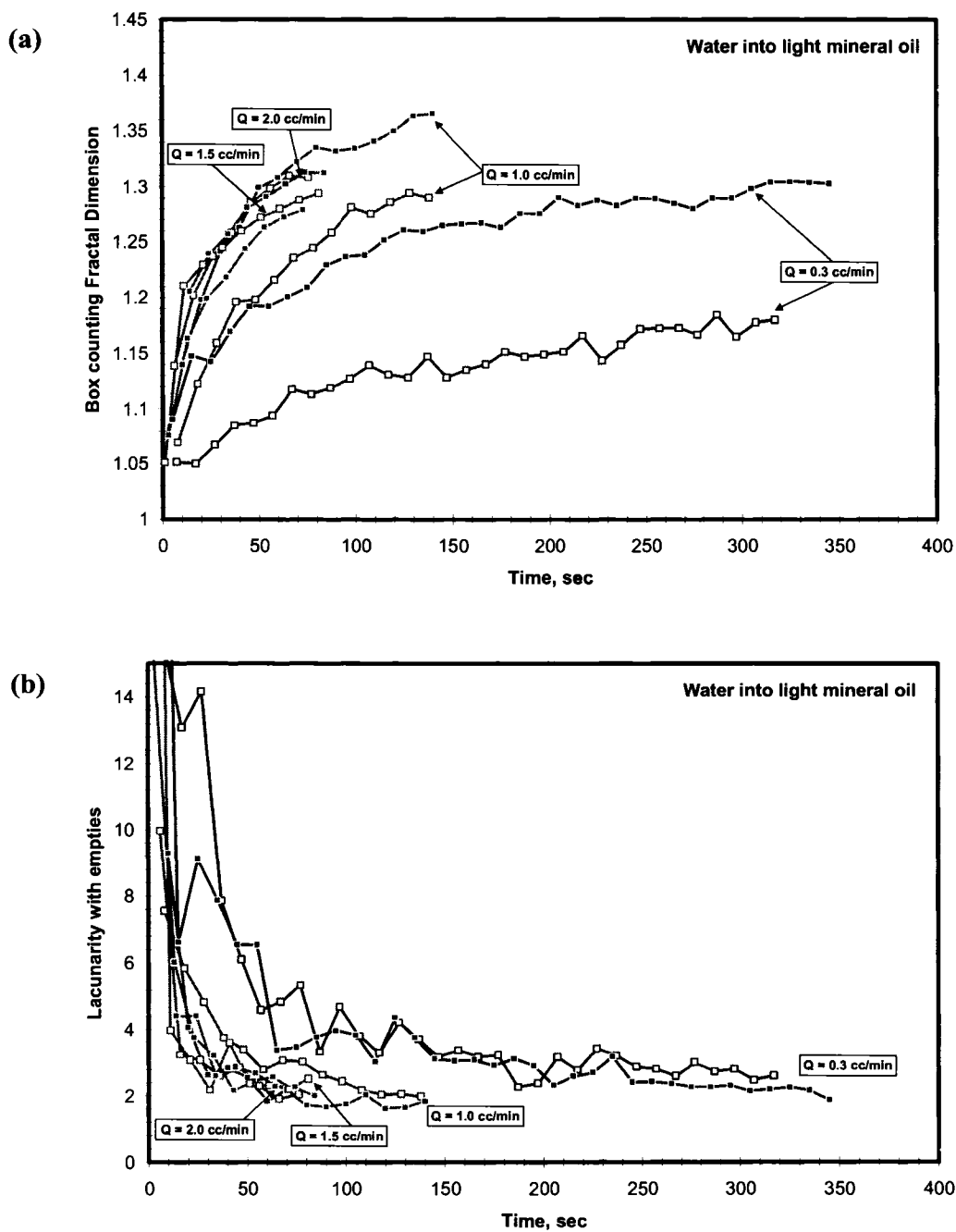


Figure 3-18: (a) Fractal dimension and (b) lacunarity as a function of time for water into light mineral oil (LMO) at four constant injection rates: 0.3, 1.0, 1.5, and 2.0 cc/min. The viscosity and interfacial tension of LMO (with surfactant) is 46.5 ± 0.5 cp and 61.8 ± 1.2 , respectively. Patterns for 0.3, 1.0, 1.5, and 2.0 cc/min are shown in Figure 3-13 to Figure 3-16. Solid points represent the case without ultrasound, and empty points with 72W, 20 kHz ultrasound.

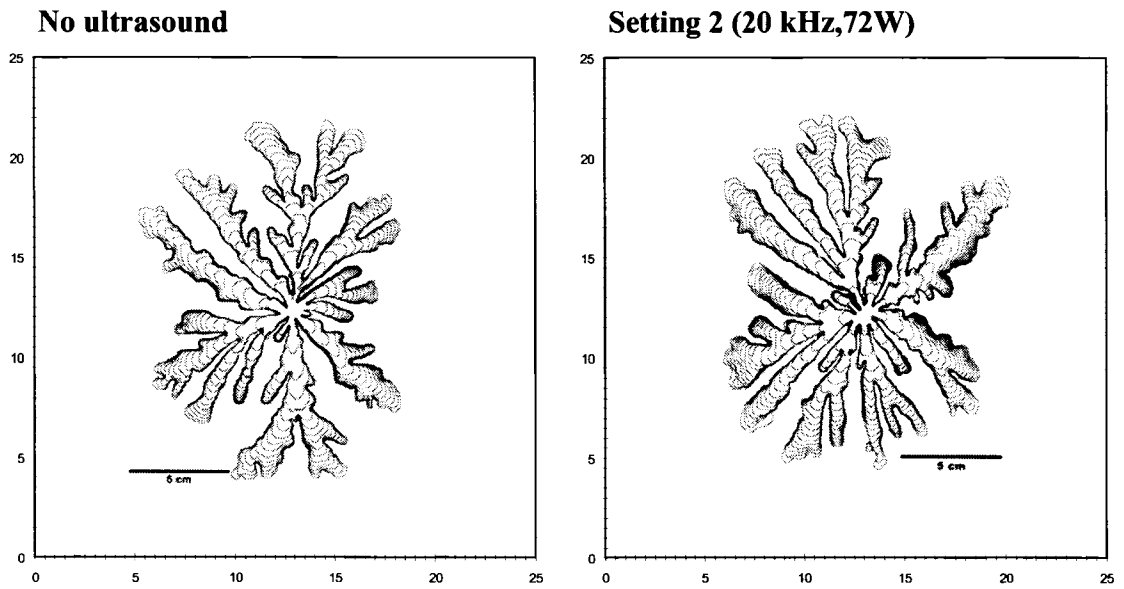


Figure 3-19: Immiscible Hele-Shaw patterns for 3% DOWFAX 2A1 injected into heavy mineral oil at a constant rate of 0.6 cc/min. The scale is in centimeters. The contours represent the location of the interface at 10 second intervals. $\mu_o = 167.0 \pm 1.7$ cp; IFT = 10.8 ± 0.2 dynes/cm.

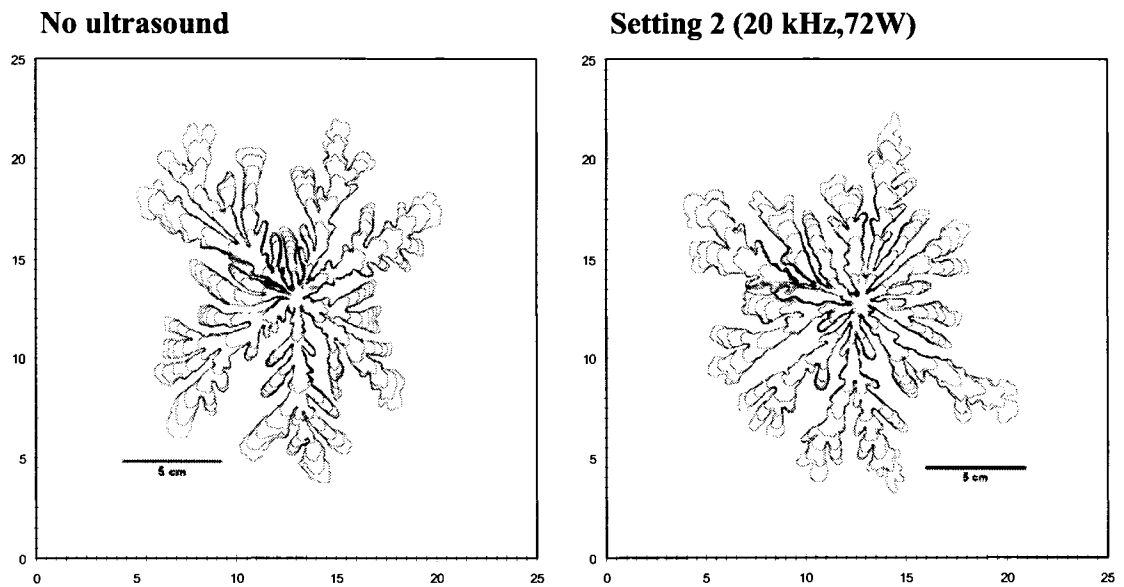


Figure 3-20: Immiscible Hele-Shaw patterns for 3% DOWFAX 2A1 injected into heavy mineral oil at a constant rate of 1.5 cc/min. The scale is in centimeters. The contours represent the location of the interface at 10 second intervals. $\mu_o = 167.0 \pm 1.7$ cp; IFT = 10.8 ± 0.2 dynes/cm.

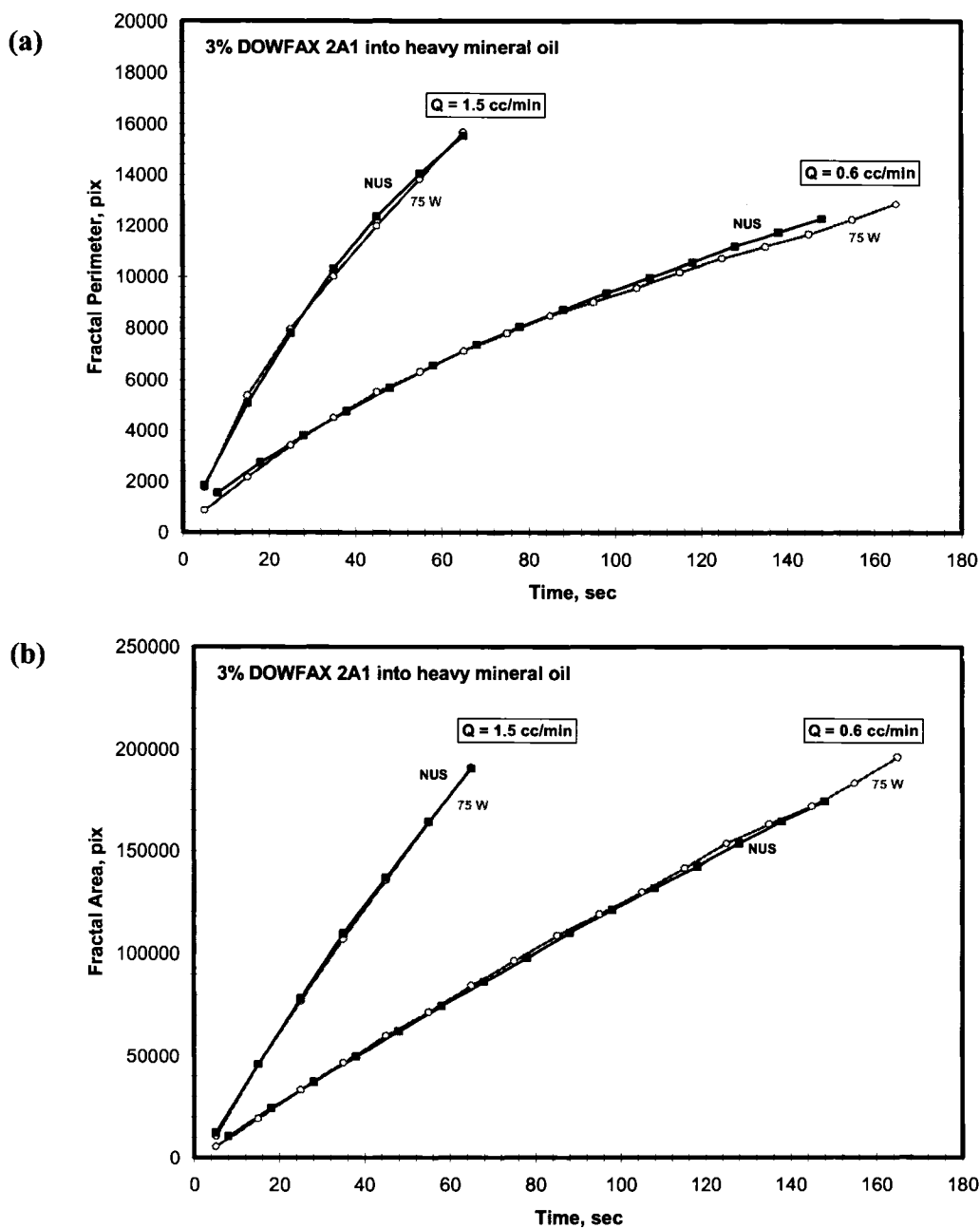


Figure 3-21: (a) Fractal perimeter and (b) fractal area as a function of time for 3% DOWFAX 2A1 into heavy mineral oil (HMO) at two constant injection rates: 0.6 and 1.5 cc/min. The viscosity and interfacial tension of HMO (with surfactant) is 167.0 ± 1.7 cp and 10.8 ± 0.2 dynes/cm, respectively. Patterns are shown in Figure 3-19 and Figure 3-20.

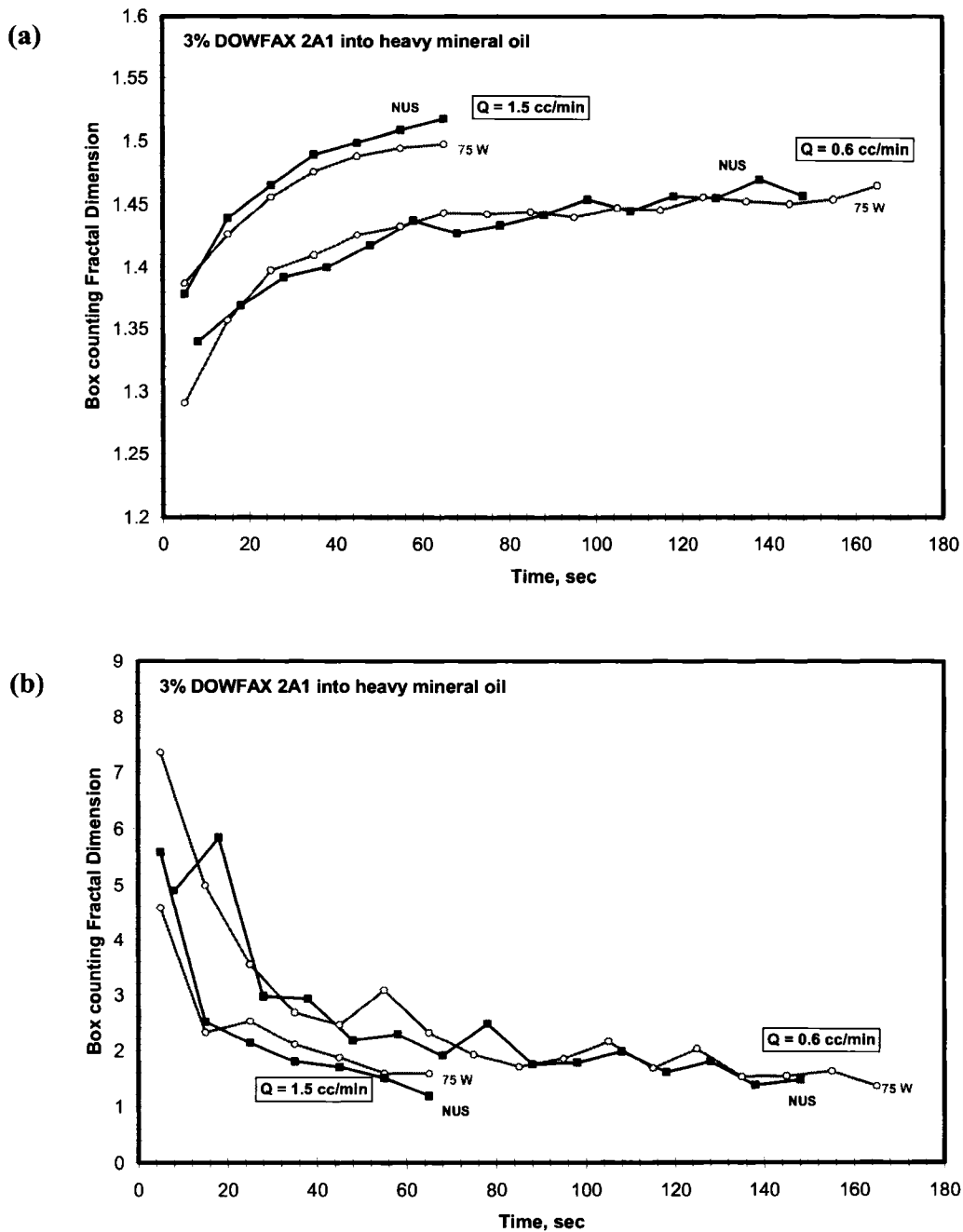


Figure 3-22: (a) Fractal dimension and (b) fractal lacunarity as a function of time for 3% DOWFAX 2A1 into heavy mineral oil (HMO) at two constant injection rates: 0.6 and 1.5 cc/min. The viscosity and interfacial tension of HMO (with surfactant) is 167.0 ± 1.7 cp and 10.8 ± 0.2 dynes/cm, respectively. Patterns are shown in Figure 3-19 and Figure 3-20.

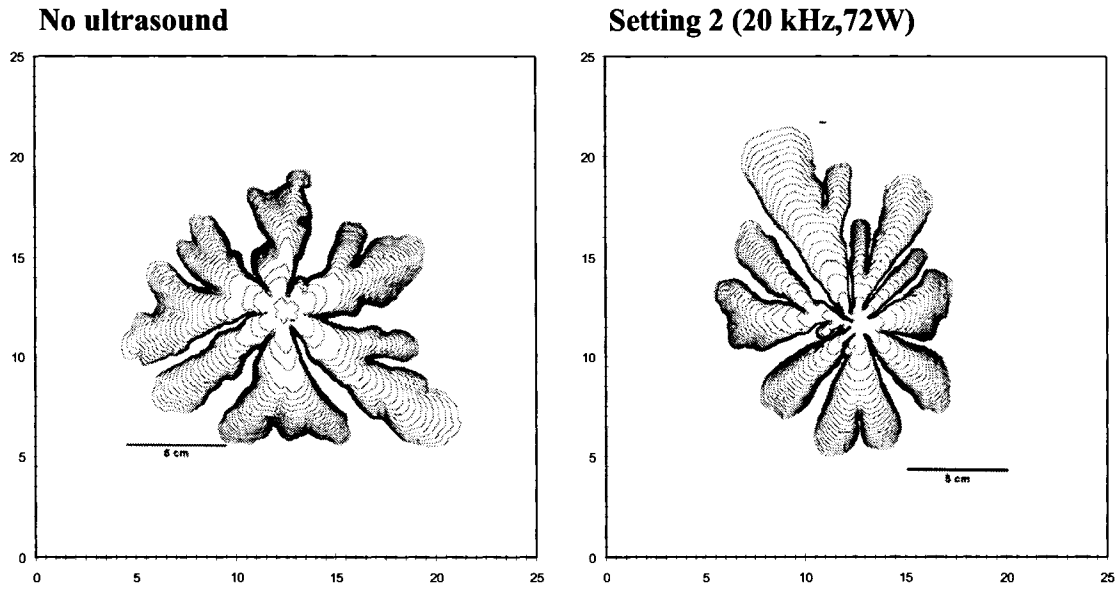


Figure 3-23: Immiscible Hele-Shaw patterns for 3% DOWFAX 2A1 injected into light mineral oil at a constant rate of 0.6 cc/min. The scale is in centimeters. The contours represent the location of the interface at 10 second intervals. $\mu_o = 46.5 \pm 0.5$ cp; IFT = 11.2 ± 0.2 dynes/cm.

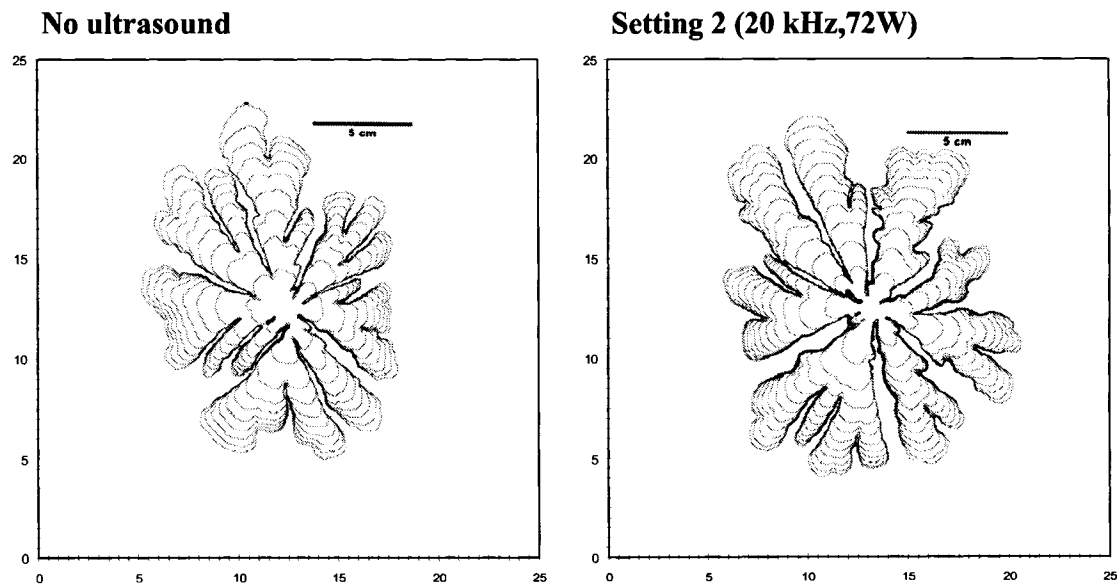


Figure 3-24: Immiscible Hele-Shaw patterns for 3% DOWFAX 2A1 injected into light mineral oil at a constant rate of 1.5 cc/min. The scale is in centimeters. The contours represent the location of the interface at 10 second intervals. $\mu_o = 46.5 \pm 0.5$ cp; IFT = 11.2 ± 0.2 dynes/cm.

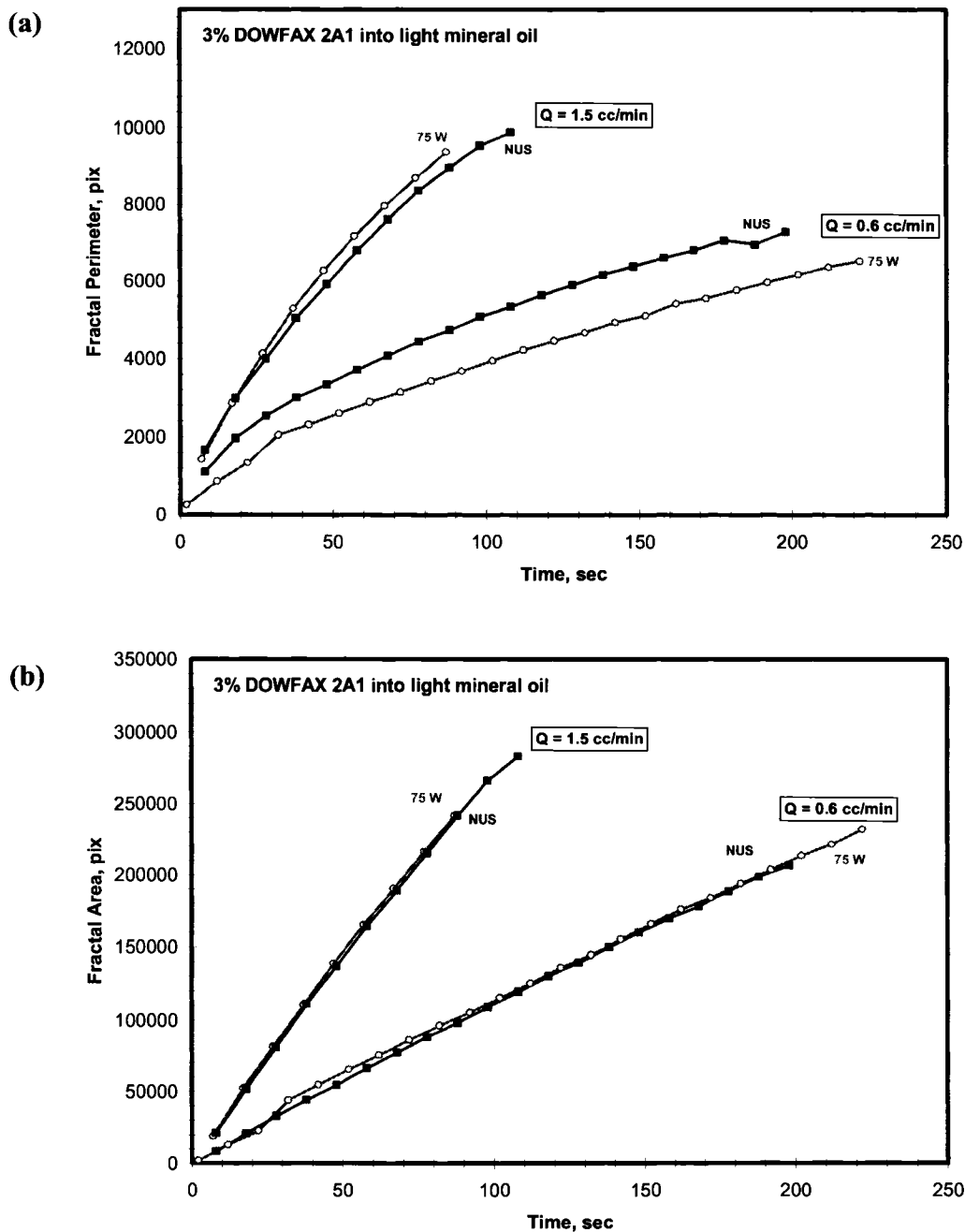


Figure 3-25: (a) Fractal perimeter and (b) fractal area as a function of time for 3% DOWFAX 2A1 into light mineral oil (LMO) at two constant injection rates: 0.6 and 1.5 cc/min. The viscosity and interfacial tension of LMO (with surfactant) is 46.5 ± 0.5 cp and 11.2 ± 0.2 dynes/cm, respectively. Patterns for 0.6 and 1.5 cc/min are shown in Figure 3-23 and Figure 3-24.

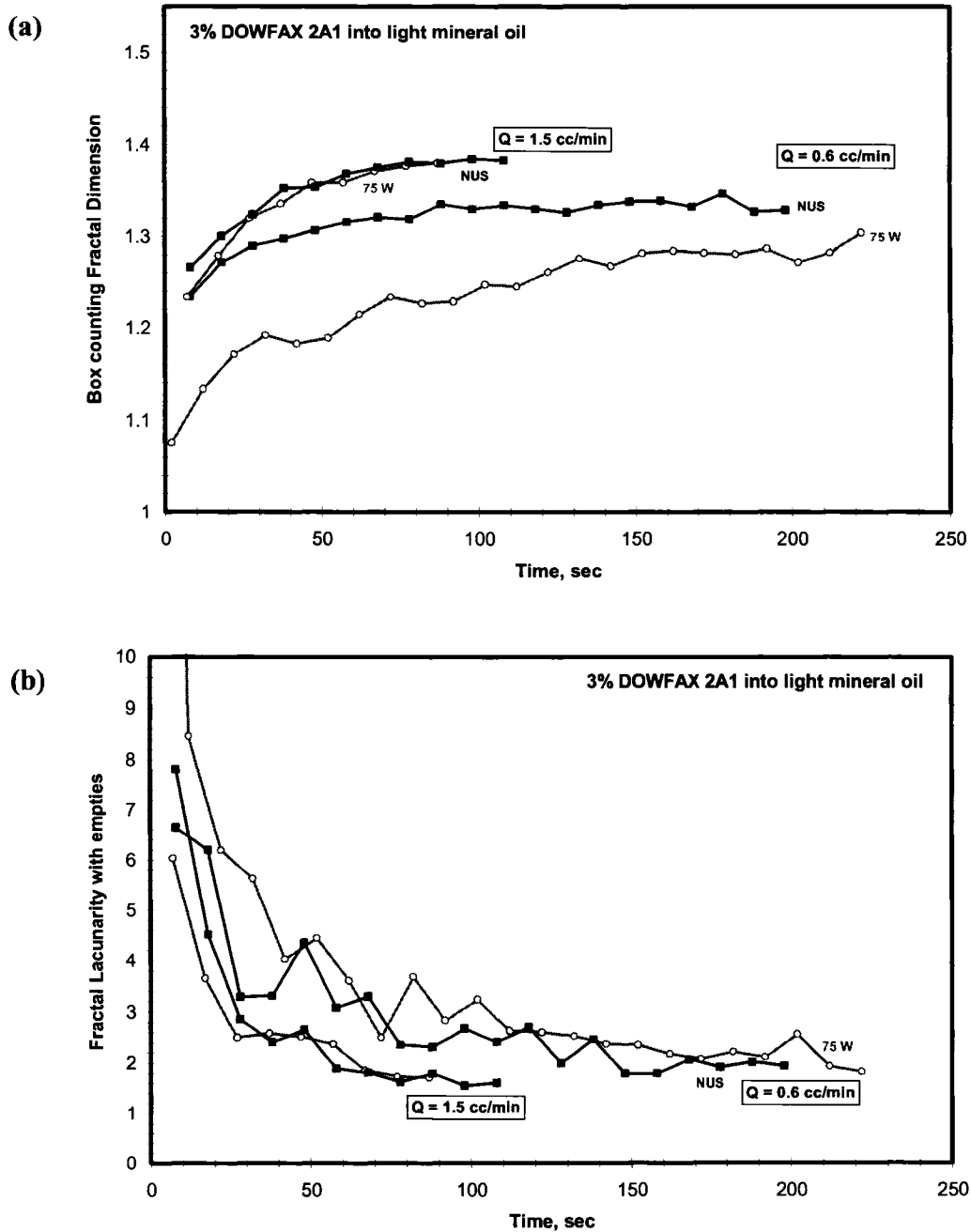


Figure 3-26: (a) Fractal dimension and (b) fractal lacunarity as a function of time for 3% DOWFAX 2A1 into light mineral oil (LMO) at two constant injection rates: 0.6 and 1.5 cc/min. The viscosity and interfacial tension of LMO (with surfactant) is 46.5 ± 0.5 cp and 11.2 ± 0.2 dynes/cm, respectively. Patterns for 0.6 and 1.5 cc/min are shown in Figure 3-23 and Figure 3-24.

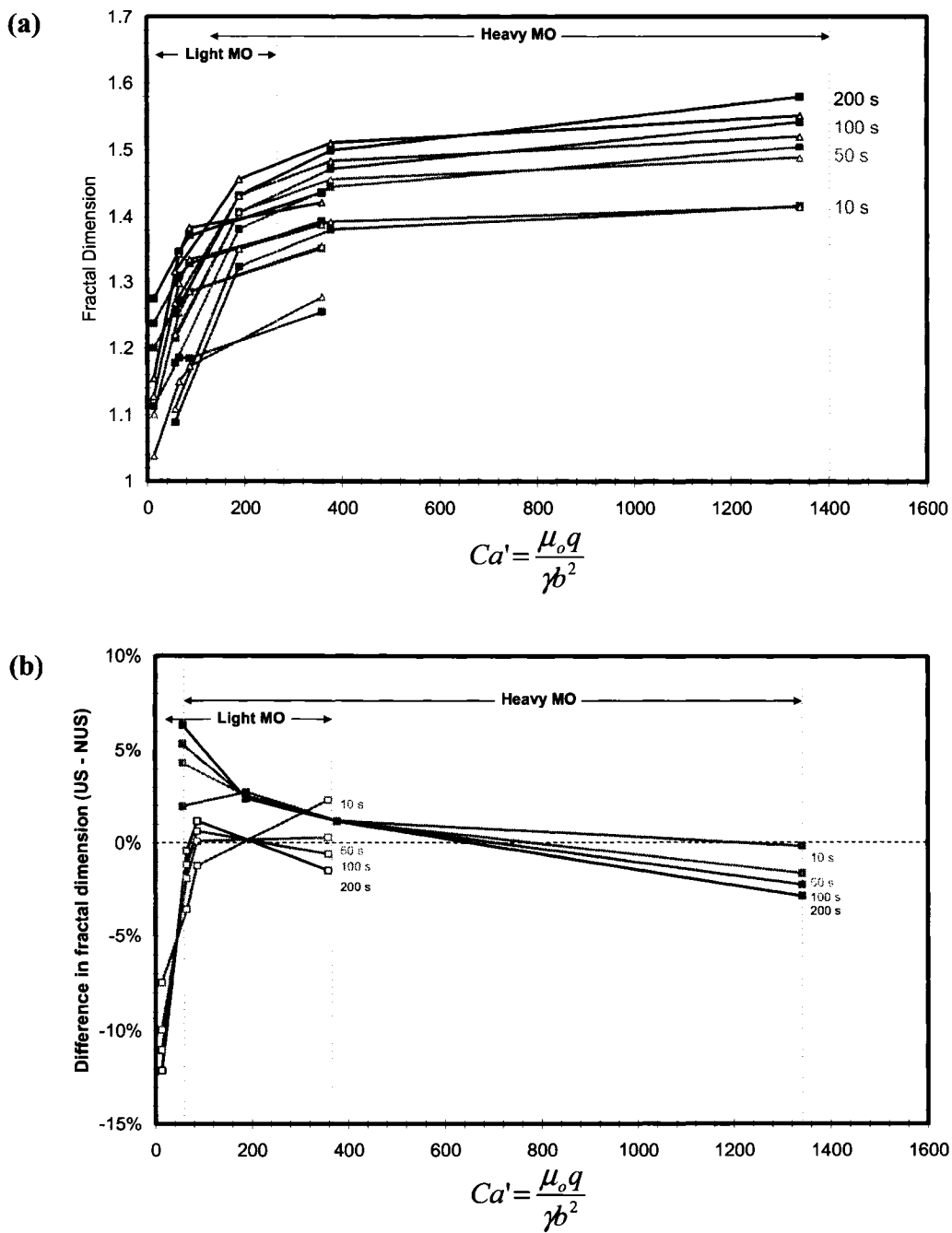


Figure 3-27: (a) Fractal dimension versus modified capillary number for light mineral oil and heavy mineral oil at different times of pattern formation. (b) Difference in fractal dimension for light and heavy mineral oil versus modified Capillary number.

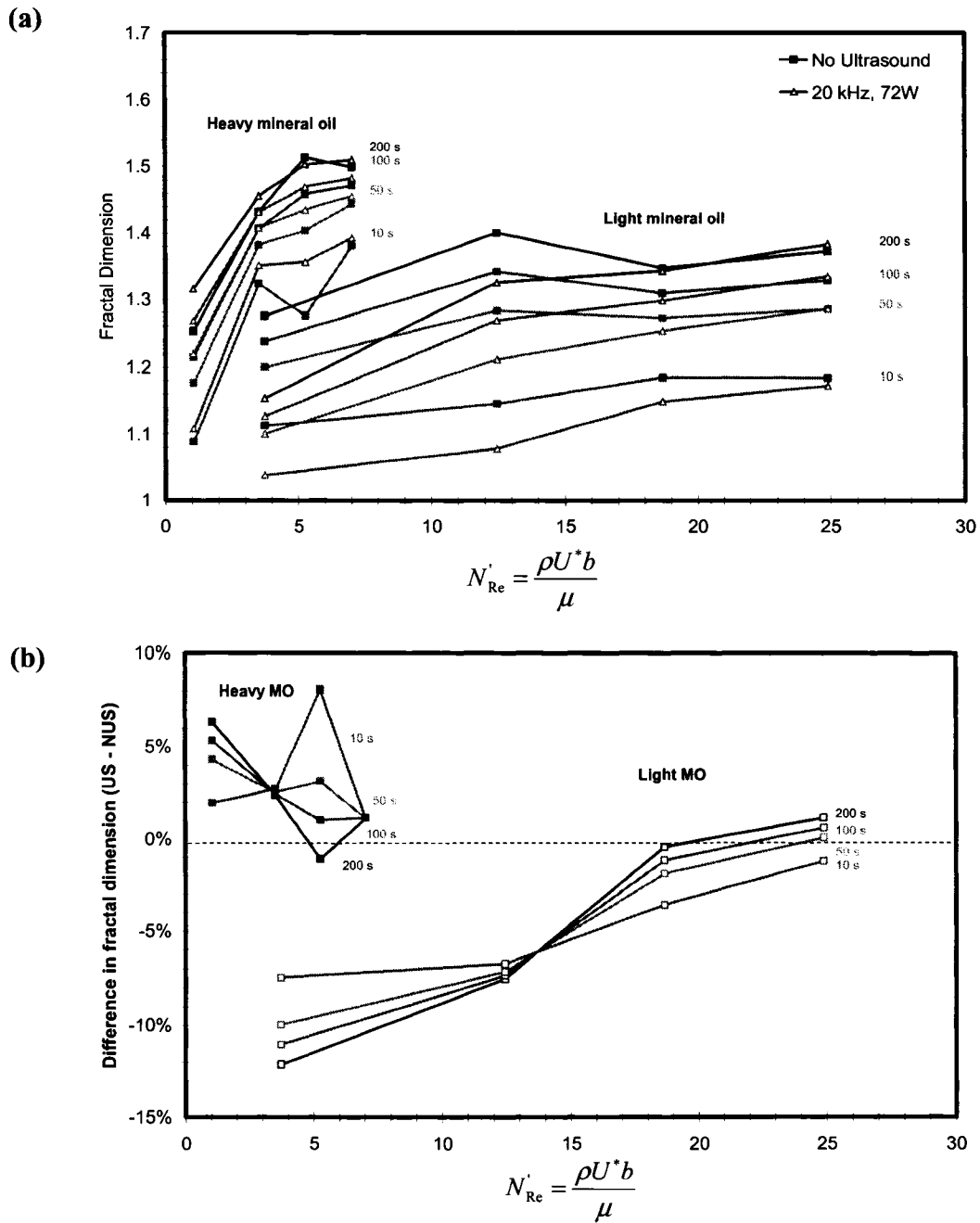


Figure 3-28: (a) Fractal dimension versus modified Reynolds number for light mineral oil and heavy mineral oil at different times of pattern formation. (b) Difference in fractal dimension for light and heavy mineral oil versus modified Reynolds number.

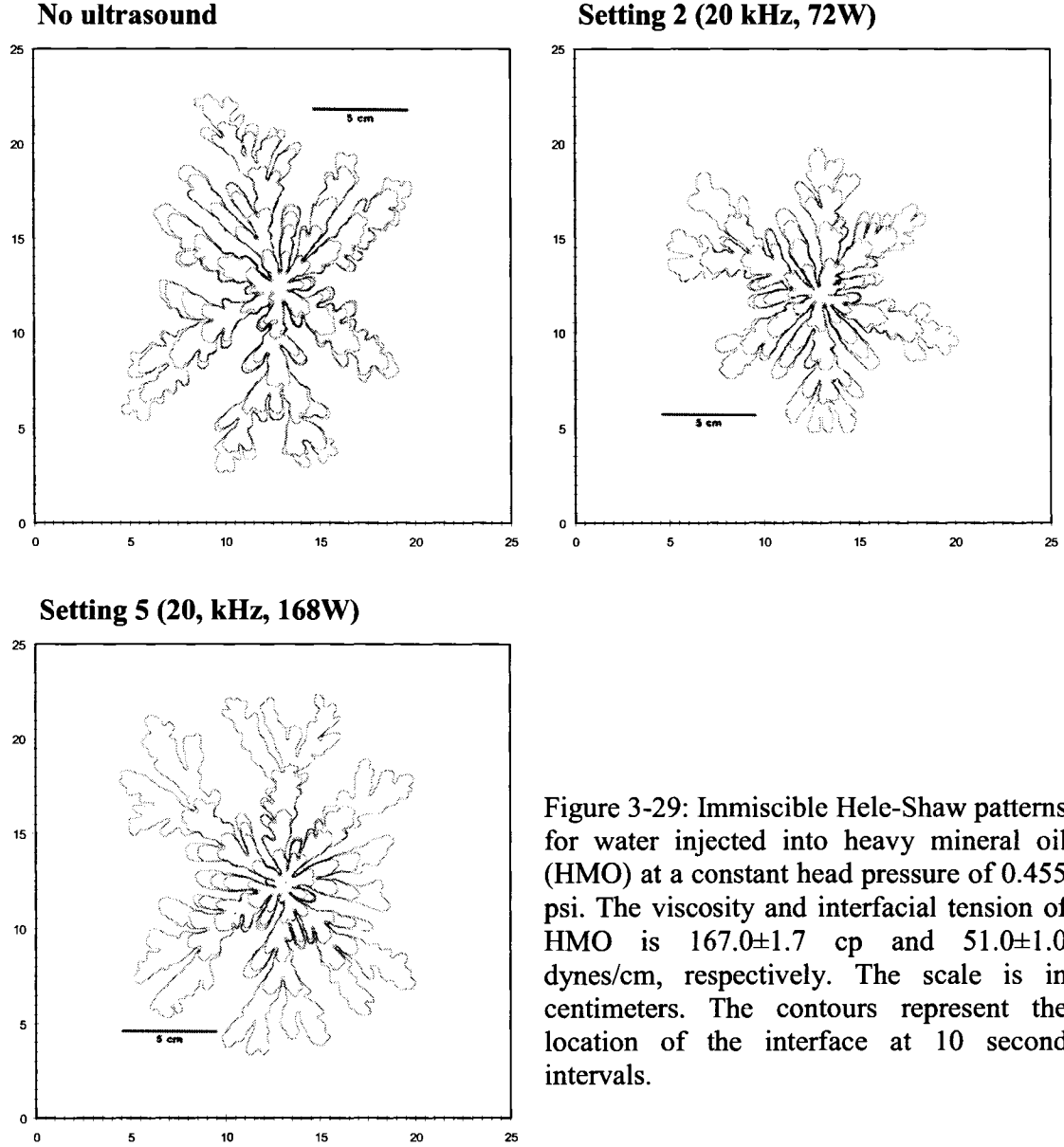


Figure 3-29: Immiscible Hele-Shaw patterns for water injected into heavy mineral oil (HMO) at a constant head pressure of 0.455 psi. The viscosity and interfacial tension of HMO is 167.0 ± 1.7 cp and 51.0 ± 1.0 dynes/cm, respectively. The scale is in centimeters. The contours represent the location of the interface at 10 second intervals.

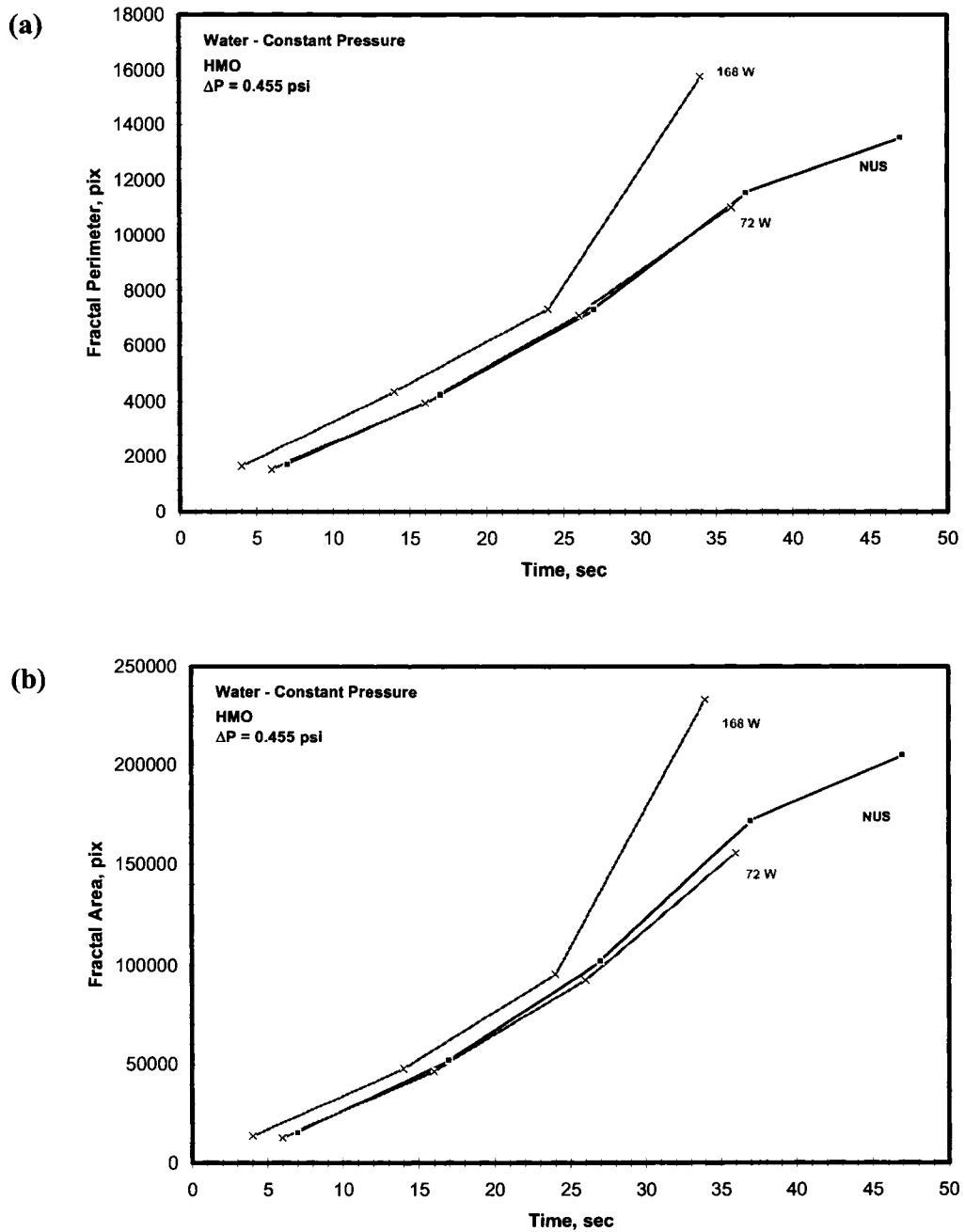


Figure 3-30: (a) Fractal perimeter and (b) fractal area as a function of time for water into HMO at a constant injection pressure of 0.455 psi. The viscosity and interfacial tension of HMO is 167.0 ± 1.7 cp and 51.0 ± 1.0 dynes/cm, respectively. Patterns are shown in Figure 3-29.

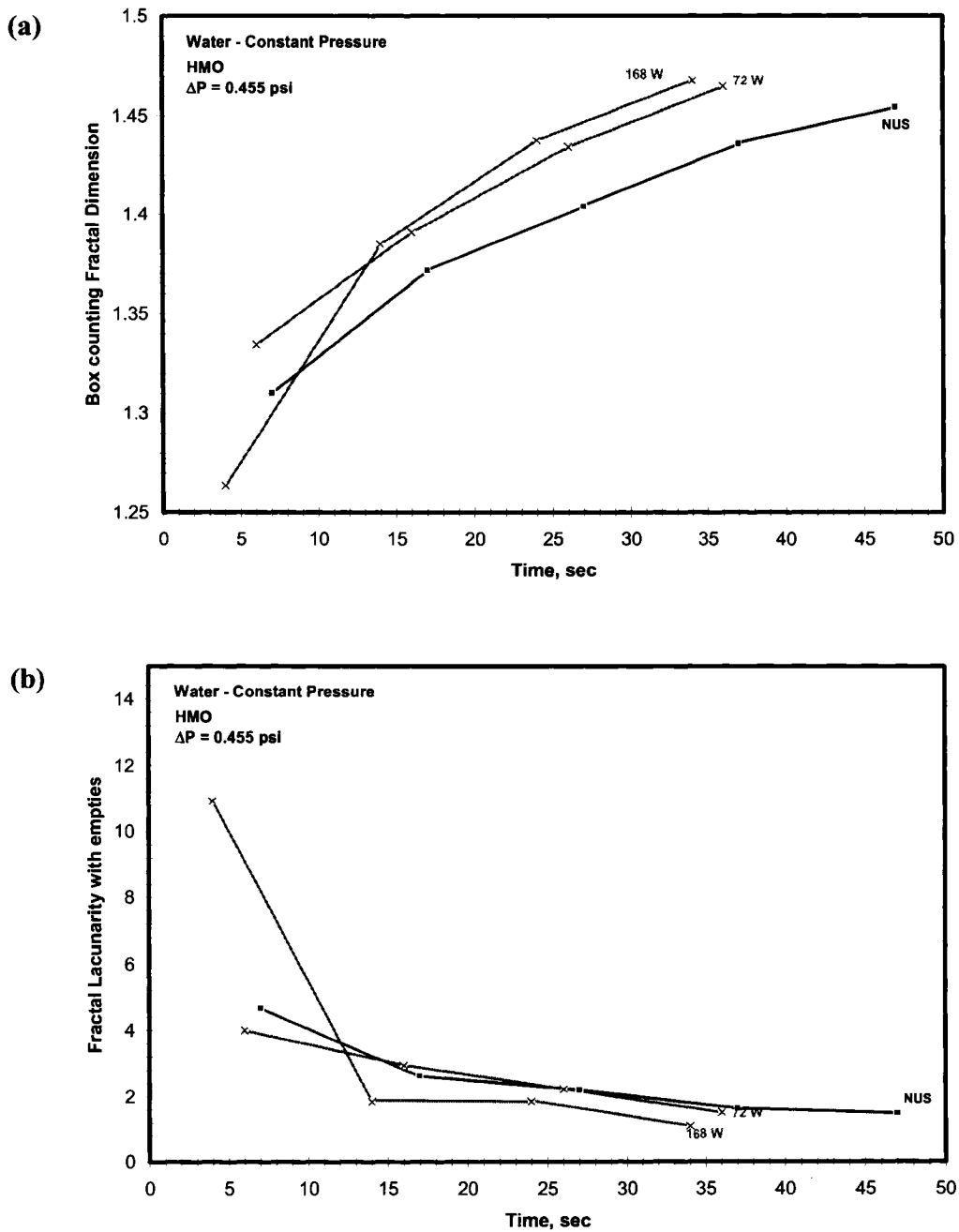


Figure 3-31: (a) Fractal dimension and (b) lacunarity as a function of time for water into HMO at a constant injection pressure of 0.455 psi. The viscosity and interfacial tension of HMO is 167.0 ± 1.7 cp and 51.0 ± 1.0 dynes/cm, respectively. Patterns are shown in Figure 3-29.

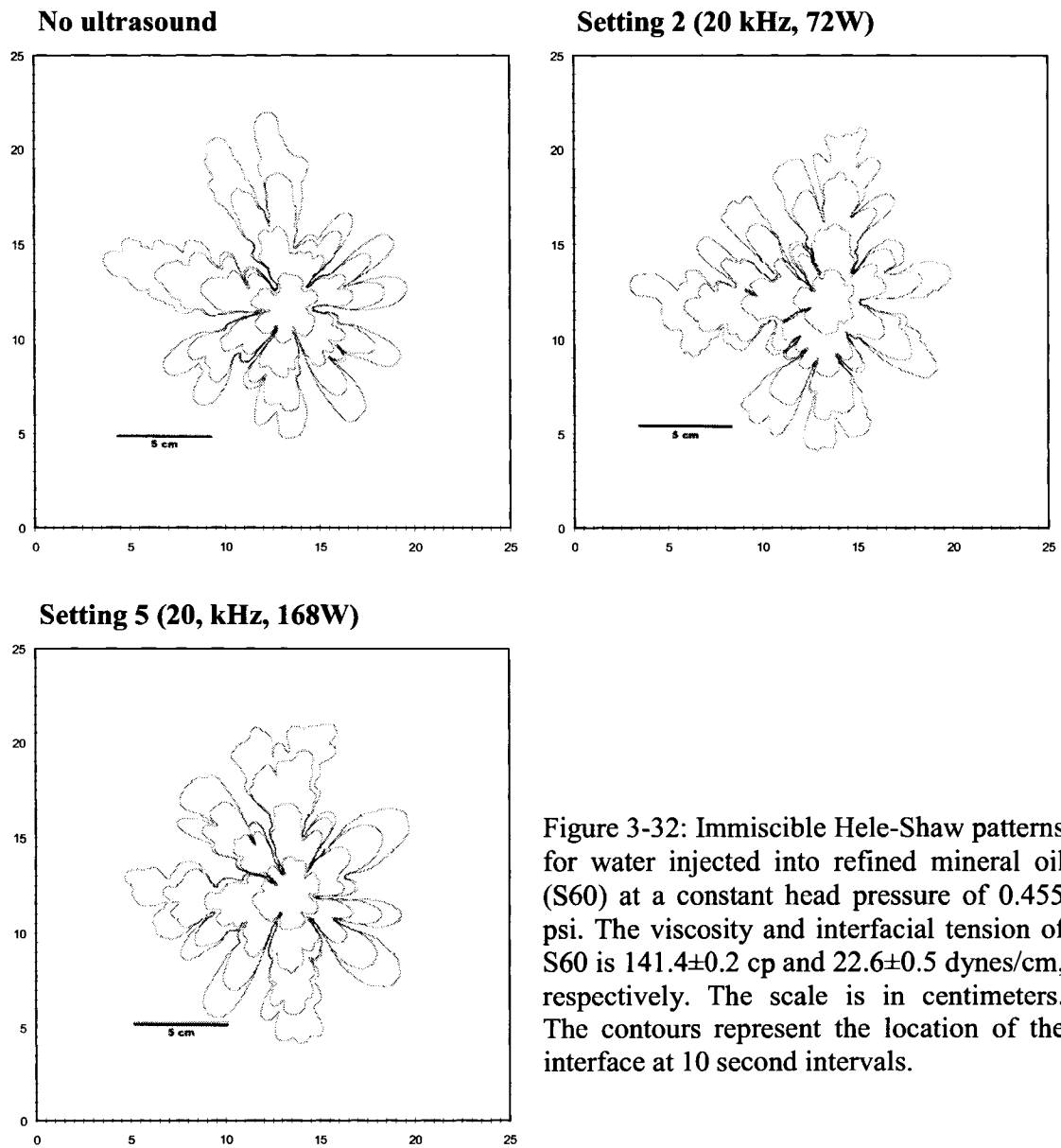


Figure 3-32: Immiscible Hele-Shaw patterns for water injected into refined mineral oil (S60) at a constant head pressure of 0.455 psi. The viscosity and interfacial tension of S60 is 141.4 ± 0.2 cp and 22.6 ± 0.5 dynes/cm, respectively. The scale is in centimeters. The contours represent the location of the interface at 10 second intervals.

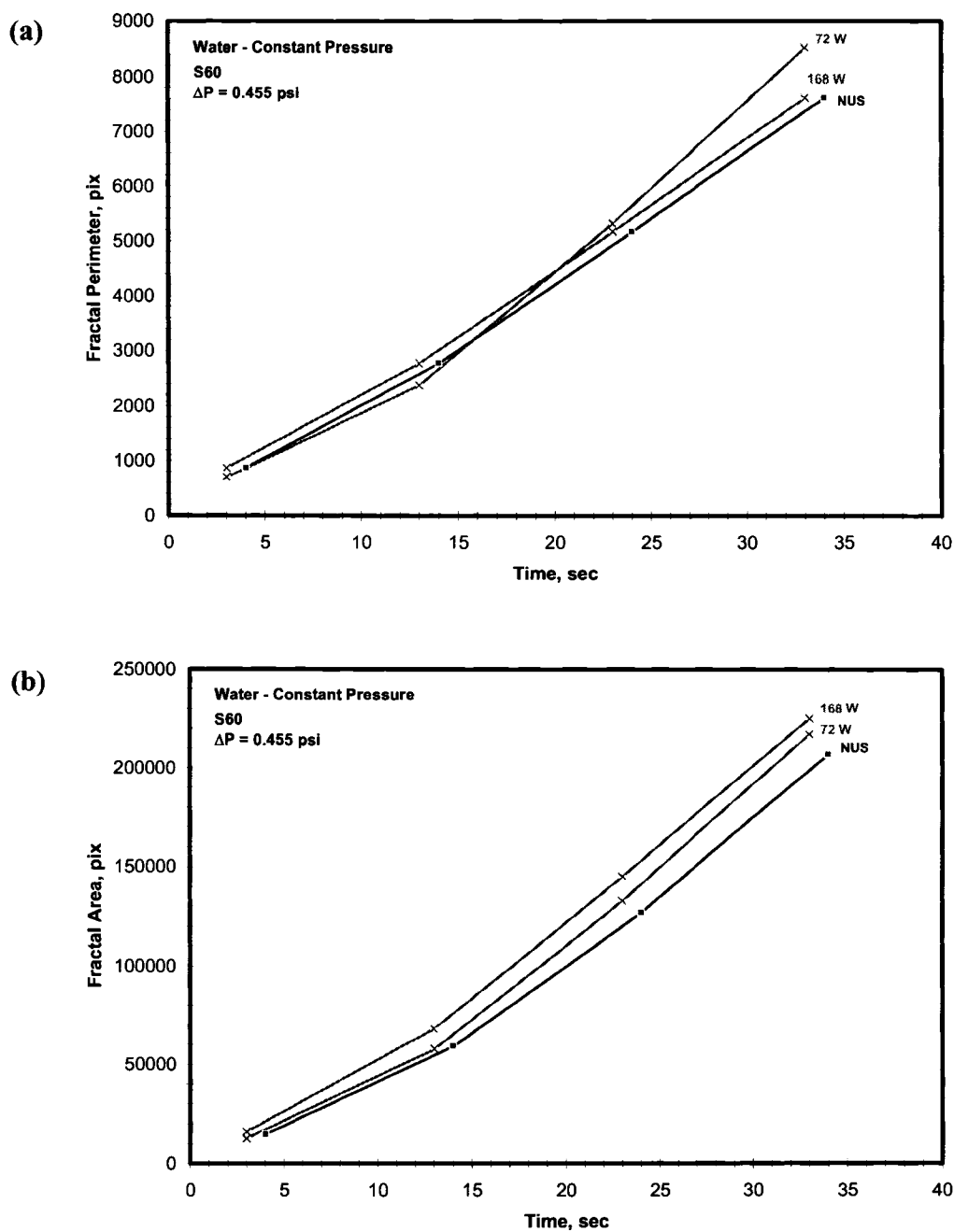


Figure 3-33: (a) Fractal perimeter and (b) fractal area as a function of time for water into S60 at a constant injection pressure of 0.455 psi. The viscosity and interfacial tension of S60 is 141.4 ± 0.2 cp and 22.6 ± 0.5 dynes/cm, respectively. Patterns are shown in Figure 3-32.

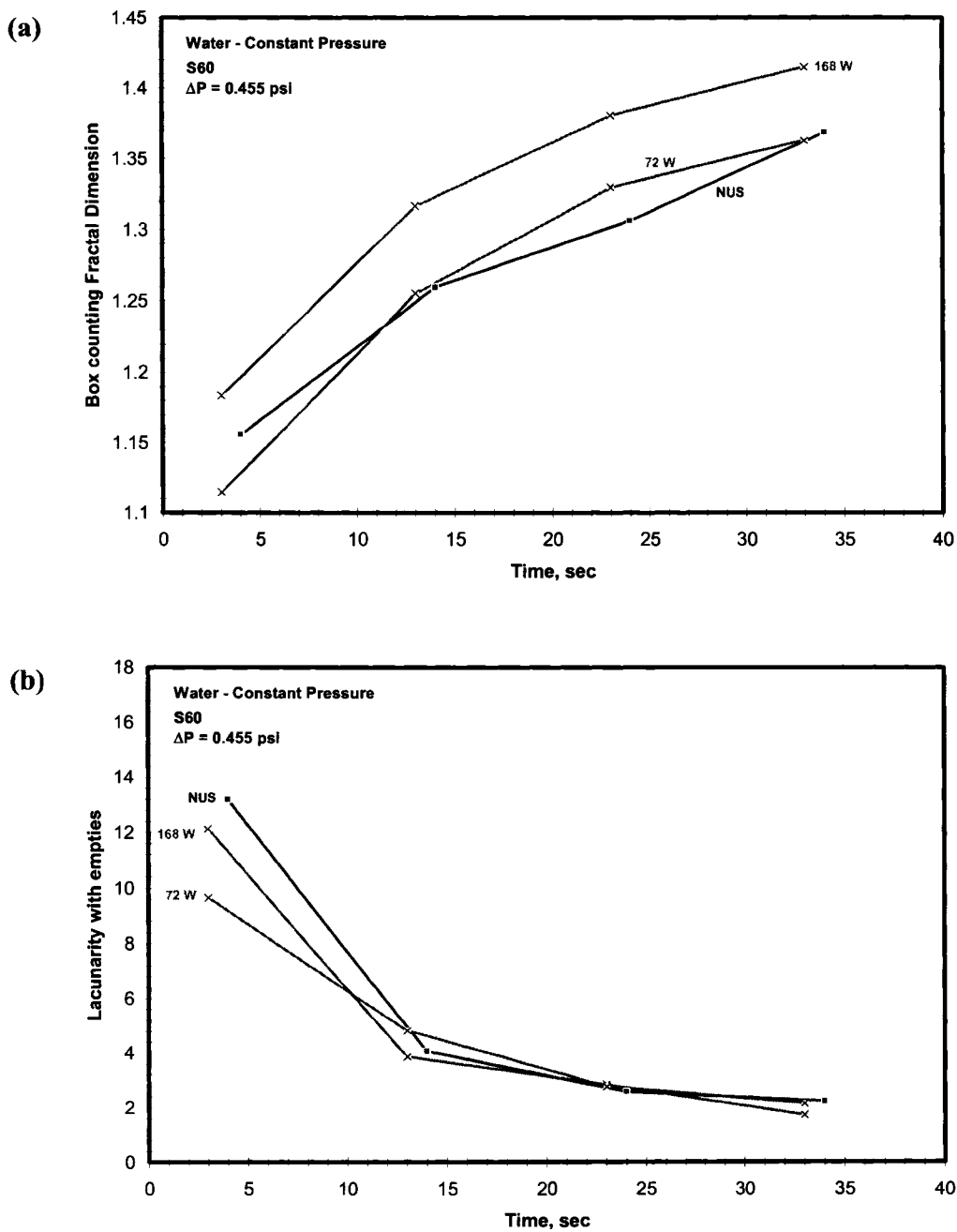


Figure 3-34: (a) Fractal dimension and (b) lacunarity as a function of time for water into S60 at a constant injection pressure of 0.455 psi. The viscosity and interfacial tension of S60 is 141.4 ± 0.2 cp and 22.6 ± 0.5 dynes/cm, respectively. Patterns are shown in Figure 3-32.

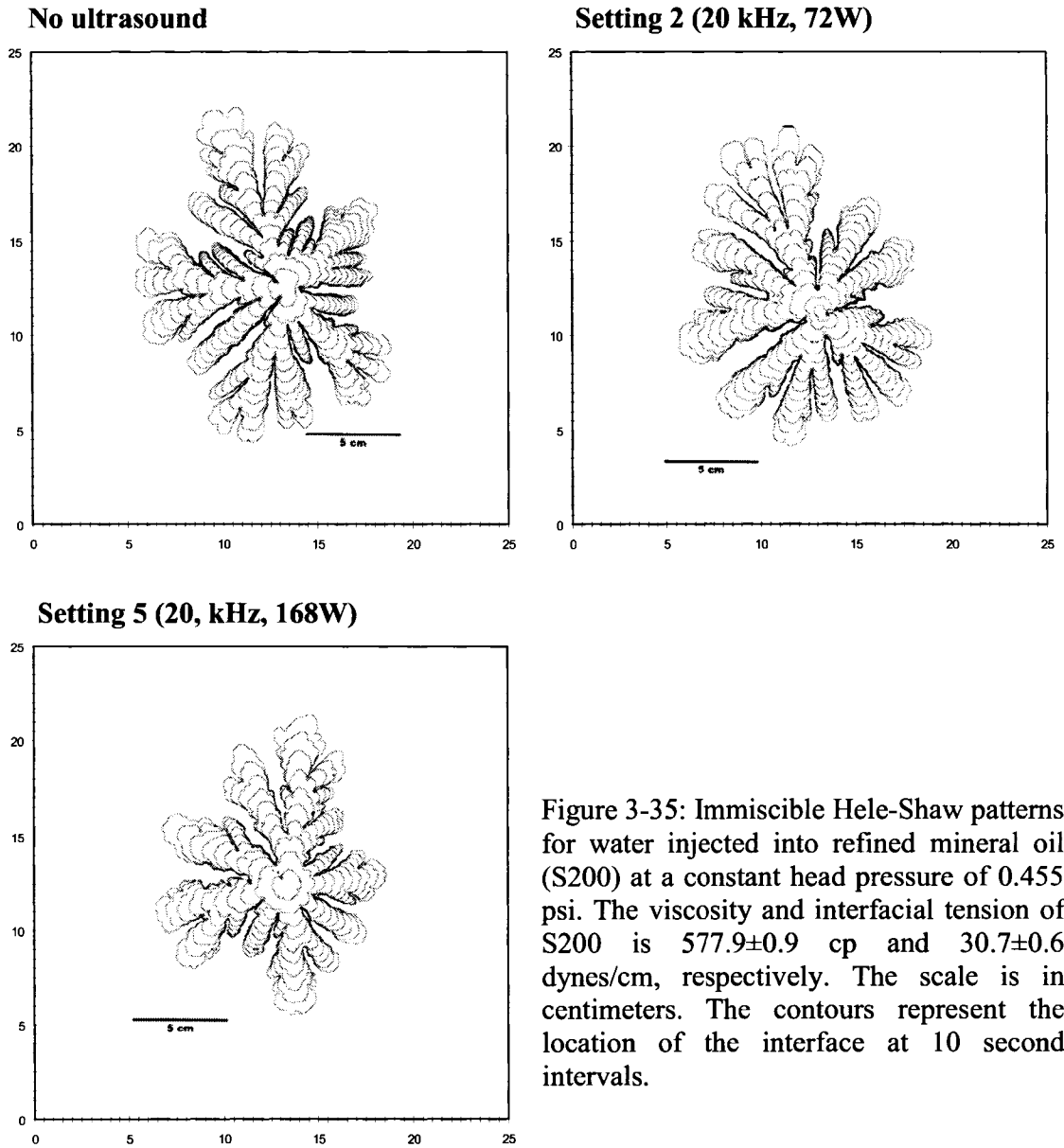


Figure 3-35: Immiscible Hele-Shaw patterns for water injected into refined mineral oil (S200) at a constant head pressure of 0.455 psi. The viscosity and interfacial tension of S200 is 577.9 ± 0.9 cp and 30.7 ± 0.6 dynes/cm, respectively. The scale is in centimeters. The contours represent the location of the interface at 10 second intervals.

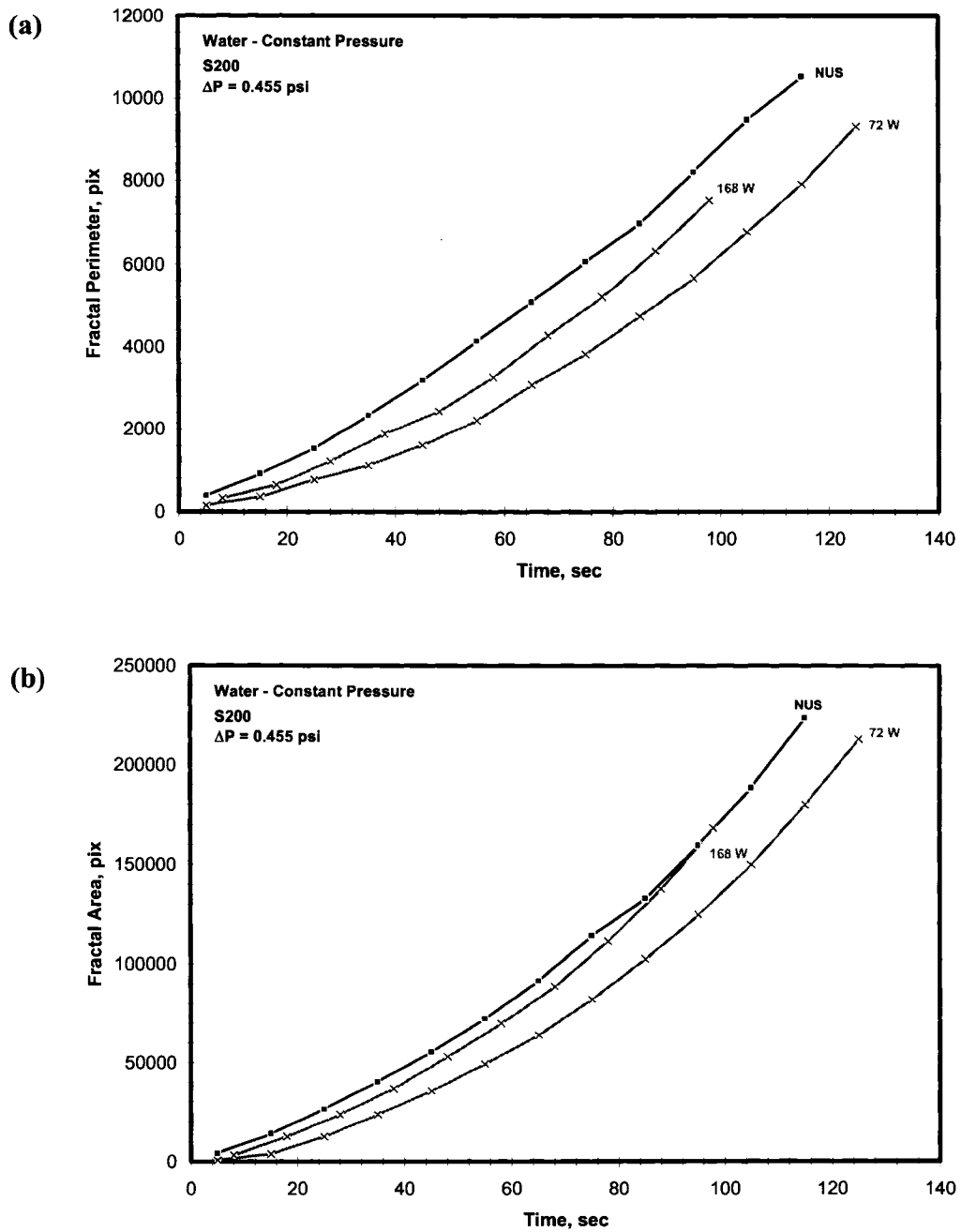


Figure 3-36: (a) Fractal perimeter and (b) fractal area as a function of time for water into S200 at a constant injection pressure of 0.455 psi. The viscosity and interfacial tension of S200 is 577.9 ± 0.9 cp and 30.7 ± 0.6 dynes/cm, respectively. Patterns are shown in Figure 3-35.

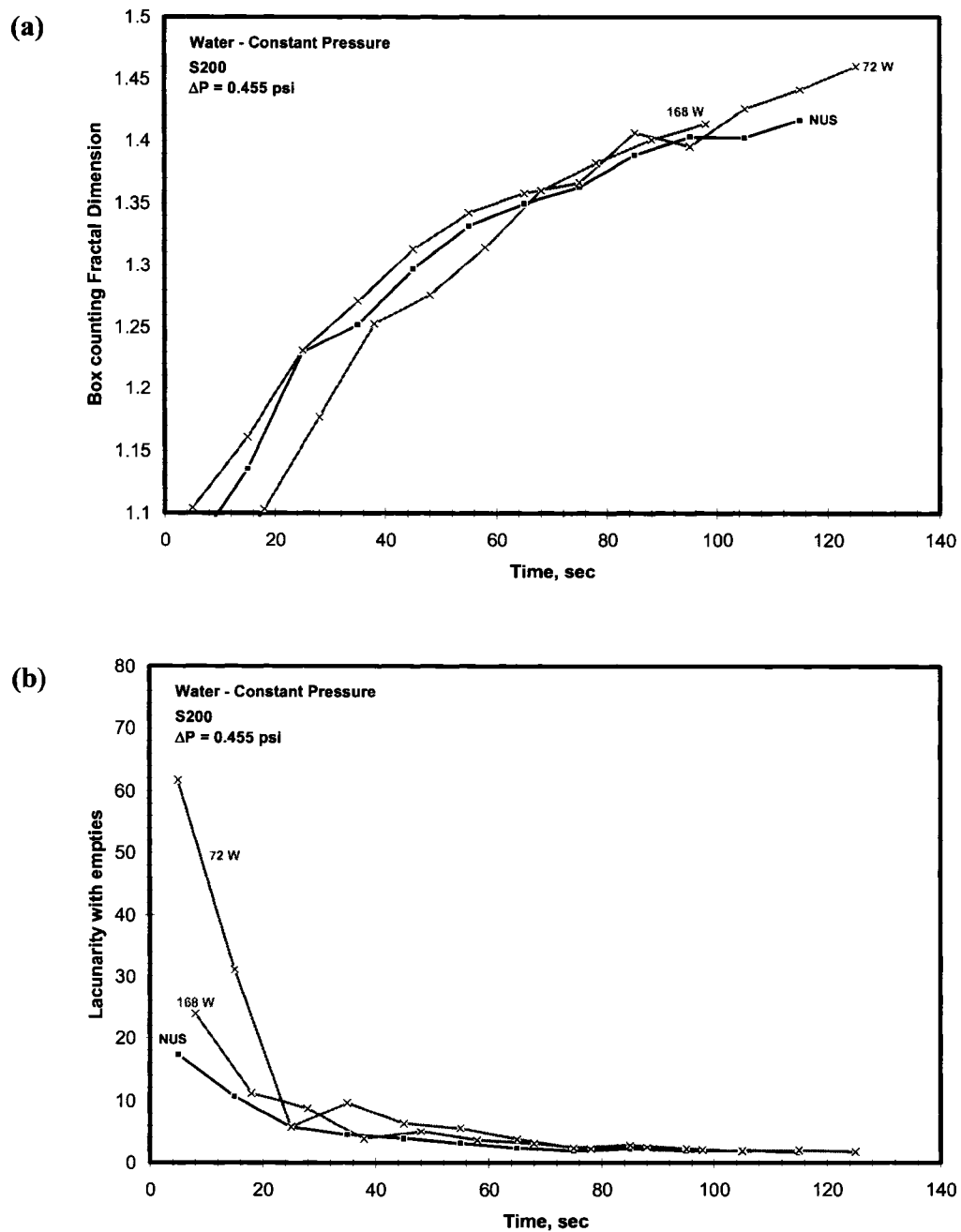


Figure 3-37: (a) Fractal dimension and (b) lacunarity as a function of time for water into S200 at a constant injection pressure of 0.455 psi. The viscosity and interfacial tension of S200 is 577.9 ± 0.9 cp and 30.7 ± 0.6 dynes/cm, respectively. Patterns are shown in Figure 3-35.

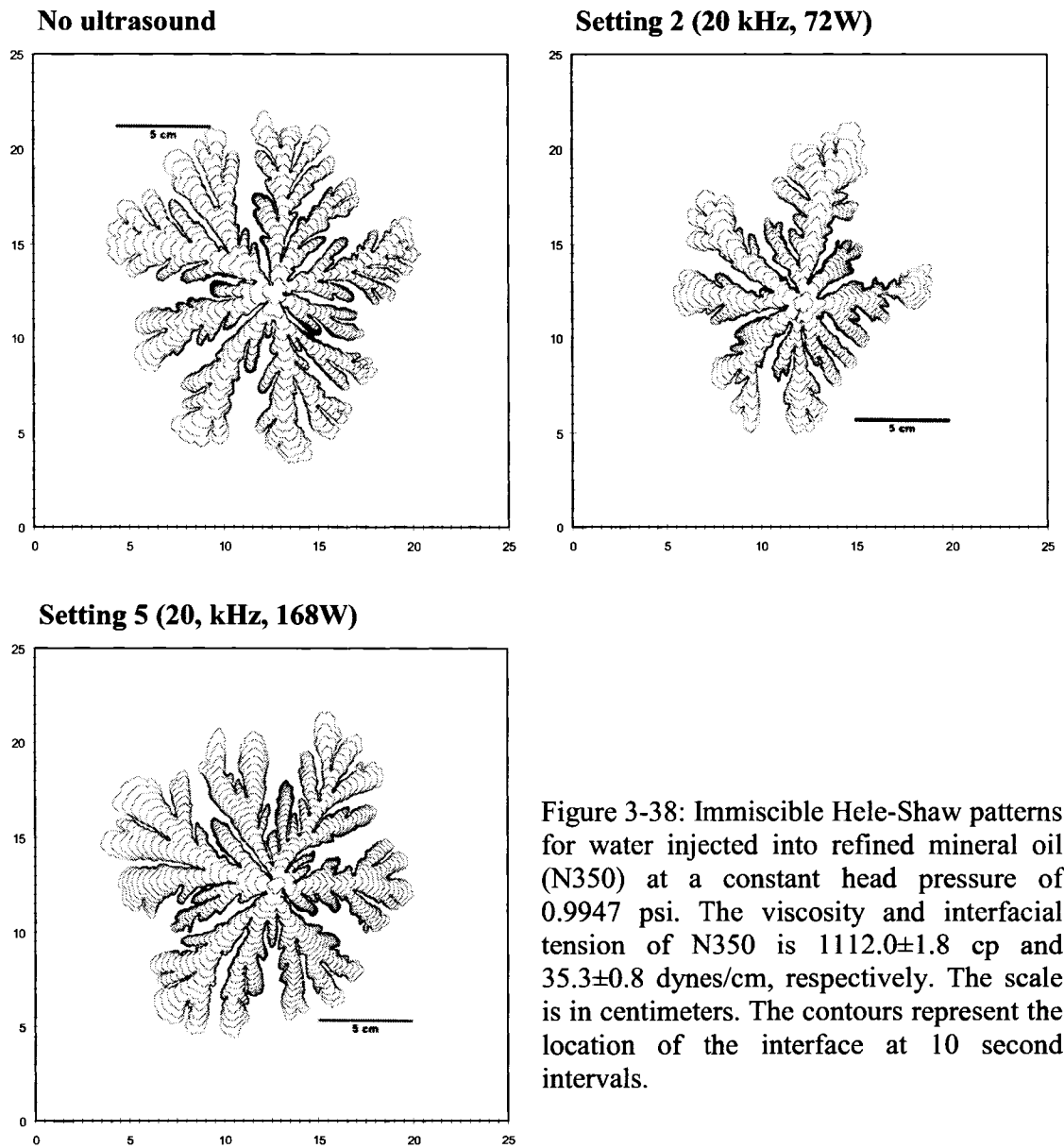


Figure 3-38: Immiscible Hele-Shaw patterns for water injected into refined mineral oil (N350) at a constant head pressure of 0.9947 psi. The viscosity and interfacial tension of N350 is 1112.0 ± 1.8 cp and 35.3 ± 0.8 dynes/cm, respectively. The scale is in centimeters. The contours represent the location of the interface at 10 second intervals.

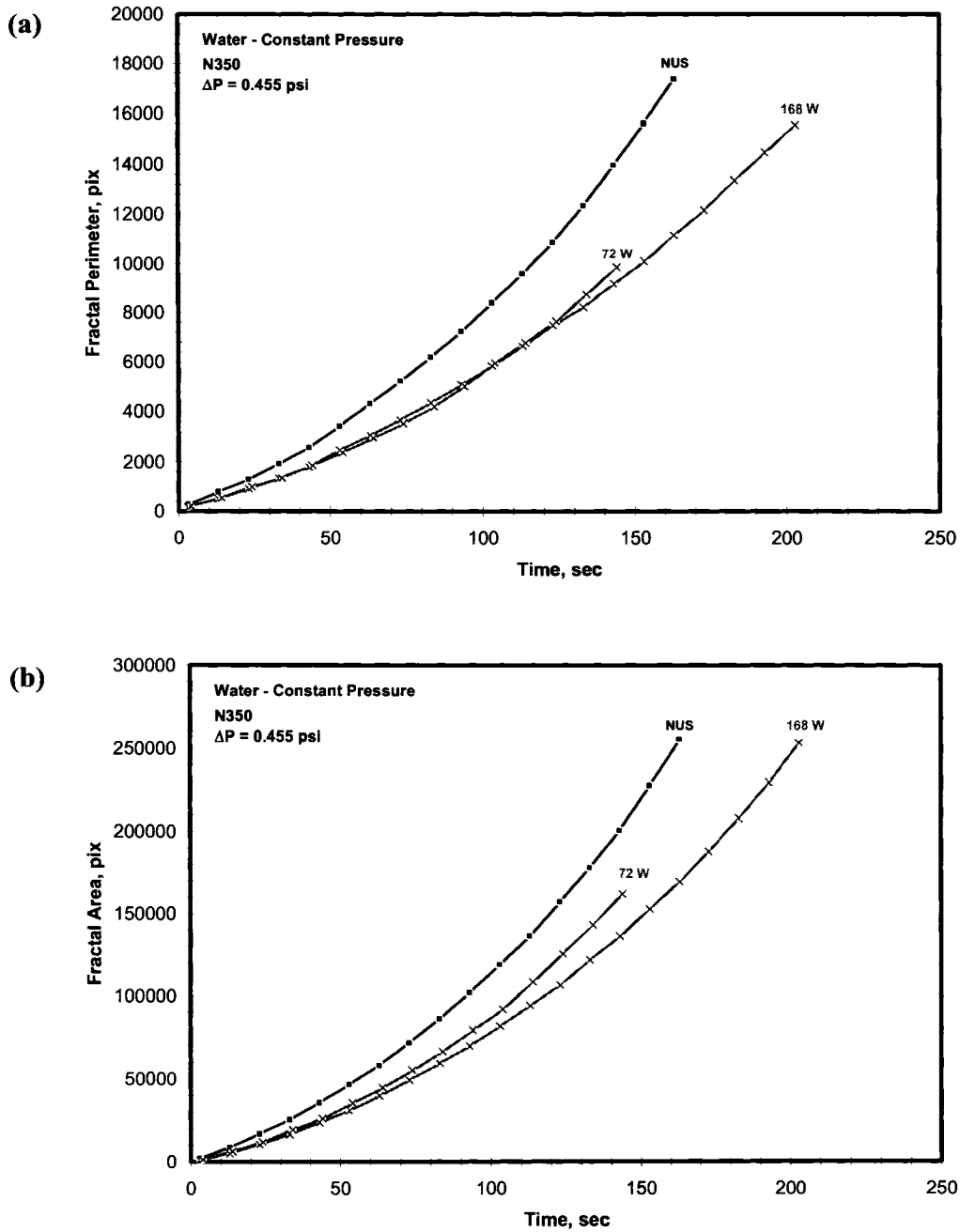


Figure 3-39: (a) Fractal perimeter and (b) fractal area as a function of time for water into N350 at a constant injection pressure of 0.455 psi. The viscosity and interfacial tension of N350 is 1112.0 ± 1.8 cp and 35.3 ± 0.8 dynes/cm, respectively. Patterns are shown in Figure 3-38.

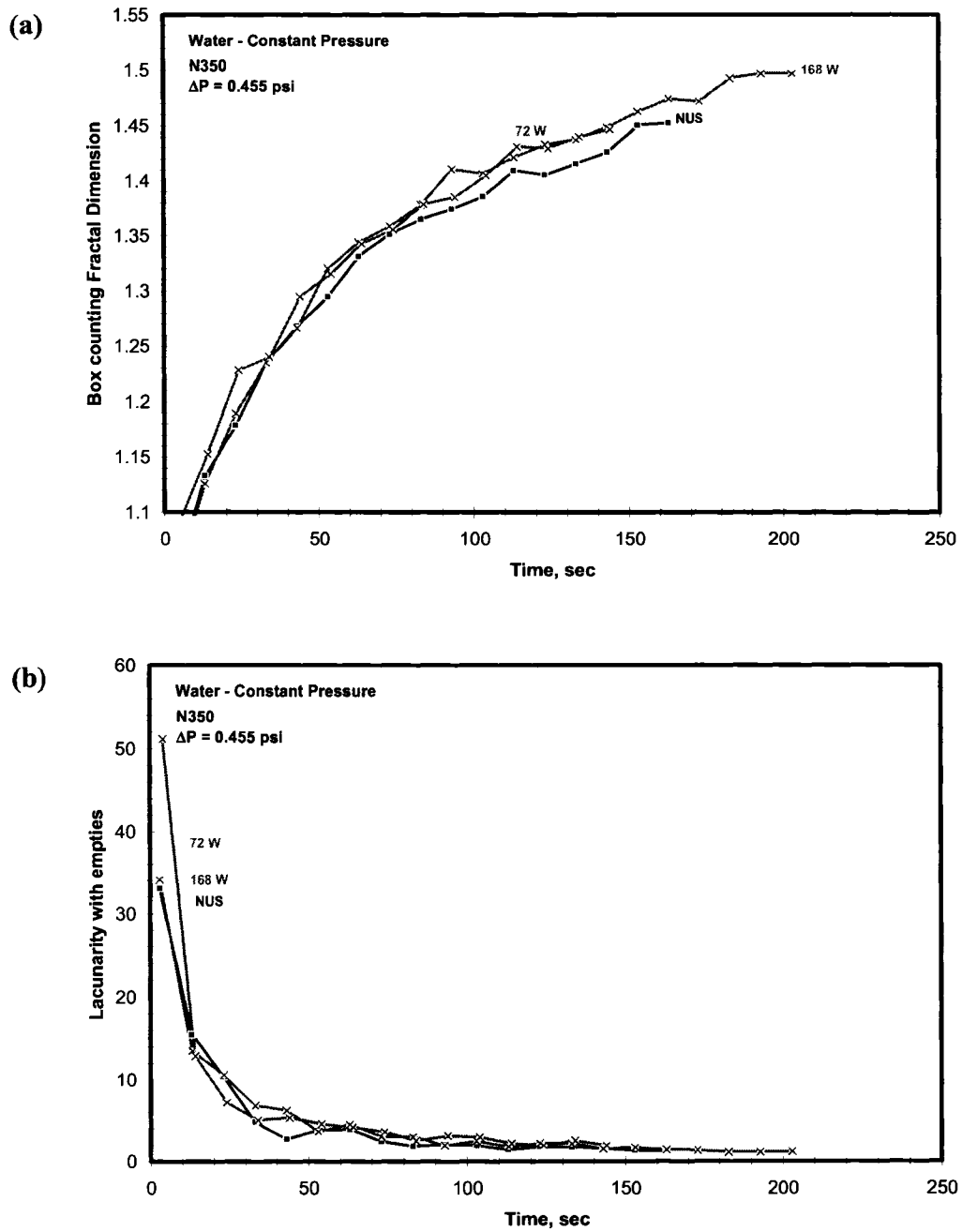
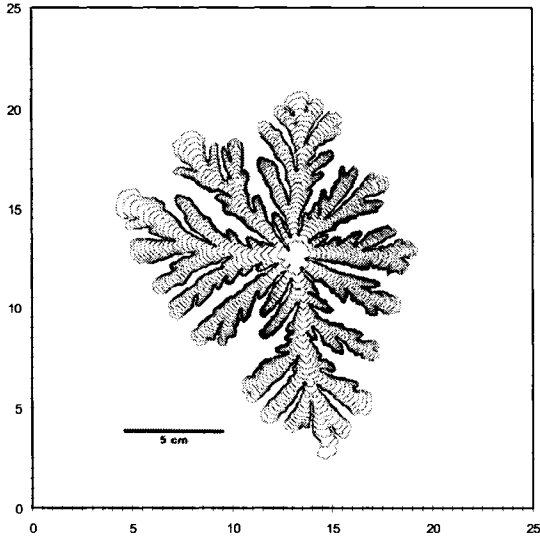
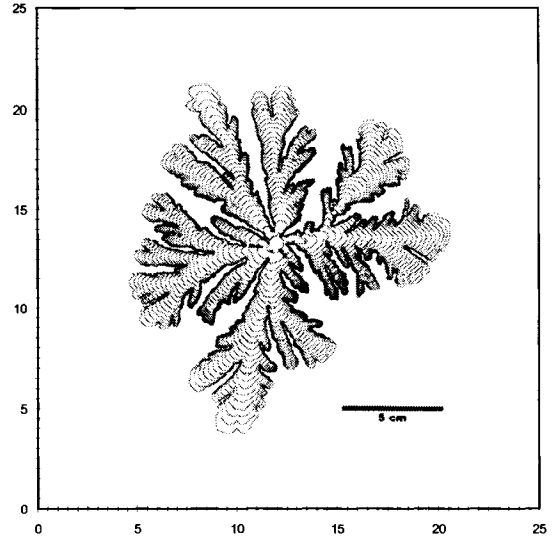


Figure 3-40: (a) Fractal dimension and (b) lacunarity as a function of time for water into N350 at a constant injection pressure of 0.455 psi. The viscosity and interfacial tension of N350 is 1112.0 ± 1.8 cp and 35.3 ± 0.8 dynes/cm, respectively. Patterns are shown in Figure 3-38.

No ultrasound



Setting 2 (20 kHz, 72W)



Setting 5 (20 kHz, 168W)

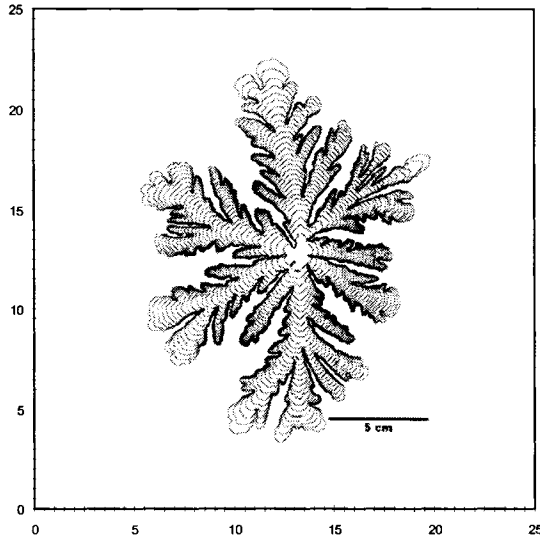


Figure 3-41: Immiscible Hele-Shaw patterns for water injected into synthetic mineral oil (S600) at a constant head pressure of 0.455 psi. The viscosity and interfacial tension of S600 is 1973 ± 3.2 cp and 38.7 ± 0.8 dynes/cm, respectively. The scale is in centimeters. The contours represent the location of the interface at 10 second intervals.

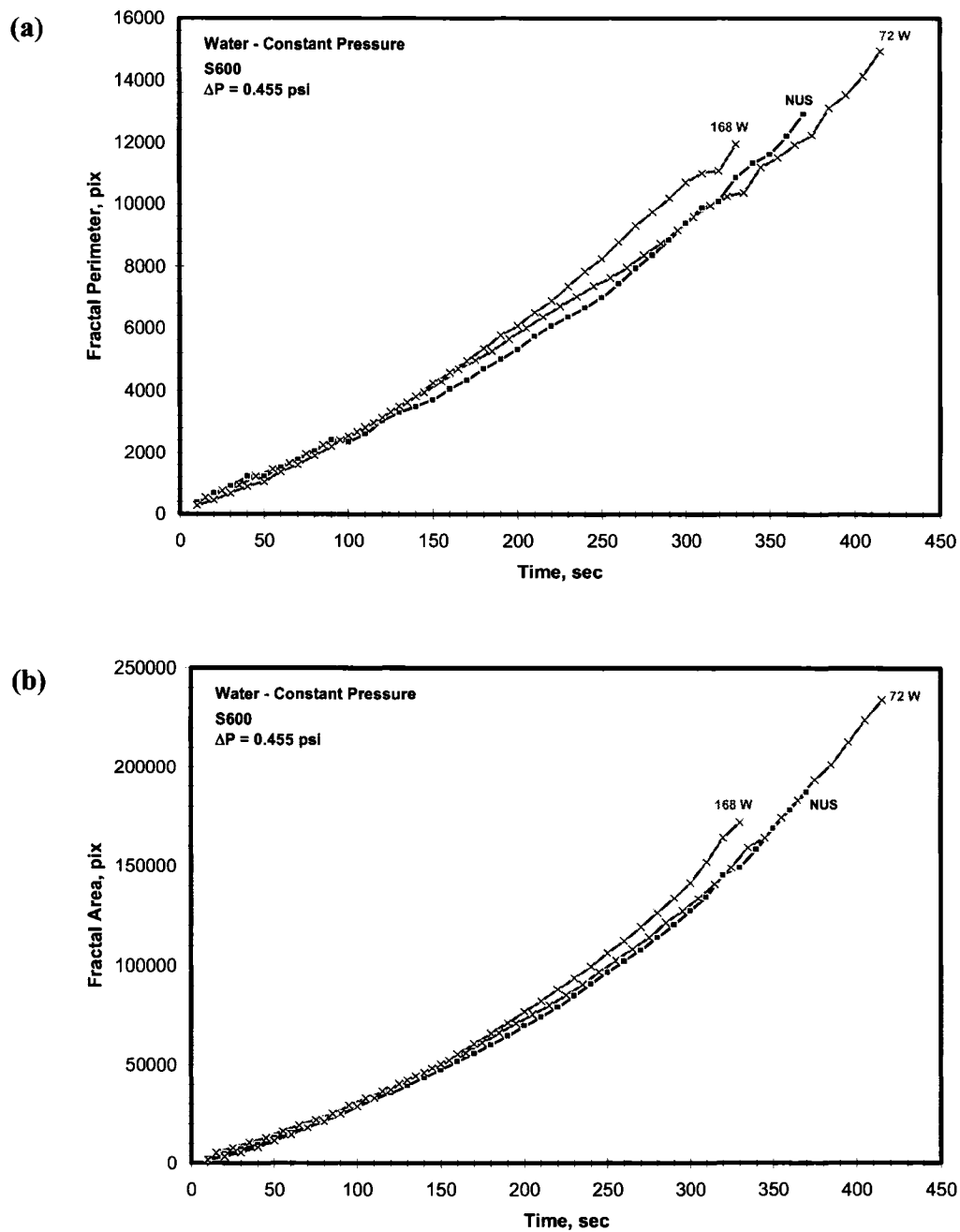


Figure 3-42: (a) Fractal perimeter and (b) fractal area as a function of time for water into S600 at a constant injection pressure of 0.455 psi. The viscosity and interfacial tension of S600 is 1973 ± 3.2 cp and 38.7 ± 0.8 dynes/cm, respectively. Patterns are shown in Figure 3-41.

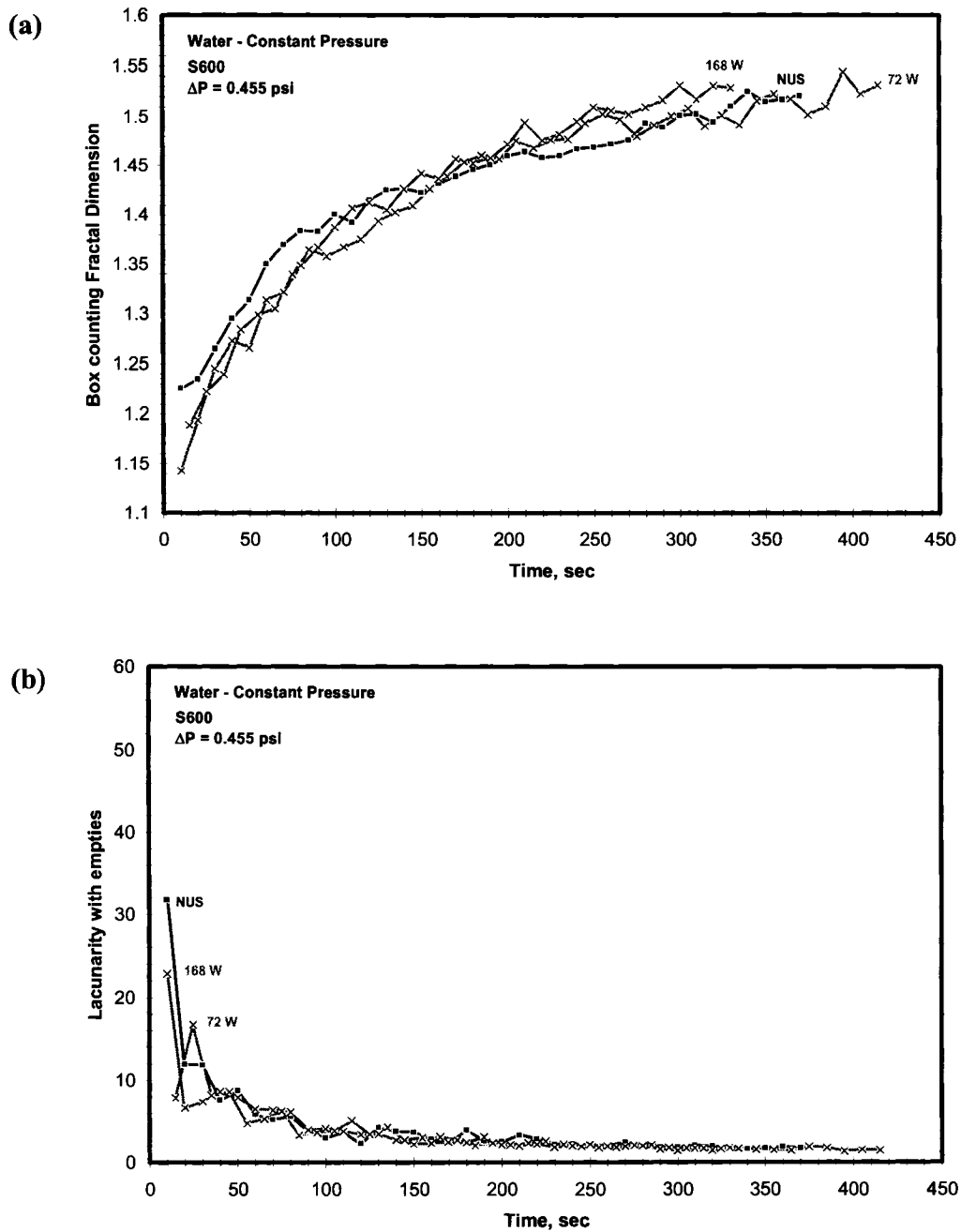


Figure 3-43: (a) Fractal dimension and (b) lacunarity as a function of time for water into S600 at a constant injection pressure of 0.455 psi. The viscosity and interfacial tension of S600 is 1973 ± 3.2 cp and 38.7 ± 0.8 dynes/cm, respectively. Patterns are shown in Figure 3-41.

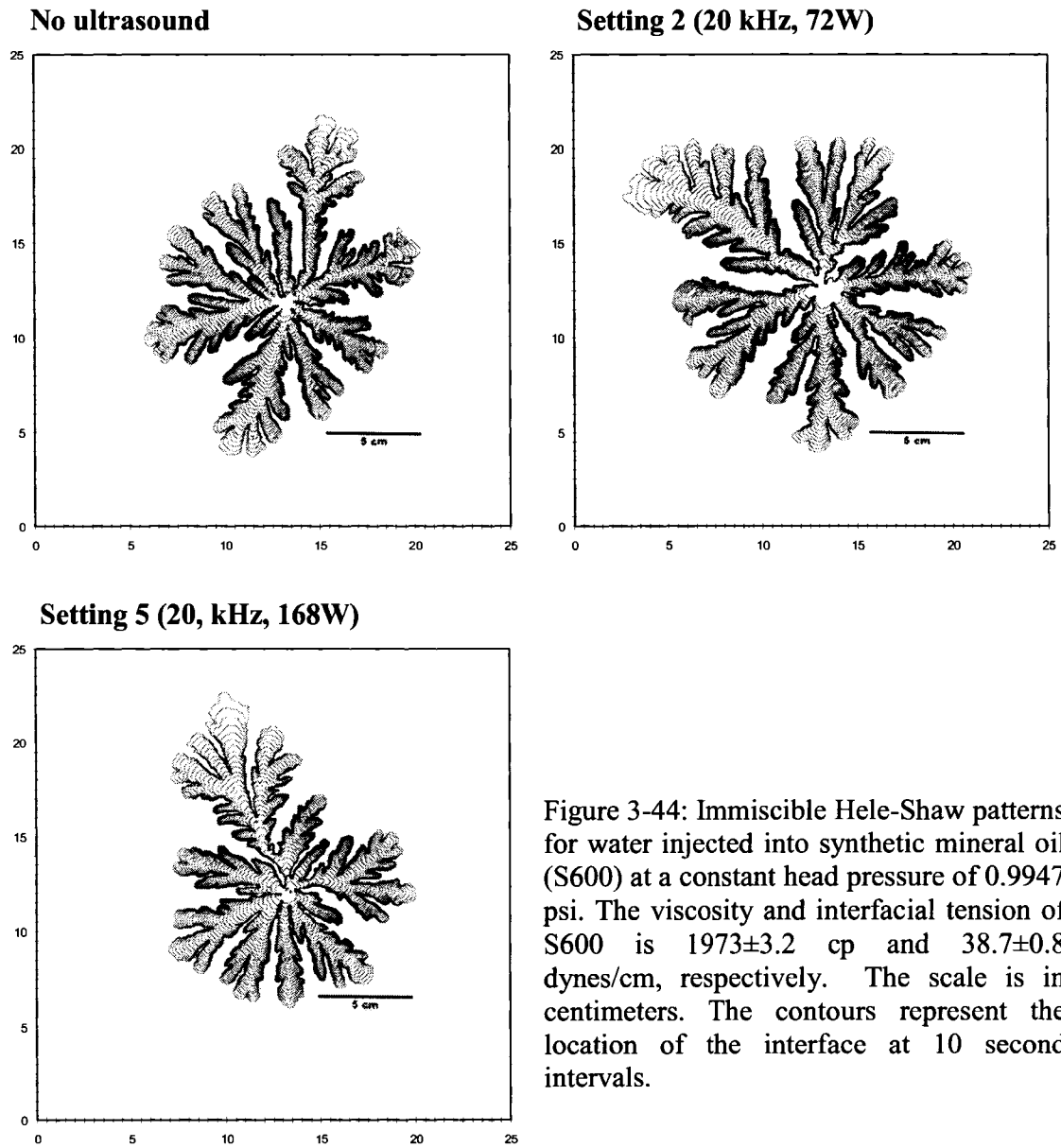


Figure 3-44: Immiscible Hele-Shaw patterns for water injected into synthetic mineral oil (S600) at a constant head pressure of 0.9947 psi. The viscosity and interfacial tension of S600 is 1973 ± 3.2 cp and 38.7 ± 0.8 dynes/cm, respectively. The scale is in centimeters. The contours represent the location of the interface at 10 second intervals.

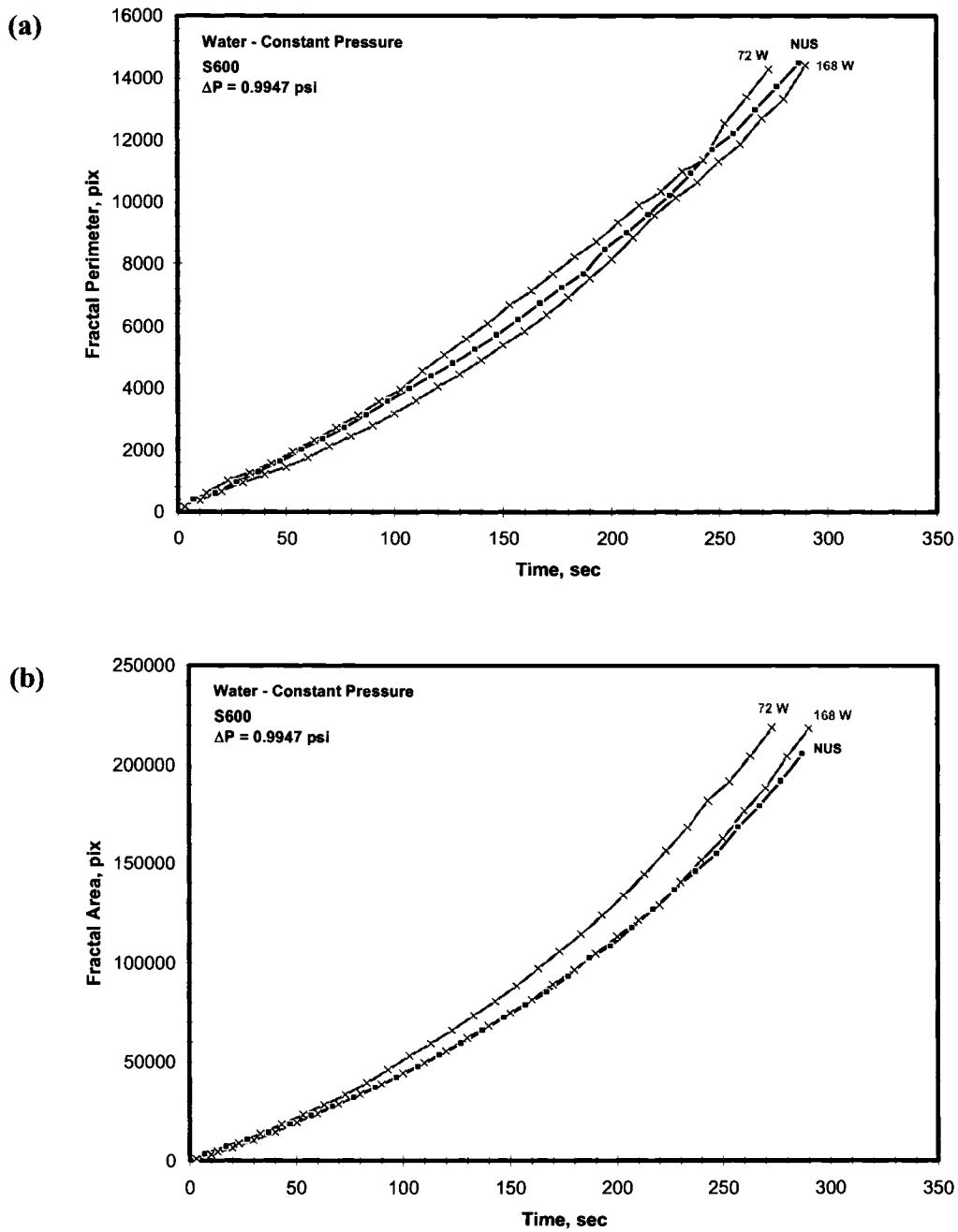


Figure 3-45: (a) Fractal perimeter and (b) fractal area as a function of time for water into S600 at a constant injection pressure of 0.9947 psi. The viscosity and interfacial tension of S600 is 1973 ± 3.2 cp and 38.7 ± 0.8 dynes/cm, respectively. Patterns are shown in Figure 3-44.

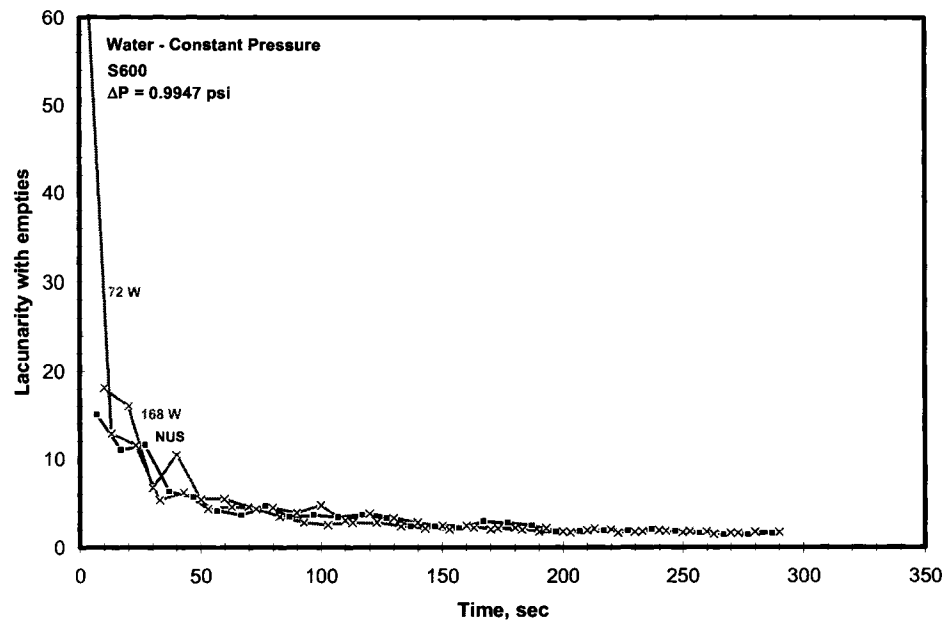
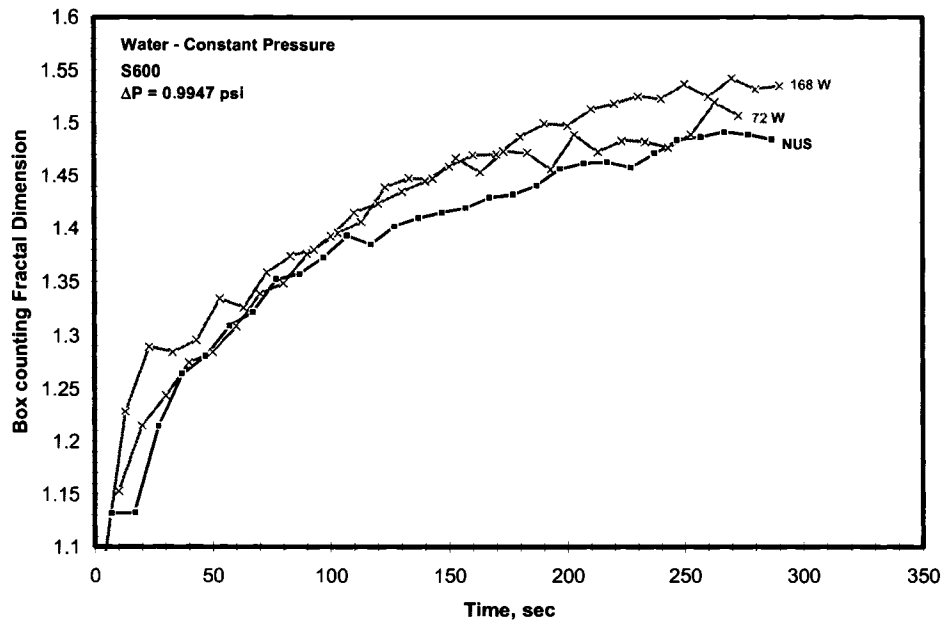


Figure 3-46: (a) Fractal dimension and (b) lacunarity as a function of time for water into S600 at a constant injection pressure of 0.9947 psi. The viscosity and interfacial tension of S600 is 1973 ± 3.2 cp and 38.7 ± 0.8 dynes/cm, respectively. Patterns are shown in Figure 3-44.

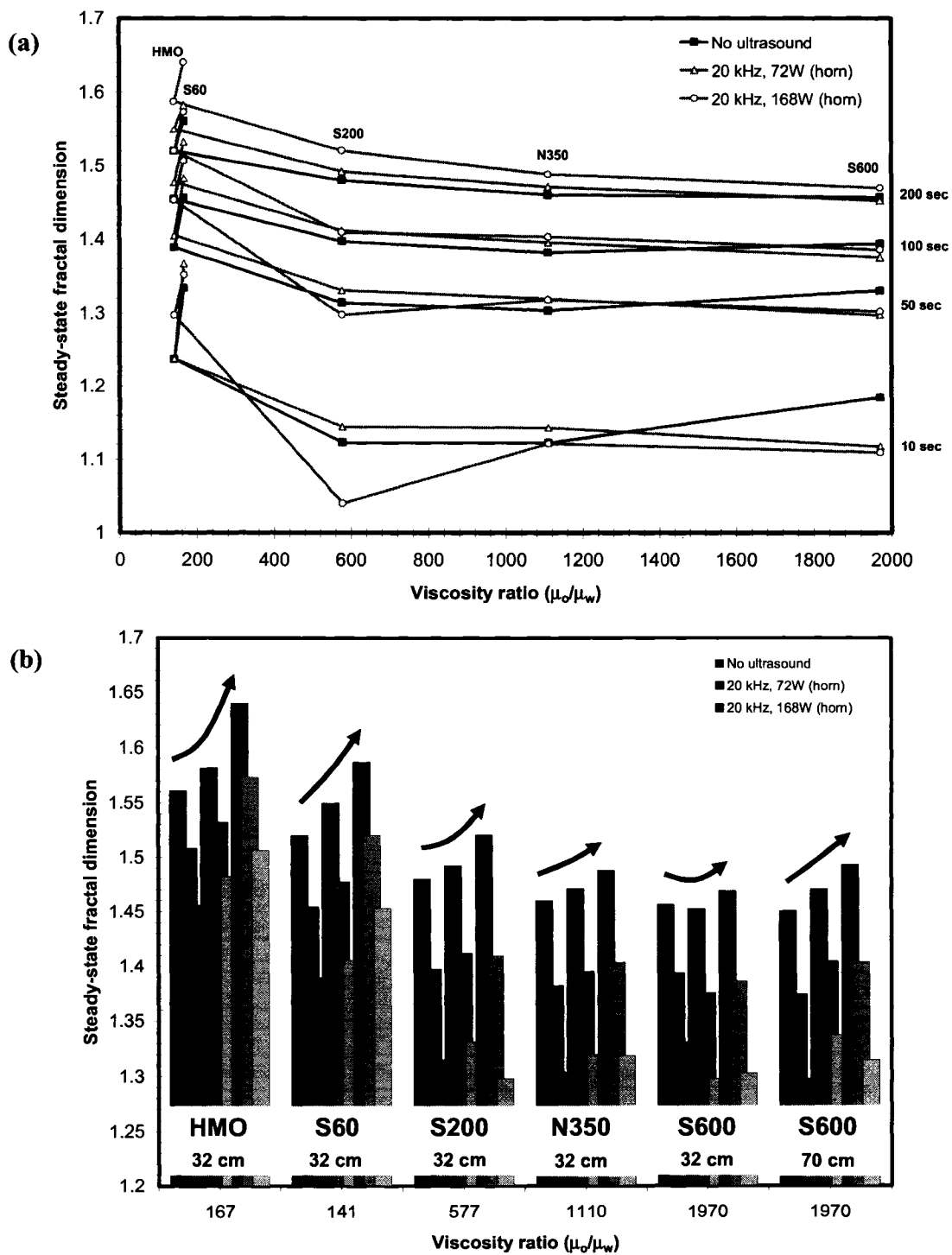
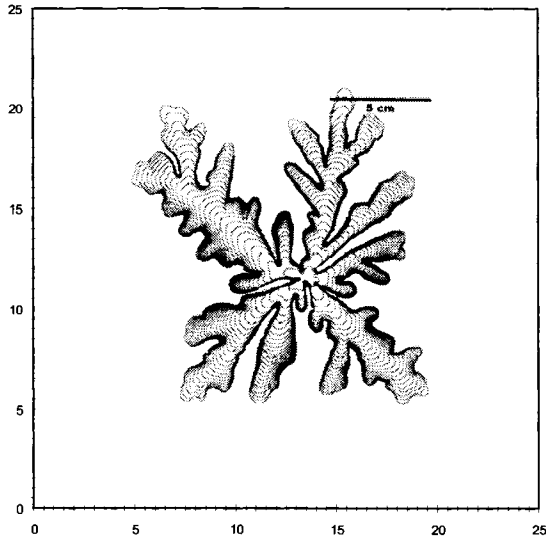
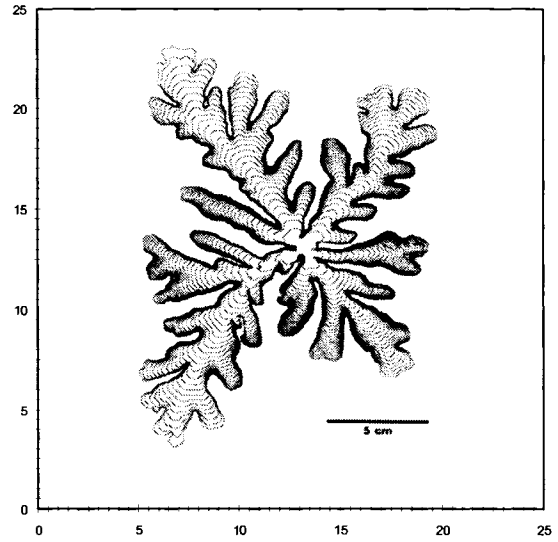


Figure 3-47: (a) Steady state fractal dimension (from logarithmic fit fitted) versus viscosity ratio for various processed mineral oils. (b) Bar chart illustrating the relative change (arrows) of fractal dimension for each processed oil.

No ultrasound



Setting 2 (20 kHz, 72W)



Setting 5 (20 kHz, 168W)

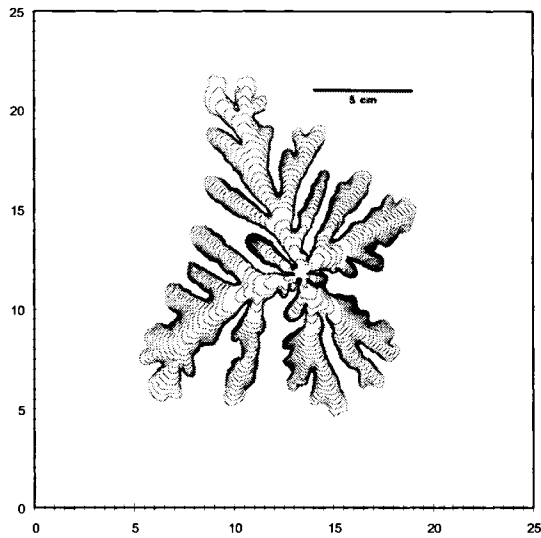
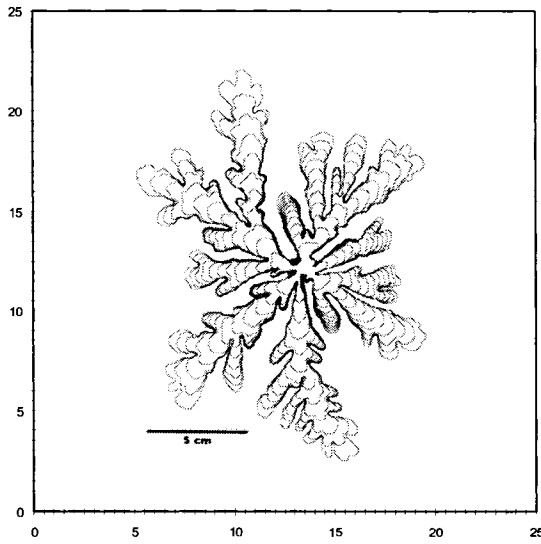
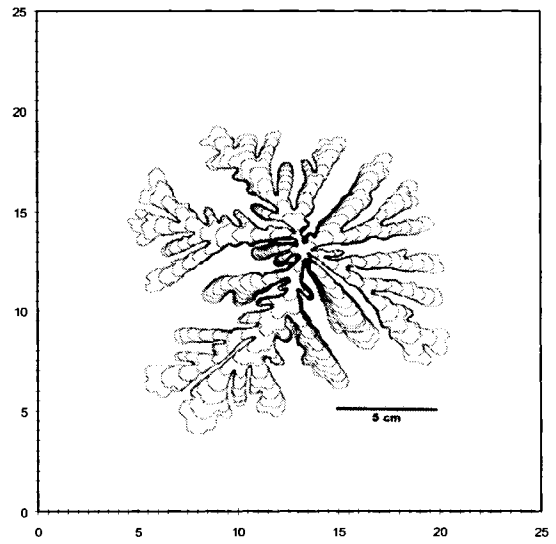


Figure 3-48: Immiscible Hele-Shaw patterns for 3% DOWFAX 2A1 injected into heavy mineral oil (HMO) at a constant head pressure of 0.1421 psi. The viscosity and interfacial tension of HMO is 167.0 ± 1.7 cp and 51.0 ± 1.0 dynes/cm, respectively. The scale is in centimeters. The contours represent the location of the interface at 10 second intervals.

No ultrasound



Setting 2 (20 kHz, 72W)



Setting 5 (20 kHz, 168W)

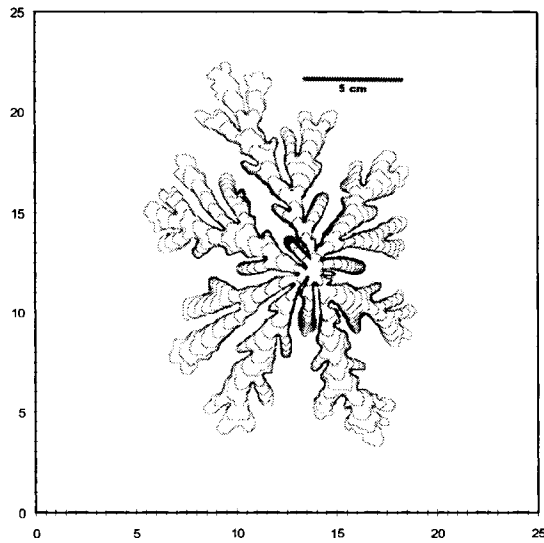
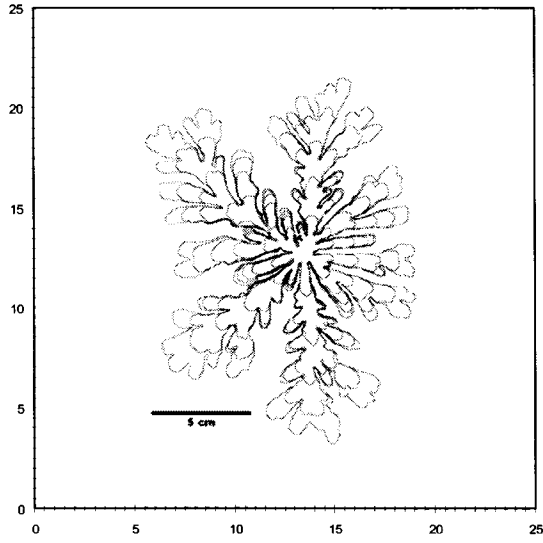
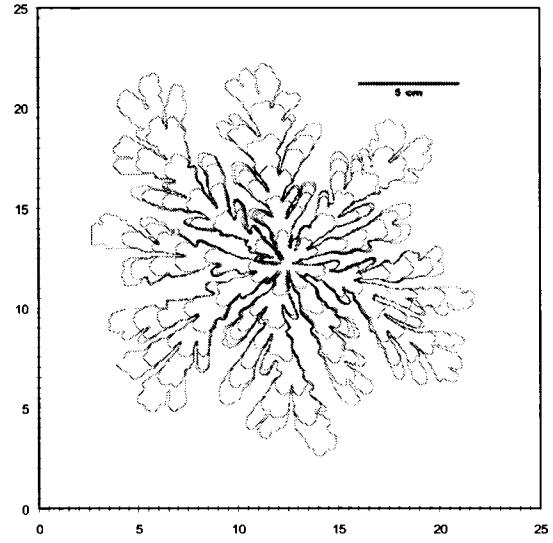


Figure 3-49: Immiscible Hele-Shaw patterns for 3% DOWFAX 2A1 injected into heavy mineral oil (HMO) at a constant head pressure of 0.2373 psi. The viscosity and interfacial tension of HMO is 167.0 ± 1.7 cp and 51.0 ± 1.0 dynes/cm, respectively. The scale is in centimeters. The contours represent the location of the interface at 10 second intervals.

No ultrasound



Setting 2 (20 kHz, 72W)



Setting 5 (20 kHz, 168W)

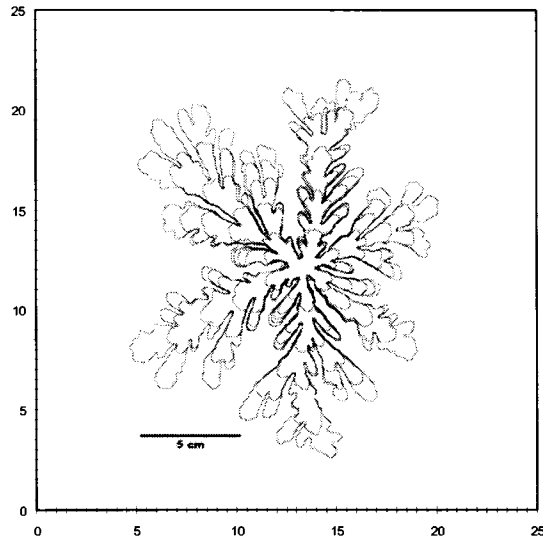


Figure 3-50: Immiscible Hele-Shaw patterns for 3% DOWFAX 2A1 injected into heavy mineral oil (HMO) at a constant head pressure of 0.357 psi. The viscosity and interfacial tension of HMO is 167.0 ± 1.7 cp and 51.0 ± 1.0 dynes/cm, respectively. The scale is in centimeters. The contours represent the location of the interface at 10 second intervals.

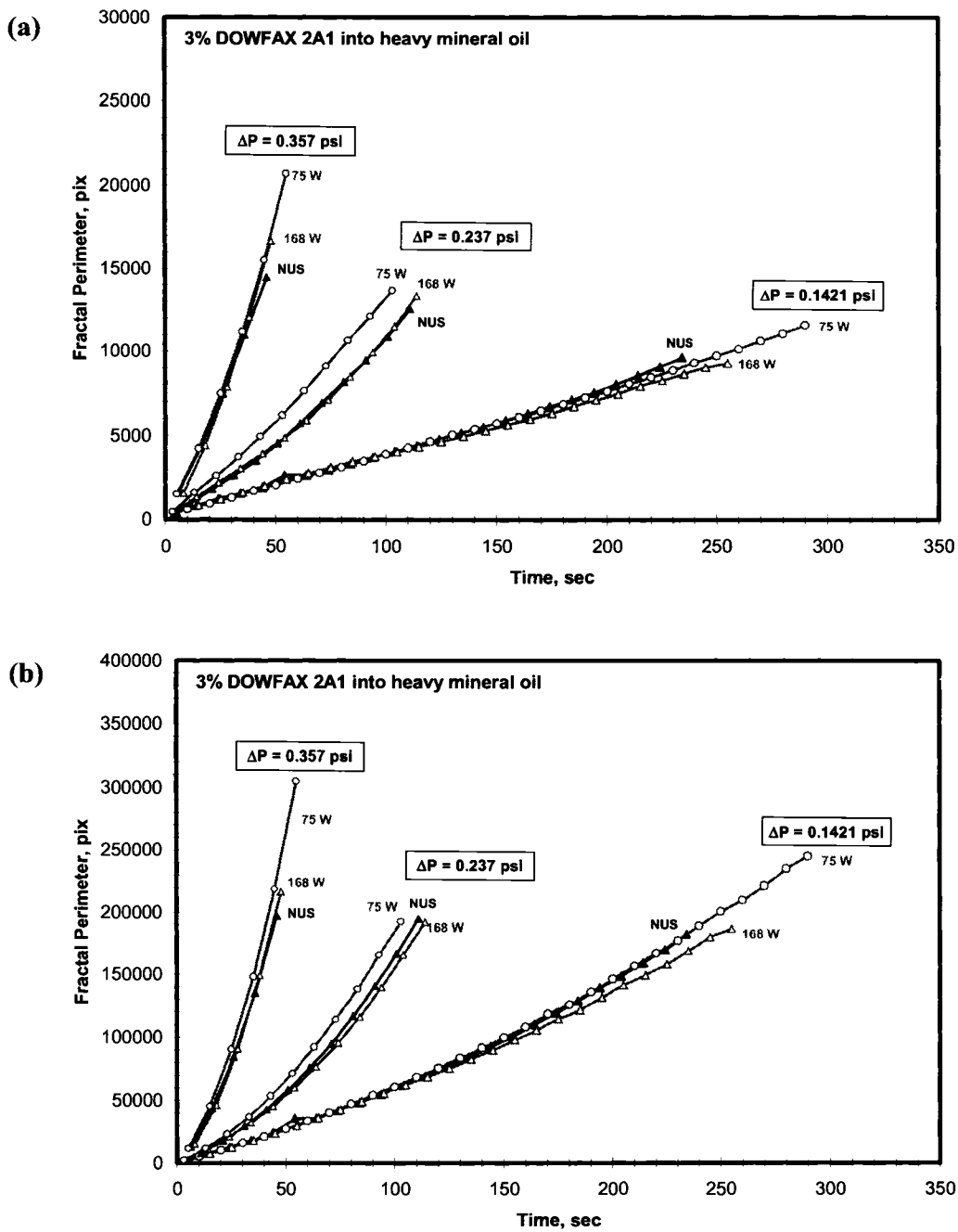


Figure 3-51: (a) Fractal perimeter and (b) fractal area as a function of time for 3% DOWFAX 2A1 into heavy mineral oil (HMO) at three constant injection pressures: 0.1421, 0.237 and 0.357 psi. The viscosity and interfacial tension of HMO (with surfactant) is 167.0 ± 1.7 cp and 10.8 ± 0.2 dynes/cm, respectively. Patterns are shown in Figure 3-48 to Figure 3-50.

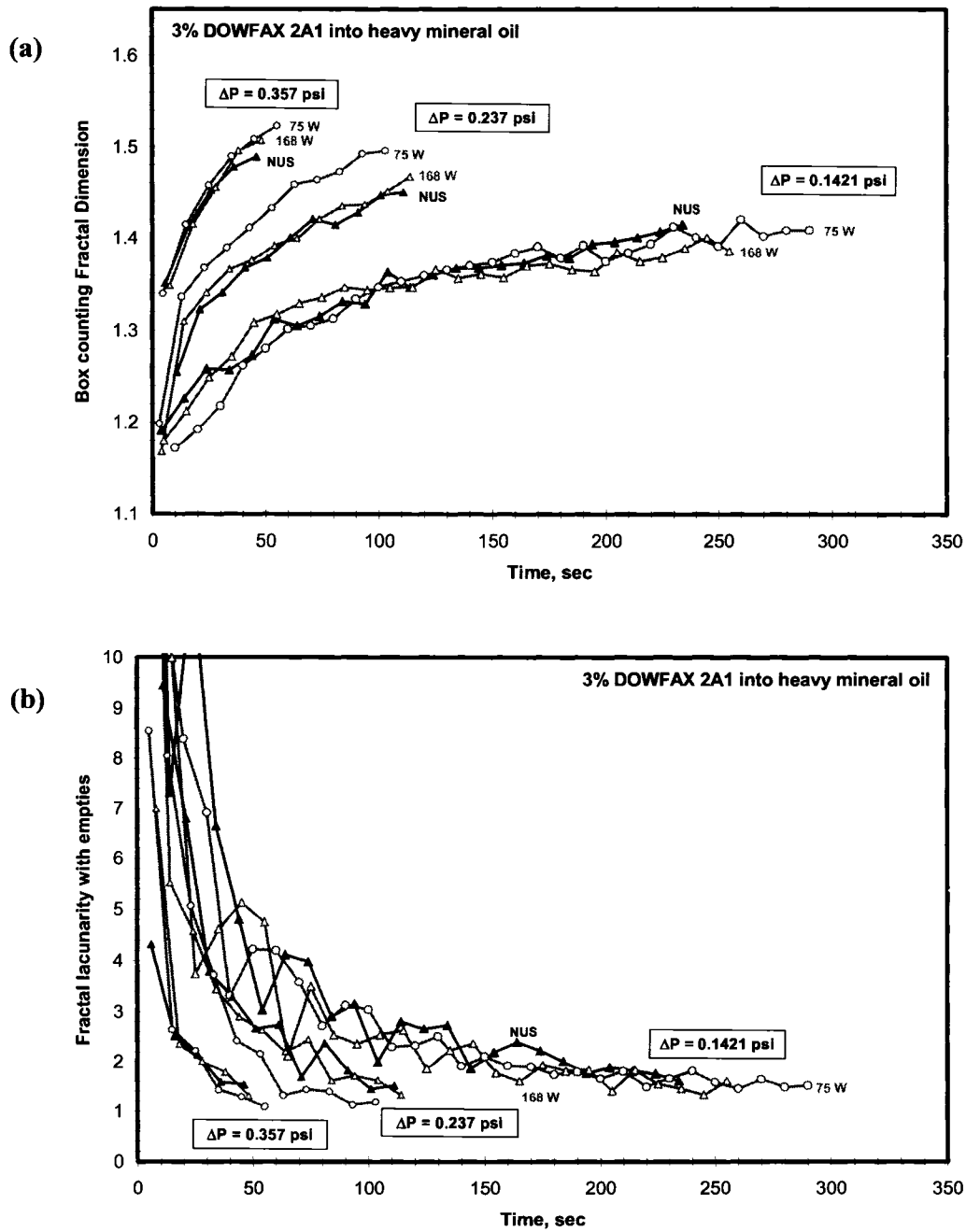


Figure 3-52: (a) Fractal dimension and (b) fractal lacunarity as a function of time for 3% DOWFAX 2A1 into heavy mineral oil (HMO) at two constant injection pressures: 0.1421 psi and 0.235 psi. The viscosity and interfacial tension of HMO (with surfactant) is 167.0 ± 1.7 cp and 10.8 ± 0.2 dynes/cm, respectively. Patterns are shown in Figure 3-48 to Figure 3-50.

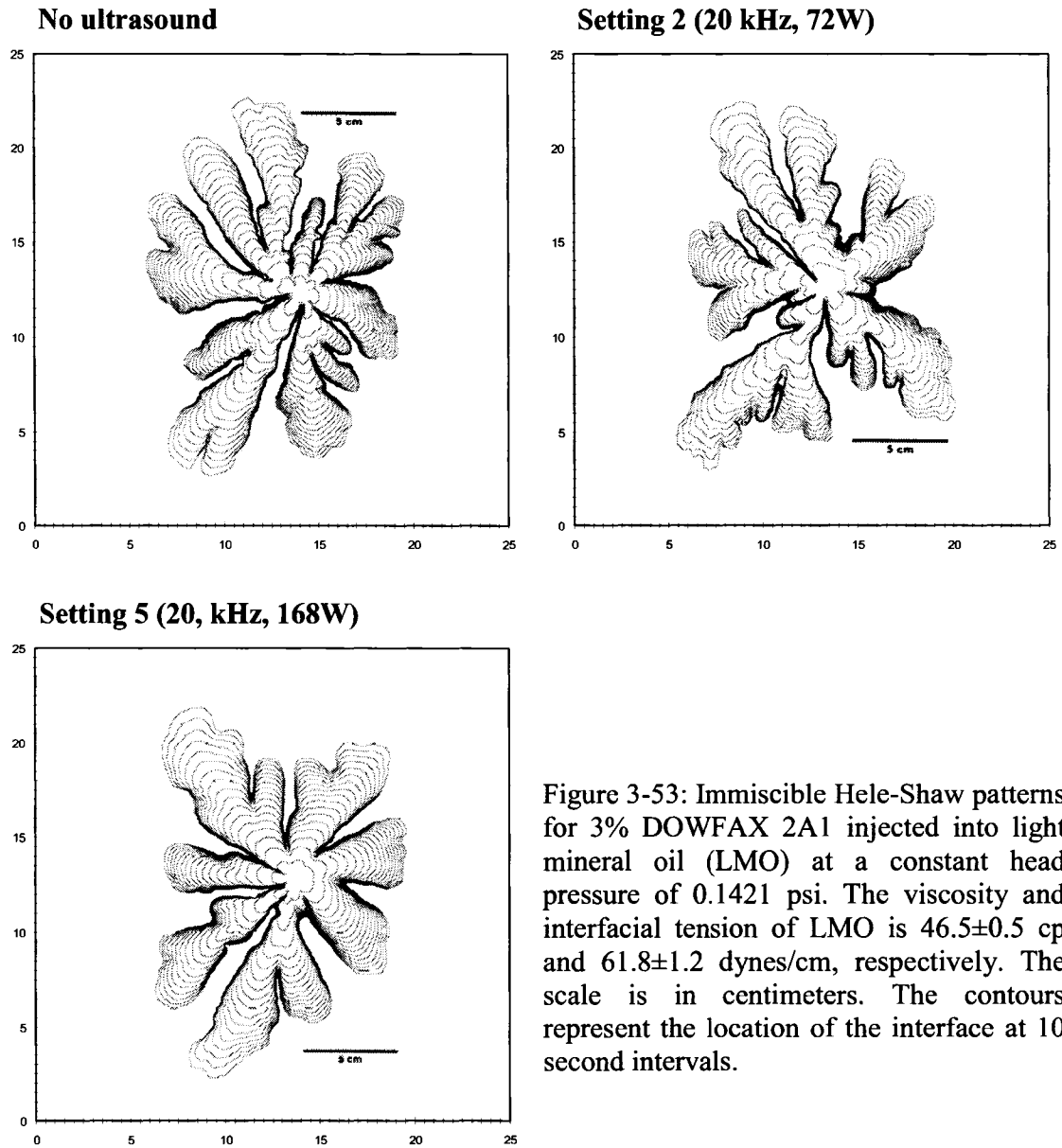
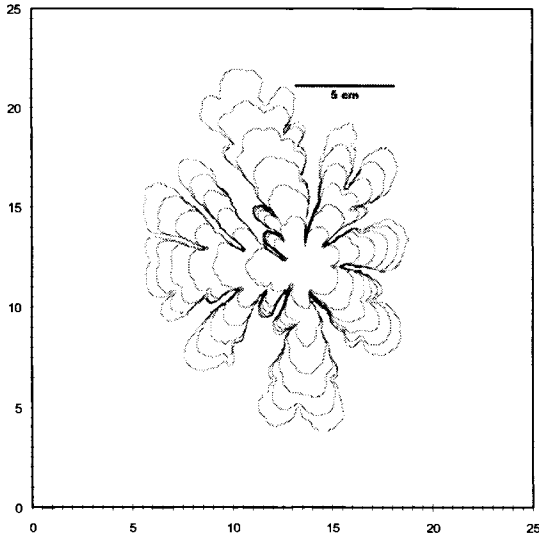
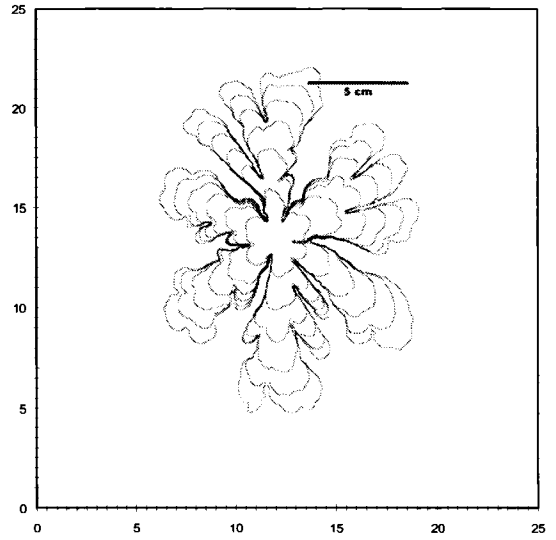


Figure 3-53: Immiscible Hele-Shaw patterns for 3% DOWFAX 2A1 injected into light mineral oil (LMO) at a constant head pressure of 0.1421 psi. The viscosity and interfacial tension of LMO is 46.5 ± 0.5 cp and 61.8 ± 1.2 dynes/cm, respectively. The scale is in centimeters. The contours represent the location of the interface at 10 second intervals.

No ultrasound



Setting 2 (20 kHz, 72W)



Setting 5 (20, kHz, 168W)

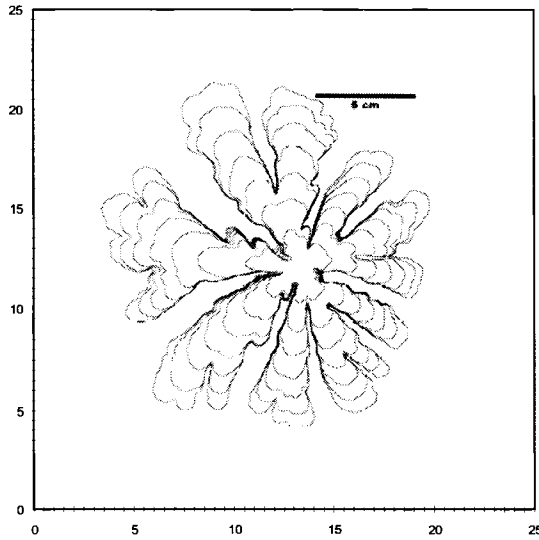


Figure 3-54: Immiscible Hele-Shaw patterns for 3% DOWFAX 2A1 injected into light mineral oil (LMO) at a constant head pressure of 0.235 psi. The viscosity and interfacial tension of LMO is 46.5 ± 0.5 cp and 61.8 ± 1.2 dynes/cm, respectively. The scale is in centimeters. The contours represent the location of the interface at 10 second intervals.

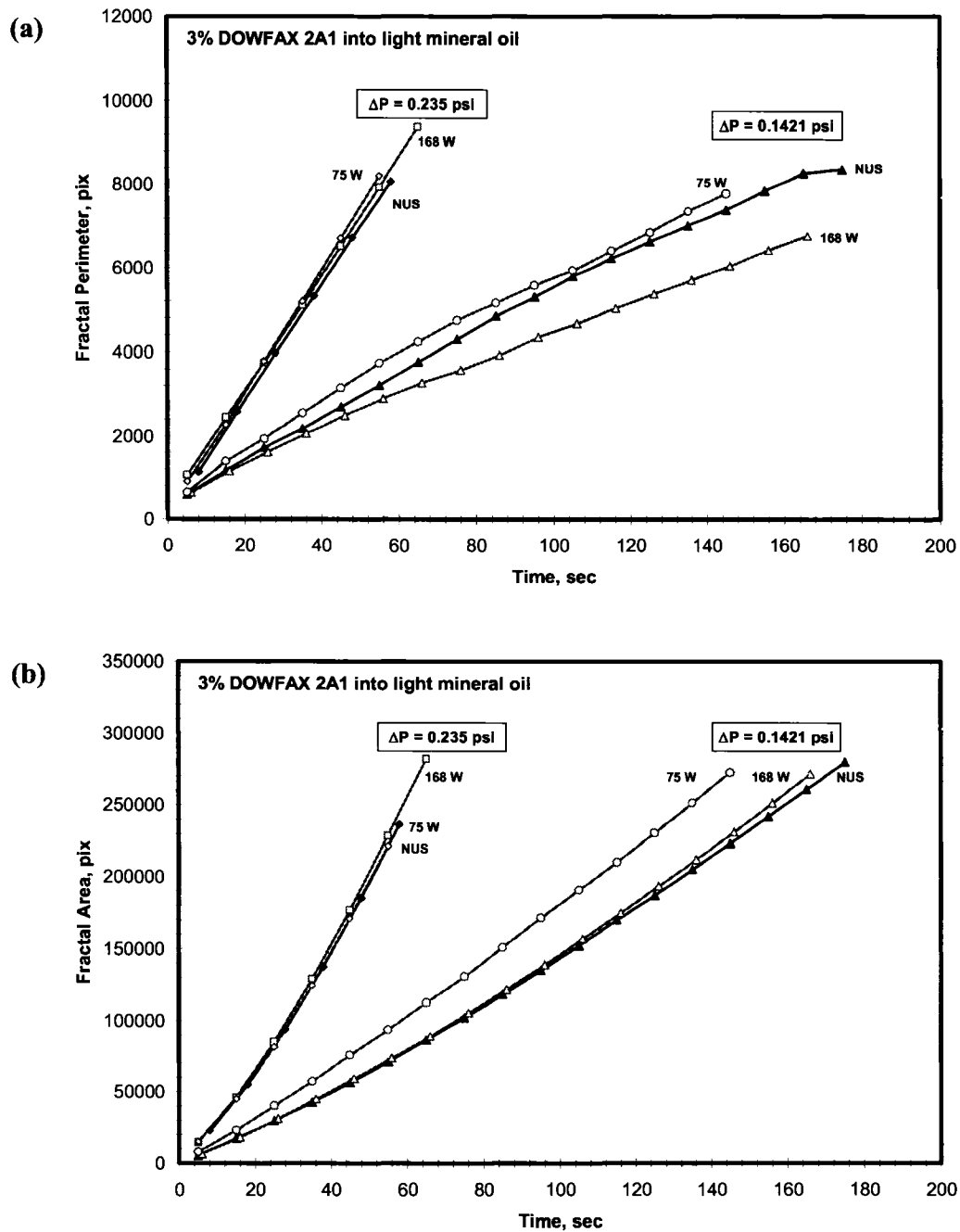


Figure 3-55: (a) Fractal perimeter and (b) fractal area as a function of time for 3% DOWFAX 2A1 into light mineral oil (LMO) at two constant injection pressures: 0.1421 psi and 0.235 psi. The viscosity and interfacial tension of LMO (with surfactant) is 46.5 ± 0.5 cp and 11.2 ± 1.2 dynes/cm, respectively. Patterns are shown in Figure 3-53 and Figure 3-54.

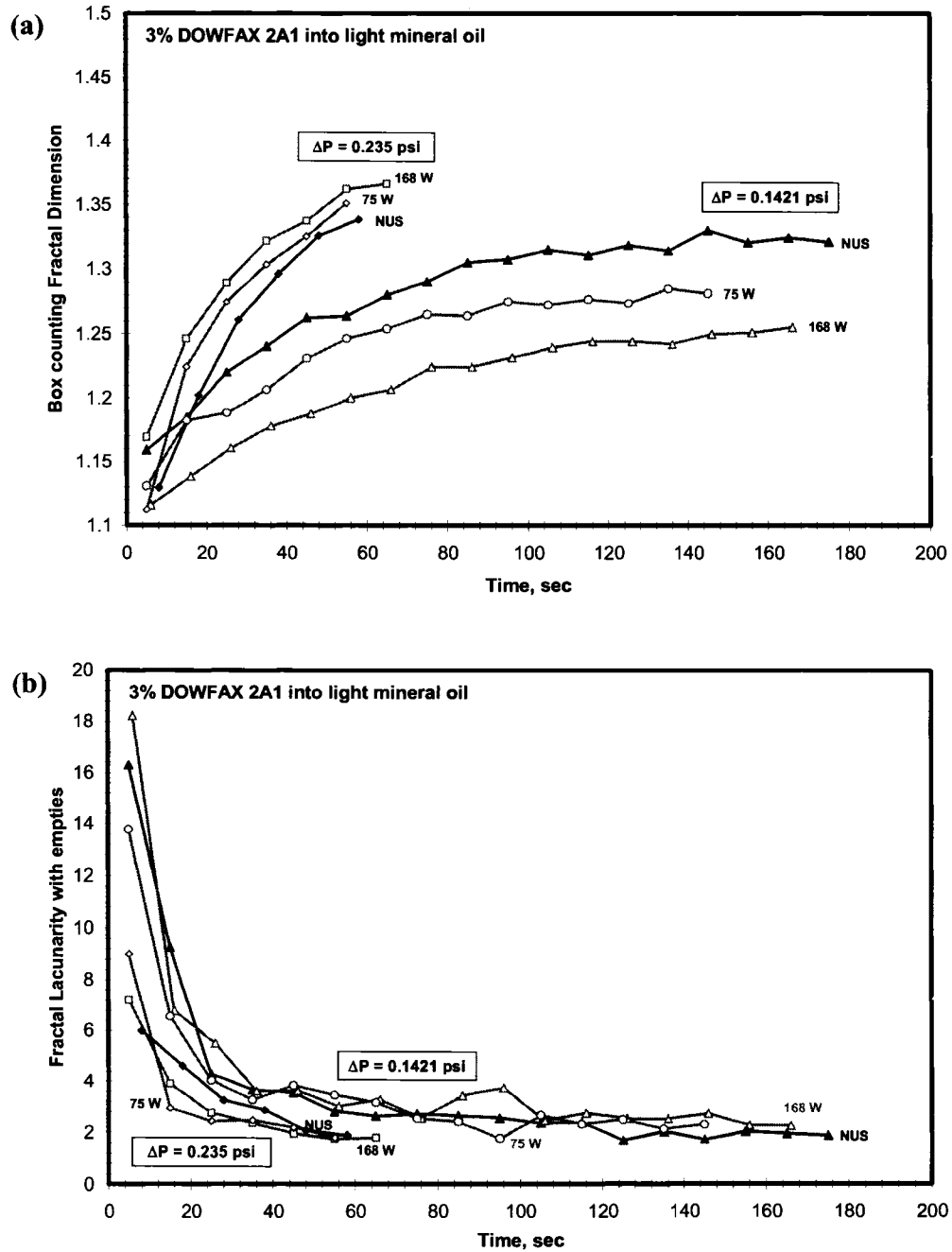
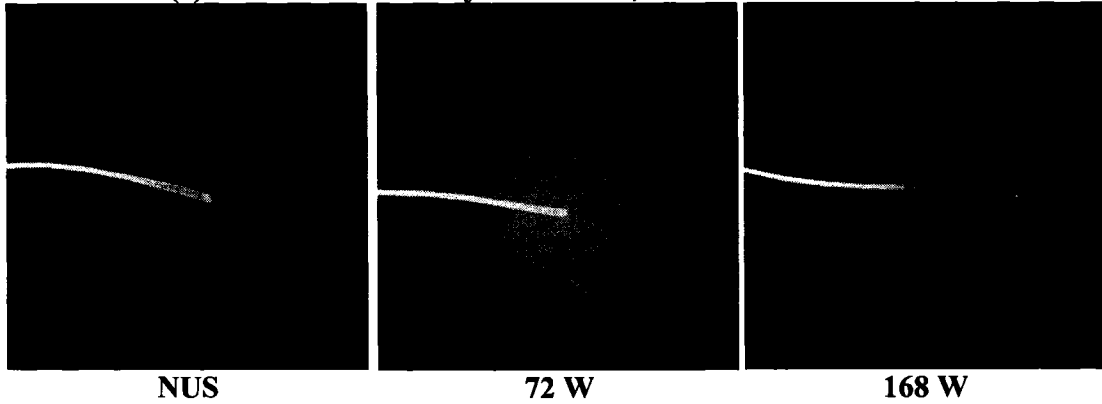


Figure 3-56: (a) Fractal dimension and (b) fractal lacunarity as a function of time for 3% DOWFAX 2A1 into light mineral oil (LMO) at two constant injection pressures: 0.1421 psi and 0.235 psi. The viscosity and interfacial tension of LMO is 46.5 ± 0.5 cp and 11.2 ± 0.2 dynes/cm, respectively. Patterns are shown in Figure 3-53 and Figure 3-54.

(a) Kerosene into heavy mineral oil; Pressure head: 9.5 cm



(b) Kerosene into light mineral oil; Pressure head: 9.5 cm

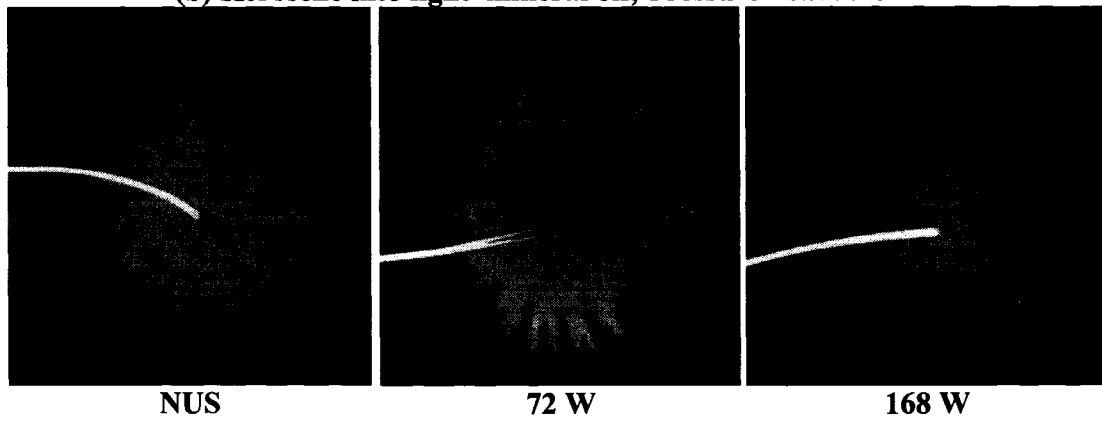
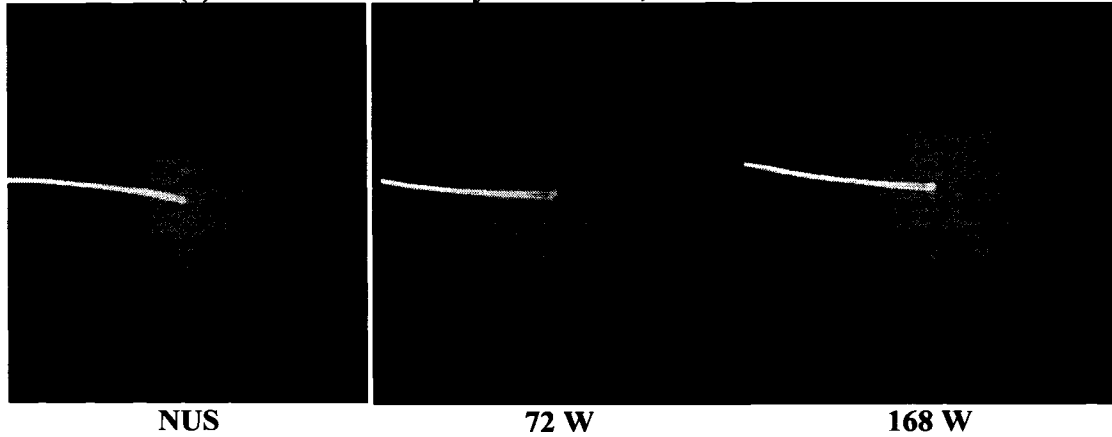


Figure 3-57: Injection profiles of miscible Hele-Shaw experiments, in which kerosene is injected at a constant head of 9.5 cm into (a) heavy mineral oil ($\mu_{\text{HMO}}/\mu_{\text{K}} = 57.6$) and (b) light mineral oil ($\mu_{\text{LMO}}/\mu_{\text{K}} = 16.0$). Two intensities of ultrasound (setting 2 = 72 W, setting 5 = 168 W) were applied to the cells. Patterns are compared to the no-ultrasound case (NUS).

(a) Kerosene into heavy mineral oil; Pressure head: 20 cm



(b) Kerosene into light mineral oil; Pressure head: 20 cm

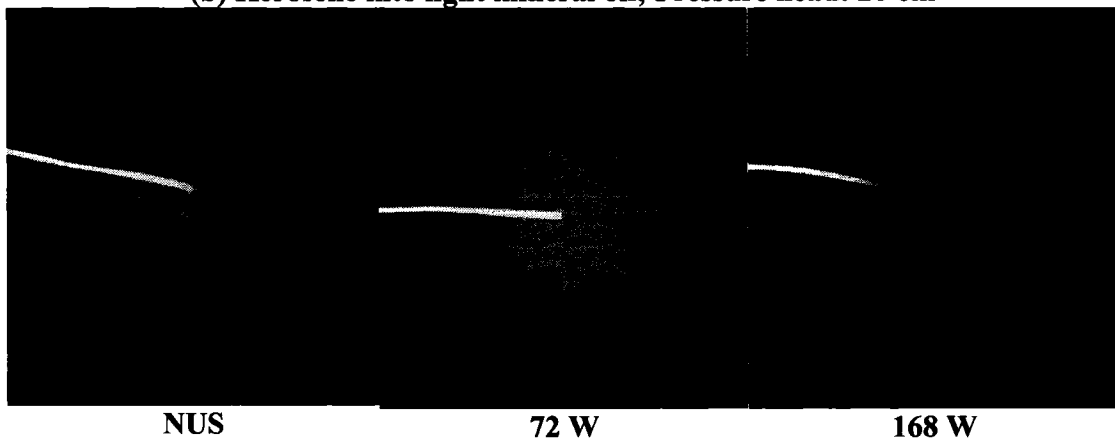


Figure 3-58: Injection profiles of miscible Hele-Shaw experiments, in which kerosene is injected at a constant head of 20 cm into (a) heavy mineral oil ($\mu_{\text{HMO}}/\mu_{\text{K}} = 57.6$) and (b) light mineral oil ($\mu_{\text{LMO}}/\mu_{\text{K}} = 16.0$). Two intensities of ultrasound (setting 2 = 72W, setting 5 = 168 W) were applied to the cells. Patterns are compared to the no-ultrasound case (NUS).

Heptane into light mineral oil; Pressure head: 3 cm

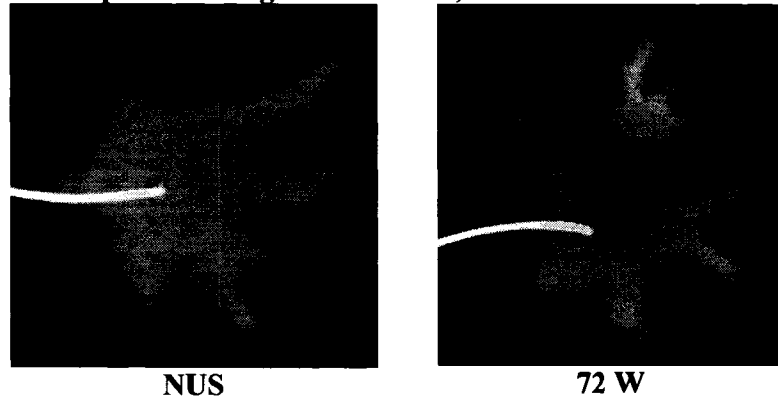
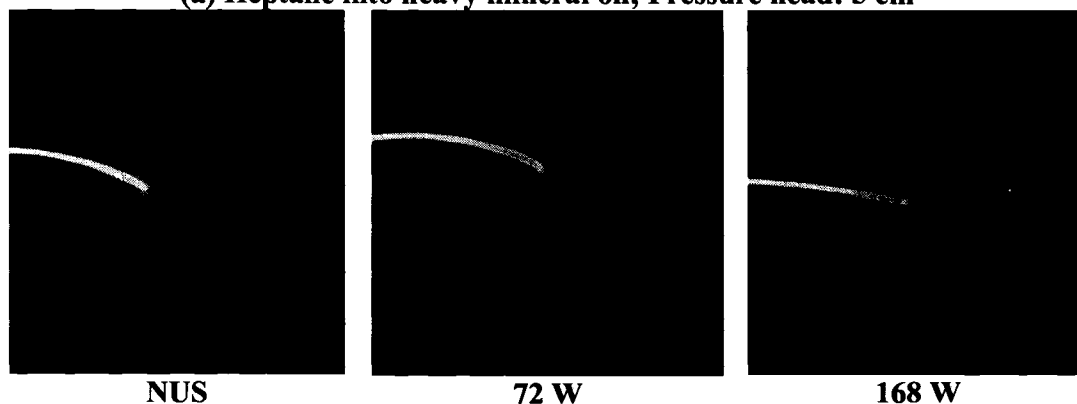


Figure 3-59: Injection profiles of miscible Hele-Shaw experiments, in which heptane is injected at a constant head of 3 cm into light mineral oil ($\mu_{LMO}/\mu_H = 110.7$). Ultrasound at setting 2 (72W) was applied to the cells. The ultrasonically stimulated pattern is compared to the no-ultrasound case (NUS).

(a) Heptane into heavy mineral oil; Pressure head: 5 cm



(b) Heptane into light mineral oil; Pressure head: 5 cm

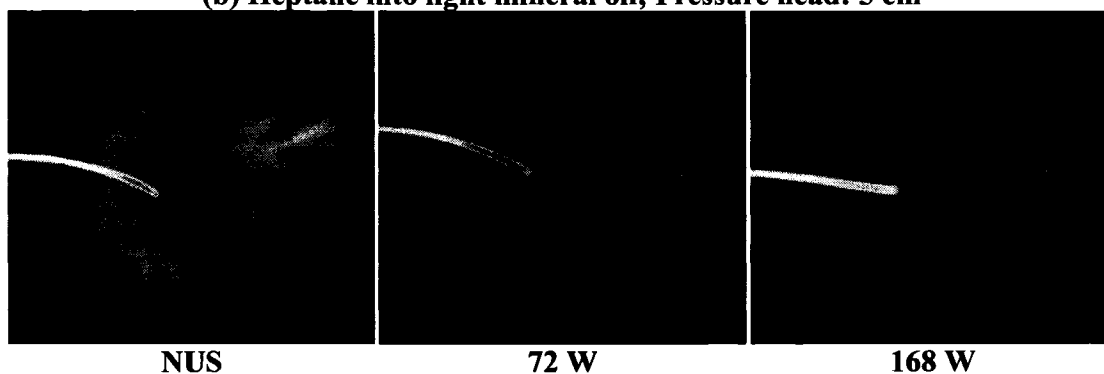


Figure 3-60: Injection profiles of miscible Hele-Shaw experiments, in which heptane is injected at a constant head of 5 cm into (a) heavy mineral oil ($\mu_{HMO}/\mu_H = 397.6$) and (b) light mineral oil ($\mu_{LMO}/\mu_H = 110.7$). Two intensities of ultrasound (setting 2 = 72W,

setting 5 = 168 W) were applied to the cells. Patterns are compared to the no-ultrasound case (NUS).

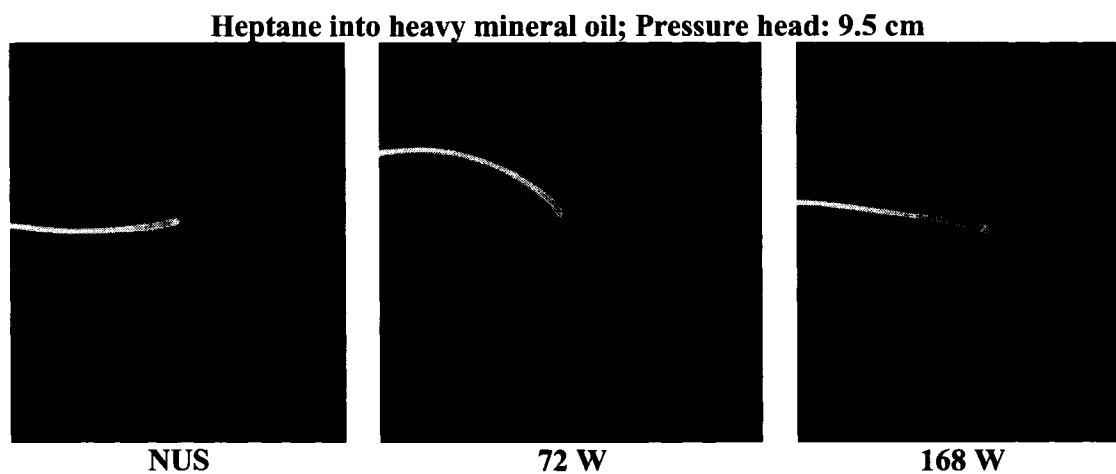
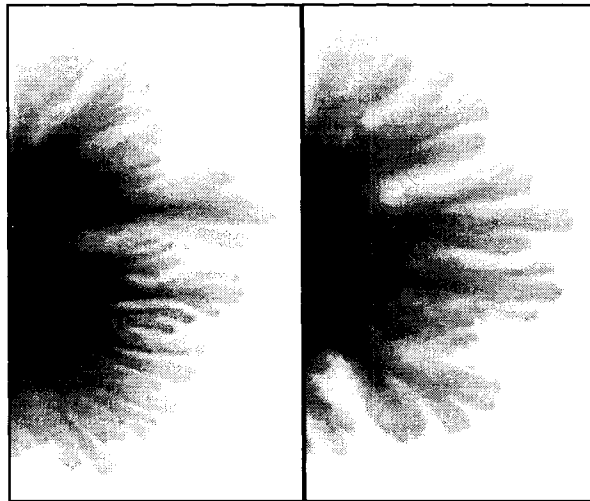


Figure 3-61: Injection profiles of miscible Hele-Shaw experiments, in which heptane is injected at a constant head of 9.5 cm into heavy mineral oil ($\mu_{HMO}/\mu_H = 397.6$). Two intensities of ultrasound (setting 2 = 72W, setting 5 = 168 W) were applied to the cells. Patterns are compared to the no-ultrasound case (NUS).

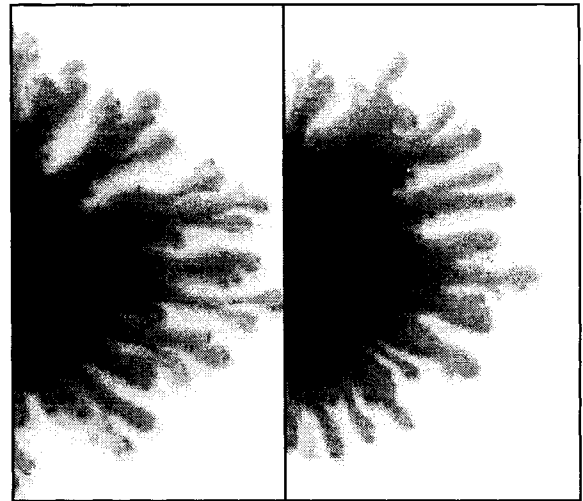
(a) Kerosene into light mineral oil – 1 cc/min



NUS

72W

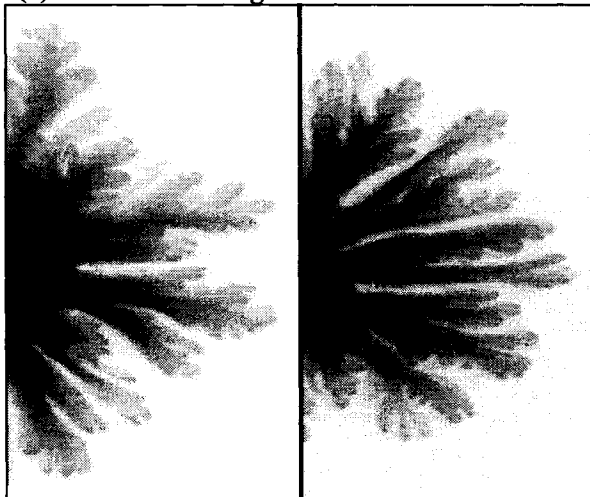
(b) Kerosene into light mineral oil – 5 cc/min



NUS

72W

(c) Pentane into light mineral oil – 5 cc/min



NUS

72W

Figure 3-62: Snap-shots of fully developed fractal patterns for various injected miscible fluids: (a) Kerosene into light mineral oil at a rate of 1 cc/min ($\mu_{LMO}/\mu_K = 16.0$), (b) Kerosene into light mineral oil at a rate of 5 cc/min ($\mu_{LMO}/\mu_K = 16.0$), (c) n-Pentane into mineral oil at 5cc/min ($\mu_{LMO}/\mu_P = 186$). Ultrasound at setting 2 (72W) was applied to the cells. Patterns are compared to the no-ultrasound case (NUS)

4 Spontaneous (Capillary) Imbibition

4.1 Introduction

In this study, a series of capillary imbibition experiments under ultrasound were conducted on sandstone and limestone plugs using a focused ultrasonic horn, as well as an ultrasonic bath. Spontaneous (capillary) imbibition is a gentle, steady process that is based on capillary suction (Zhou, *et al.* 2000; Morrow and Mason 2001). Typical imbibition curves of capillary pressure vs. wetting phase saturation are shown in **Figure 4-1**. Generally, capillary suction relies on both rock properties (matrix permeability, size, pore geometry, wettability, heterogeneity and boundary conditions), and fluid properties (viscosity of the phases and interfacial tension, and may strongly vary with aging and chemical treatment (Viksund *et al.* 1998; Abismail *et al.* 1999; Zhou *et al.* 2000; Morrow and Mason 2001; Fischer and Morrow 2005). Unlike forced imbibition or drainage, spontaneous imbibition benefits from the absence of viscous (and in the case of small core samples, gravitational forces), making it a suitable experiment for highlighting the role of interfacial forces. This is especially true during counter-current imbibition. When interfacial tension is reduced, the role of capillary imbibition is reduced, and buoyant forces become the dominant displacement mechanism.

The oil industry uses spontaneous imbibition to characterize fluid inflow from a fracture into the rock matrix (Leverett 1941; Leverett *et al.* 1942; Graham and Richardson 1959; Mattax and Kyte 1962). For a review of current modeling methods of imbibition, the reader is referred to the works of Cil (1997) and Babadagli *et al.* (2005). Much experimental attention has been paid on characterizing and scaling spontaneous

water imbibition for gas-liquid-rock and oil-water-rock systems (e.g. Reis and Cil 1993; Zhang *et al.* 1996; Kim and Whitesides 1997; Akin *et al.* 2000; Li and Horne 2001; Babadagli 2002; Zhou *et al.* 2002; Li and Horne 2004; Babadagli *et al.* 2005).

During capillary imbibition, the wetting fluid percolates along the grain surface and invades the smallest pores during early times. As a consequence, the non-wetting phase is pushed out of the pore into adjacent sites. An illustration of the capillary imbibition process within pores under co-current and counter-current flow is shown in **Figure 4-3**. In the case of co-current imbibition, oil and water flow in the same direction. In some cases, the “exit” pore throat is too narrow to allow oil drops from penetrating to an adjacent pore (due to capillary and gravitational forces), resulting in oil flowing in the opposite direction of the wetting phase. Such process is dubbed counter-current flow, and can be induced by introducing a no-flow boundary. Various models have been proposed to predict spontaneous imbibition into rock, and in the broadest sense can be classified as diffusive/stochastic and pore-scale percolation (Sahimi 1993). The following information may be extracted from spontaneous capillary imbibition data:

- a) The time at which the first drop of oil is produced: It is still unclear from literature how the initial offset of imbibition recovery relates to fluid and rock properties. We speculate that since dynamic capillary pressure drops with increasing wetting phase saturation (illustrated in **Figure 4-1**), one expects from first principles that the imbibition process will only initiate once the capillary pressure within the pores is less than the hydrostatic pressure of the invading phase. Such process depends primarily on wettability, viscosity and interfacial tension. Earlier onset of imbibition implies a faster rate of penetration of the wetting fluid into the matrix.

- b) Recovery rate depends on the ease by which oil ganglia are mobilized to adjacent pores; i.e. wettability, permeability, viscosity ratio and interfacial tension (Morrow and Mason 2001; Fischer and Morrow 2005). Lower interfacial tension results in lower capillary pressures at the pore throats. As more and more wetting fluid invades the matrix, the capillary threshold within the pore drops, causing further displacement of oil. The initial slope of the recovery profile can be related to an effective capillary pressure using Handy's formula (Handy 1960):

$$Q = \sqrt{\left(\frac{2P_{c,eff}k_w\phi A^2 S_w}{\mu_w}\right)t} \quad 4-1$$

Therefore, the imbibition rate is proportional to the square root of time, with a proportionality constant depending on effective capillary pressure, $P_{c,eff}$, water permeability, k , porosity, ϕ , the surface area of the core, A , the water saturation, S_w , and water viscosity, μ_w .

- c) Final recovery is an indicator of how much residual oil is left behind. Recovery is usually higher when interfacial tension is low, and wettability of the non-oleic phase is high. In the case of long vertical cores, gravity may also affect final recovery (Babadagli 2002).

Recovery rates and final recovery also depend strongly on the nature of the boundary, and consequently the flow conditions within the pores, i.e. co-current or counter-current flow (Mattax and KYTE 1962; Hamon and Vidal 1986; Cil 1997; Babadagli *et al.* 2005).

This chapter will start with a description of the rock and fluid properties, the experimental approach, the experimental set-up, and a brief discussion about errors and repeatability. We will then present results and a thorough analysis and discussion of the data. Finally, we conclude with our results, and suggest further work.

4.2 Experimental Setup

4.2.1 Rock and Fluid Properties

A total of more than 80 cylindrical core plugs were cut from blocks of homogeneous Berea sandstone, and heterogeneous Indiana limestone outcrop samples, and saturated for 48 hours with either mineral oil or kerosene using a vacuum desiccating chamber. Diameters and lengths of the cores were in the range of 2.5 to 2.52 and 6.4 to 7.8 cm, respectively. After cutting the core samples, they were washed with water and dried at 80°C for at least two days, after which they were cooled at ambient conditions. The average permeability and porosity of the sandstone cores was determined to be 300 md and 21%, respectively. The average permeability and porosity of Indiana limestone was determined to be 7 md and 17%. Porosity values were estimated by saturating dry cores in water and oil, and measuring the change in weight. The relative variation in pore-volume between water and oil saturated volumes is approximately 8% (see **Figure 4-2**). This is a good indicator on the clay content of the Berea sandstone samples. In order to avoid such error, it would have been necessary to saturate the cores with brine first, and let the cores be immersed for about 10 days to establish ionic equilibrium between the rock clays and the brine. This was not done, because such method may alter the original properties of the rock, and raise its NaCl content after drying. It was therefore decided to

use the pore volume obtained after saturation with oil, and trust that the relative error is the same for all cores.

All cores with the exception of air-water experiments were used only once to avoid undesirable alterations in wettability and grain structure due to contamination, cleaning, and matrix damage generated by ultrasonic vibrations. For air-water spontaneous imbibition, we reused the same cores to minimize the error due to clay swelling. Water saturated cores were dried in an oven at 80°C for one day. Some of the samples were coated with epoxy from all sides except one of the ends to obtain truly counter-current imbibition (**Figure 4-3**). Such experiments will be labeled as “coated”.

The imbibition behavior of three types of saturation fluids was studied: light mineral oil, kerosene and air. To cover a broad range of viscosity, density, interfacial tension, and wettability cases, solutions of water, brine (15,000 and 150,000 ppm NaCl), anionic surfactant (Sodium Dodecyl Diphenyloxide Disulfonate, DOWFAX 2A1), non-ionic surfactant (Alcohol Ethoxylate, Tergitol 15-S-7) and polymer (Xanthan Gum) were prepared as the aqueous phase. A flow chart of the experimental strategy is shown in **Figure 4-5**. The properties of the fluids and corresponding absolute error at standard conditions (no ultrasound) are presented in **Table 4-1** and **Table 4-2**. Surfactant properties are tabulated in **Table 4-3** and **Table 4-4**. The interfacial tension and surface tension between aqueous and oleic phase was measured using a standard tungsten ring tensiometer (the Du Nouy method). Viscosity values were either measured using a rotational viscometer, or were obtained from the manufacturer (Canon Instruments). Density was determined by weighing a syringe filled with 5 cm³ of fluid. To avoid ultrasonic cavitation close to the core walls, all solutions were carefully de-aerated in

vacuum. We noticed that the effect of cavitation is more severe during air-water experiments, because bubbles block the pores at the outer wall of the core plug.

Reduction of interfacial tension was achieved by adding different volumes of anionic and nonionic surfactant to de-aerated water. The critical micelle concentration (CMC) of DOWFAX 2A1 (anionic), DOWFAX 3B0 (anionic) and Tergitol 15-S-7 (nonionic) was measured to occur at a concentration of about 1 wt%, 3 wt% and 0.0039 wt%, respectively. **Figure 4-6** shows a graph of aqueous surface tension and interfacial tension to mineral oil vs. Tergitol 15-S-7 concentration at standard atmospheric conditions. **Figure 4-7** presents the aqueous surface tension and interfacial tension to mineral oil vs. DOWFAX 2A1 and DOWFAX 3B0 concentration at atmospheric conditions.

Xanthan gum polymer concentrations of 0.03, 0.05, 0.09, 0.1 and 0.15 wt% were applied to increase the viscosity of the aqueous solution. Brine solutions of de-aerated water with 15,000 and 150,000 ppm NaCl were mixed to explore the effect of alkalinity on spontaneous imbibition, especially in high clay-content Berea sandstone.

We applied an oil based coloring agent to both kerosene and mineral oil to distinguish the two phases. Such dye, although applied at very low concentrations, may change the wettability characteristics of the cores slightly. This effect is assumed to be the same for all samples, and therefore, should not considerably contribute to the observed variations.

4.2.2 Experimental setup

The experimental setup is shown in **Figure 4-8**. Cores were placed inside imbibition tubes with a graduated cylinder allowing volume measurements with a precision of ± 0.1

cc. A homogeneous ultrasonic field was generated using a bench-top Branson ultrasonic bath (cleaner) operating at 40kHz and 2kW. To investigate the effect of concentrated sonication, we also employed an ultrasonic horn capable of generating a frequency of 20 kHz and power up to 250 W/cm². The horn was equipped with a 3/4 inch sapphire coated titanium tip, which was calibrated calorimetrically to correspond to the wattage reading from the generator. In fact, the wattage reading from the generator displays the required electrical power to drive the transducer at a particular displacement amplitude. To ensure consistent insonication, we made sure that all experiments were run at the same power settings. **Figure 4-9** illustrates the relationship between power setting and the transducer excitation amplitude. Generally, Setting 2 and Setting 5 correspond to 25 W and 48 W, respectively.

The temperature within the ultrasonic bath increases with exposure time due to the high power output of the horn. This increase may influence the experimental results slightly by reducing the viscosity and interfacial tension of the fluids. A plot of bath temperature versus time for two power settings is shown in **Figure 4-10**. We observed that temperature increases quasi-logarithmically with time. In a period of 750 minutes, the temperature within the ultrasonic bath rose by 5 °C for Setting 2 [LO], and by 8 °C for Setting 5 [HI] intensity. Expansion of the pores and alterations of fluid properties due to this temperature change is therefore negligible. Nonetheless, we decided to add a water circulation system to maintain room temperature during experiments requiring an extended period of time.

Since all samples were positioned equidistantly from the horn, and made use of the same imbibition cells, attenuation due to the carrying fluid and the imbibition cells is

believed to be minor. Each experiment was repeated with and without ultrasound (control experiment using similar core from the same block). The relative performance between the ultrasonically stimulated performance and the control was then compared and analyzed.

4.2.3 Procedure

Dry cores were placed within a desiccator filled with the oleic phase, and allowed to saturate under vacuum for 2 days. After saturation, cores were weighed and placed in the imbibition cell. After securely sealing the cell with a rubber stopper, the aqueous phase was slowly introduced via a funnel. The oil recovery was monitored versus time with and without ultrasound. Ultrasound was applied at two intensities: 25W [Setting 2] and 48W [Setting 5]. Occasionally, the cores were weighed using a string attached to a portable scale (via a hook) to verify that the volumes measured from the graded imbibition tube match the change in weight due to fluid influx. In some of the surfactant experiments, we observed a stable emulsion (**Figure 4-11**), which slightly increased the measured volume of produced fluid. In such case, volumes were corrected from the weight of the cores. Error in recorded volume is approximately $\pm 2\%$. For every reading, the cores were carefully shaken to liberate any oil drops that remained attached to the core wall. On average, the volumes obtained by weighing the cores agree with the volumetric recording to approximately 3% accuracy.

For air-water spontaneous imbibition experiments, high precision Scout Pro scales were used to measure water influx into core samples. Core samples were suspended via a stainless wire into an ultrasonic bath, and the resulting change in weight due to water in-flux was measured at intervals of 5 seconds. The resulting data was then transferred

into an Excel sheet using a Labview data acquisition system. Pore volume measurements were performed by vacuum saturating all cores with water for 2 days.

4.3 Results and Discussion

A cross-correlation comparison plot of final recovery without ultrasound vs. final recovery with ultrasound for all spontaneous imbibition experiments is shown in **Figure 4-12**. The solid 45° line represents the case when the response of capillary imbibition under ultrasound equals that of the control (NUS). Dashed lines at 5% increments indicate the percent deviation from the control. It can be seen that ultrasound significantly enhanced the spontaneous imbibition recovery of oil for most fluid pairs (25 runs). Only 8 experiments yielded a reduction in recovery when ultrasound was applied. Recovery changes within $\pm 5\%$ should be considered as unchanged, because they fall within the nominal error discussed previously. This section will present the results of each fluid pair, and discuss possible origins of the observed behavior.

4.3.1 Water into dry core samples

4.3.1.1 Berea sandstone

Both the recovery rate and final recovery for counter-current air-water imbibition into Berea sandstone (**Figure 4-13**) was significantly enhanced under ultrasound, yielding an additional recovery of up to 10% PV. The opposite was true for co-current imbibition, reducing the ultimate recovery by 5% PV while leaving the recovery rate unchanged.

4.3.1.2 Indiana limestone

A similar response was noticed with air-water imbibition into less water-wet limestone (**Figure 4-14**). The recovery from co-current spontaneous imbibition of water into dry limestone was reduced for both the ultrasonic bath and under ultrasound from the horn. It appeared that the reduction was more significant with the ultrasonic bath (40 kHz) than with the ultrasonic horn (20 kHz), implying a frequency dependence during the process. Higher frequency ultrasound may be more effective at mobilizing air bubbles within the core. Recovery rate remained unchanged. The opposite was observed during counter-current imbibition of water into limestone. Here, recovery is progressively improved with frequency, yielding an additional recovery of up to 7% with the ultrasonic horn. The recovery from the ultrasonic bath was comparable to the control case.

4.3.1.3 Discussion

The apparent dependence on the displacement process (boundary), as well as on frequency, is primarily due to the high density contrast and surface tension between air and water. In the case of co-current displacement, the absence of boundaries facilitates bubble migration outward from the center, with a preferential upward flow (**Figure 4-15**).

Water influx is from all sides, and initially fastest at the bottom end. Although strongly wettability-driven, the process is also influenced by buoyancy. On the other hand, during counter-current imbibition with only one end open to flow, air is forced to migrate opposite to the buoyant force (**Figure 4-16**). Therefore, such process is predominantly capillary driven, generating a “piston-type” displacement front. Capillary forces must overcome the buoyant forces, resulting in water moving upward, and air moving downward.

The relative magnitude of the dominant forces changes in the presence of ultrasonic radiation. One of the possible mechanisms behind the enhancement or reduction in recovery under co-current and counter-current spontaneous imbibition is due to air bubble vibration and streaming. Bubbles strongly affect the acoustic properties of liquids due to the large contrast in compressibility and viscosity of the gas and liquid. Predominant features in a liquid with bubbles are high dispersion and low sound speeds over a wide range of frequencies. Bubbles trapped in porous media may oscillate with ultrasound, and absorb most of the ultrasonic energy (Herskowitz *et al.* 1999; Herskowitz *et al.* 2000). For co-current spontaneous imbibition under ultrasound, bubble vibrations within the pore generates an oscillating pressure field, which is out of phase with the liquid vibration. Such process prevents bubbles from migrating into adjacent pores, and therefore reduces both the percolation rate, as well as the final recovery. On the other hand, for counter-current imbibition with only the bottom end subjected to the aqueous phase, the piston-like displacement front creates a stable interface between air and water, and only residual air trapped in pores oscillate under ultrasound. As observed by Aarts *et al.* (1999), compressibility of the fluids within porous media has a strong influence on net

induced flow caused by transversal wave deformations of the pore-walls. Higher density contrast yields to enhancement in induced fluid flow. Such effect is magnified with fluid pairs that have high interfacial tension, because deformations in pore-walls cause fluctuations in capillary pressure. As a consequence of the counter-current nature of the displacement, the vibrational energy applied on the residual bubbles may improve air mobilization (slip effect), and accelerate the percolation process. In the case of limestone, which is less water wet, the rate of water invasion is reduced and the water film along pore walls is thinner. Consequently, less air is trapped in pores, and both the effect of bubble oscillation and capillary pressure are suppressed. Although we observe the same imbibition trend, with decreasing production at different frequencies of ultrasound for co-current flow, and increasing production for counter-current flow, the overall response is not as extreme as for water-wet sandstone.

Additionally, unlike limestone, the rate of recovery for counter-current imbibition into sandstone is dramatically improved. We speculate that such recovery rate improvement is due to a positive enhancement due to water wettability. For highly water-wet sandstone, the rate of water invasion is high, resulting in more pronounced water films along pore walls. Interactions between such water films, and resonating air bubbles may yield more effective air mobilization.

4.3.2 Water and brine into mineral oil and kerosene

4.3.2.1 Water

Figure 4-17 shows the imbibition recovery performance of water into Berea sandstone, saturated with either light mineral oil or kerosene. Both co-current (**Figure 4-17-a**) and

counter-current (**Figure 4-17-b**) boundary conditions were investigated. When all sides are open to flow, we observed an improvement in recovery rate with both light mineral oil and kerosene. The final recovery for light mineral oil improved by an incremental 20% PV as compared to the control experiment, while the recovery of kerosene remained relatively unchanged. For the counter-current boundary condition, on the other hand, the recovery under ultrasound deteriorated for both light mineral oil and kerosene. In fact, while both recovery and recovery rate for light mineral oil remained unaltered under ultrasound, the recovery performance of kerosene depreciated dramatically by over 22% PV.

When the mineral oil–water control sample was introduced to the ultrasonic field, we observed an additional 4% incremental recovery (tertiary recovery), while the production from the kerosene control remained unchanged. On the other hand, after turning off the ultrasound for the counter-current kerosene sample, we observed a dramatic jump in production, which stabilized at the final recovery value obtained from the control. The differing results observed under counter-current and co-current imbibition for kerosene and light mineral oil may be due to the dissimilar wettability properties to silicates, as well as the difference in interfacial tension. During co-current displacement, such difference manifests itself in the formation of surface films and ganglia coalescence. Light mineral oil, having an interfacial tension of 61.8 dynes/cm, does not easily coalesce in the presence of water when no ultrasound is applied. Under an ultrasonic field, however, coalescence of ganglia is enhanced due to Bjerknes forces, resulting in a higher ultimate recovery. Since kerosene has a lower interfacial tension than light mineral oil, the effect of ultrasonically induced coalescence is less pronounced,

resulting in a similar ultimate recovery as with the control case. The enhancement in recovery rate for both kerosene and light mineral oil can be explained by the fact that surface films, which are preventing the mobilization of oil droplets into neighboring pores, are destroyed by ultrasound. It must be noted that the effect of clays in Berea sandstone (>3%) may also influence the relative performance of the fluid pairs under ultrasound. Ultrasound may mobilize clays or reduce clay swelling, resulting in an increase in water inflow and oil expulsion.

4.3.2.2 Brine

In order to eliminate the effect of clay swelling, we ran a series of experiments with brine at two concentrations of NaCl; i.e. 15,000 ppm and 150,000 ppm NaCl aqueous solutions. **Figure 4-18** presents recovery curves for brine imbibition into Berea sandstone saturated with light mineral oil. In the case of 15,000 ppm NaCl brine solution, we investigated the effect of two different intensities on the imbibition process. The control experiment (non-ultrasonic, NUS) recovered 35% OIIP at a rate of 0.06% per minute. Ultrasound at setting 2 did not dramatically alter the recovery rate, but increased the ultimate recovery by an additional 10% OIIP. Ultrasound at setting 5 yielded an improvement in final recovery up to and additional 9% OIIP. It can be concluded from these results that the final recovery is proportional to the ultrasonic intensity applied, while the recovery rate is relatively unaffected by ultrasonic vibrations. One possible mechanism responsible for this additional recovery is the generation of a more stable displacement front due to pore vibrations and localized pressure perturbations, leaving less oil unswept during the process. On the other hand, when we swapped the cores, so that the un-sonicated control cores were subjected to ultrasound and the ultrasonically stimulated cores were removed from the ultrasonic field, no considerable increase in recovery was observed. Therefore, ultrasound did not effectively mobilize oil once it was trapped in the pores. It can be concluded that ultrasonic vibrations assist in the dynamic process of mobilizing trapped oil blobs, but does not serve as an effective means to improving recovery after water imbibition.

Raising the salinity of brine to 150,000 ppm NaCl had a considerable impact on the performance of ultrasonically stimulated imbibition. From **Figure 4-18**, it can be seen

that an increase in salinity improved both the recovery rate and the final recovery of the process, resulting in up to 15% PV improvement in final oil recovery, compared to 15,000 ppm NaCl brine. Introducing ultrasound to highly saline brine resulted in an additional 20% improvement, resulting in a final recovery of 63% OOIP. This improvement is primarily due to the reduction in the effect of clay within the Berea sandstone. Fine clay particles may influence the liquid-liquid interactions within pores. Clay particles absorb the imbibing water, reducing the water mobility within the pores. Lower water invasion results in reduced oil mobilization. Swollen clay may also act to considerably dissipate the ultrasound. Meanwhile, the absence of swollen clay particles at high salinity, improves water invasion into pores, resulting in better migration of oil droplets, and possibly improved coalescence.

In fact, after aging samples in light mineral oil for one month, we observed a considerable reduction in recovery rate as well as ultimate recovery (**Figure 4-19-a**). The lowered wettability to water effectively diminished the water invasion due to imbibition, causing less oil to be mobilized within pores. We witnessed a minor improvement of final recovery under ultrasound, but a strong enhancement of recovery rate at early stages. This can be seen in the cross-comparison plot shown in **Figure 4-19-b**.

4.3.3 Anionic and nonionic surfactant solutions

4.3.3.1 DOWFAX 3B0

Figure 4-20 (a) and **(b)** shows imbibition recovery curves of light mineral oil using 1% and 5% Alkyldiphenyloxide Disulfonic Acid (DOWFAX 3B0) solutions as aqueous phase in Berea sandstone. Vibration at setting 2 and 5 were continuously applied using an

ultrasonic horn. It can be seen that for 1% DOWFAX 3B0, i.e. below the critical micelle concentration (CMC), the improvement of recovery under ultrasound is minimal, with higher recovery observed at elevated intensities. Recovery of oil using 5% surfactant (above CMC) resulted in a substantial increase in ultimate recovery and production rate, compared to no-ultrasound control (NUS). The incremental recovery consistently improved with increasing intensity setting, yielding an incremental recovery of 20% PV at setting 2, and 28% PV at setting 5. A cross-comparison plot of the recovery curves under ultrasound as compared to the control is presented in **Figure 4-21**.

4.3.3.2 DOWFAX 2A1

Based on these results, another variant of Alkyldiphenyloxide Disulfonic Acid, namely DOWFAX 2A1, was tested as well. Imbibition curves for concentrations of 1%, 3% and 5% DOWFAX 2A1 into light mineral oil are presented in **Figure 4-22-a**. Unlike observations made with DOWFAX 3B0, changes in ultimate recovery varied by less than $\pm 10\%$, which is within the expected uncertainty margin associated with these imbibition experiments. The recovery rate, however, was raised by up to 35% (**Figure 4-22-b**), clearly surpassing the expected limit due to uncertainty.

Recovery of kerosene in Berea sandstone using 5% DOWFAX 2A1 yielded contrasting results, and mainly depended on the ultrasonic intensity applied (**Figure 4-23-a**). At setting 2, both the recovery rate and ultimate recovery were marginally improved as compared to the control. Recovery rate at setting 5 did not deviate greatly from that obtained with setting 2. The initiation time, however, was delayed by several minutes and ultimate recovery was considerably lower. When ultrasound was removed, additional

14% incremental oil was recovered, resulting in a similar ultimate recovery as with setting 2. This considerable jump in recovery is shown in **Figure 4-23-b**.

After aging the sandstone samples for one month, we observed that for concentrations close to the CMC, the recovery rate improved by up to 60% (**Figure 4-24-b**). At higher concentrations, however, recovery rates did not seem to alter considerably under ultrasound. At all concentrations the ultimate recovery was only marginally enhanced by up to 8% as compared to the control experiments.

4.3.3.3 Tergitol 15-S-7

Since both DOWFAX 3B0 and DOWFAX 2A1 are anionic surfactants which exhibit low surfactant adsorption to silicates, we decided to investigate the effect of nonionic surfactant in Berea sandstone, as well. The nonionic surfactant Tergitol 15-S-7 (Alcohol Ethoxylate) was applied to both kerosene and light mineral oil saturated Berea sandstone samples.

Figure 4-25-a presents recovery curves vs. time of light mineral oil for a series of Tergitol 15-S-7 concentrations. For 0.1% and 1.0%, we observed a reduction in recovery under ultrasound, while for 0.5%, we witnessed an 18% improvement in recovery, implying that there exists a concentration at which the ultrasonic process is optimized. The shape of the recovery curves did not noticeably change under ultrasound. Interestingly, the recovery of kerosene in sandstone using 1% Tergitol 15-S-7 behaved identically to the recovery performance observed with light mineral oil (**Figure 4-26**). This similarity was not observed with anionic surfactant.

4.3.3.4 Discussion

Several reasons may be responsible for the apparent improvement in recovery with surfactant under ultrasound with both light mineral oil and kerosene:

- Ultrasound may increase solubility of surfactant in water, thereby decreasing the interfacial tension. A decrease in interfacial tension will reduce the capillary pressure within pores, thus mobilizing trapped oil more effectively.
- Ultrasound may reduce the surfactant adsorption rate onto the sandstone matrix as a consequence of increasing the solubility of the surfactant, improving the wettability of the aqueous phase. This process may be more severe with anionic surfactants than with nonionic surfactants.
- Development of micro-emulsion (micelles) under ultrasound. Just after 100 min, we observed that the surfactant solution changed into a semi transparent, foggy micro-emulsion (**Figure 4-11**). Therefore, operating ultrasound at surfactant concentrations above CMC accelerates the generation of micelles which may enhance oil recovery.

Surfactant adsorption/desorption may be responsible for the observed variations in recovery under ultrasound for kerosene and mineral oil saturated sandstone (Brinck *et al.* 1998a, 1998b). The adsorption levels for both anionic and nonionic surfactants are similar in magnitude, although adsorption of nonionic surfactants on sandstone is usually higher, and is relatively insensitive to solution salinity. Negligible adsorption was observed in sulfonates containing alkyl chains shorter than 9 (Trogus *et al.* 1977; Lawson 1978). (Mannhardt *et al.* 1994) studied the adsorption of anionic surfactants in Berea

sandstone at various temperatures and salinity, and found that adsorption increases with decreasing surfactant solubility. Varadaraj *et al.* (1994) investigated the wettability alteration caused by various surfactant types, and found that wetting rate is higher for ethoxylates than for sulfates, while wetting effectiveness was higher for sulfates. Although the concentration of 5% alkydiphenyloxide disulfonic acid and 1% ethoxylated alcohol are both significantly higher than the CMC, the latter demonstrated very little alteration of both recovery rate and ultimate recovery of kerosene and mineral oil when ultrasound was applied. 5% alkydiphenyloxide disulfonic, on the other hand, resulted in significant improvement in recovery rate of mineral oil, and contrasting results in both recovery and recovery rate of kerosene at higher ultrasonic intensity. When comparing kerosene recovery via 1% alcohol ethoxylate, we observed very similar results (compare **Figure 4-25** and **Figure 4-26**).

Since interfacial tension of both sulfonates and ethoxylates is relatively similar, capillary forces cannot be the dominating factor contributing to the different behavior in recovery under ultrasound. Micro-emulsions were produced in both cases, as well. Therefore, micelles cannot be responsible of the significant difference either. The governing mechanism must be controlled by a sensitive interplay between the increase in surfactant solubility and decrease in adsorption due to ultrasonic mixing. We demonstrated the role of surfactant adsorption by comparing the imbibition performance of both anionic and nonionic surfactants. Depending on the level of adsorption, one expects that the wettability of Berea alters over time, severely affecting the recovery rate, as well as the ultimate recovery.

4.3.4 Spontaneous imbibition of Xanthan gum solution into Berea sandstone

The effect of ultrasound on spontaneous imbibitions of polymer solutions was investigated to study the effect of viscosity. Imbibition of polymers into porous media has been investigated extensively (see e.g. Ghedan and Poettmann 1991; Babadagli 2002). **Figure 4-27** shows recovery curves of various concentrations of Xanthan gum imbibing into Berea sandstone cores saturated with mineral oil. The recovery curve of 150,000 ppm NaCl brine has been added for comparison. Without ultrasound, we observed that the recovery of oil decreases with increasing xanthan gum concentration. Introducing ultrasound at setting 2 did not follow this trend. Instead, it is apparent that ultrasonic stimulation is optimal at intermediate concentrations. Low concentrations of xanthan gum (0.05%) did not show any significant improvement in recovery under ultrasound. On the other hand, 0.1 wt% and 0.1 wt% xanthan gum solutions favorably responded to ultrasound by significantly increasing recovery rate, and yielding up to 25% PV incremental oil as compared to the control.

We observed a direct proportionality between the ultrasonic intensity and final recovery (**Figure 4-28**). This was not true in the case of the 0.09% Xanthan gum solution. Here, the low intensity ultrasound proved to be more effective at recovering oil by imbibition. This result can be explained by considering the polymer structure. Xanthan gum is an anionic polysaccharide string with a cellulose backbone and trisaccharide side chains and repeating pentasaccharide units. When contacting with water, Xanthan gum forms alpha helices as a secondary structure, which entangle and bind the water molecules. High frequency vibrations by ultrasound increase the entanglement, and cause the helices to vibrate. Ultrasonic energy may also break down larger components of the

polymer, and cause depolymerization (Kulicke *et al.* 1993; Gronroos *et al.* 2004). Additionally, ultrasound homogenizes the mixture and prevents formation of suspensions and flocculation. We expect that there is an optimum intensity and concentration at which ultrasonic stimulation is maximized. This is illustrated clearly in **Figure 4-29** .

4.3.5 Husky crude oil

Figure 4-30 shows the recovery curves and the cross-comparison plots for brine and surfactant imbibition into Berea sandstone cores saturated with light Husky crude oil. It can be seen that in the case of brine invasion, both the early recovery rate and the final recovery are substantially improved under ultrasound. With surfactant, however, only recovery rate is improved by 20%, while the final recovery for both ultrasound and no ultrasound remained unaltered.

4.4 Conclusions

1. A series of spontaneous imbibition experiments were run to investigate the effect of ultrasound on the capillary dynamics within porous media. Various fluid pairs and boundary conditions were explored to account for a wide range of interfacial tension, wettability, density and viscosity.
2. For most fluid pairs, we noted a considerable enhancement in recovery, and recovery rate.
3. Altering the fluid properties of the aqueous and oleic phases had a unique response on the overall performance of the spontaneous imbibition process under ultrasound. Furthermore, the nature of the flow, i.e. co-current or counter-current, resulted in entirely different responses for the same fluid pairs, and strongly depended on interfacial tension and density.
4. We investigated the spontaneous imbibition of water into dry sandstone and limestone cores under ultrasound, at two boundary conditions. It was observed that the recovery rate is relatively unchanged under ultrasound, and that for co-current flow (all sides open), the final recovery considerably decreased. The opposite is true for counter-current flow with all sides closed except the bottom end, where both the recovery rate and the final recovery were improved. A similar, but less dramatic, response was observed with limestone. For co-current imbibition, the final recovery gradually decreased with frequency, while the recovery rate remained unchanged. The opposite was noted for counter-current flow. Bubble vibration and improved acoustic streaming of air, as well as the destruction of surface films are believed to be responsible for the observed trends.

5. Spontaneous imbibition of water into Berea sandstone saturated with kerosene and light mineral oil yielded opposite results as with air. For co-current flow, both the rate and the final recovery of kerosene and light mineral oil improved. The increase was observed to be higher with light mineral oil (higher viscosity, higher IFT) than with kerosene (low viscosity, intermediate IFT). For the counter-current process, we observed a minor decrease in recovery and no change in rate with light mineral oil, whereas, the kerosene rate and recovery severely reduced. After discontinuing insonication, the final kerosene recovery restored to the non-ultrasonic recovery value.
6. When using brine as an aqueous phase, we observed a substantial increase in recovery as compared to water. In fact, both recovery rate and final recovery are proportional to salinity. Two substantial findings have been derived from these experiments. Firstly, based on experiments with 15,000 ppm NaCl solutions, final recovery increases with increasing intensity setting. The recovery rate was unaffected. Secondly, for saline concentrations as high as 150,000 ppm NaCl, ultrasound improved the recovery by up to 15% PV incremental oil. Secondly, aging reduced the final recovery at high salinity, but still reacted favorably to ultrasonic stimulation. The curvature of the ultrasonically stimulated production rate was almost linear, compared to a more concave curvature observed with the non-ultrasonic control.
7. Three surfactants (two anionic and one nonionic) were tested at various concentrations below and above CMC. We observed the following trends:

- a. With DOWFAX 3B0, recovery is relatively insignificant at concentrations close to the CMC. At a concentration much above the CMC, recovery increases with increased ultrasonic intensity, reaching recovery improvements up to 18% PV incremental oil.
- b. DOWFAX 2A1 did not exhibit the same behavior as DOWFAX 3B0. Recovery rate was substantially improved during insonication, while the improvement in final recovery remained below 10%. After aging cores for 1 month, we found that the recovery rate severely improved for concentrations close to the CMC (up to 60%), while the improvement in ultimate recovery remained below 10%. Interestingly, the recovery rate at higher concentrations seemed to be only marginally improved (below 10%). When using high concentration DOWFAX 2A1 with kerosene saturated Berea, we observed that at high intensity, ultrasound yielded unfavorable final recovery values. After discontinuing the ultrasound, however, recovery surged up, and stabilized at the recovery value obtained for low intensity ultrasound.
- c. Experiments with anionic surfactant (Tergitol 15-S-7) suggest that there is an optimal concentration at which the ultrasonic process is maximized. At a concentration of 0.5%, we noted a recovery increase of up to 40%. A reduction in recovery rate was observed with both 0.1% and 1.0% Tergitol. When comparing the performance of 1% Tergitol for kerosene and mineral oil saturated samples, we observed a minor reduction in

recovery (~5%) and recovery rate (20% for kerosene, 10% for light mineral oil).

Reduction of surfactant adsorption as a consequence of improved solubility has been proposed to account for the observed behavior of both anionic and nonionic surfactant.

8. Results for spontaneous imbibition of Xanthan gum into light mineral oil saturated Berea sandstone showed interesting results. Recovery under ultrasound is improved at higher surfactant concentrations. However, there seems to be an optimal intensity and concentration at which recovery is maximized. We determined that spontaneous imbibition of xanthan gum is maximized when using low concentrations of xanthan gum at high intensity. Ultrasonic depolymerization and deflocculation may be possible causes for this observation.
9. Experiments with Husky crude oil using both surfactant (DOWFAX 2A1) and brine (150,000 ppm NaCl) yielded promising results. Ultrasound improved the recovery rate with surfactant by up to 20%, but did not considerably enhance the final recovery. On the other hand, when using brine, we noted a surge in recovery rate (up to 65%), and a spectacular increase in final recovery (up to 23%).
10. Further work need to be done in understanding the influence of initial water on the recovery of oil through spontaneous imbibition.
11. In order to understand the behavior of air-water imbibition, we suggest micro-model visualization experiments under ultrasound. Such study may complement some of the assumptions made in Chapter 2.

12. We only investigated the response of capillary imbibition on continuous sonication. Pulsed sonication may yield more favorable production.

Table 4-1: Fluid properties of oleic and aqueous phases used in spontaneous imbibition experiments. All values were measured at standard atmospheric conditions. DOWFAX 2A1 = Sodium Dodecyl Diphenyloxide Disulfonate. Tergitol 15-S-7 = Alcohol Ethoxylate.

Fluid	Density⁽¹⁾ g/cc	Viscosity⁽²⁾ cp	Surface Tension⁽³⁾ dynes/cm
Water	0.9982 ± 0.0010	1.0 ± 0.02	71.0 ± 1.4
Water + 150,000 ppm NaCl	1.1163 ± 0.0010	1.20 ± 0.06	69.9 ± 1.4
Water + 15,000 ppm NaCl	1.0096 ± 0.0010	1.20 ± 0.06	70.5 ± 1.4
Water + 1% DOWFAX 2A1	0.9997 ± 0.0010	2.44 ± 0.12	33.8 ± 0.7
Water + 3% DOWFAX 2A1	1.0027 ± 0.0010	5.32 ± 0.27	34.1 ± 0.7
Water + 5% DOWFAX 2A1	1.0058 ± 0.0010	8.20 ± 0.41	34.6 ± 0.7
Water + 0.1% TERGITOL 15-S-7	0.9982 ± 0.0010	1.05 ± 0.05	30.1 ± 0.6
Water + 0.5% TERGITOL 15-S-7	0.9982 ± 0.0010	1.25 ± 0.06	27.8 ± 0.6
Water + 1.0% TERGITOL 15-S-7	0.9981 ± 0.0010	1.50 ± 0.08	27.5 ± 0.6
Water + 0.03% Xanthan gum	0.92 ± 0.0010	15.00 ± 0.75	68.0 ± 3.4
Water + 0.05% Xanthan gum	0.93 ± 0.0010	25.00 ± 1.25	66.5 ± 3.3
Water + 0.1% Xanthan gum	0.94 ± 0.0010	42.00 ± 2.10	65.0 ± 3.3
Light Mineral Oil	0.8383 ± 0.0050	46.5 ± 0.5	31.5 ± 0.6
Heavy Mineral Oil	0.8508 ± 0.0050	167.0 ± 1.7	34.3 ± 0.7
Kerosene	0.768 ± 0.0050	2.9 ± 0.03	27.2 ± 0.5
S60	0.8757 ± 0.0014	141.4 ± 0.2	33.8 ± 0.7
S200	0.8876 ± 0.0014	577.9 ± 0.9	35.6 ± 0.7
N350	0.8885 ± 0.0014	1112.0 ± 1.8	36.6 ± 0.7
S600	0.8913 ± 0.0014	1973.0 ± 3.2	37.8 ± 0.8
Husky Crude Oil	0.8548 ± 0.0050	19.0 ± 0.5	30.2 ± 0.6

(1) Weight-Volume method using a 5cc syringe

(2) Rotational viscometer (Fann 35A) at 300 rpm; Viscosity values for S60, S200, N350 and S600 were obtained from Canon Instrumentation Company (A2LA Certificate #1262.01)

(3) Du Nouy type tensiometer (Fisher Scientific Tensiometer; Platinum-Iridium ring)

Table 4-2: Interfacial tension data for all fluid pairs used in this thesis. All values were measured at standard atmospheric conditions.

Heavy Fluid	Light Fluid	Interfacial Tension dynes/cm
Water	Air	71.0 ± 1.4
1% DOWFAX 2A1	Air	33.8 ± 0.7
3% DOWFAX 2A1	Air	34.1 ± 0.7
5% DOWFAX 2A1	Air	34.6 ± 0.7
0.1% TERGITOL 15-S-7	Air	30.1 ± 0.6
0.5% TERGITOL 15-S-7	Air	27.8 ± 0.6
1.0% TERGITOL 15-S-7	Air	27.5 ± 0.6
150,000 ppm NaCl	Air	69.9 ± 1.4
15,000 ppm NaCl	Air	70.5 ± 1.4
Water	Light MO	61.8 ± 1.2
150,000 ppm NaCl	Light MO	46.2 ± 0.9
15,000 ppm NaCl	Light MO	53.2 ± 1.1
1% DOWFAX 2A1	Light MO	10.1 ± 0.2
3% DOWFAX 2A1	Light MO	11.2 ± 0.2
5% DOWFAX 2A1	Light MO	12.0 ± 0.2
0.1% TERGITOL 15-S-7	Light MO	8.6 ± 0.2
0.5% TERGITOL 15-S-7	Light MO	8.2 ± 0.2
1.0% TERGITOL 15-S-7	Light MO	8.1 ± 0.2
0.05% Xanthan gum	Light MO	56.0 ± 1.1
0.1% Xanthan gum	Light MO	53.3 ± 1.1
Water	Heavy MO	51.0 ± 1.0
3% DOWFAX 2A1	Heavy MO	10.8 ± 0.2
Water	Kerosene	40.7 ± 0.8
5% DOWFAX 2A1	Kerosene	10.4 ± 0.2
1.0% TERGITOL	Kerosene	6.9 ± 0.1
Water	S60	22.6 ± 0.5
Water	S200	30.7 ± 0.6
Water	N350	35.3 ± 0.7
Water	S600	38.7 ± 0.8
3% DOWFAX 2A1	Husky Crude	9.1 ± 0.2
150,000 ppm NaCl	Husky Crude	24.6 ± 0.5

Measured using a Du Nouy type tensiometer (Fisher Scientific Tensiometer; Platinum-Iridium ring)

Table 4-3: Properties of DOWFAX 2A1 and DOWFAX 3B0 surfactants (extracted from a pamphlet by Dow Chemical Company).

Typical Property	DOWFAX 2A1	Typical Property	DOWFAX 3B0
Appearance	Clear amber liquid	Appearance	Clear amber liquid
Hydrophobe Source	Tetrapropylene	Hydrophobe Source	C ₁₀ alpha-olefin
Average Molecular wt.	576	Average Molecular wt.	498
Active Ingredient, min	45%	Active Ingredient, min	45%
Density, g/cc @25°C	1.10 – 1.20	Density, g/cc @25°C	1.03 – 1.20
Viscosity, cp @25°C	145	Viscosity, cp @25°C	110
CMC, g/100g in 0.1 M NaCl	0.007		

Table 4-4: Properties of Tergitol 15-S-7 surfactant (extracted from a pamphlet by Dow Chemical Company).

Hydroxyl Number mg KOH/g	109
Molecular Weight (calculated from OH#)	515
Degree of Ethoxylation, mole/mole, avg	7.3
Degree of Ethoxylation, wt%	62
Actives Content, wt%	100
Water, wt%	0.05
Cloud Point (1% aqueous solution), °C (°F)	37 (99)
Pour Point, °C (°F)	2 (36)
pH (1% aqueous solution)	6.8
Viscosity at 25°C, cP	51
Color, APHA (Pt-Co)	40
Appearance at 25°C	Clear liquid
Specific Gravity at 20/20°C	0.992
Flash Point, Pensky-Martens Closed Cup, ASTM D 93, °C (°F)	187 (369)
HLB Number (calculated)	12.4
Surface Tension (1% aqueous solution), dynes/cm	28

* Determined on commercial material whose properties may vary within Union Carbide's specification limits. Values shown are not intended for specification process.

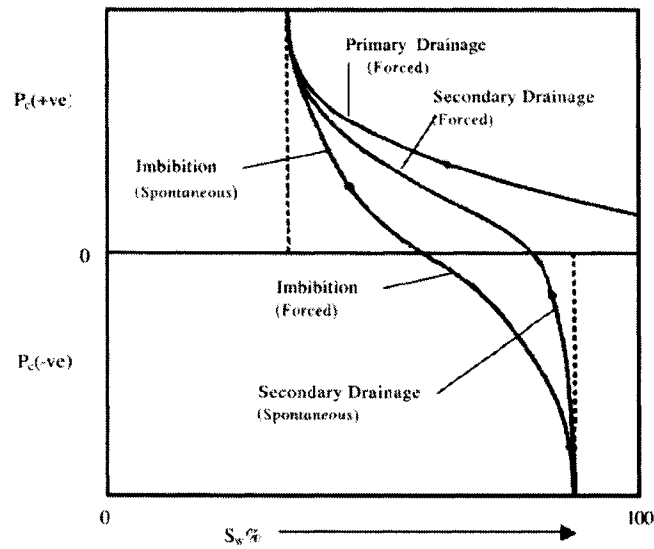


Figure 4-1: Illustration of spontaneous and forced imbibition and drainage capillary pressure curves. Adapted from Morrow and Mason (2001).

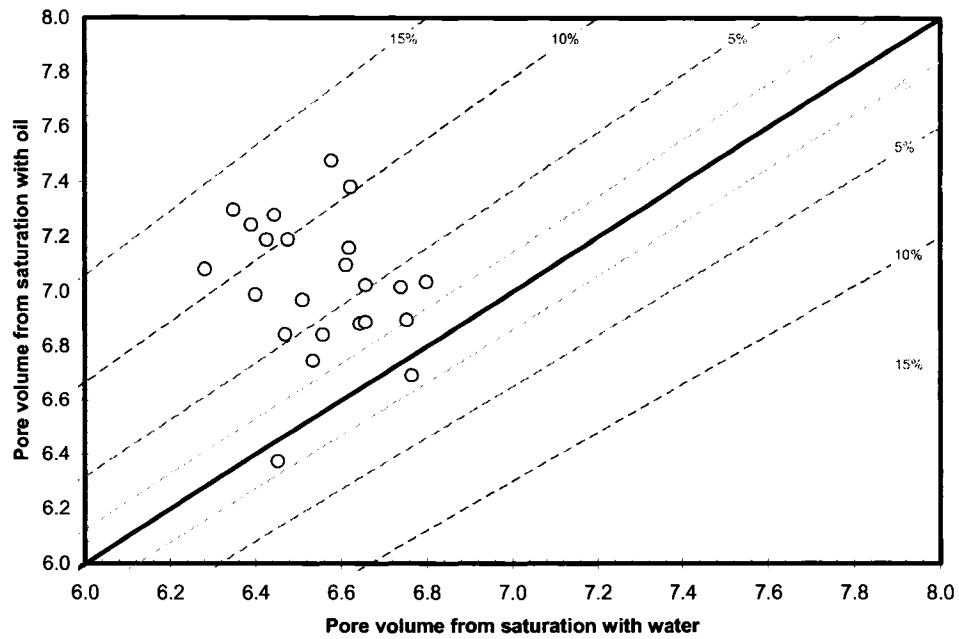


Figure 4-2: Cross correlation plot of pore volumes measured from oil saturated cores vs. pore volumes from water saturated cores. This plot illustrates the severity of clay content in Berea sandstone.

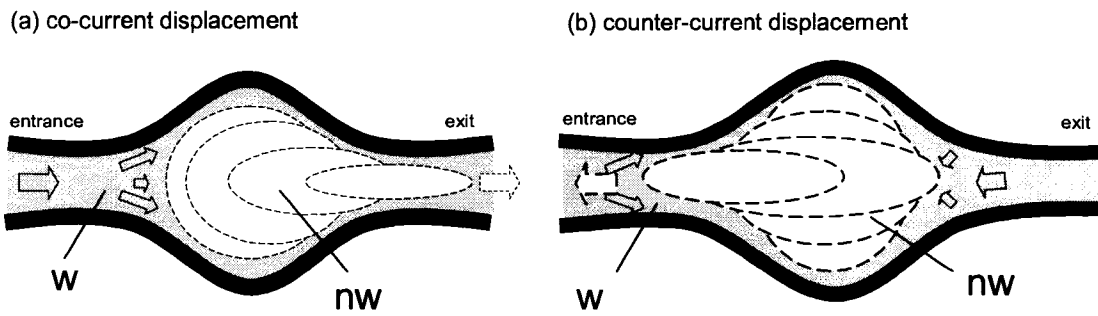


Figure 4-3: Illustration of (a) co-current and (b) counter-current fluid invasion into pores by spontaneous capillary imbibition. In (a), the wetting phase (blue) penetrates the pore from the “entrance” throat via pore adsorption, and pushes oil (white) into adjacent pores. In (b), the wetting phase enters the pore by wetting the pore walls, while the oil is flowing in the opposite direction, mainly due to high capillary pressure at the “exit” throat. [w = wetting phase, nw = non-wetting phase.]

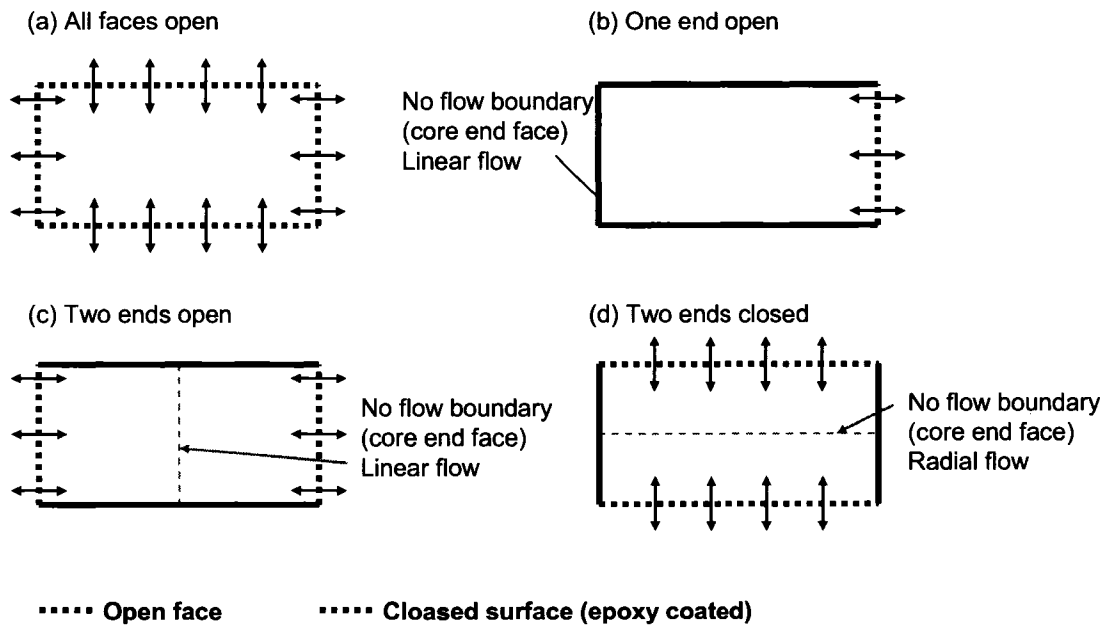


Figure 4-4: Definition of boundary conditions for core samples used in the works of Mattax and Kyte (1962), Zhang *et al.* (1996), and Babadagli *et al.* (2005). Figure adapted from Morrow and Mason (2001).

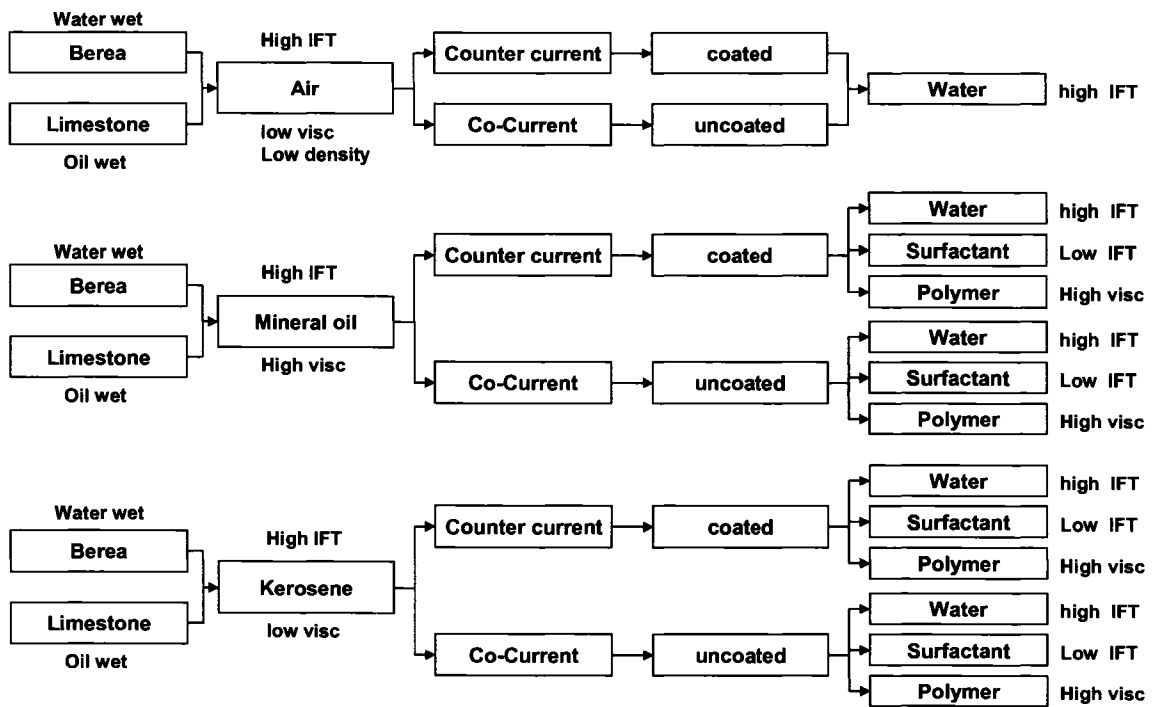


Figure 4-5: Flow chart illustrating all spontaneous imbibition experiments with different fluid pairs, rock types and boundary conditions.

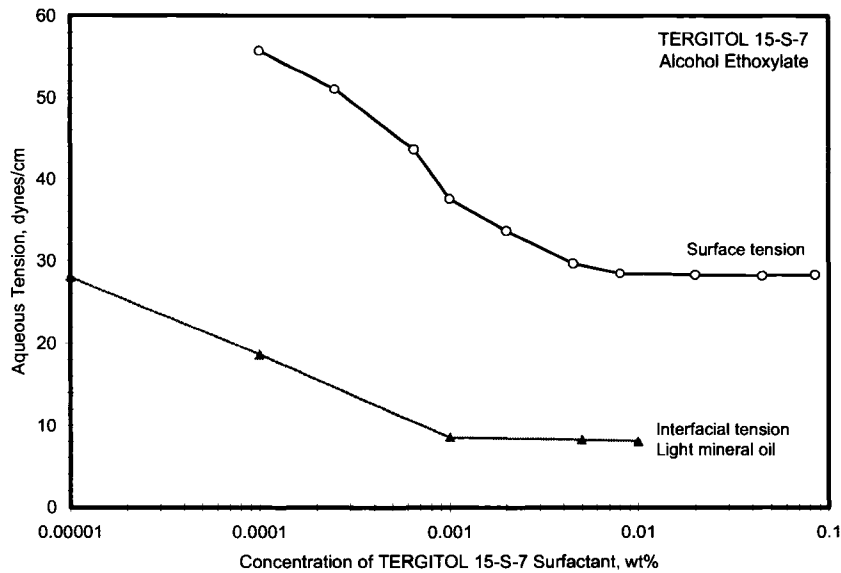


Figure 4-6: Aqueous surface tension and interfacial tension with light mineral oil vs. concentration for TERGITOL™ 15-S-7 surfactant at 25°C. (Surface tension values adopted from Dow Chemical company brochure).

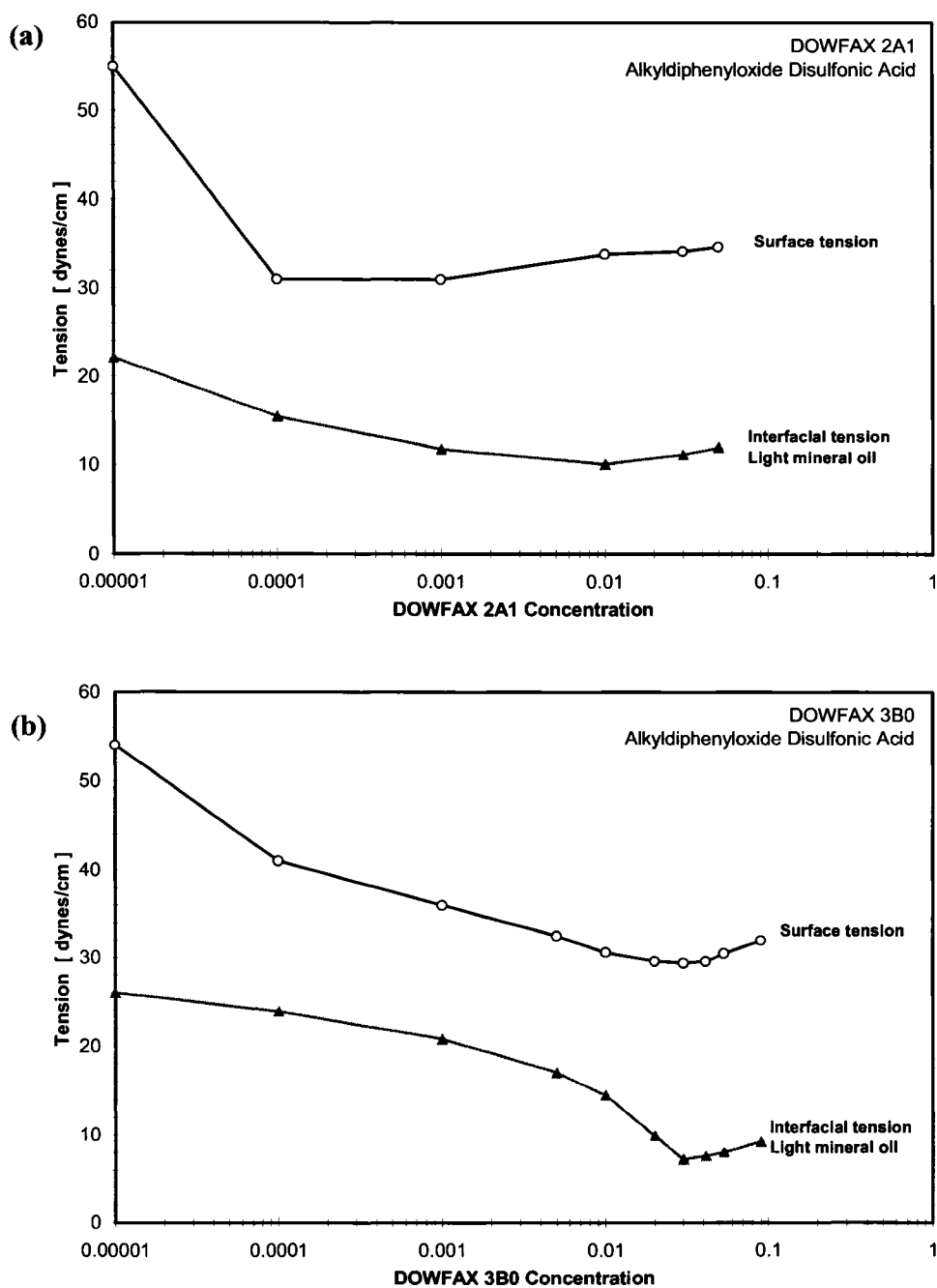


Figure 4-7: Aqueous surface tension and interfacial tension with light mineral oil vs. concentration for (a) DOWFAX™ 2A1 and (b) DOWFAX™ 3B0 surfactant at 25°C. (Surface tension values adopted from Dow Chemical company brochure).

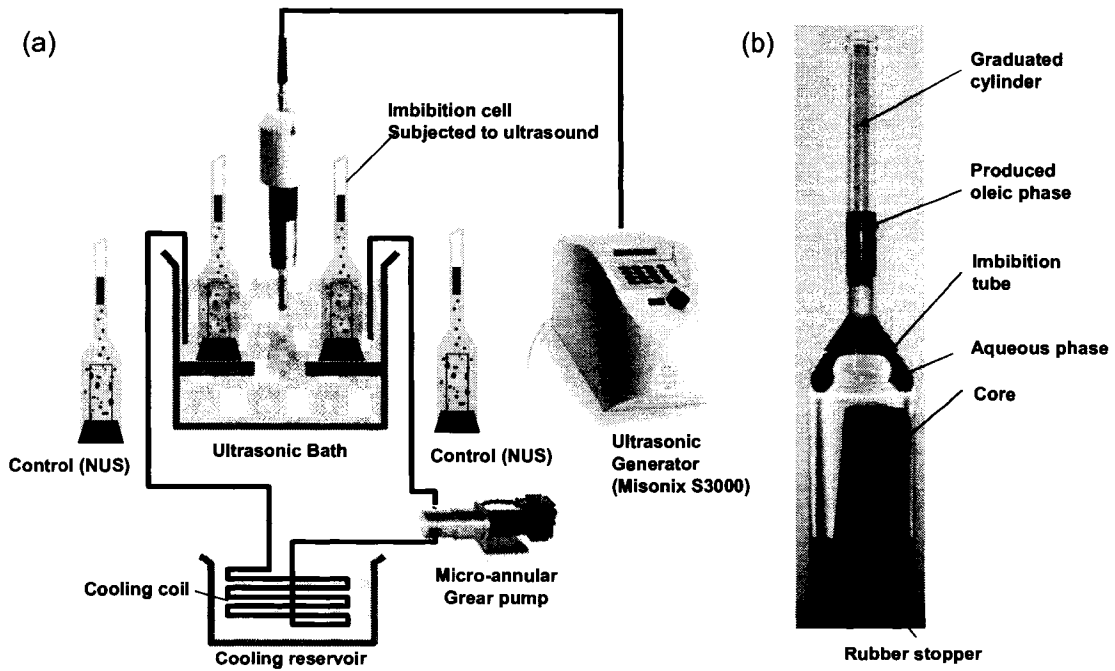


Figure 4-8: (a) Schematic of the experimental setup of imbibition experiments, (b) the glass imbibition cell used to collect oil affluent from a saturated core immersed in an aqueous phase.

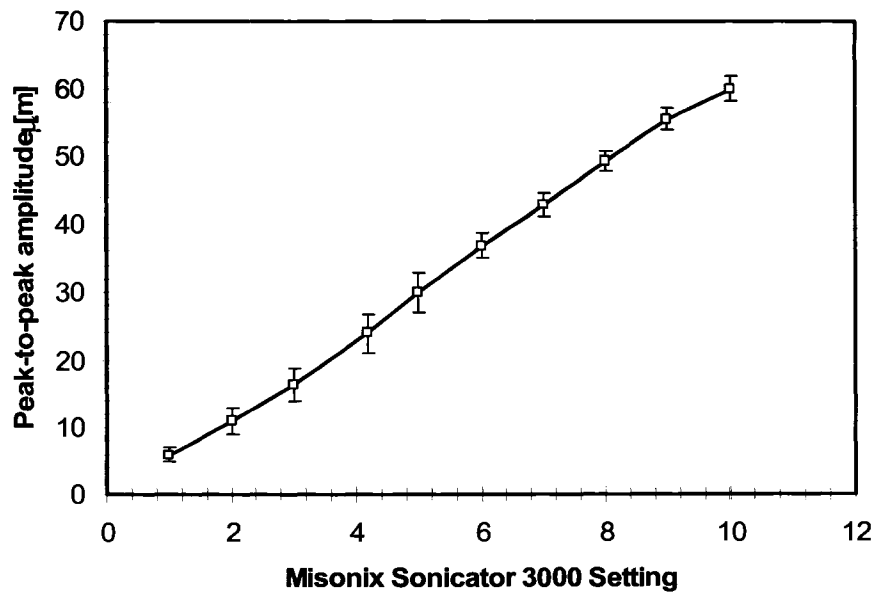


Figure 4-9: Conversion chart of peak-to-peak amplitude for a 3/4" horn versus setting number.

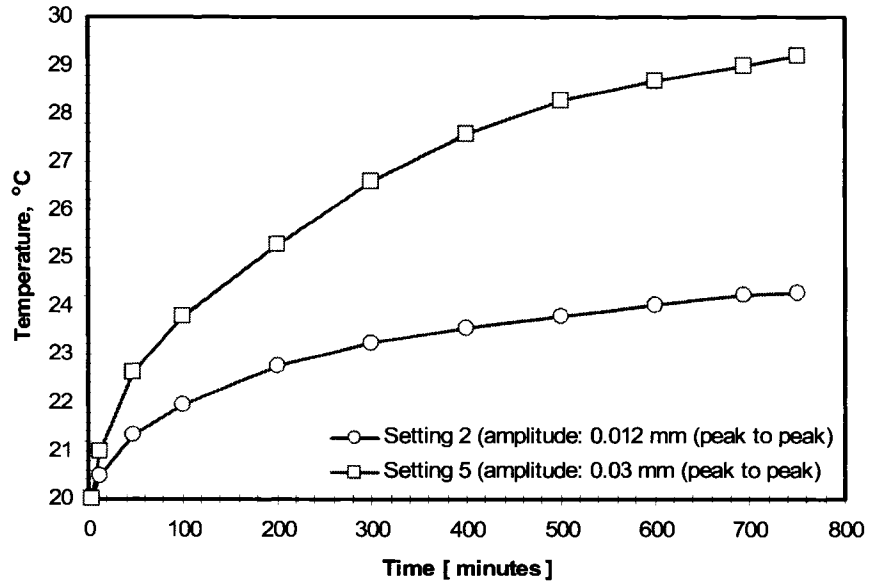


Figure 4-10: Temperature change within the ultrasonic bath at Setting 2 (LO) and 5 (HI). These settings correspond to peak to peak amplitudes of 0.012 mm and 0.03 mm, respectively.

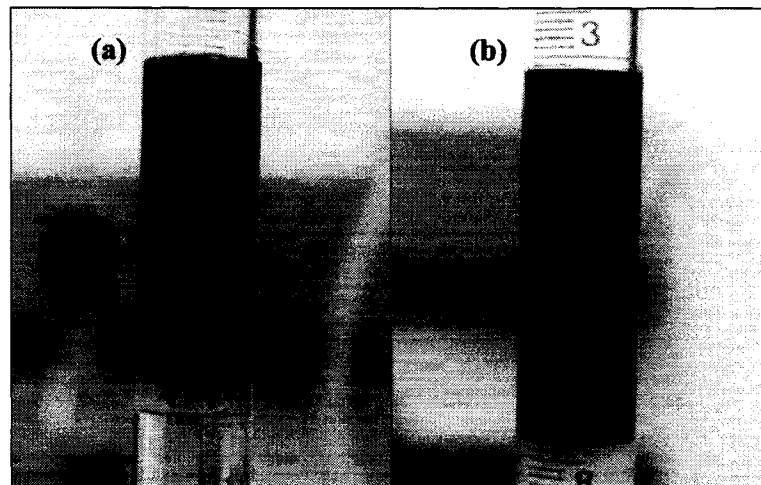


Figure 4-11: Emulsification during surfactant experiments. (a) 3% DOWFAX 2A1 with light mineral oil, (b) 3% DOWFAX 2A1 with Husky crude oil.

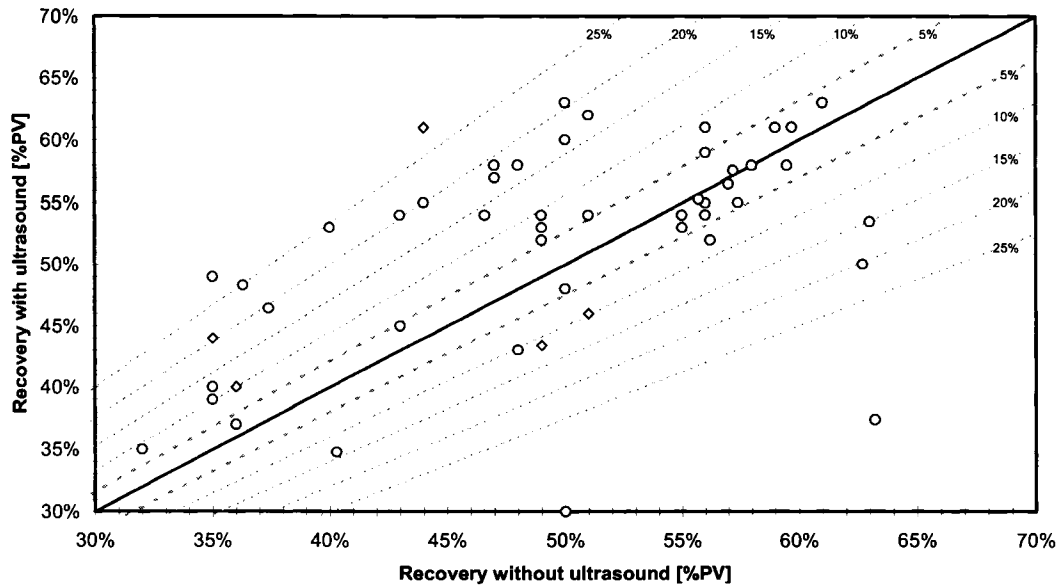


Figure 4-12: Summary of final recovery with and without ultrasound for all fluid pairs. The 45° line in (b) represents the case when the response equals to that of the control. Dashed lines signify the percent deviation (%) from the control case. Recovery below $\pm 5\%$ deviation from the 45° line is believed to be within the uncertainty range of imbibition experiments, and therefore assumed to be unaffected by ultrasound.

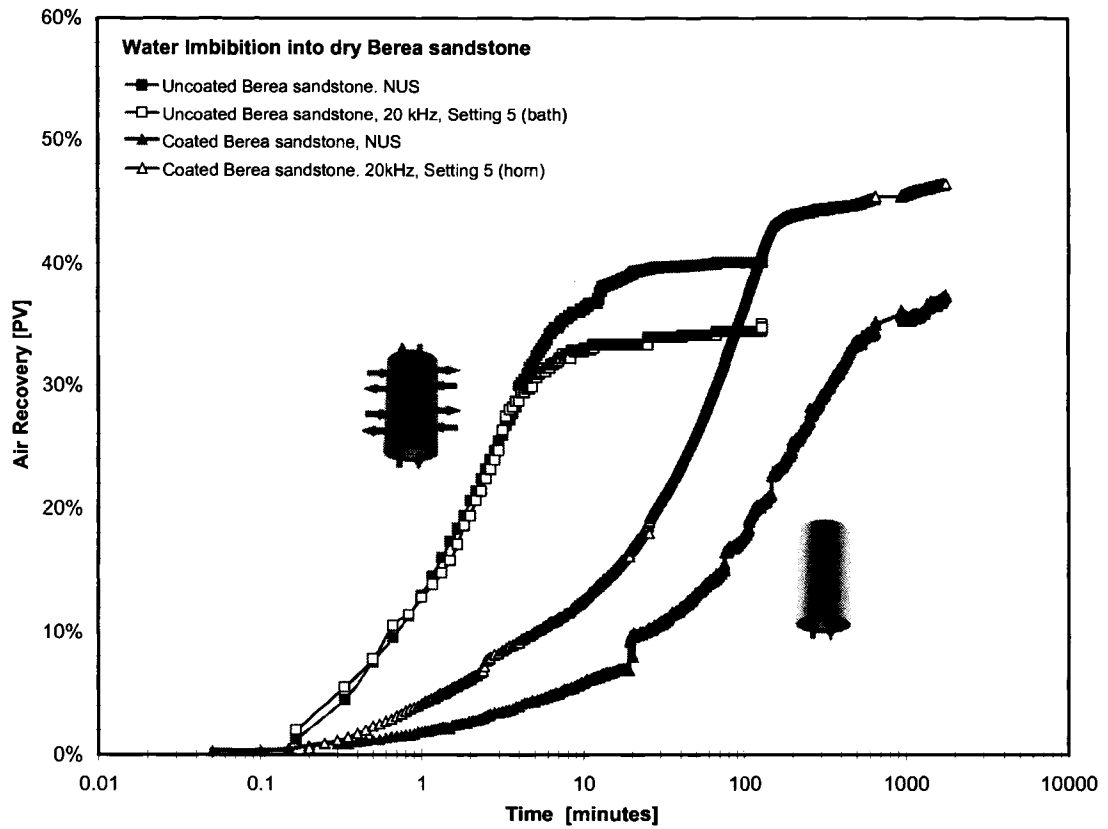


Figure 4-13: Air recovery vs. imbibition time of water imbibing into dry Berea sandstone. Blue curves represent the imbibition performance under ultrasound with a horn (20 kHz, Setting 5). Red curves represent the control without the application of ultrasound. Both co-current and counter-current scenarios are shown.

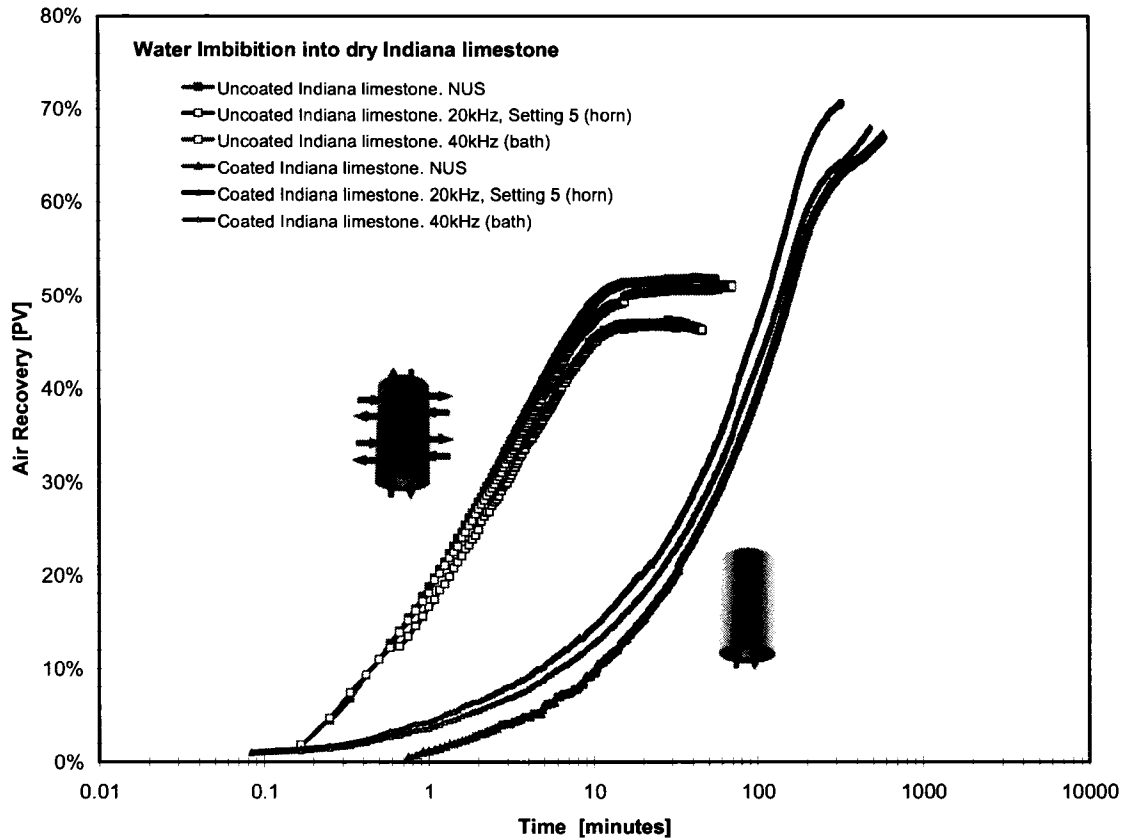


Figure 4-14: Air recovery vs. imbibition time of water imbibing into dry Indiana limestone. Blue and green curves represent the imbibition performance under ultrasound with a horn (20 kHz, Setting 5) and ultrasonic bath (40 kHz), respectively. Red curves represent the control without the application of ultrasound. Both co-current and counter-current scenarios are shown.

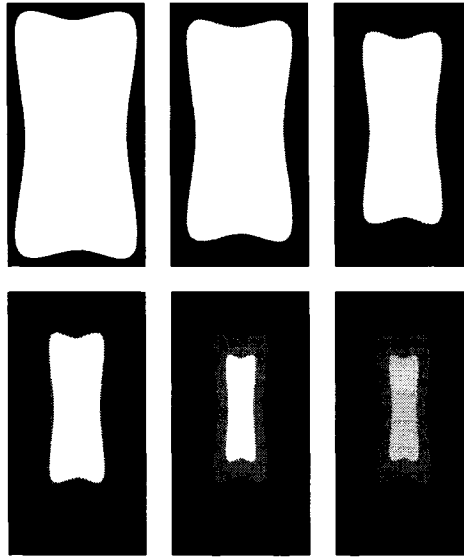


Figure 4-15: Illustration of the frontal propagation of water imbibing into dry, strongly water-wet Berea sandstone in the absence of a boundary. (Based on the CT scanner results by Garg, Nikraves *et al.* (1996). The displacement is governed by partially counter-current, capillary dominated imbibition with buoyant forces present. Air preferentially moves upwards.

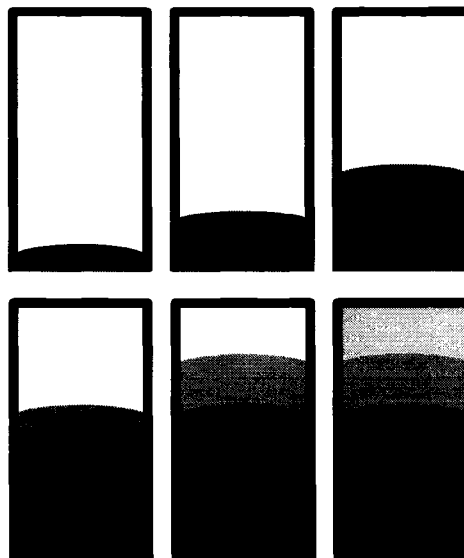


Figure 4-16: Illustration of the frontal propagation of water imbibing into dry, strongly water-wet Berea sandstone when all sides except the bottom end are sealed with epoxy. (Based on the CT scanner results by Garg, Nikraves *et al.* (1996). The displacement is

entirely governed by counter-current, capillary dominated imbibition with air flowing opposite to the upward buoyant force.

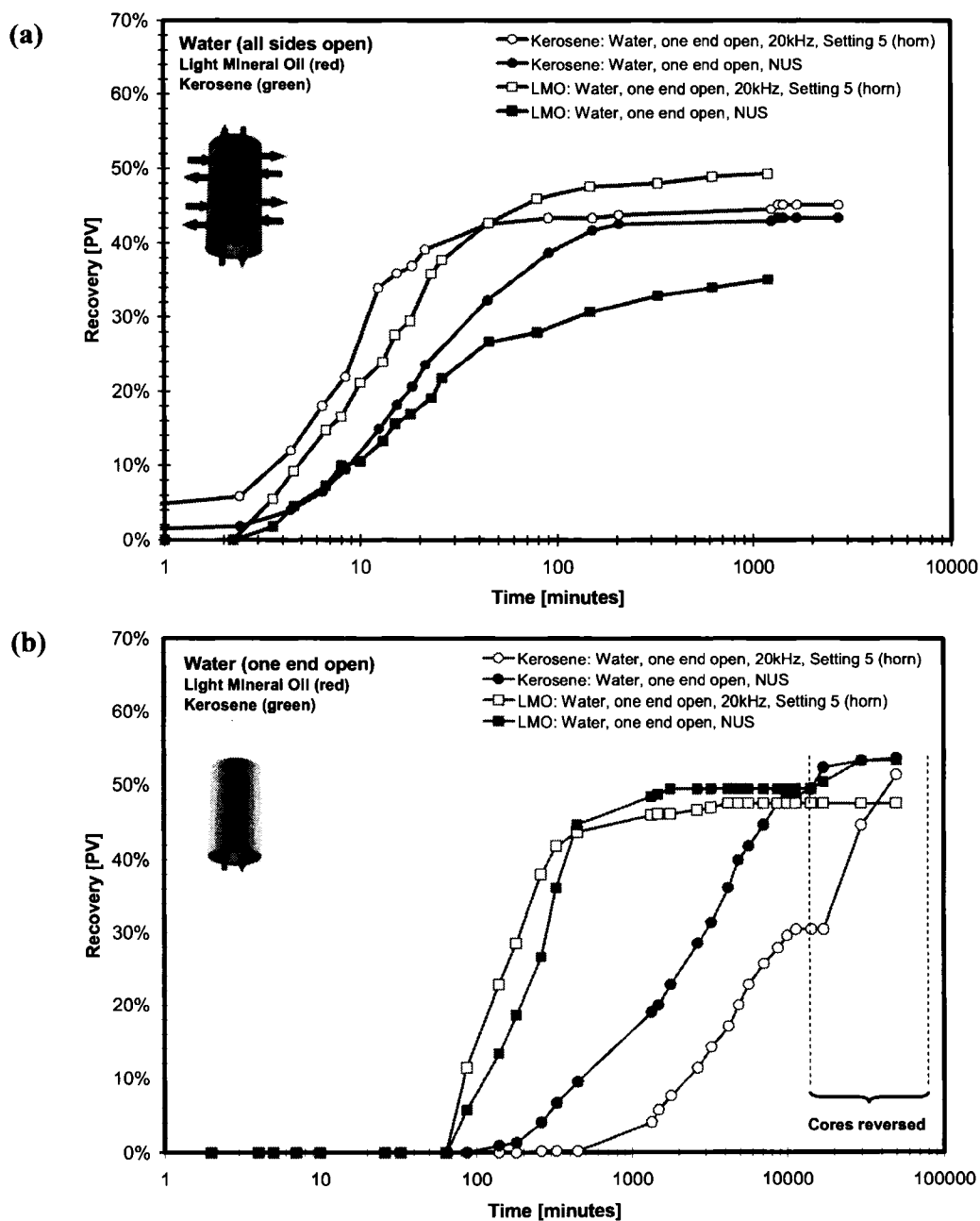


Figure 4-17: Oil recovery vs. time during spontaneous imbibition of water into kerosene and light mineral oil saturated Berea sandstone at two intensities of ultrasound for two boundary conditions: (a) all sides open (uncoated), (b) bottom end open (coated). The dashed interval outlines the recovery when imbibition cells are reversed.

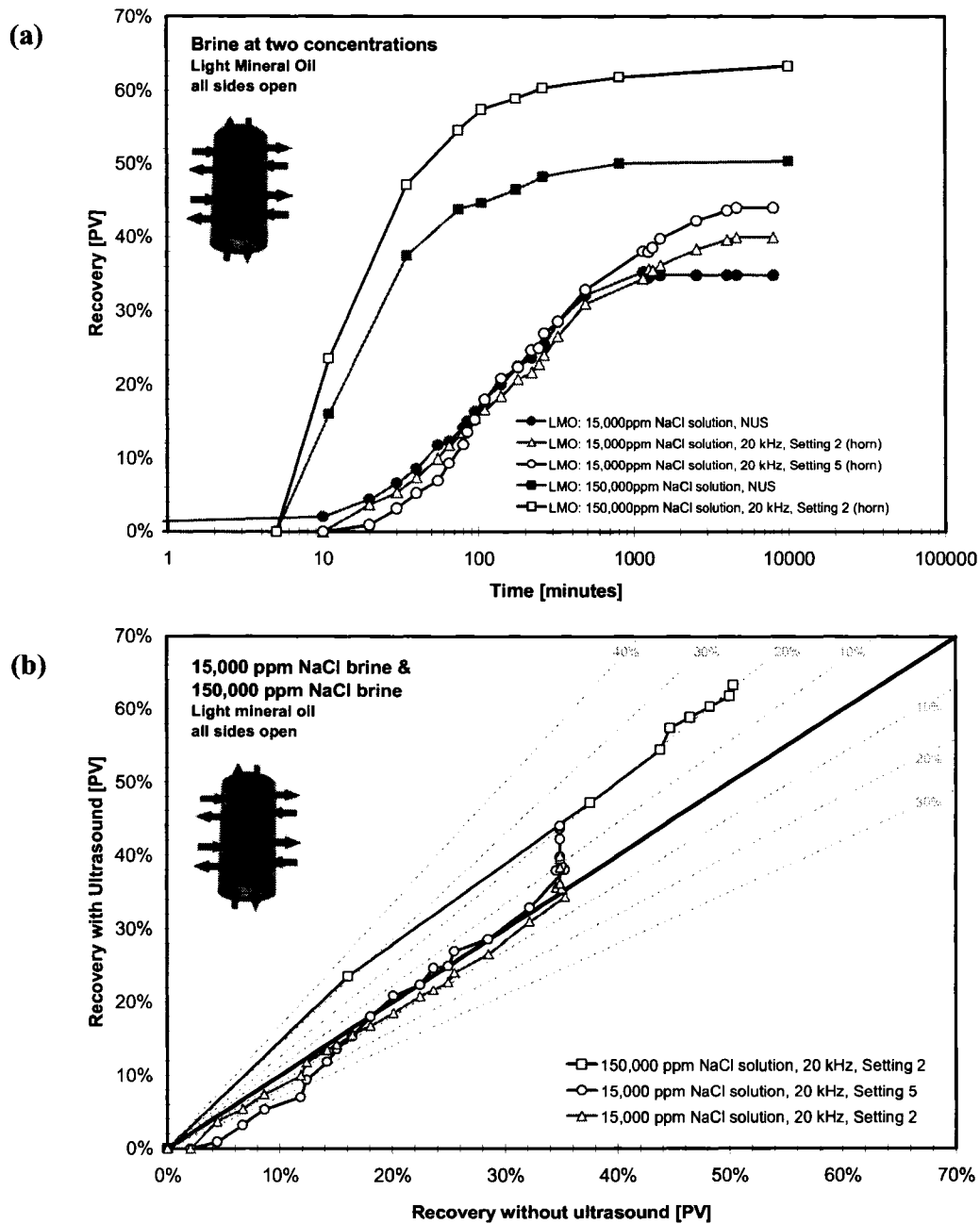


Figure 4-18: (a) Oil recovery vs. time, and (b) cross-comparison plot, of spontaneous imbibition of 15,000 ppm and 150,000 ppm NaCl aqueous solution into light mineral oil saturated Berea sandstone (all sides open) at two intensities of ultrasound, as compared to no ultrasound. Red curves correspond to control conditions without ultrasound. The 45° line in (b) represents the condition when the response under ultrasound equals that of the control. Dashed lines signify the percent (%) deviation from the control.

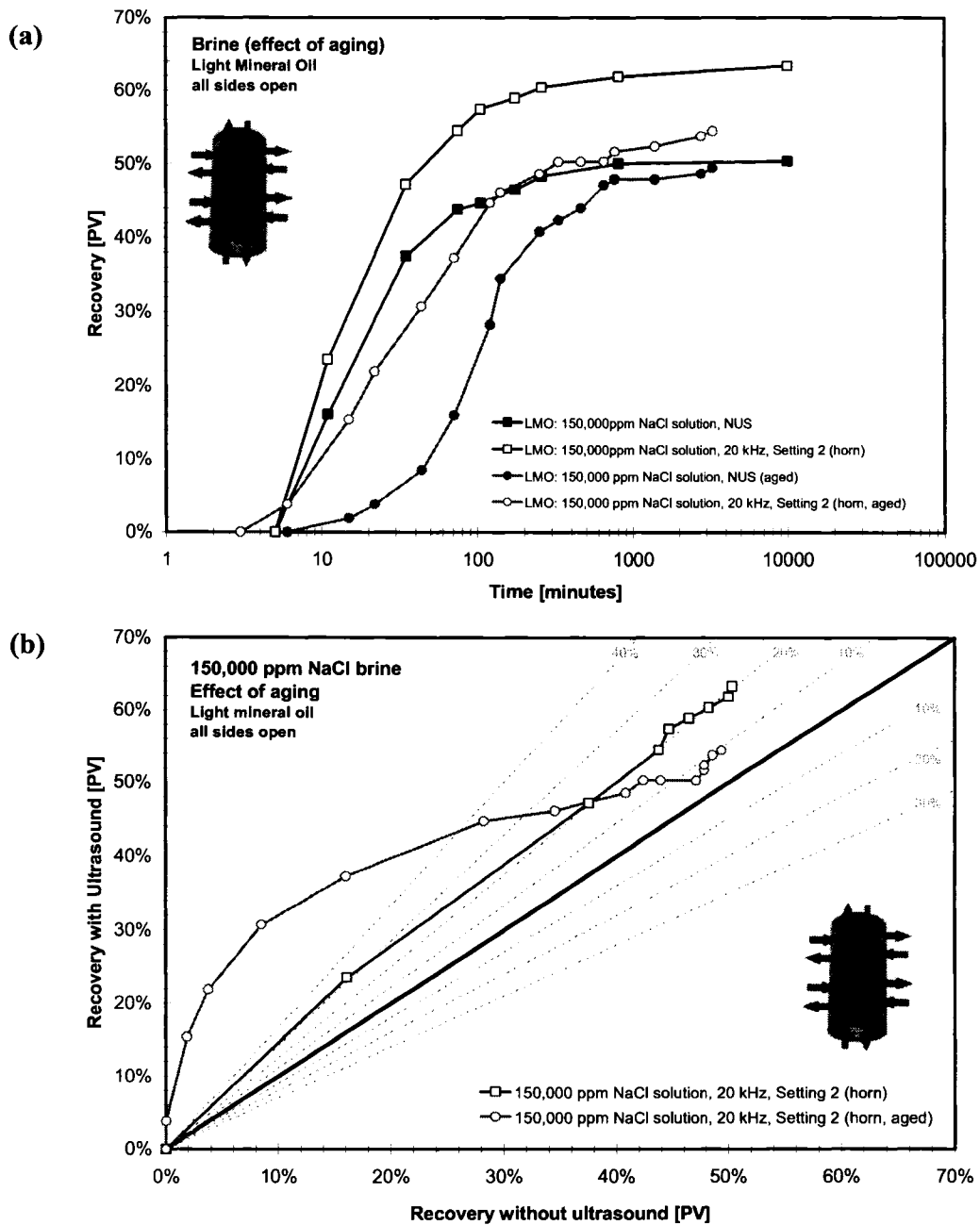


Figure 4-19: (a) Oil recovery vs. time and (b) cross-comparison plot, during spontaneous imbibition under ultrasound of 150,000 ppm NaCl brine solution into light mineral oil saturated Berea sandstone (all sides open) before and after aging for one month. The 45° line in (b) represents the condition when the response under ultrasound equals that of the control. Dashed lines signify the percent (%) deviation from the control.

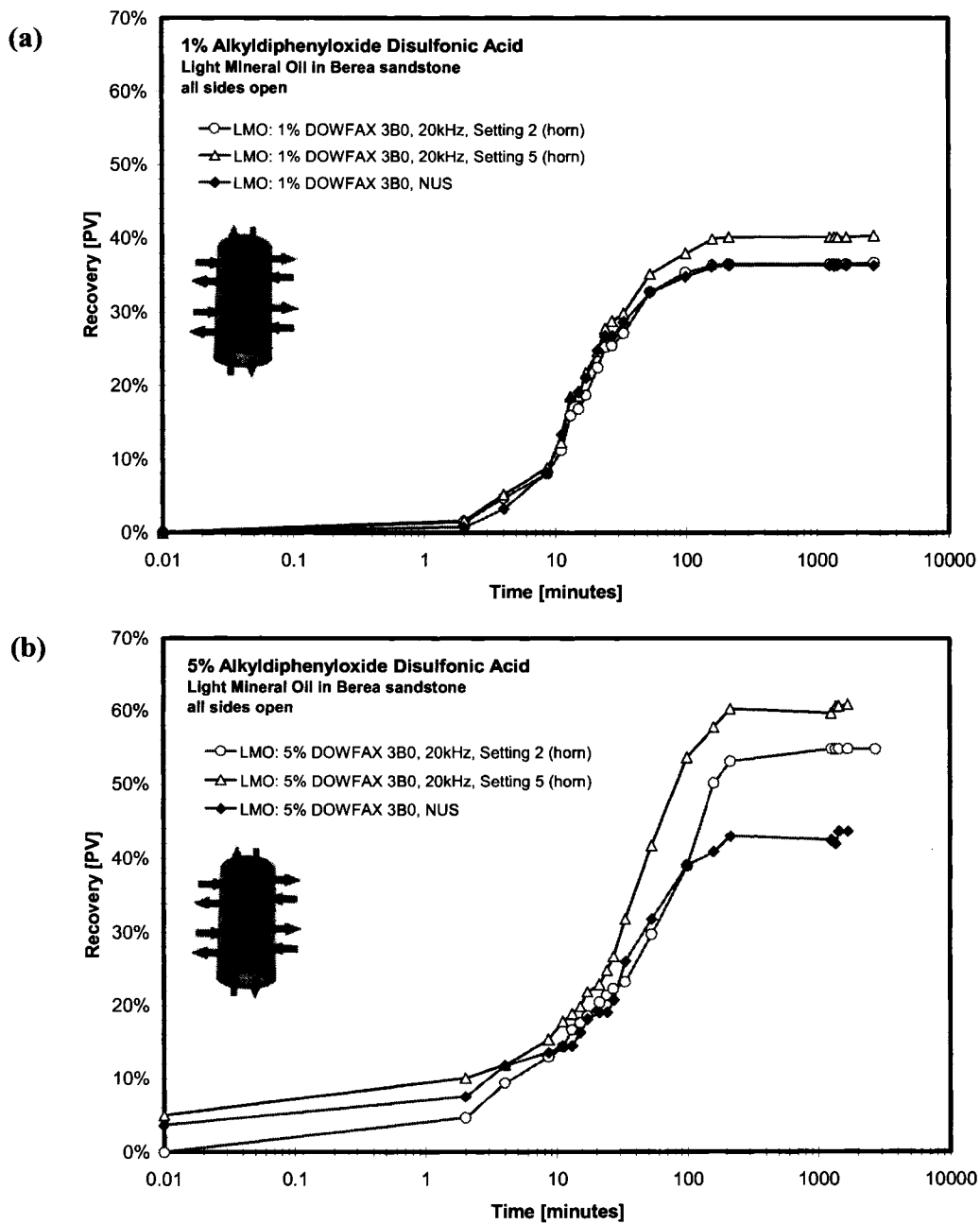


Figure 4-20: Oil recovery vs. time during spontaneous imbibition of (a) 1% Alkyldiphenyloxide Disulfonic Acid, and (b) 5% Alkyldiphenyloxide Disulfonic Acid, into light mineral oil saturated Berea sandstone (all sides open) at two intensities of ultrasound. Red curves illustrate control conditions without ultrasound.

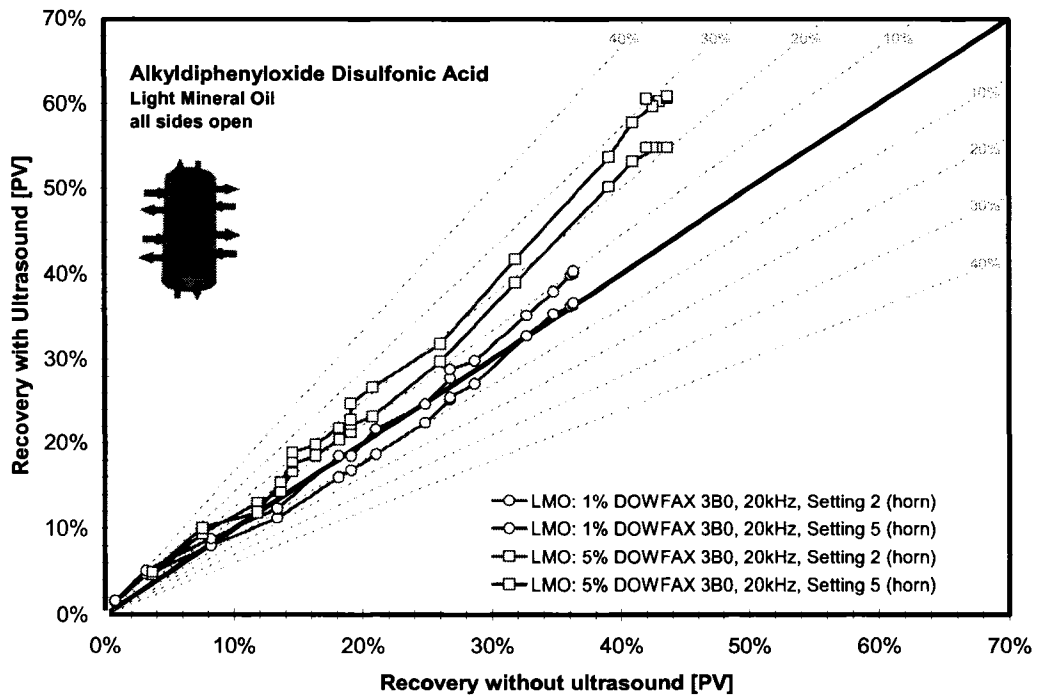


Figure 4-21: Cross-comparison plot of oil recovery during spontaneous imbibition of 1% Alkyldiphenyloxide Disulfonic Acid, and 5% Alkyldiphenyloxide Disulfonic Acid, into light mineral oil saturated Berea sandstone (all sides open) at two intensities of ultrasound. The 45° line represents the condition when the response under ultrasound equals that of the control. Dashed lines signify the percent (%) deviation from the control.

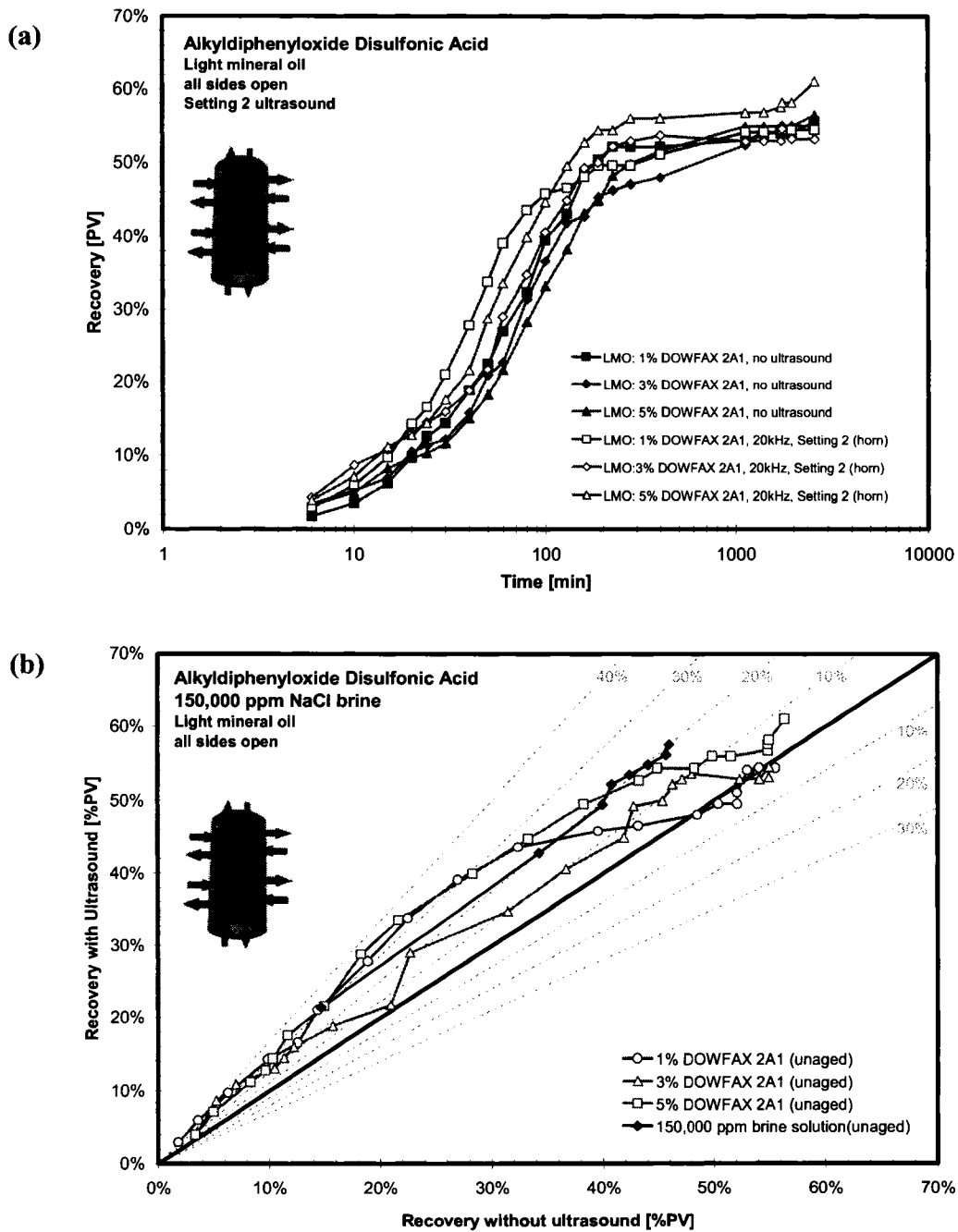


Figure 4-22: (a) Oil recovery vs. time, and (b) cross-comparison plot, of the spontaneous imbibition of various Alkyldiphenyloxide Disulfonic Acid solutions into light mineral oil saturated Berea sandstone (all sides open) under ultrasound. For comparison, we also added the imbibition performance after using a 150,000 ppm brine solution as aqueous phase. The 45° line in (b) represents the case when the response equals to that of the control. Dashed lines signify the percent deviation (%) from the control case.

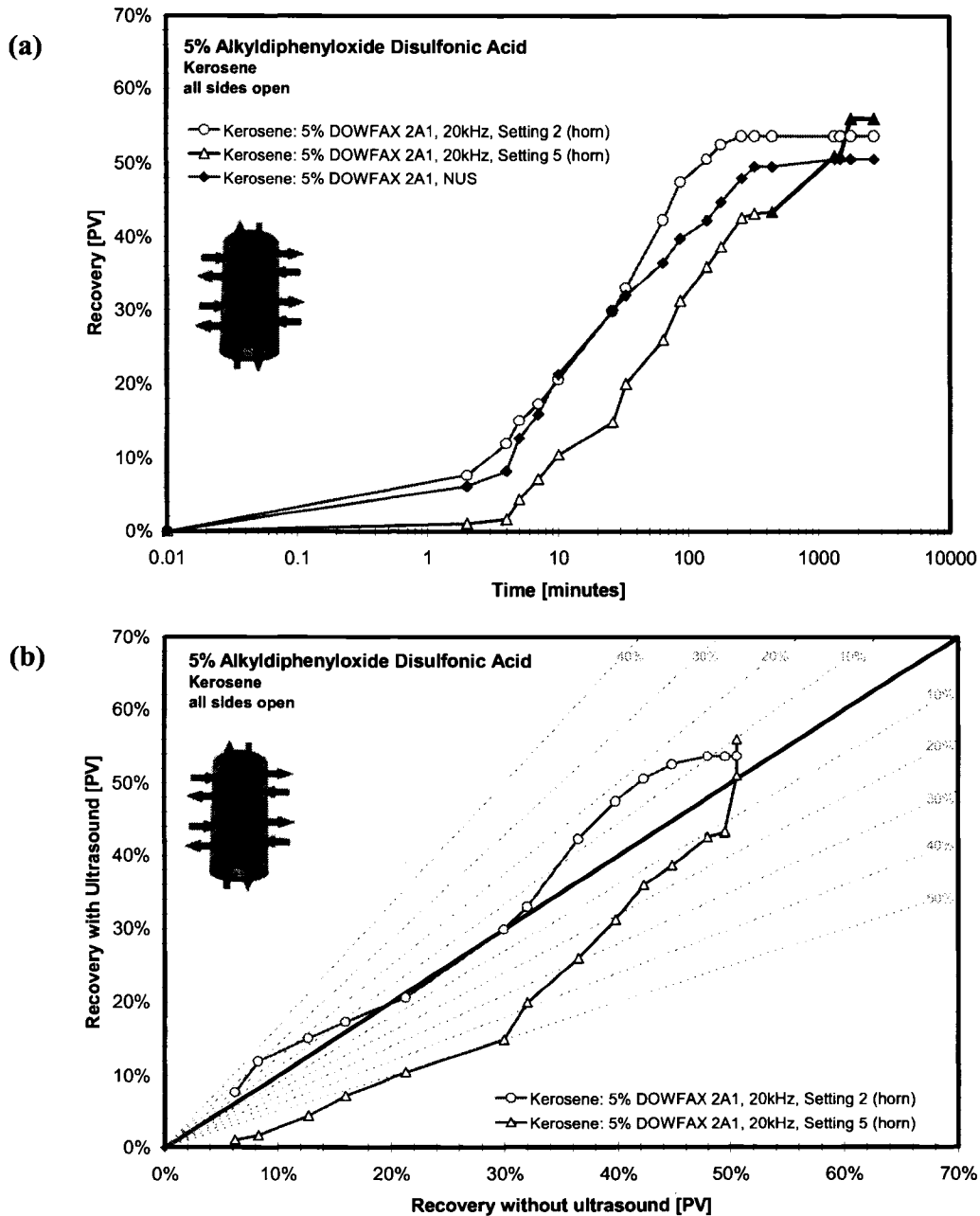


Figure 4-23: (a) Oil recovery vs. time, and (b) cross-comparison plot, of the spontaneous imbibition of 5% Alkyldiphenyloxide Disulfonic Acid solutions into kerosene saturated Berea sandstone (all sides open) at two intensities of ultrasound. The 45° line in (b) represents the case when the response equals to that of the control. Dashed lines signify the percent deviation (%) from the control case.

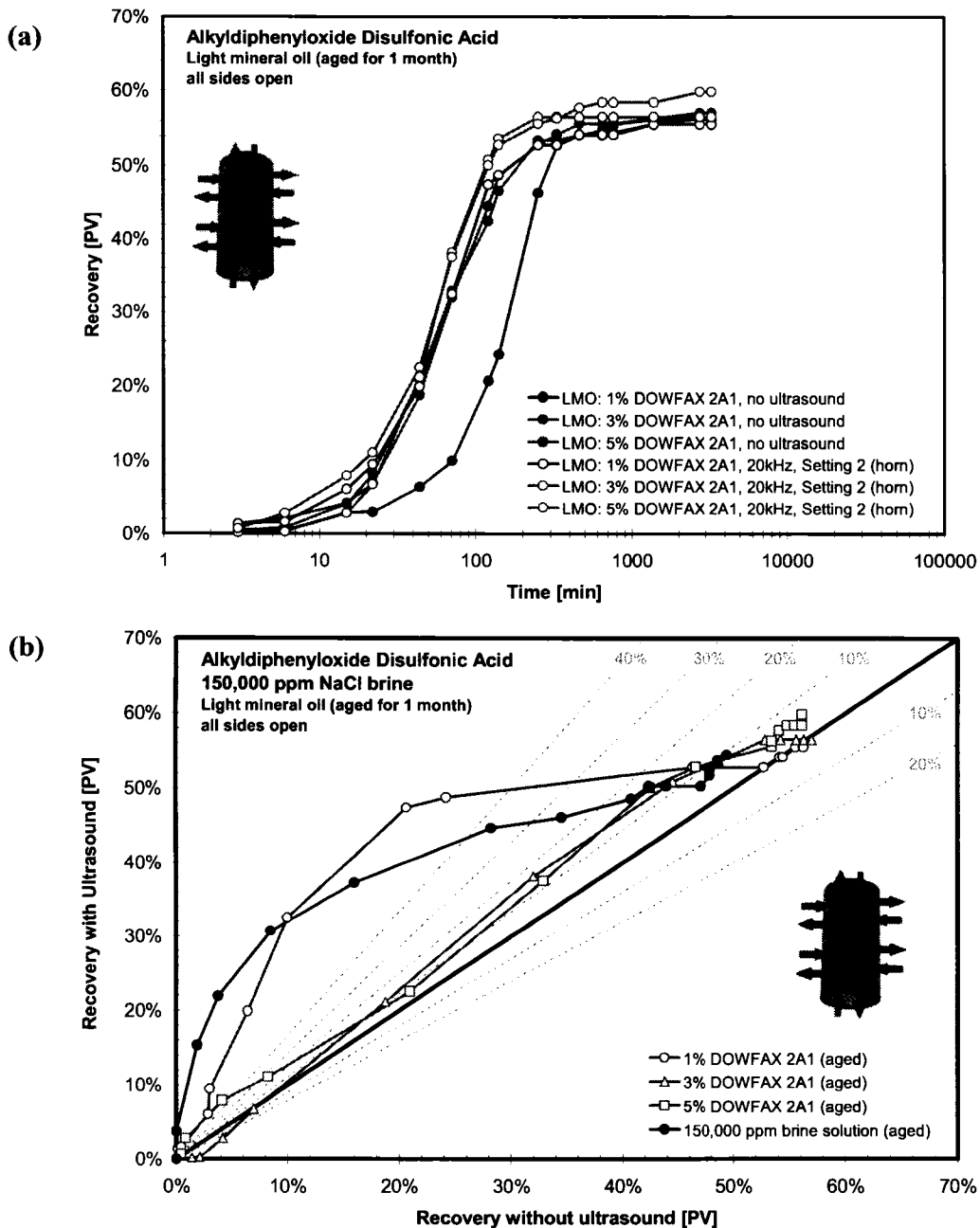


Figure 4-24: (a) Oil recovery vs. time, and (b) cross-comparison plot, of the spontaneous imbibition of various Alkyldiphenyloxide Disulfonic Acid solutions into light mineral oil saturated Berea sandstone (all sides open) under ultrasound after aging samples for one month. For comparison, we also added the imbibition performance of 150,000 ppm brine solution as aqueous phase. The 45° line in (b) represents the case when the response equals to that of the control. Dashed lines signify the percent deviation (%) from the control case.

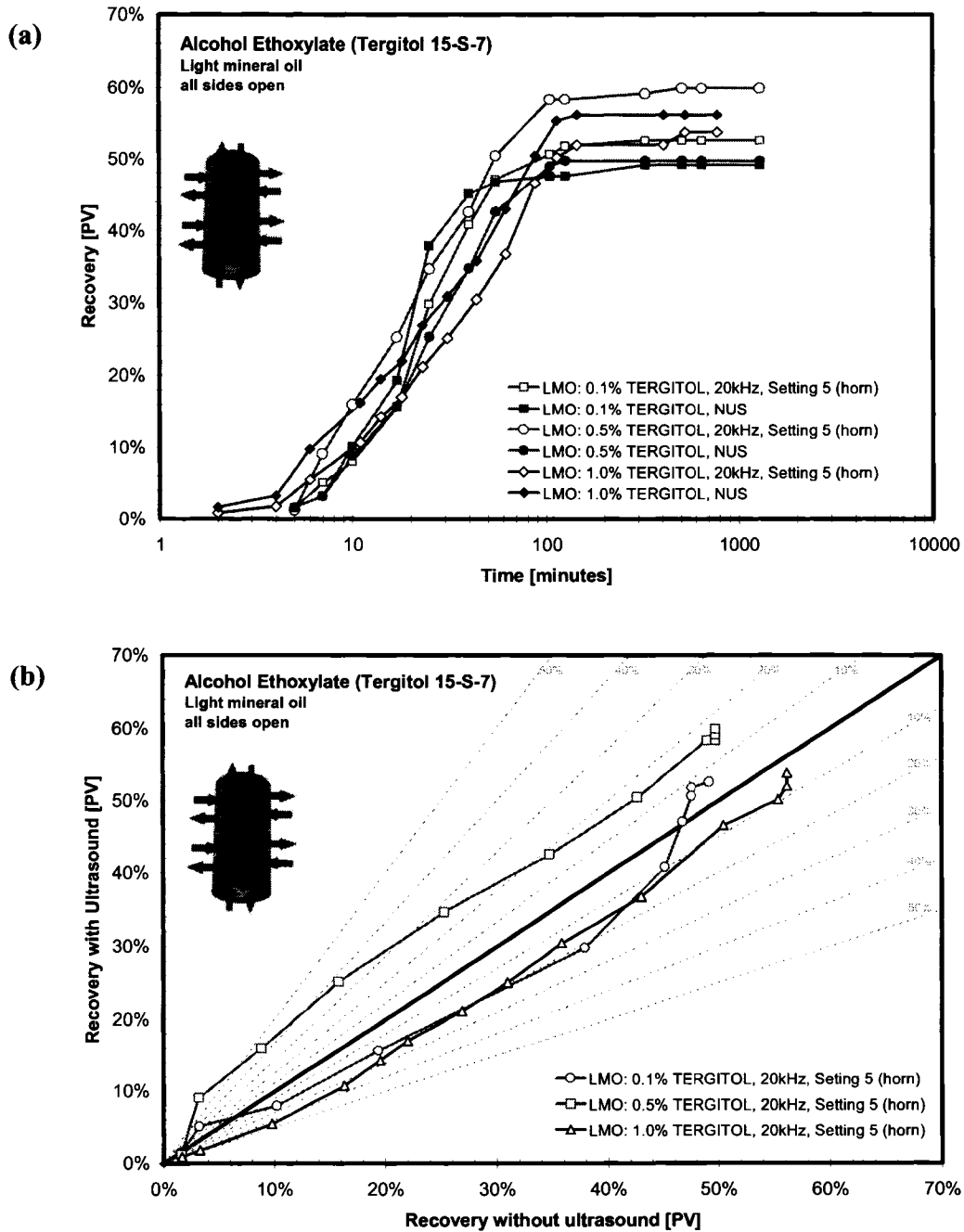


Figure 4-25: (a) Oil recovery vs. time, and (b) cross-comparison plot, of the spontaneous imbibition of various Alcohol Ethoxylate solutions into light mineral oil saturated Berea sandstone (all sides open) under ultrasound (Setting 5). The 45° line in (b) represents the case when the response equals to that of the control. Dashed lines signify the percent deviation (%) from the control case.

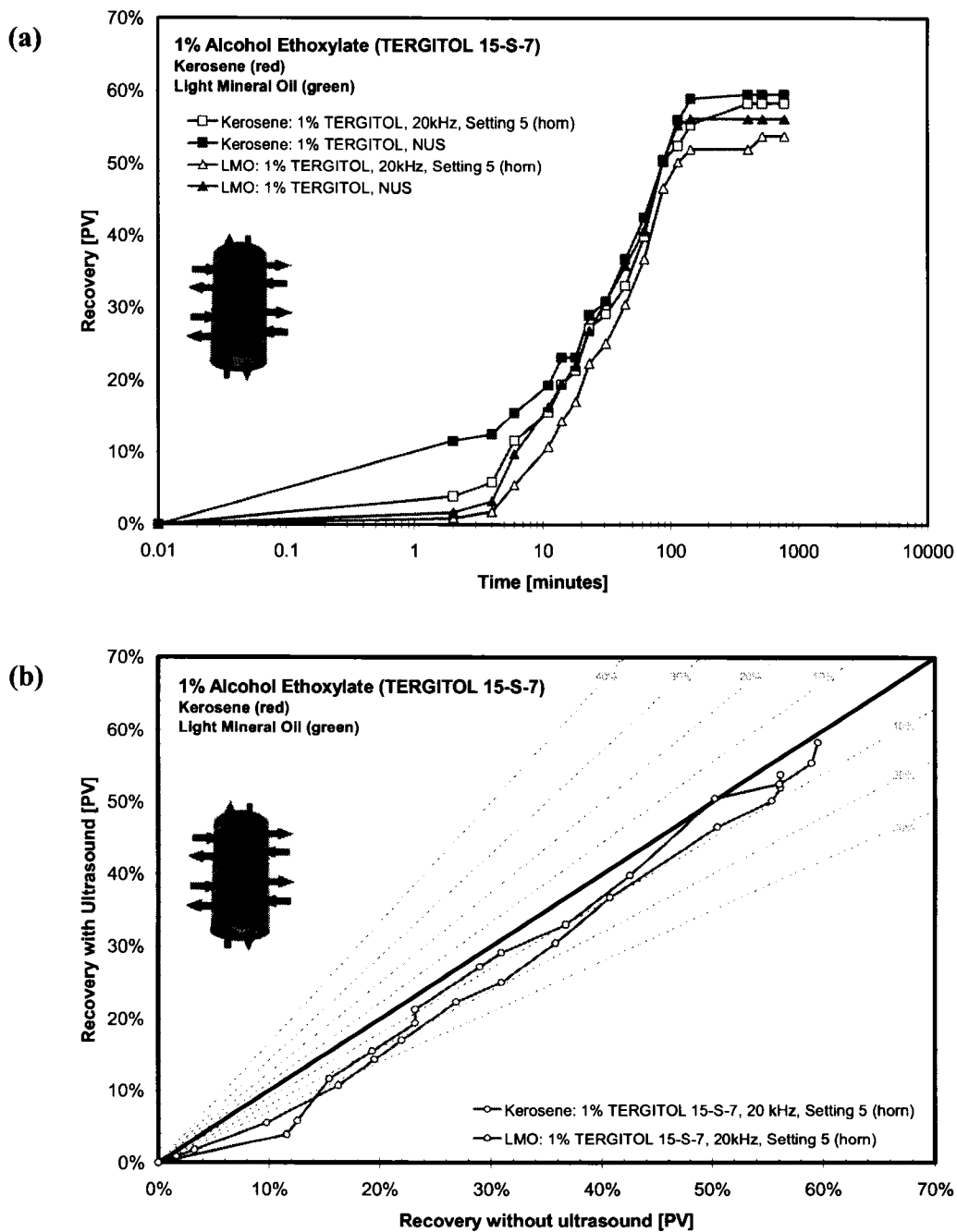


Figure 4-26: (a) Oil recovery vs. time, and (b) cross-comparison plot, of the spontaneous imbibition of 1% Alcohol Ethoxylate solution into kerosene and light mineral oil saturated Berea sandstone (all sides open) under ultrasound (Setting 5). The 45° line in (b) represents the case when the response equals to that of the control. Dashed lines signify the percent deviation (%) from the control case.

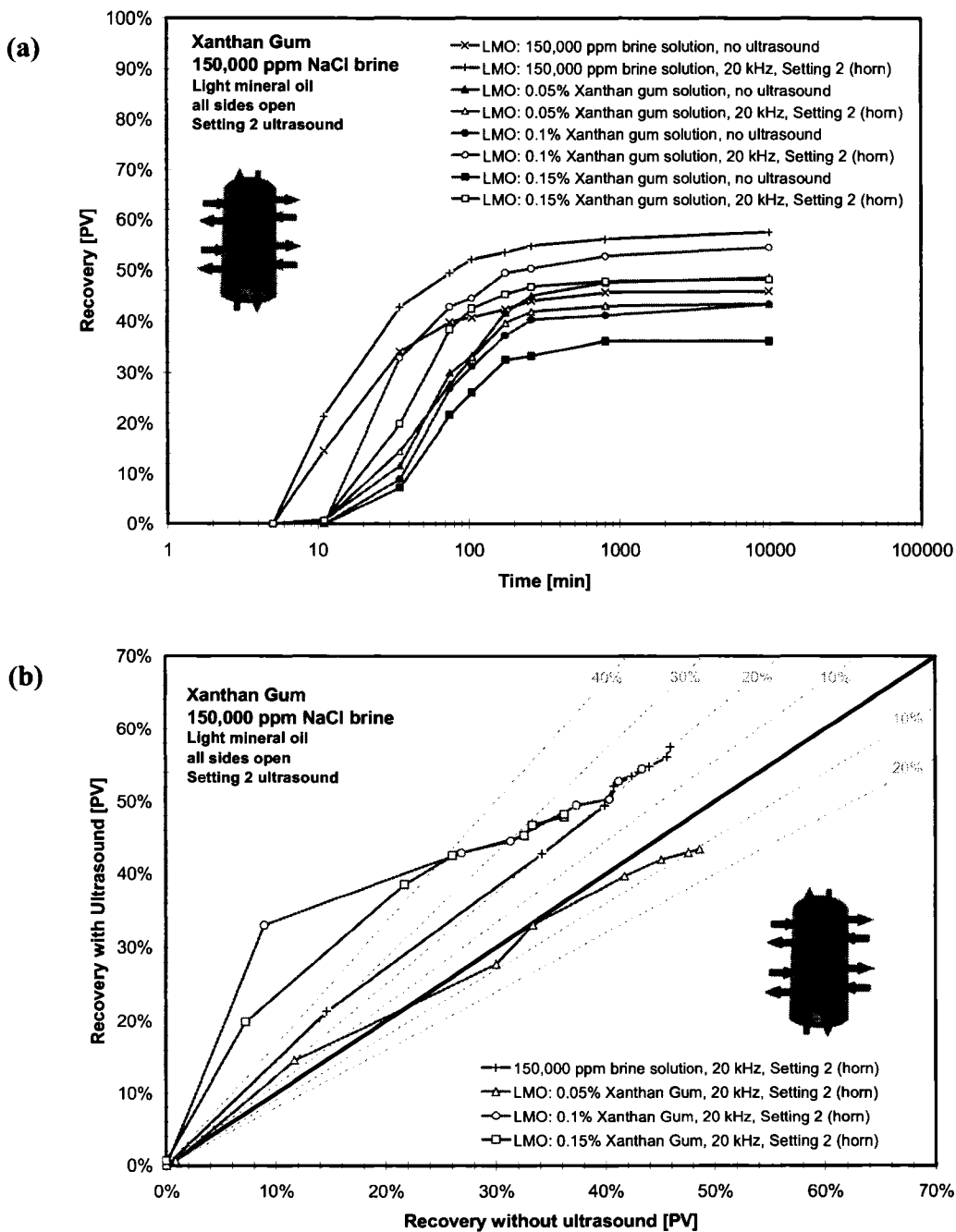


Figure 4-27: (a) Oil recovery vs. time, and (b) cross-comparison plot, of the spontaneous imbibition of various xanthan gum solutions into light mineral oil saturated Berea sandstone (all sides open) under ultrasound (Setting 2). For comparison, we also added the imbibition performance after using a 150,000 ppm brine solution as aqueous phase. The 45° line in (b) represents the case when the response equals to that of the control. Dashed lines signify the percent deviation (%) from the control case.

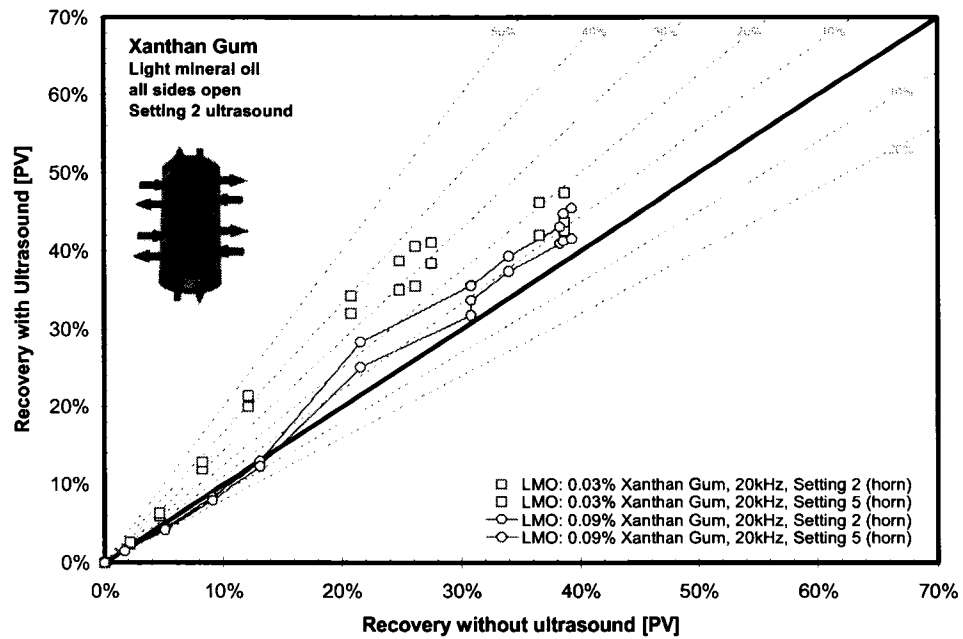


Figure 4-28: Cross-comparison plot of the spontaneous imbibition of 0.03 wt% and 0.09 wt% Xanthan gum solutions into light mineral oil saturated Berea sandstone (all sides open) under two ultrasonic settings. The 45o line represents the case when the response equals to that of the control. Dashed lines signify the percent deviation (%) from the control case.

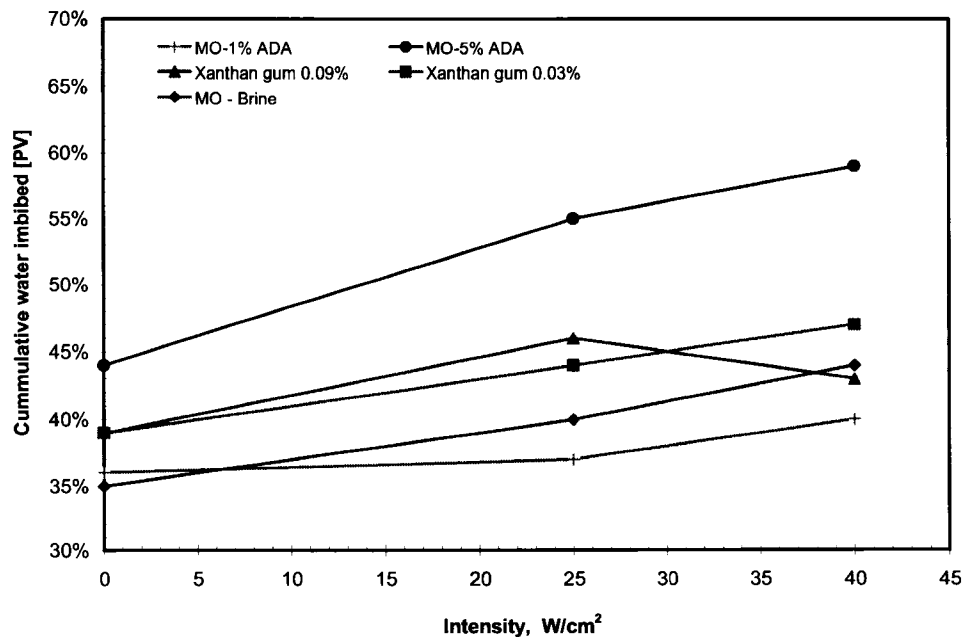


Figure 4-29: Cumulative water imbibed versus ultrasonic intensity for various fluid pairs. [MO: light mineral oil, ADA: DOWFAX 3B0]

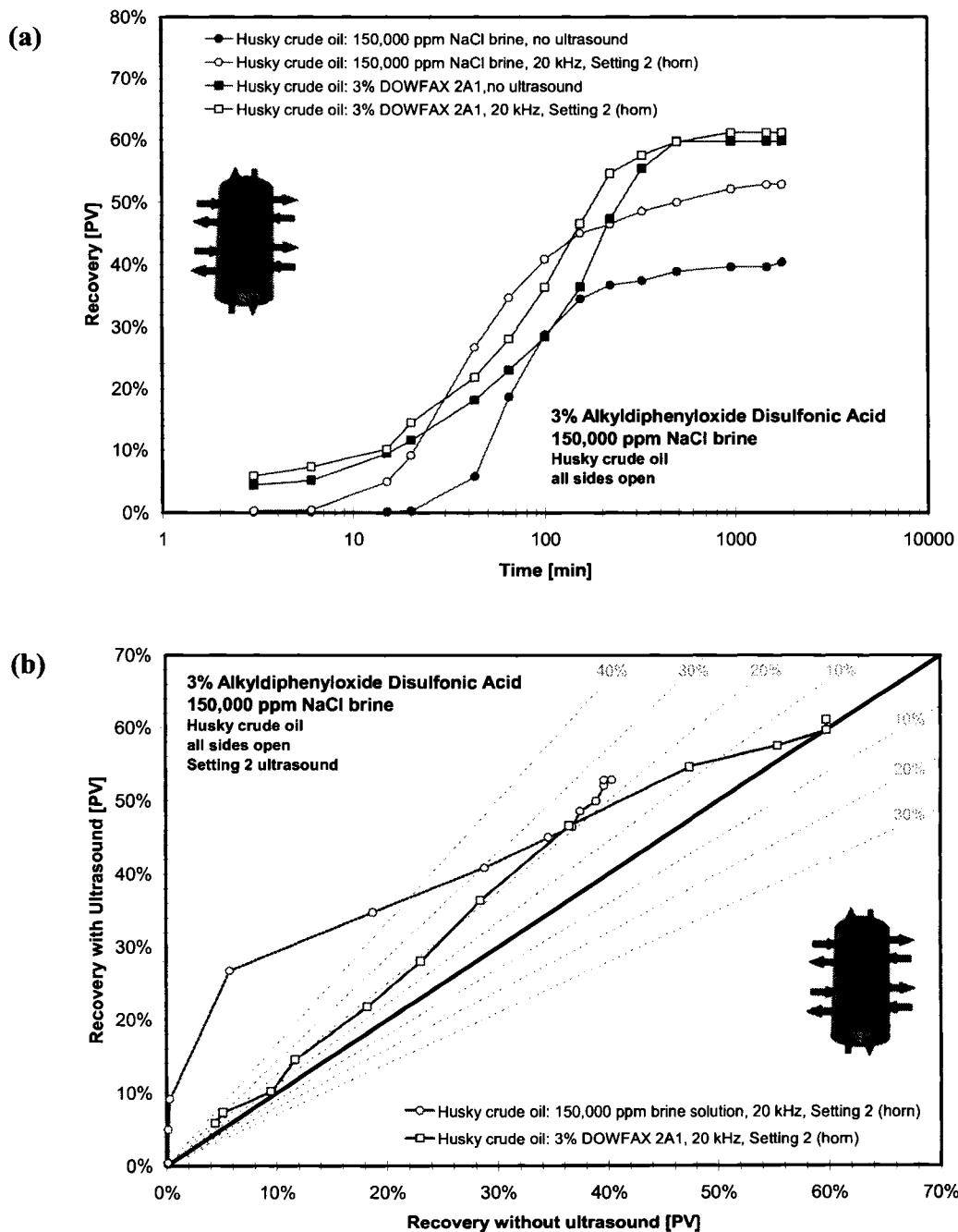


Figure 4-30: (a) Oil recovery vs. time, and (b) cross-comparison plot, of the spontaneous imbibition of 150,000 ppm NaCl brine and 3% Alyldiphenyloxide Disulfonic acid solution into crude oil saturated Berea sandstone (all sides open) under ultrasound (Setting 2). The 45° line in (b) represents the case when the response equals to that of the control. Dashed lines signify the percent deviation (%) from the control case.

References

- AARTS, A. C. T. and G. OOMS (1998). "Net flow of compressible viscous liquids induced by traveling waves in porous media." Journal of Engineering Mathematics **34**(4): 435-450.
- AARTS, A. C. T., *et al.* (1999). "Enhancement of Liquid Flow Through a Porous Medium by Ultrasonic Radiation." SPE Journal **4**(4): 321-327.
- ABAD-GUERRA, B. P. (1976). Methods for restoring productivity to gas wells in the Clinton sand of Ohio: A laboratory and field experiment, Pennsylvania State University. **Ph.D. thesis**
- ABISMAIL, B., *et al.* (1999). "Emulsification by ultrasound: drop size distribution and stability." Ultrasonics Sonochemistry **6**(1-2): 75-83.
- ABOUSLEIMAN, Y., *et al.* (1996). "Poroviscoelastic analysis of borehole and cylinder problems." Acta Mechanica **119**(1-4): 199-219.
- ABRASHKIN, A., *et al.* (2005). "A possible mechanism of the acoustic action on partially fluid-saturated porous media." Acoustical Physics **51**(1): S12-S22(1).
- AKIN, S., *et al.* (2000). "Spontaneous imbibition characteristics of diatomite." Journal of Petroleum Science and Engineering **25**(3-4): 149-165.
- BABADAGLI, T. (2002). "Dynamics of capillary imbibition when surfactant, polymer, and hot water are used as aqueous phase for oil recovery." Journal of Colloid and Interface Science **246**(1): 203-213.
- BABADAGLI, T., *et al.* (2005). SPE 92111 - Evaluation of Matrix-Fracture Transfer Functions for Countercurrent Capillary Imbibition. 2005 Asia Pacific Oil & Gas Conference and Exhibition, Jakarta, Indonesia.
- BEAR, J. (1988). Dynamics of fluids in porous media. New York, Dover.

- BERESNEV, I. A. and P. A. JOHNSON (1994). "Elastic-Wave Stimulation of Oil Production - a Review of Methods and Results." Geophysics **59**(6): 1000-1017.
- BERESNEV, I. A., *et al.* (2005). "Elastic waves push organic fluids from reservoir rock." Geophysical Research Letters **32**(13): L13303.
- BERNABE, Y. (1997). "The Frequency Dependence of Harmonic Fluid Flow Through Networks of Cracks and Pores." Pure and Applied Geophysics **149**(3): 489-506.
- BERRYMAN, J. G. (1981). "Elastic Wave-Propagation in Fluid-Saturated Porous-Media." Journal of the Acoustical Society of America **69**(2): 416-424.
- BIOT, M. A. (1956a). "Theory of Propagation of Elastic Waves in a Fluid-Saturated Porous Solid .1. Low-Frequency Range." Journal of the Acoustical Society of America **28**(2): 168-178.
- BIOT, M. A. (1956b). "Theory of Propagation of Elastic Waves in a Fluid-Saturated Porous Solid .2. Higher Frequency Range." Journal of the Acoustical Society of America **28**(2): 179-191.
- BIOT, M. A. (1962). "Mechanics of Deformation and Acoustic Propagation in Porous Media." Journal of Applied Physics **33**(4): 1482.
- BJERKNES, V. F. K. (1906). Fields of Force. New York, Columbia University Press.
- BJORNDALEN, N. and M. R. ISLAM (2004). "The effect of microwave and ultrasonic irradiation on crude oil during production with a horizontal well." Journal of Petroleum Science and Engineering **43**(3-4): 139-150.
- BLAKE, F. G. (1949). "Bjerknes Forces in Stationary Sound Fields." Journal of the Acoustical Society of America **21**(5): 551-551.
- BONNET, G. (1987). "Basic Singular Solutions for a Poroelastic Medium in the Dynamic-Range." Journal of the Acoustical Society of America **82**(5): 1758-1762.

- BRINCK, J., *et al.* (1998a). "Kinetics of nonionic surfactant adsorption and desorption at the silica-water interface: Binary systems." Langmuir **14**(20): 5863-5876.
- BRINCK, J., *et al.* (1998b). "Kinetics of nonionic surfactant adsorption and desorption at the silica-water interface: One component." Langmuir **14**(5): 1058-1071.
- BUCKINGHAM, M. J. (1997). "Theory of acoustic attenuation, dispersion, and pulse propagation in unconsolidated granular materials including marine sediments." Journal of the Acoustical Society of America **102**(5): 2579-2596.
- BUCKINGHAM, M. J. (1999). "Theory of compressional and transverse wave propagation in consolidated porous media." Journal of the Acoustical Society of America **106**(2): 575-581.
- BUCKINGHAM, M. J. (2005). "Compressional and shear wave properties of marine sediments: Comparisons between theory and data." Journal of the Acoustical Society of America **117**(1): 137-152.
- CHAMPION, B., *et al.* (2004). "The application of high-power sound waves for wellbore cleaning." SPE Production & Facilities **19**(3): 113-121.
- CHAPMAN, A. M. and J. J. L. HIGDON (1992). "Oscillatory Stokes-Flow in Periodic Porous-Media." Physics of Fluids a-Fluid Dynamics **4**(10): 2099-2116.
- CHARLAIX, E., *et al.* (1988). "Experimental-Study of Dynamic Permeability in Porous-Media." Physical Review Letters **61**(14): 1595-1598.
- CHEN, J. D. (1989). "Growth of Radial Viscous Fingers in a Hele-Shaw Cell." Journal of Fluid Mechanics **201**: 223-242.
- CHEN, W. I. (1969). Influence of Ultrasonic Energy Upon the Rate of Flow of Liquids Through Porous Media. Chemical Engineering, West Virginia University. **Ph.D. thesis**: 141.

- CHERSKIY, N. V., *et al.* (1977). "The effect of ultrasound on permeability of rocks to water." Trans.(Doklady) USSR Acad. Sci., Earth Sci. Sect. **232**: 201-204.
- CHUOKE, R. L., *et al.* (1959). "The Instability of Slow, Immiscible, Viscous Liquid-Liquid Displacements in Permeable Media." Transactions of the American Institute of Mining and Metallurgical Engineers **216**: 188-194.
- CIL, M. (1997). An Investigation of countercurrent imbibition recovery in naturally fractured reservoirs with experimental analysis and analytical modeling, University of Texas at Austin. **Ph.D. thesis**: 265.
- CRAMER, C. (2004). Continuous Drop Formation at a Capillary Tip and Drop Deformation in a Flow Channel. Laboratory of Food Process Engineering. Zurich, Switzerland, Swiss Federal Institute of Technology (ETH). **Ph.D. thesis**: 181.
- DACCORD, G. and J. NITTMANN (1986). "Radial Viscous Fingers and Diffusion-Limited Aggregation - Fractal Dimension and Growth Sites." Physical Review Letters **56**(4): 336-339.
- DERESIEWICZ, H. (1974). "Effect of Boundaries on Wave-Propagation in a Liquid-Filled Porous Solid .11. Waves in a Plate." Bulletin of the Seismological Society of America **64**(6): 1901-1907.
- DERESIEWICZ, H. and A. LEVY (1967). "Effect of Boundaries on Wave Propagation in a Liquid-Filled Porous Solid .X. Transmission through a Stratified Medium." Bulletin of the Seismological Society of America **57**(3): 381-&.
- DERESIEWICZ, H. and J. T. RICE (1962). "The effect of boundaries on wave propagation in a liquid-filled porous solid: III. Reflection of plane waves at a free plane boundary (general case)." Bulletin of Seismology Society of America **52**: 595.
- DEZHKUNOV, N. V. and T. G. LEIGHTON (2004). "Study into Correlation between the Ultrasonic Capillary Effect and Sonoluminescence." J. Eng. Phys. Thermophys. **77**(1): 53-61.

- DUHON, R. D. (1964). An Investigation of the Effect of Ultrasonic Energy on the Flow of Fluids in Porous Media, University of Oklahoma. **Ph.D. thesis**
- DUHON, R. D. and J. M. CAMPBELL (1965). SPE 1316 - The Effect of Ultrasonic Energy on Flow Through Porous Media. 2nd Annual Eastern Regional Meeting of SPE/AIME, Charleston, WV.
- DUNIN, S. and V. N. NIKOLAEVSKII (2005). "Nonlinear waves in porous media saturated with live oil." Acoustical Physics **51**(1): S61-S66(1).
- DUNN, K. and T. F. YEN (2001). "A plausible reaction pathway of asphaltene under ultrasound." Fuel Processing Technology **73**(1): 59-71.
- DUNN, K. J. (1986). "Acoustic Attenuation in Fluid-Saturated Porous Cylinders at Low-Frequencies." Journal of the Acoustical Society of America **79**(6): 1709-1721.
- DUSSEAULT, M., *et al.* (2000). "Pressure pulsing: The ups and downs of starting a new technology." Journal of Canadian Petroleum Technology **39**(4): 13.
- DVALI, M. F. and O. M. SUMAROKOV (1968). "A new method of removing paraffin from tubes and wellbores." Oil Industry (Neftianoye Khoziastvo) **2**: 45-48.
- DYBLENKO, V. P., *et al.* (1989). "Percolation Phenomena and Processes in Saturated Porous Media under the Vibro-Wave Action, in Ways of Intensification of Oil Production (Putu intensivatsii dobychi nefi)." Proc. (Trudy) Basharki Research and Design Institute of Oil (Bashnipineft): 45-51.
- EGGERS, J. and T. F. DUPONT (1994). "Drop Formation in a One-Dimensional Approximation of the Navier-Stokes Equation." Journal of Fluid Mechanics **262**: 205-221.
- ELLIS, C. A. (1966). An Investigation of an Ultrasonic, High Pressure Waterflood in a Linear Porous Medium. Petroleum Engineering, University of Oklahoma. **Ph.D. thesis: 78.**

- FAIRBANKS, H. V. (1976). Ultrasonic Stimulation of Liquid Flow. Ultrasonics Symposium.
- FAIRBANKS, H. V. and W. I. CHEN (1971). "Ultrasonic acceleration of liquid flow through porous media." A.I.Ch.E. Sonochem. Eng. **67**: 105.
- FENG, S. and D. L. JOHNSON (1983a). "High-Frequency Acoustic Properties of a Fluid Porous Solid Interface .1. New Surface-Mode." Journal of the Acoustical Society of America **74**(3): 906-914.
- FENG, S. and D. L. JOHNSON (1983b). "High-Frequency Acoustic Properties of a Fluid Porous Solid Interface .2. The 2D Reflection Greens-Function." Journal of the Acoustical Society of America **74**(3): 915-924.
- FERNANDEZ, J. and G. M. HOMS Y (2003). "Viscous fingering with chemical reaction: effect of in-situ production of surfactants." Journal of Fluid Mechanics **480**: 267-281.
- FISCHER, H. and N. R. MORROW (2005). Spontaneous Imbibition with Matched Liquid Viscosities. 2005 SPE Annual Technical Conference and Exhibition, Dallas, Texas.
- FRENKEL, J. (1944). "On the theory of seismic and seismoelectric phenomena in a moist soil." Journal of Physics **111**(5): 230-241.
- FRENKEL, J. (2005). "On the theory of seismic and seismoelectric phenomena in a moist soil." Journal of Engineering Mechanics-ASCE **131**(9): 879-887.
- GADIEV, S. M. (1977). Use of vibrations in oil production (Ispol'zovaniye vibratsii v dobyche nefi). Moscow, Nedra Press.
- GAITAN, D. F., *et al.* (1992). "Sonoluminescence and Bubble Dynamics for a Single, Stable, Cavitation Bubble." Journal of the Acoustical Society of America **91**(6): 3166-3183.

- GANIEV, R. F., *et al.* (1989). "Wave mechanism for the acceleration of a liquid flowing in capillaries and porous media." Sov. Phys. Dokl. **34**: 267-283.
- GARG, A., *et al.* (1996). SPE35737 - CT Scan and Neural Network Technology for Construction of Detailed Distribution of Residual Oil Saturation During Waterflooding. 66th Western Regional Meeting, Alaska, USA.
- GHDAN, S. G. and F. H. POETTMANN (1991). "Effect of Polymers on the Imbibition Process: A Laboratory Study." SPE Reservoir Engineering: 84-90.
- GOLLAPUDI, U. K., *et al.* (1994). SPE 27377 - Ultrasonic Treatment for Removal of Asphaltene Deposits During Petroleum Production. 1994 SPE Int. Symposium on Formation Damage Control, Lafayette, LA.
- GRAHAM, D. R. (1997). Steady and oscillatory flow through model porous media, University of Illinois. **M.Sc. thesis**
- GRAHAM, D. R. (1999). Acoustic stimulation of multiphase flow in porous media, University of Illinois. **Ph.D. thesis**
- GRAHAM, D. R. and J. J. L. HIGDON (2000a). "Oscillatory flow of droplets in capillary tubes. Part 1. Straight tubes." Journal of Fluid Mechanics **425**: 31-53.
- GRAHAM, D. R. and J. J. L. HIGDON (2000b). "Oscillatory flow of droplets in capillary tubes. Part 2. Constricted tubes." Journal of Fluid Mechanics **425**: 55-77.
- GRAHAM, D. R. and J. J. L. HIGDON (2002a). "Oscillatory forcing of flow through porous media. Part 1. Steady flow." Journal of Fluid Mechanics **465**: 213-235.
- GRAHAM, D. R. and J. J. L. HIGDON (2002b). "Oscillatory forcing of flow through porous media. Part 2. Unsteady flow." Journal of Fluid Mechanics **465**: 237-260.
- GRAHAM, J. W. and J. G. RICHARDSON (1959). "Theory and Application of Imbibition Phenomena in Recovery of Oil." Transactions of the American Institute of Mining and Metallurgical Engineers **216**: 377-381.

- GRONROOS, A., *et al.* (2004). "Ultrasonic depolymerization of aqueous carboxymethylcellulose." Ultrasonics Sonochemistry **11**(1): 9-12.
- GUAN, X. and R. PITCHUMANI (2003). "Viscous fingering in a Hele-Shaw cell with finite viscosity ratio and interfacial tension." Journal of Fluids Engineering-Transactions of the ASME **125**(2): 354-364.
- GUREVICH, B., *et al.* (1999). "Validation of the slow compressional wave in porous media: Comparison of experiments and numerical simulations." Transport in Porous Media **36**(2): 149-160.
- HAMON, G. and J. VIDAL (1986). SPE 15852 - Scaling-Up the Capillary Imbibition Process From Laboratory Experiments on Homogeneous and Heterogeneous Samples. 1986 European Petroleum Conference, London, United Kingdom.
- HANDY, L. L. (1960). "Determination of Effective Capillary Pressure for Porous Media from Imbibition Data." Trans. AIME **219**: 75.
- HARKINS, W. D. and F. E. BROWN (1919). "The determination of surface tension (free surface energy), and the weight of falling drops - The surface tension of water and benzene by the capillary height method." Journal of the American Chemical Society **41**: 499-524.
- HAYWORTH, C. B. and R. E. TREYBAL (1950). "Drop Formation in 2-Liquid-Phase Systems." Industrial and Engineering Chemistry **42**(6): 1174-1181.
- HERSKOWITZ, M., *et al.* (1999). "Acoustic waves in a liquid-filled bed with microbubbles." Acustica **85**(6): 793-799.
- HERSKOWITZ, M., *et al.* (2000). "Attenuation of ultrasound in porous media with dispersed microbubbles." Ultrasonics **38**(1-8): 767-769.
- HILPERT, M., *et al.* (2000). "Capillarity-induced resonance of oil blobs in capillary tubes and porous media." Geophysics **65**(3): 874-883.

- HOMSY, G. M. (1987). "Viscous Fingering in Porous-Media." Annual Review of Fluid Mechanics **19**: 271-311.
- HORBLIT, W. (1951). De-waxing oil in an ultrasonic field, Colorado School of Mines **Ph.D. thesis**.
- IASSONOV, P. P. and I. A. BERESNEV (2003). "A model for enhanced fluid percolation in porous media by application of low-frequency elastic waves." Journal of Geophysical Research-Solid Earth **108**(B3): -.
- IOVENITTI, J. L., *et al.* (1996). Acoustically Enhanced Remediation: Phase II-Technology Scaling. 1996 DOE Conference on Industry Partnerships to Deploy Environmental Technology, Morgantown, WV.
- JAFFRIN, M. Y. and A. H. SHAPIRO (1971). "Peristaltic Pumping." Annual Review of Fluid Mechanics **3**: 13.
- JAFFRIN, M. Y., *et al.* (1969). "Peristaltic Transport." Journal of Applied Mechanics **36**(2): 379.
- JOHNSON, D. L., *et al.* (1987). "Theory of Dynamic Permeability and Tortuosity in Fluid-Saturated Porous-Media." Journal of Fluid Mechanics **176**: 379-402.
- JOHNSON, P. A. and K. R. MCCALL (1994). "Observation and Implications of Nonlinear Elastic-Wave Response in Rock." Geophysical Research Letters **21**(3): 165-168.
- KARPERIEN, A. (2005). FracLac V.2. NSW, Australia, Charles Stuart University.
- KARPERIEN, A. (2006). DLA StacksGenerator. NSW, Australia, Charles Stuart University.
- KATSUYAMA, T. and K. NAGATA (1999). "Behavior of the dripping faucet over a wide range of the flow rate." Journal of the Physical Society of Japan **68**(2): 396-400.
- KIM, E. and G. M. WHITESIDES (1997). "Imbibition and flow of wetting liquids in noncircular capillaries." Journal of Physical Chemistry B **101**(6): 855-863.

- KIM, Y. U. and M. C. WANG (2003). "Effect of ultrasound on oil removal from soils." Ultrasonics **41**(7): 539-542.
- KIYONO, K. and N. FUCHIKAMI (1999). "Dripping faucet dynamics by an improved mass-spring model." Journal of the Physical Society of Japan **68**(10): 3259-3270.
- KOSTROV, S. and W. WOODEN (2005). "In situ seismic stimulation shows promise for revitalizing mature fields." Oil & Gas Journal **103**(15): 43-49.
- Kulicke, W. M., *et al.* (1993). "Improved NMR Characterization of High-Molecular-Weight Polymers and Polyelectrolytes through the Use of Preliminary Ultrasonic Degradation." Makromolekulare Chemie-Macromolecular Chemistry and Physics **194**(3): 751-765.
- KUZNETSOV, L. and E. M. SIMKIN (1990). "Transformation and interaction of geophysical fields in lithosphere (Preobrazovaniye i vzaimodeystviye geofizicheskikh poley v litosfere)." Nedra Press.
- KUZNETSOV, O. L., *et al.* (2002). "Seismic techniques of enhanced oil recovery: Experimental and field results." Energy Sources **24**(9): 877-889.
- KUZNETSOV, O. L., *et al.* (1998). "Improved oil recovery by application of vibro-energy to waterflooded sandstones." Journal of Petroleum Science and Engineering **19**(3-4): 191-200.
- LAWSON, J. B. (1978). The Adsorption of Non-Ionic Surfactants on Sandstone and Carbonate. 1978 SPE Symposium on Improved Methods for Oil Recovery, Tulsa, OK.
- LEVERETT, M. C. (1941). "Capillary behavior in porous solids." Transactions of the American Institute of Mining and Metallurgical Engineers **142**: 152-169.
- LEVERETT, M. C., *et al.* (1942). "Dimensional-model studies of oil-field behavior." Transactions of the American Institute of Mining and Metallurgical Engineers **146**: 175-192.

- LI, K. W. and R. N. HORNE (2001). "Characterization of spontaneous water imbibition into gas-saturated rocks." SPE Journal **6**(4): 375-384.
- LI, K. W. and R. N. HORNE (2004). "An analytical scaling method for spontaneous imbibition in gas/water/rock systems." SPE Journal **9**(3): 322-329.
- LI, W. Q., *et al.* (2005). "Vibration-induced mobilization of trapped oil ganglia in porous media: Experimental validation of a capillary-physics mechanism." Journal of Colloid and Interface Science **289**(1): 193-199.
- LIEBOVITCH, L. S. and T. TOTH (1989). "A Fast Algorithm to Determine Fractal Dimensions by Box Counting." Physics Letters A **141**(8-9): 386-390.
- LIN, J. R. and T. F. YEN (1993). "An Upgrading Process through Cavitation and Surfactant." Energy & Fuels **7**(1): 111-118.
- MANDELBROT, B. B. (1983). The fractal geometry of nature. San Francisco, W.H. Freeman.
- MANNHARDT, K., *et al.* (1994). "Adsorption of Foam-Forming Surfactants in Berea Sandstone." Journal of Canadian Petroleum Technology **33**(2): 34-43.
- MARTIEN, P., *et al.* (1985). "The Chaotic Behavior of the Leaky Faucet." Physics Letters A **110**(7-8): 399-404.
- MATTAX, C. C. and J. R. KYTE (1962). "Imbibition Oil Recovery from Fractured, Water-Drive Reservoir." Transactions of the Society of Petroleum Engineers of AIME **225**(2): 177-184.
- MAXWORTHY, T. (1987). "The Nonlinear Growth of a Gravitationally Unstable Interface in a Hele-Shaw Cell." Journal of Fluid Mechanics **177**: 207-232.
- MAY, S. E. and J. V. MAHER (1989). "Fractal Dimension of Radial Fingering Patterns." Physical Review A **40**(3): 1723-1726.

- MCLEAN, J. W. and P. G. SAFFMAN (1981). "The Effect of Surface-Tension on the Shape of Fingers in a Hele Shaw Cell." Journal of Fluid Mechanics **102**(Jan): 455-469.
- METTIN, R., *et al.* (1997). "Bjerknes forces between small cavitation bubbles in a strong acoustic field." Physical Review E **56**(3): 2924-2931.
- MIKHAILOV, V. M., *et al.* (1975). "Study of ultrasonic effect on percolation process in porous media." Proc. (Trudy) All Union Research Institute of Nuclear Geophysics and Geochemistry **24**: 78-87.
- MOHOLKAR, V. S. and M. M. C. G. WARMOESKERKEN (2004). "Investigations in mass transfer enhancement in textiles with ultrasound." Chemical Engineering Science **59**(2): 299-311.
- MOHOLKAR, V. S., *et al.* (2004). "Mechanism of mass-transfer enhancement in textiles by ultrasound." AIChE Journal **50**(1): 58-64.
- MORROW, N. R. and G. MASON (2001). "Recovery of oil by spontaneous imbibition." Current Opinion in Colloid & Interface Science **6**(4): 321-337.
- NAGY, P. B. (1992). "Observation of a New Surface-Mode on a Fluid-Saturated Permeable Solid." Applied Physics Letters **60**(22): 2735-2737.
- NAGY, P. B. (1993). "Slow-Wave Propagation in Air-Filled Permeable Solids." Journal of the Acoustical Society of America **93**(6): 3224-3234.
- NERETIN, V. D. and V. A. YUDIN (1981). "Results of experimental study of the influence of acoustic treatment on percolation processes in saturated porous media." Topics in Nonlinear Geophysics (Voprosi nelineinoy geofisiki): All Union Research Institute of Nuclear Geophysics and Geochemistry: 132-137.
- NIKOLAEVSKII, V. N. (1989). "Mechanism of Vibroaction for Oil Recovery from Reservoirs and Dominant Frequencies." Doklady Akademii Nauk SSSR **307**(3): 570-575.

- NIKOLAEVSKII, V. N. (1992). "Rock Vibration and Finite Oil Recovery." Fluid Dynamics **27**(5): 689-696.
- NIKOLAEVSKII, V. N. and G. S. STEPANOVA (2005). "Nonlinear seismic and the acoustic action on the oil recovery from an oil pool." Acoustical Physics **51**: S131-S139.
- NIKOLAEVSKIY, V. N., *et al.* (1996). "Residual oil reservoir recovery with seismic vibrations." SPE Production & Facilities **11**(2): 89-94.
- NORRIS, A. N. (1989). "Stoneley-Wave Attenuation and Dispersion in Permeable Formations." Geophysics **54**(3): 330-341.
- NULL, H. R. and H. F. JOHNSON (1958). "Drop Formation in Liquid-Liquid Systems from Single Nozzles." AIChE Journal **4**(3): 273-281.
- OHKAWA, K. (2006). "Confirmation of the Biot theory for water-saturated sands at high frequencies and effects of scattering on the attenuation of sound waves (L)." Journal of the Acoustical Society of America **119**(2): 709-711.
- PARK, C. W. and G. M. HOMS Y (1985). "The Instability of Long Fingers in Hele Shaw Flows." Physics of Fluids **28**(6): 1583-1585.
- PATERSON, L. (1984). "Diffusion-Limited Aggregation and 2-Fluid Displacements in Porous-Media." Physical Review Letters **52**(18): 1621-1624.
- PELLICER, J., *et al.* (2000). "On the demonstration of the Young-Laplace equation in introductory physics courses." Physics Education **35**(2): 126-129.
- PLONA, T. J. (1980). "Observation of a 2Nd Bulk Compressional Wave in a Porous-Medium at Ultrasonic Frequencies." Applied Physics Letters **36**(4): 259-261.
- PLOTNICK, R. E., *et al.* (1996). "Lacunarity analysis: A general technique for the analysis of spatial patterns." Physical Review E **53**(5): 5461-5468.
- PLOURABOUE, F. and E. J. HINCH (2002). "Kelvin-Helmholtz instability in a Hele-Shaw cell." Physics of Fluids **14**(3): 922-929.

- POESIO, P. and G. OOMS (2004). "Formation and ultrasonic removal of fouling particle structures in a natural porous material." Journal of Petroleum Science and Engineering **45**(3-4): 159-178.
- POESIO, P., *et al.* (2004). "Removal of small particles from a porous material by ultrasonic irradiation." Transport in Porous Media **54**(3): 239-264.
- PRAUD, O. and H. L. SWINNEY (2005). "Fractal dimension and unscreened angles measured for radial viscous fingering." Physical Review E **72**(1): -.
- PRIDE, S. R., *et al.* (1993). "Drag Forces of Porous-Medium Acoustics." Physical Review B **47**(9): 4964-4978.
- PROKHORENKO, P. P., *et al.* (1982). "Calculating the Process of Filling of Microcapillaries with Liquids under Ultrasonic Action." Soviet Journal of Nondestructive Testing-USSR **18**(4): 326-331.
- RASBAND, W. S. (1997-2005). ImageJ. Maryland, USA, U.S. National Institute of Health.
- RASOLOFOSAON, P. N. J. (1988). "Importance of Interface Hydraulic Condition on the Generation of 2Nd Bulk Compressional Wave in Porous-Media." Applied Physics Letters **52**(10): 780-782.
- RAUSEO, S. N., *et al.* (1987). "Development of Radial Fingering Patterns." Physical Review A **35**(3): 1245-1251.
- RAVAZZOLI, C. L., *et al.* (2003). "Acoustic and mechanical response of reservoir rocks under variable saturation and effective pressure." Journal of the Acoustical Society of America **113**(4): 1801-1811.
- REDDI, L. N., *et al.* (1993). "Feasibility of Ultrasonic Enhancement of Flow in Clayey Sands." Journal of Environmental Engineering **119**(4): 746-752.

- REDDI, L. N. and S. CHALLA (1994). "Vibratory Mobilization of Immiscible Liquid Ganglia in Sands." Journal of Environmental Engineering-ASCE **120**(5): 1170-1190.
- REDDI, L. N. and H. WU (1996). "Mechanisms involved in vibratory destabilization of NAPL ganglia in sands." Journal of Environmental Engineering-ASCE **122**(12): 1115-1119.
- REIS, J. C. and M. CIL (1993). "A Model for Oil Expulsion by Countercurrent Water Imbibition in Rocks - One-Dimensional Geometry." Journal of Petroleum Science and Engineering **10**(2): 97-107.
- RENNA, L. (2001). "Mass on a spring map for the dripping faucet at low flow rates." Physical Review E **6404**(4): -.
- RIERA, E., *et al.* (2004). "Mass transfer enhancement in supercritical fluids extraction by means of power ultrasound." Ultrasonics Sonochemistry **11**(3-4): 241-244.
- ROBERTS, P. M., *et al.* (2001). "Enhanced DNAPL transport in a sand core during dynamic stress stimulation." Environmental Engineering Science **18**(2): 67-79.
- ROBERTS, P. M., *et al.* (2000). "Ultrasonic removal of organic deposits and polymer-induced formation damage." SPE Drilling & Completion **15**(1): 19-24.
- ROZIN, Y. P., *et al.* (1984). "On the Meniscus Motion in a Capillary under the Effect of Supersound." Ukrainskii Fizicheskii Zhurnal **29**(10): 1522-1525.
- ROZIN, Y. P., *et al.* (2001). "The local heating of a liquid in a capillary due to ultrasonic action." Journal of Molecular Liquids **93**(1-3): 55-59.
- ROZINA, E. Y. (2002). "Effect of pulsed ultrasonic field on the filling of a capillary with a liquid." Colloid Journal **64**(3): 359-363.

- ROZINA, E. Y. and Y. P. ROZIN (1994). "The Experimental Investigation of the Kinetics of Filling up the Capillary in Cavitation Regime." Ukrainskii Fizicheskii Zhurnal **39**(5-6): 570-574.
- SADEGHI, K. M., *et al.* (1994). "Sonochemical Treatment of Fossil-Fuels." Energy Sources **16**(3): 439-449.
- SADEGHI, K. M., *et al.* (1992). "A New Process for Tar Sand Recovery." Chemical Engineering Communications **117**: 191-203.
- SADEGHI, K. M., *et al.* (1990). "Novel Extraction of Tar Sands by Sonication with the Aid of Insitu Surfactants." Energy & Fuels **4**(5): 604-608.
- SAFFMAN, P. G. and G. TAYLOR (1958). "The Penetration of a Fluid into a Porous Medium or Hele-Shaw Cell Containing a More Viscous Liquid." Proceedings of the Royal Society of London Series a-Mathematical and Physical Sciences **245**(1242): 312-&.
- SAHIMI, M. (1993). "Flow Phenomena in Rocks - from Continuum Models to Fractals, Percolation, Cellular-Automata, and Simulated Annealing." Reviews of Modern Physics **65**(4): 1393-1534.
- SCHOEPEL, R. J. and A. W. HOWARD (1966). SPE 1507 - Effect of Ultrasonic Irradiation on Coalescence and Separation of Crude Oil-Water Emulsions. 41st Annual Fall Meeting of the SPE/AIME, Dallas, TX.
- SHAPIRO, A. H., *et al.* (1969). "Peristaltic Pumping with Long Wavelengths at Low Reynolds Number." Journal of Fluid Mechanics **37**: 799-&.
- SHEDID, S. A. (2002). "A novel technique of asphaltene deposition treatment using ultrasonic irradiation." Petroleum Science and Technology **20**(9-10): 1097-1118.
- SHEDID, S. A. (2004). "An ultrasonic irradiation technique for treatment of asphaltene deposition." Journal of Petroleum Science and Engineering **42**(1): 57-70.

- SHENG, P. and M. Y. ZHOU (1988). "Dynamic Permeability in Porous-Media." Physical Review Letters **61**(14): 1591-1594.
- SHRAIMAN, B. and D. BENSIMON (1984). "Singularities in Nonlocal Interface Dynamics." Physical Review A **30**(5): 2840-2842.
- SIMKIN, E. M. (1993). "A possible mechanism of vibroseismic action on an oil-bearing bed." Journal of Engineering Physics and Thermophysics **64**(4): 355-359.
- SIMKIN, E. M. and M. L. SURGUCHEV (1991). Advanced vibroseismic technique for water flooded reservoir stimulation, Mechanism and field tests results. The 6th European IOR Symposium, Stavanger, Norway.
- SIMKIN, É. M., *et al.* (1991). "Effect of elastic vibrations on the capillary imbibition of water by oil-saturated porous media." Dokl. Akad. Nauk SSSR **317**: 1334.
- SIMONOV, B. F., *et al.* (2000). "Vibro-seismic stimulation of oil bearing formations from the surface." Neftyanoe Khozyaistvo(5): 41-46.
- SMEULDERS, D. M. J., *et al.* (1992). "Dynamic Permeability - Reformulation of Theory and New Experimental and Numerical Data." Journal of Fluid Mechanics **245**: 211-227.
- SPANOS, T., *et al.* (2003). "Pressure pulsing at the reservoir scale: A new IOR approach." Journal of Canadian Petroleum Technology **42**(2): 16-28.
- STOLL, R. D. (2002). "Velocity dispersion in water-saturated granular sediment." Journal of the Acoustical Society of America **111**(2): 785-793.
- STOLL, R. D. and G. M. BRYAN (1970). "Wave Attenuation in Saturated Sediments." Journal of the Acoustical Society of America **47**(5): 1440-&.
- TAKABATAKE, S., *et al.* (1988). "Peristaltic Pumping in Circular Cylindrical-Tubes - a Numerical Study of Fluid Transport and Its Efficiency." Journal of Fluid Mechanics **193**: 267-283.

- TAMURA, S., *et al.* (2005). "Liquid adhesion to an ultrasonically vibrating end surface." Journal of Applied Physics **98**(6): 063524-063524-6.
- TROGUS, F. J., *et al.* (1977). "Static and Dynamic Adsorption of Anionic and Nonionic Surfactants." Society of Petroleum Engineers Journal **17**(5): 337-344.
- TSIKLAURI, D. (2002). "Phenomenological model of propagation of the elastic waves in a fluid-saturated porous solid with nonzero boundary slip velocity." Journal of the Acoustical Society of America **112**(3): 843-849.
- TSIKLAURI, D. and I. BERESNEV (2001). "Non-Newtonian effects in the peristaltic flow of a Maxwell fluid." Physical Review E **64**03(3): -.
- TUFAILE, A., *et al.* (1999). "Simulations in a dripping faucet experiment." Physics Letters A **255**(1-2): 58-64.
- VAKHITOV, G. G. and E. M. SIMKIN (1985). "Use of physical fields in oil recovery (Ispol'zovaniye fizicheskikh poley dlia izvlecheniya nefi iz plastov)." Nedra Press.
- VAN DER BAS, F., *et al.* (2004). SPE 88767 - Near Wellbore Stimulation by Acoustic Waves. 11th Abu Dhabi International Petroleum Exhibition and Conference, Abu Dhabi, U.A.E.
- VARADARAJ, R., *et al.* (1994). "Influence of Surfactant Structure on Wettability Modification of Hydrophobic Granular Surfaces." Journal of Colloid and Interface Science **167**(1): 207-210.
- VENKITARAMAN, A., *et al.* (1995). "Ultrasonic Removal of near-Wellbore Damage Caused by Fines and Mud Solids." SPE Drilling & Completion **10**(3): 193-197.
- VIKSUND, B. G., *et al.* (1998). Initial water saturation and oil recovery from chalk and sandstone by spontaneous imbibition. 1998 International Symposium of the Society of Core Analysts, The Hague, Netherlands.

- VOGLER, E. T. and C. V. Chrysikopoulos (2004). "An experimental study of acoustically enhanced NAPL dissolution in porous media." AICHE Journal **50**(12): 3271-3280.
- VOUTERS, M., *et al.* (2004). "Ultrasounds: an industrial solution to optimize costs, environmental requests and quality for textile finishing." Ultrasonics Sonochemistry **11**(1): 33-38.
- WILKINSON, M. C. (1972). "Extended Use of, and Comments on, Drop-Weight (Drop-Volume) Technique for Determination of Surface and Interfacial Tensions." Journal of Colloid and Interface Science **40**(1): 14-&.
- WINKLER, K. W., *et al.* (1989). "Permeability and Borehole Stoneley Waves - Comparison between Experiment and Theory." Geophysics **54**(1): 66-75.
- WITTEN, T. A. and L. M. SANDER (1981). "Diffusion-Limited Aggregation, a Kinetic Critical Phenomenon." Physical Review Letters **47**(19): 1400-1403.
- WONG, S. W., *et al.* (2003). SPE 82198 - Near Wellbore Stimulation by Acoustic Waves. 2003 SPE European Formation Damage Conference, The Hague, Netherlands.
- WONG, S. W., *et al.* (2004). "High-power/high-frequency acoustic stimulation: A novel and effective wellbore stimulation technology." SPE Production & Facilities **19**(4): 183-188.
- YACHMENEV, V. G., *et al.* (1998). "Use of ultrasonic energy in the enzymatic treatment of cotton fabric." Industrial & Engineering Chemistry Research **37**(10): 3919-3923.
- YEN, T. F. and K. DUNN (1999). "Conversion of a refinery asphaltene under ultrasound." Abstracts of Papers of the American Chemical Society **217**: U233-U233.
- YIN, F. and Y. C. FUNG (1969). "Peristaltic Waves in Circular Cylindrical Tubes." Journal of Applied Mechanics **36**(3): 579-&.
- ZASLAVSKII, Y. M. (2002). "Experimental study of the motion of liquid droplets in a capillary under vibration." Acoustical Physics **48**(1): 50-53.

- ZHANG, X. G. (1999a). "Dynamics of drop formation in viscous flows." Chemical Engineering Science **54**(12): 1759-1774.
- ZHANG, X. G. (1999b). "Dynamics of growth and breakup of viscous pendant drops into air." Journal of Colloid and Interface Science **212**(1): 107-122.
- ZHANG, X. G. and O. A. BASARAN (1995). "An Experimental-Study of Dynamics of Drop Formation." Physics of Fluids **7**(6): 1184-1203.
- ZHANG, X. Y., *et al.* (1996). "Experimental verification of a modified scaling group for spontaneous imbibition." SPE Reservoir Engineering **11**(4): 280-285.
- ZHOU, D., *et al.* (2002). "Scaling of counter-current imbibition processes in low-permeability porous media." Journal of Petroleum Science and Engineering **33**(1-3): 61-74.
- ZHOU, M. Y. and P. SHENG (1989). "First-Principles Calculations of Dynamic Permeability in Porous-Media." Physical Review B **39**(16): 12027-12039.
- ZHOU, X. M., *et al.* (2000). "Interrelationship of wettability, initial water saturation, aging time, and oil recovery by spontaneous imbibition and waterflooding." SPE Journal **5**(2): 199-207.
- ZIMMERMANN, C. and M. STERN (1994). "Analytical Solutions For Harmonic Wave Propagation in Poroelastic Media." Journal of Eng. Mech. **120**(10): 2154.
- ZOBNIN, A. I., *et al.* (1988). "Linearized Equations of Motion of a Viscous Fluid in a Porous Medium of Periodic Structure." Fluid Dynamics **23**(2): 260-266.

Appendix A: Equipment

Ultrasonic Equipment:

Misonix Sonicator® 3000
Misonix Sonicator® 3000 generator
Misonix ¼” Horn
Misonix ½” Horn (for Floccell™)
Misonix Microtip Horn
Misonix Floccell™
Misonix Booster Horn
Sonabox Enclosure

Purchased from:

Mandel Scientific Company Inc.
2 Admiral Place
Guelph, Ontario
N1G 4N4
www.mandel.ca

Pumps:

Kent Scientific Genie (syringe pump)

THE KENT SCIENTIFIC
CORPORATION
1116 Litchfield Street
Torrington, CT 06790
TEL: (860)626-1172
FAX: (860)626-1179

HNP Mikrosysteme MZR-7205 (micro
annular gear pump)

HNP Mikrosysteme GmbH
Juri-Gagarin-Ring 4
D-19370 Parchim
GERMANY

Chemicals:

Kerosene, Light Mineral Oil, Heavy
Mineral Oil, Pentane, Heptane, Toluene,
Acetone, Ethanol, NaCl

Fisher Scientific Company
112 Colonnade Road
Ottawa, Ontario
K2E 7L6

S60, S200, N350, S600

CANNON Instrument Company
2139 High Tech Road
State College PA 16803, USA

DOWFAX 2A1, 3B0
TERGITOL 15-S-7

Dow Chemical Canada Inc.
Suite 2100
450 - 1st Street S.W.
Calgary, Alberta T2P 5H1

Fluorescent dye: IFWB-C0 and DFSB-
K43

Risk Reactor
21544 Newland Street
Huntington Beach, California 92646,
USA

Accessories:

Fittings, tubing, valves

Swagelok Company
31400 Aurora Road
Solon, Ohio, 44139, USA

Darklight

Spencer Gifts
West Edmonton Mall
2472, 8882 - 170 Street
Edmonton, Alberta, Canada
T5T 4M2

Visualization:

Canon EOS Rebel
Canon Optura Xi

Canon Canada Inc.
6390 Dixie Road
Mississauga, Ontario
L5T 1P7

Appendix B: Publications resulting from this work

1. **Hamida, T.** and Babadagli, T.: "Effects of Ultrasonic Waves on Immiscible and Miscible Displacement in Porous Media," SPE 95327, 2005 SPE Annual Technical Conference and Exhibition, Dallas, TX, 9-12 Oct., 2005.
2. **Hamida, T.** and Babadagli, T.: "Investigations on the Capillary Interaction of Different Oleic and Aqueous Phases between Matrix and Fracture Under Ultrasonic Waves," SPE 94105, SPE EUROPEC / EAGE Annual Conf., 13-16 Jun 2005, Madrid, Spain.
3. **Hamida, T.** and Babadagli, T.: "Investigations on Capillary and Viscous Displacement under Ultrasonic Waves," Paper No. 2005-132, CIM 56th Annual Technical Meeting, Canadian International Petroleum Conference, Calgary, Canada, 7-9 June 2005 (extended abstract).
4. **Hamida, T.** and Babadagli, T.: "Effect of Ultrasonic Waves on the Capillary Imbibition Recovery of Oil," SPE 92124, SPE Asia Pacific Oil & Gas Conf. and Exh., 12 - 14 April 2005, Jakarta, Indonesia.
5. Babadagli, T., Hatiboglu, C. U. and **Hamida, T.**: "Evaluation of Matrix-Fracture Transfer Functions for Counter-Current Capillary Imbibition," SPE 92111, SPE Asia Pacific Oil & Gas Conf. and Exh., 12 - 14 April 2005, Jakarta, Indonesia
6. Babadagli, T. and **Hamida, T.**: "Multiphase Flow in Porous Media Under Ultrasonic Waves," The Stanford-Herriot-Watt Reservoir Description and Modeling Forum, Tiburon, CA, USA, Aug. 28-Sept. 2, 2005 (invited).
7. **Hamida, T.** and Babadagli, T.: "Investigations on Capillary and Viscous Displacement under Ultrasonic Waves," Technical Note, *J. of Canadian Pet. Tech.*, Feb. 2006, 16-19.
8. **Hamida, T.** and Babadagli, T.: "Analysis of Capillary Interaction and Oil Recovery under Ultrasonic Waves," submitted to *Transport in Porous Media*, for publication (in review) 2006.
9. **Hamida, T.** and Babadagli, T.: "Viscous Fingering during Miscible and Immiscible Displacement under Ultrasonic Waves," to be submitted to *J. of Fluid Mechanics* for publication 2006.
10. **Hamida, T.** and Babadagli, T.: "Effects of Ultrasonic Waves on Immiscible Displacement in Consolidated Porous Media due to Capillary Imbibition," to be submitted to *Ultrasonics Sonochemistry*, for publication 2006.